

POLITECNICO DI MILANO

Scuola di Ingegneria Industriale

Corso di Laurea in
Ingegneria Meccanica



Curve squeal noise modelling: the influence of a second contact
point

Relatore: Prof. Roberto Corradi
Relatore: Prof. David J. Thompson
Co-relatore: Dr. Giacomo Squicciarini

Tesi di Laurea di:
Samuele Usberti Matr. 769098

Anno Accademico 2012-2013

A mio padre

Acknowledgements

I would like to say '*Thank you!!!*' at the professor David Thompson for supervising, helping and guiding me during my work of thesis and because I had the possibility to learn a lot of things. A special thanks goes also to Giacomo Squicciarini that helped me during my work in many ways and in particular because he transmitted me the passion to learn and know the things. Finally, I would like to thank Roberto Corradi because gave me the possibility to do this fantastic work and helped me during my dissertation with Andrea Barbera.

Contents

Contents	i
Estratto in lingua italiana	1
Introduction	7
1 Railway curve squeal: state of the art	13
2 Squeal noise measurements	21
2.1 Sirio tram in Milan (Italy)	21
2.1.1 Experimental modal analysis of the wheel	22
2.1.2 Noise and vibration measurements	34
2.2 British Rail Class 150 Sprinter in North Wales	50
3 Wheel finite element modelling	57
3.1 Resilient wheel of Sirio tram	57
3.1.1 Procedure to determine the rubber parameters for the FE model	57
3.1.2 First model	62
3.1.3 Second model	65
3.1.4 Third model	69
3.1.5 Fourth model	70
3.2 Class 15x wheel	77
4 Numerical model for tramcar vehicle dynamics simulation	81
4.1 The vehicle model	82
4.2 Wheel-rail contact model	84
4.3 Steady-state behaviour	85
4.4 Numerical results - Simulation with gauge of 1445 mm	88

4.4.1	Lateral displacements	88
4.4.2	Vertical forces	89
4.4.3	Lateral forces	90
4.4.4	Longitudinal forces	92
4.4.5	Numerical results at the contact points	92
4.5	Numerical results - Simulation with gauge of 1447 mm	102
4.5.1	Numerical results at the contact points	102
4.6	Numerical results - Simulation with gauge of 1450 mm	106
4.6.1	Numerical results at the contact points	106
4.7	Conclusion	110
5	Rolling friction model and self-excited vibration	113
5.1	Rolling friction model	114
5.1.1	Friction curve	114
5.1.2	Theoretical model adopted for the friction curve in adhering	115
5.1.3	Heuristic formula for falling friction in sliding	115
5.1.4	Hertz contact spring	116
5.2	Self-excited vibration	116
5.2.1	Equations of motion	116
5.2.2	Self-excited vibration	118
5.2.3	Self-excited vibration in a single-mode wheel	120
6	Squeal model for single wheel/rail contact	123
6.1	Wheel/rail rolling contact dynamics	124
6.1.1	Wheel/rail rolling contact dynamics in the time domain	124
6.1.2	Wheel/rail rolling contact dynamics in the frequency domain	128
6.2	Self-excited vibration loop in the frequency domain	135
6.3	Stability analysis for the frequency domain loop	136
6.3.1	Stability analysis for the lateral motion	136
6.3.2	Stability analysis for the general system	137
6.4	Wheel/rail structural dynamics for time domain model	137
6.4.1	Wheel structural dynamics	138
6.4.2	Rail structural dynamics	139
6.5	Self-excited vibration loop in the time domain	141
6.6	Results	144

6.6.1	Friction curve	144
6.6.2	Analysis in frequency domain	145
6.6.3	On understanding the shift in frequency	164
6.6.4	Analysis in time domain	172
7	Squeal model for two contact points	177
7.1	Analysis in frequency domain	178
7.2	Analysis in the time domain	190
7.3	Results	193
7.3.1	Case of British Rail Class 150 Sprinter	194
7.3.2	Case of Sirio tram in Milan	207
	Conclusions	217
	A Rigid transformation of dynamic properties	219
	Bibliography	225
	List of Figures	231
	List of Tables	241

Abstract

A real case of a city tramcar in Milan generating very high curve squeal noise levels has motivated research in this area considering the simultaneous presence of two contact points. Along with this example another one from the British Railways will also be explored. In this thesis available measurements are summarised in a qualitative manner in order to highlight the most important frequencies involved and a theoretical model in the frequency and time domain is developed with the aim of predicting curve squeal tones. Results are presented from a frequency domain point of view. Good matching is found between numerically predicted and measured unstable frequencies and a peculiar shift toward higher frequencies is found both in measurements and predictions.

Key words: Finite element model, numerical model for dynamics simulation, friction model, self-excited vibration loop, curve squeal noise model, two contact points, frequency domain, time domain.

Sommario

Un caso reale di tram circolante a Milano che genera livelli elevati di rumore di stridio in curva ha motivato la ricerca in questa area considerando la contemporanea presenza di due punti di contatto. Durante questo lavoro, è stato studiato un altro caso proveniente dalla ferrovia Britannica. In questa tesi sono disponibili misurazioni riassunte in maniera qualitativa allo scopo di evidenziare le più importanti frequenze coinvolte. È stato sviluppato un modello teorico nel dominio delle frequenze e del tempo con lo scopo di prevedere i toni di stridio in curva, i risultati presentati sono nel dominio delle frequenze. È stata trovata una buona corrispondenza sulle frequenze instabili, fra quelle misurate e quelle predette numericamente. Inoltre, un particolare spostamento verso alte frequenze è stato osservato sia nelle misurazioni che in quelle previste.

Parole chiave: Modello a elementi finiti, modello numerico per simulazioni dinamiche, modello di attrito, modello di rumore di stridio in curva, due punti di contatto, dominio delle frequenze, dominio del tempo.

Estratto in lingua italiana

Il trasporto ferroviario fu la prima forma di trasporto meccanizzato su terra [1]; è una importante forma di trasporto e lo rimarrà nel prossimo futuro. Al giorno d'oggi il trasporto su rotaia, oltre a garantire lunghi tratti di percorrenza, è in grado di risolvere problemi di congestione in aree popolate come le città.

L'inquinamento acustico e le vibrazioni generate dal trasporto su rotaia, sfortunatamente, ne limitano la promozione. Il rumore generato può essere causato da due diversi principali meccanismi: vibrazioni strutturali dovute al contatto ruota/rotaia e fluttuazioni aerodinamiche dovute alla turbolenza dell'aria, in particolare all'interazione tra vento e solidi. La prima è la principale fonte di disturbo per treni che viaggiano a una velocità inferiore ai 300 km/h, mentre la seconda domina il livello di rumore per treni che percorrono a velocità superiori.

Thompson e Jones [2] divisero il rumore ferroviario in tre basilari categorie:

- Rolling noise è il principale contributo di vibrazione che si verifica sui rettilinei, causato dalle ondulazioni della ruota e della rotaia (rugosità) le quali inducono una vibrazione relativa verticale.
- Impact noise è una forma estrema di rolling noise dovuto alle discontinuità superficiali di ruota e rotaia.
- Squeal noise si verifica in curve strette e di solito è indotto da un meccanismo di eccitazione laterale. Più stretta è la curva e maggiore è la possibilità che l'emissione di stridio possa presentarsi. Ecco il motivo per il quale questo tipo di inquinamento acustico si verifica principalmente nei centri urbani dove la presenza delle strutture civili obbligano la messa a terra dei binari a volte con curve a piccolo raggio. Questo tipo di rumore è spesso fastidioso per la popolazione e qualche volta può diventare un vero e proprio problema per le persone che vivono vicino alla carreggiata dei tram.

L'oggetto di questo lavoro è una investigazione di quest'ultimo aspetto. I due obbiettivi cardinali della tesi sono rivedere e aggiornare il modello squeal sviluppato da Zhenyu Huang [3] e utilizzarlo per cercare di comprendere un specifico caso di rumore di stridio in curva misurato a Milano nel 2010 [4] e di un secondo esempio proveniente dalla flotta Sprinter della ferrovia britannica.

Il lavoro centrale di Huang fu quello di descrivere la generazione di stridio in curva tramite un modello in anello chiuso autoeccitato rappresentante le relazioni tra ruota/rotaia e le forze di contatto. Eseguendo l'analisi di stabilità nel dominio delle frequenze, i possibili modi di vibrare della ruota coinvolti in stridio furono evidenziati per una particolare combinazione ruota-rotaia, mentre l'integrazione nel dominio del tempo dell'anello potrebbe fornire l'intensità dello stridio. In questo modello la ruota è descritta tramite una rappresentazione a elementi finiti mentre la rotaia attraverso modelli analitici sofisticati contenenti l'accoppiamento laterale-torsionale che si verifica ad elevate frequenze. Il contatto è descritto in termini di relazioni non-lineari tra coefficienti d'attrito e pseudoslittamenti: particolare attrito adesivo nella zona di piccoli pseudoslittamenti a decadimento nella regione di scorrimento. Il contatto tra ruota e rotaia fu permesso, all'inizio, solamente in un'unica posizione di contatto, ma parte del lavoro di ricerca descritto nella tesi è stato dedicato al miglioramento del modello originale per permettere la contemporanea presenza di due punti di contatto. Inoltre, siccome questo fenomeno è lontano dall'essere deterministico e parametri come temperatura, umidità e sporcizia o particelle sulla rotaia possono avere un forte effetto sul suo verificarsi, nel modello nel dominio del tempo con uno e due punti di contatto, alcuni parametri di input sono, nella versione aggiornata del software, definiti come variabili incerte. Come risultato, il modello è usato per dare valori di frequenza di possibili autovalori instabili del sistema mentre l'intervallo dei parametri incerti è attraversato in modo casuale.

Come accennato in precedenza, due differenti casi sono stati investigati da un punto di vista sperimentale allo scopo di verificare la bontà del modello migliorato con due punti di contatto. Il primo riguarda un tram con ruote elastiche indipendenti in curve molto strette (caso tram Sirio a Milano) mentre il secondo riguarda treni in curve con 'check-rail'(caso Class 150 Sprinter nel nord del Galles).

Il primo caso investigato è anche la motivazione di questa ricerca che ha attual-

mente la sua origine in una campagna sperimentale svolta a Milano nel 2010-2011 coinvolgendo il Politecnico di Milano e i servizi locali di trasporto ATM. Questa campagna mirava a investigare l'alto livello di rumore presente in diverse curve strette attorno la città durante il passaggio del nuovissimo tram chiamato Sirio. Questo tram è montato su ruote elastiche indipendenti. Prima di tutto, una procedura di analisi modale sperimentale ha permesso la caratterizzazione della ruota in termini di quelle che sono state considerate le più importanti frequenze naturali, rapporti di smorzamento e forme modali fino a 4 kHz. Successivamente, sono state eseguite misurazioni simultanee di vibrazione del binario, della ruota e del rumore irradiato durante il transito del tram lungo una curva stretta. Importanti caratteristiche sono state osservate durante le misurazioni e vengono riassunte in questa tesi nel Capitolo 2, comunque una semplice soluzione per attenuare il fenomeno non è stata trovata, inoltre non è possibile spiegare alcuni aspetti basandosi solo su questi risultati. Ciò che risultò chiaro fin dall'inizio fu la contemporanea presenza di più di un contatto, essendo, per la ruota anteriore interna, la flangia interna spesso in contatto con la controrotaia e la flangia esterna della ruota esterna in contatto con la testa della rotaia.

Gli scorsi anni, il dipartimento di ingegneria meccanica del Politecnico di Milano fu intensamente coinvolto allo scopo di investigare il comportamento dinamico del tram caratterizzato da diverse configurazioni strutturali, soluzioni progettuali (per esempio, telaio del carrello articolato, ruote indipendenti) e condizioni operative (per esempio, raggio di curvatura e velocità operativa). Il modello numerico sviluppato [5], [6] ha la capacità, per ogni particolare istante di tempo, di riprodurre il comportamento dinamico del veicolo in termini di stato stazionario e transitorio (per esempio, dovuto all'inserimento in curva o all'eccitazione dovuta all'irregolarità della rotaia). Siccome lo stridio prende forma sotto specifiche condizioni operative, i parametri relazionati con il comportamento stazionario in curva sono necessari per una corretta investigazione del fenomeno. Per questa ragione, allo scopo di ottenere questi parametri, una simulazione di tram in curva potrebbe essere eseguita usando l'implementato simulatore di tram sviluppato a Milano. Parecchi e interessanti risultati potrebbero essere ottenuti da questa simulazione, come la posizione dei punti di contatto tra ruota e rotaia, pseudoslittamenti longitudinali e laterali e la distribuzione di forze sulle diverse ruote (vedere Capitolo 4). Questi sono stati utilizzati come input per il modello di stridio adottato in questa tesi per predire il verificarsi di questo fenomeno.

Il secondo caso investigato riguarda le nuove unità Class 150 Sprinter. Quando questo treno fu introdotto sulle tratte da Llandudno a Blaenau Ffestiniog nel nord del Galles, un numero di reclami nacquero dall'intenso rumore di stridio generato durante la curva. Per ragioni di sicurezza, alcune curve di queste rotaie furono attrezzate con 'check-rail'. Un programma di misurazione fu eseguito nel Maggio del 1987 nel quale microfoni furono posizionati vicino ad ogni ruota dell'assile anteriore [7]. Osservando l'analisi in frequenza risultò chiaro che le frequenze coinvolte nello stridio erano correlate ai modi radiali della ruota. La causa di questo particolare problema fu riconosciuta nelle forze verticali di adesione/scorrimento agenti tra 'check-rail' e flangia interna della ruota.

Perciò, lo scopo è di riprodurre questa particolare condizione di contatto tra flangia interna e 'check-rail' e verificare tramite il modello con due punti di contatto che le frequenze predette siano correlate a modi radiali.

Struttura della tesi

Questa tesi si divide in sette capitoli come segue:

Capitolo 1. Stridio in curva: stato dell'arte. In questo capitolo si riporta una panoramica di cosa fu investigato e scoperto nei precedenti anni riguardo il rumore di stridio.

Capitolo 2. Misurazioni del rumore di stridio. In questo capitolo le misurazioni eseguite a Milano durante il transito del tram Sirio in curve strette sono illustrate allo scopo di investigare quali frequenze sono coinvolte nella generazione del rumore. L'ultima parte riguarda le misurazioni eseguite in Galles allo scopo di investigare il verificarsi dello stridio quando il treno Sprinter percorre curve attrezzate con 'check-rail'.

Capitolo 3. Modellazione della ruota ad elementi finiti. In questo capitolo il modello a elementi finiti del tram Sirio e treno Sprinter sono descritti.

Capitolo 4. Modello numerico per simulazione dinamica del tram. In questo capitolo un modello numerico sviluppato dal Politecnico di Milano è descritto allo scopo di ottenere i parametri necessari relazionati con il comportamento stazionario in curva nel caso del tram Sirio.

Capitolo 5. Modello di attrito e vibrazioni autoeccitate. Nella prima

parte di questo capitolo è descritto il modello di attrito adottato nella formulazione di Huang, mentre nella seconda parte viene affrontato un problema classico di vibrazioni autoeccitate, una massa su un nastro in movimento.

Capitolo 6. Modello di stridio per singolo contatto ruota/rotaia.

In questo capitolo è stato descritto il modello di stridio in curva sviluppato da Huang. Il modello in anello chiuso autoeccitato nel dominio delle frequenze è usato per investigare la stabilità. Poi, l'anello di vibrazione autoeccitato in forma di stato permette, tramite integrazione 'step-by-step', di calcolare le risposte nel dominio del tempo.

Capitolo 7. Modello di stridio per due punti di contatto. In questo capitolo il modello di Huang aggiornato con due punti di contatto nel dominio delle frequenze e del tempo è ampiamente descritto. I risultati ottenuti dal caso Sirio e Sprinter sono presentati nel dominio delle frequenze.

Introduction

Railways were the first practical form of mechanized land transport [1]. They remain an important form of transport and will remain so in the near future. Nowadays railways are the best solution to the problem of congestion in populated areas.

Unfortunately, the environmental effects of noise and vibration work against this promotion of railways. Railway noise can be generated by two main mechanisms: structural vibration due to the wheel and rail contact and aerodynamic fluctuations due to the air turbulence when wind flows over solid objects. The first one is the main mechanism of noise source for trains running below the speed of 300 km/h, while the second one dominates the noise level for trains running at speeds above 300 km/h.

Thompson and Jones [2] divided railway noise into three main categories:

- Rolling noise is the main contribution on straight track and is caused by undulations of the wheel and rail surfaces (roughness) which induce a vertical relative vibration.
- Impact noise is an extreme form of rolling noise occurring at discontinuities of the wheel or rail surface.
- Squeal noise, occurring on tight radius curves, is usually induced by a lateral excitation mechanism. The shorter is the curve radius, the higher are the possibilities that squealing emission may appear. Short radius curves are present in urban tracks because of the presence of pre-existing buildings. This kind of noise emission is often annoying for the people and sometimes becomes a very important problem for people living near the tracks.

Indeed, curve squeal noise is the research area of this work. The two main aims of the thesis are to review and update the curve squeal model developed

by Zhenyu Huang [3] and to use this model for bringing more understating in a specific real case of tram curve squeal noise measured in Milan, Italy in 2010 [4]. Along with this example another one from the British Railways Sprinter fleet will also be explored.

The central work of Huang's thesis was to describe curve squeal noise generation by means of a self-excited feedback loop model representing relations between wheel/rail motions and contact forces. By performing stability analysis in the frequency domain the possible wheel vibration modes involved in squeal were highlighted for a particular combination of wheel rail, while a time domain integration of the loop could provide the intensity of squeal. In this model the wheel is considered through a Finite Element representation while the rail through advanced analytical models accounting for lateral-torsional coupling occurring at high frequencies. The contact is described in terms of a nonlinear relationship between friction coefficients and creepage: in particular adhering friction at small creepages and falling friction in sliding. Contact between wheel and rail was initially only allowed at one single position but part of the research work described in this thesis has been devoted to improving the original model for allowing two contact positions to occur at the same time.

Moreover, since it is known that the curve squeal phenomenon is far from being deterministic and parameters like temperature, humidity and even dirt and particles on the rail can have a strong effect on its occurrence, in the frequency domain model with one and two contact points, some input parameters are, in the updated version of the software, defined as uncertain variables. As a result, the model is used to give the frequency values of possible unstable eigenvalues of the system while the range of uncertain parameters is randomly spanned.

As stated above, two different cases have been investigated from an experimental point of view in order to verify the suitability of the improved model with two contact points. The first one considers a city tramway with independent resilient wheels on very sharp curves (case-Sirio tram in Milan) while the second one considers train on a curve with check-rail (case-British Rail Class 150 Sprinter in North Wales).

The first case investigated was also the original motivation of this research that has its origin in an experimental campaign that took place in Milan in 2010-

2011 involving Politecnico di Milano and the local transport service ATM. It was aimed at investigating the high level of curve squeal noise present in several tight curves around the city during the passages of the newest rolling stock tram named Sirio. This tram is fitted with resilient independent wheels. Firstly, experimental modal analysis procedures allowed characterising the wheel in terms of natural frequencies, damping ratios and mode shapes up to 4 kHz that were believed to be the most important. Afterwards, simultaneous measurements of rail vibration, wheel vibration and radiated noise were performed during the tramcar transit in a sharp curve. Many interesting features were captured during measurements and they will be summarized later on in this thesis (see Chapter 2), however a simple solution for mitigating the phenomenon was not found and moreover some details could not entirely be explained by looking at the results. What was clear from the beginning was the simultaneous presence of more than one contact point. For the front inner wheel of a bogie, this was the flange back often in contact with the rail grooved head while the flange of the outer wheel was in contact with the rail running head.

During the last years, the Mechanical Engineering Department of Politecnico di Milano was extensively involved in order to investigate the dynamic behaviour of tramcars characterized by different structural configurations, design solutions (e.g., articulated bogie frames, independently rotating wheel) and operating condition (e.g., curve radius and operation speed). The developed numerical model [5], [6] has the capability, at each particular instant in time, to reproduce the vehicle dynamic behaviour during the curve in terms of steady-state and transient behaviour (e.g., due to curve negotiation or track irregularity excitation). Since the squealing takes place under specified operation conditions, the parameters related with steady-state curving behaviour are needed for a correct investigation of the phenomenon. For this reason, in order to obtain these parameters, a case of a tramcar running in a curved track could be performed using the implemented tramcar simulator developed in Milan. Many interesting results could be obtained from this simulation, like the position of the contact points between wheel and rail, longitudinal and lateral creepages and the force distribution on the different wheels (see chapter 4). These have been input into the curve squeal model adopted in this thesis to predict the occurrence of this phenomenon.

The second case investigated regards the Class 150 Sprinter units in the UK. When this train was introduced on the Llandudno to Blaenau Ffestiniog line

in North Wales, a number of complaints arose from the intense squealing noise generated during curving. The track on these curves was fitted with check rails. A measurement programme was performed in May 1987 in which microphones were placed adjacent to each wheel of the leading bogie of a Class 150 unit [7]. From the frequency analysis it was clear that the frequencies involved in squeal were correlated with radial modes of the wheel. The cause of this particular squeal problem was believed to be due to vertical stick/slip forces acting between the check rail and the wheel flange.

Therefore, the aim is to reproduce this particular contact condition between flange back and check rail and verify by means of the model with two contact points that the predicted frequencies are correlated to radial modes.

Structure of the thesis

This dissertation is divided into seven chapters as follows:

Chapter 1. Railway curve squeal: state of the art. In this chapter an overview of what was investigated and discovered in previous years regarding the squeal noise phenomenon is described.

Chapter 2. Squeal noise measurements. In this chapter the measurements performed in Milan during the transit of a Sirio tram in a sharp curve are illustrated in order to investigate which frequencies are involved for generating squeal. The last part considers the measurements performed in Wales in order to investigate the occurrences of squeal noise when a Sprinter train negotiates curves fitted with check rails.

Chapter 3. Wheel finite element modelling. In this chapter the finite element model of Sirio tram and Sprinter train wheels are described.

Chapter 4. Numerical model for tramcar vehicle dynamics simulation. In this chapter a numerical model developed by Politecnico di Milano is described in order to obtain the necessary parameters related with steady-state curving behaviour in the case of the Sirio tram.

Chapter 5. Rolling friction model and self-excited vibration. First part of this chapter describes the friction model adopted in the Huang's model. In the second part the classic self-excited vibration problem, a mass on a moving

belt, is studied.

Chapter 6. Squeal model for single wheel/rail contact. In this chapter the curve squeal model developed by Huang is described. The frequency domain self-excited feedback loop model is used to investigate the stability. Then, the state-space self-excited vibration loop allows, by step-by-step integration, the time domain responses to be calculated.

Chapter 7. Squeal model for two contact points. In this chapter the improved Huang's model with two contact points in frequency and time domain is described. Results obtained from the case of the Sirio tram and Sprinter train are presented in terms of frequency domain.

Chapter 1

Railway curve squeal: state of the art

Curve squeal is a high-pitched noise that can disturb residents and occupants of trains and trams. This phenomenon is induced when the tramcar negotiates curved track but in particular it is generated from the unstable response of a railway wheel and rail. In this coupling configuration between bogie and rails, the real velocity direction of the bogie is not equal to the motion direction. For this reason a lateral relative velocity occurs which causes a sliding between wheel and rail. The creepage can be used to describe this sliding within the contact region and is defined as the ratio of the relative velocity between two bodies in rolling contact and the rolling velocity. The stick/slip phenomenon generated by the lateral sliding velocity induces a lateral creep force which originates the excitation of the wheel and the rail. The sound radiation generated from the wheel and rail vibrations is the reason for the squeal noise.

Von Stappenbeck [8] was the first to suggest, in 1954, that the lateral creep force is the main reason for generating squeal noise. Then, he observed, by measurements, that the high sound pressure levels of squealing noise can be assigned to the natural frequencies of the wheel only and in particular at the inner front wheel.

Rudd [9], in 1976, proposed that the squeal noise might be excited by the different wheel/rail contact conditions: lateral creepage at the contact between wheel tyre and rail tread, wheel flange rubbing on the rail gauge face, and longitudinal creepage at the contact on the wheel tyre due to differential slip. Despite occasional conflicting results, almost all curve squeal noise experiments carried

out reinforce the Von Stappenbeck's hypothesis [8] that the lateral creep forces are responsible for generating squeal. Rudd also confirmed, using a simple wheel-rail model with measured impedances, that the sound radiation of the rail may be neglected in comparison to the wheel [8].

Rudd gave little attention to differential slip or flange rubbing as mechanisms for squeal, but most of the work was focused on the lateral creepage excitation mechanism. He was the first to indicate that the wheel response is unstable due to the decreasing friction forces at large sliding velocities when the friction forces are saturated. The slope of the friction curve in the falling regime is not constant [10] and this nonlinearity limits the unstable response to a stable amplitude (limit cycle).

Many of the subsequent models that appear in the literature adopt parts of Rudd's approach to the theoretical modeling of squeal. Most of the models begin by assuming a characteristic of the creepage-dependent friction coefficient. Van Ruiten [11], for example, applied Rudd's model to trams.

In a review article, Remington [12] described the state of knowledge of railway curve squeal up to 1985. Based on the analyses of published curve squeal literature and related experimental results, he pointed out that to resolve questions on curve squeal noise it would be necessary to develop a comprehensive analytical model of squeal. He suggested that this model should include finite element models of railway wheel dynamics, numerical models for the dynamics of bogies in curves and details of the friction coefficient versus creepage. Since then, a number of increasingly complex models for curve squeal, consisting of various sub-models, have been published.

Fingberg's investigations [13] in 1990 were aimed at realizing wheel-rail noise models for rolling and squealing noise, which describe the entire path from the excitation up to the human ear.

The model takes into account dynamic behaviour of the bogie during curving motion, details of the friction coefficient versus creepage, wheel and rail vibration characteristics and sound radiation characteristics.

The actual position of the contact and the actual creepages between the wheel and the rail were determined by numerical simulations of the curving behaviour of the bogie.

Kalker's theory [14] of rolling contact was adopted to consider the relations be-

tween the tangential forces in the contact area and the creepages. Unfortunately, this theory considers a constant sliding friction coefficient which is not satisfied in respect to squealing noise. Experiments by Remington [12] showed that the friction coefficient can decrease with increasing sliding velocity. Recently Fletcher's measurements [15] added more understanding on how the friction characteristics at large creepages depend on the contact point condition (dry or lubricated). Kraft [10] interpreted the falling region theoretically and gave an analytical approximation for friction characteristics. For modelling curve squeal Kraft's representation of friction coefficient can be included in Kalker's theory.

A mathematical rail model with diagonal mass, damping and stiffness matrices was calculated, a so-called modal model. This modal model was approximated to the calculated transfer function using a least-squares approximation.

The natural frequencies and the mode shapes of the railway wheel were calculated by finite elements. According to symmetry, only half of the wheelset had to be modelled.

To calculate the sound radiation characteristics of the wheel, the boundary element method was used. Fingberg showed that for railway wheels, modal expansion techniques are applicable not only for the vibration analysis but also for sound radiation investigations. Thus, the acoustical quantities such as sound field, sound power and radiation efficiency were calculated for the mode shapes only.

Some numerical results for the sound radiation were compared with measurements using a steel model wheel at a scale of 1:5. The total sound power was calculated from the vibration velocities of the wheel. A lateral creep of 2% and a longitudinal creep of 0% were taken into account. The overall level of velocity at the wheel contact point and the total sound power were shown as a function of the rolling velocity. The overall level of velocity grew monotonically. The total sound power showed some maxima and minima which were a consequence of the varying dominant frequency in the sound power. Unfortunately, Fingberg's measurements of squealing noise were not well-enough documented in detail for a direct comparison of measurement and calculation. The numerical results, however, showed good qualitative agreement with what was known from experiments.

Finally, the model was used to assess the level of damping required to eliminate squeal under a range of creepage configurations.

Fingberg's work was extended further by Périard [16], who included a submodel for the train body and considered more complicated wheel designs. Périard treated curve squeal as a transient phenomenon with irregular motion as the train enters

or leaves the curve.

Heckl [17] in 2000 modelled the squeal noise phenomenon by considering an annular disc model which was excited at a point on the edge by an oscillating lateral force. The disc had a uniform thickness and several out-of-plane modes. This model is analogous to a railway wheel when traversing tight curves.

The numerical simulations using this model produced time histories for the disc velocity with two distinct stages. In the first stage the lateral creep force was linear and a slip condition was induced. The results showed an unstable growth of the amplitudes. In the second stage the lateral force became non-linear and a stick-slip oscillation was induced. A limit cycle oscillation arose with a velocity amplitude which was equal to the lateral relative velocity. Heckl observed that the limit cycle amplitude determines the intensity of the squeal: the slip section is responsible for the instability, the stick section is responsible for the limit cycle. Investigating the squeal noise phenomenon, Heckl observed that wheel modes may play a relevant part in the stability behaviour and the limit cycle. She saw that whether or not an individual mode is unstable depends strongly on the damping of that mode.

The second part of Heckl's investigation [18] presented a frequency domain method which uses the disc model to assess which modes would be unstable, but only for the case of pure slip.

The final part of Heckl's investigation [19] studied active control to prevent the instabilities associated with squeal noise generation.

De Beer [20] in 2003 presented a frequency domain model of curve squeal noise due to lateral creepage. The model takes into account the contact mechanics, contact dynamics, wheel dynamics and rail dynamics.

To describe the contact mechanics, he expressed the forces and displacements as a quasi-static and a fluctuating part. Then, for very small vibration amplitude, the non-linear creepage-dependent friction coefficient $\mu(\gamma)$ was linearized. Therefore, the lateral force was written as a result of vertical force and creepage following the characteristics of the friction element.

The TWINS software package [21] was used to calculate the wheel, rail and contact spring mobilities.

The Nyquist criterion was used to determine whether or not squeal noise occurs and at which frequency. It was shown that squeal noise can occur at the fre-

quencies of the axial wheel modes. De Beer saw that the lateral contact position on the wheel tyre influences the occurrence of squeal noise and which resonance frequency becomes dominant.

A laboratory test rig, which comprised a scale model of a wheel, was prepared to generate squeal noise due to the lateral creepage. The measurements were performed in a well-controlled environment. This test rig was used for validation of the theoretical model.

The friction coefficient of the rolling contact was measured as a function of the rolling angle. This was performed for a situation in which squeal noise occurs and in a situation without squeal noise. For the non-squealing case agreement between experiment and calculations was good. For the squealing case, it was expected from theory that the friction coefficient would diminish. This was confirmed in the measurements, although the effect was much greater than indicated by the calculations.

The model of De Beer was extended by Monk-Steel and Thompson [22] in 2003 by including the case of wheel flange contact, which occurs at the leading outer wheel (and possibly the trailing inner wheel) in sharp curves.

Chiello et al. [23] in 2006 presented a curve squeal model including not only tangential dynamics (friction force) but also normal dynamics on the wheel/rail contact zone. The model can predict the unstable wheel modes and the corresponding squeal level and spectrum. The numerical results agreed with the experimental results given in a companion paper [24], where a parametric study on a 1/4 scale test rig was performed. In this experiment Koch et al. investigated the following parameters: rolling speed, wheel/rail lateral position, angle of attack and vertical load. The results showed that the squeal sound pressure amplitudes increase in direct proportion to rolling speed and to angle of attack. In addition, the influence of vertical load and lateral contact position were shown to be negligible. These results were in accordance with the field experiments on a metro system [25]. Furthermore, the results showed, in accordance with Von Stappenbeck's experiments [8], that the inner wheel of the leading axle is the major radiator of squeal noise. Koch also found that the curve squeal disappears when the wheel flange is in contact with the rail. This would appear in agreement with Bleedorn's experiments [26], which showed that flange rubbing alone doesn't produce squeal. Finally, although the numerical results showed that only

a friction coefficient decreasing with increasing creepage is able to destabilize the system and induce wheel vibrations, the measurement of the corresponding friction in dry condition was not able to identify this negative slope. A hypothesis was proposed to explain this phenomenon that the instantaneous friction coefficient may decrease with contact velocity whereas the average friction coefficient remains constant with the angle of attack, but this was not validated.

Zhenyu Huang [3] in 2007 developed a model, which can predict curve squeal. The central work of this thesis was to build a self-excited feedback loop model, representing relations between the wheel/rail motions and the contact forces (see Figure 1.1). As in the other models described so far only one contact point between wheel and rail is considered.

In order to build this model, a FE model of the wheel and an analytical model

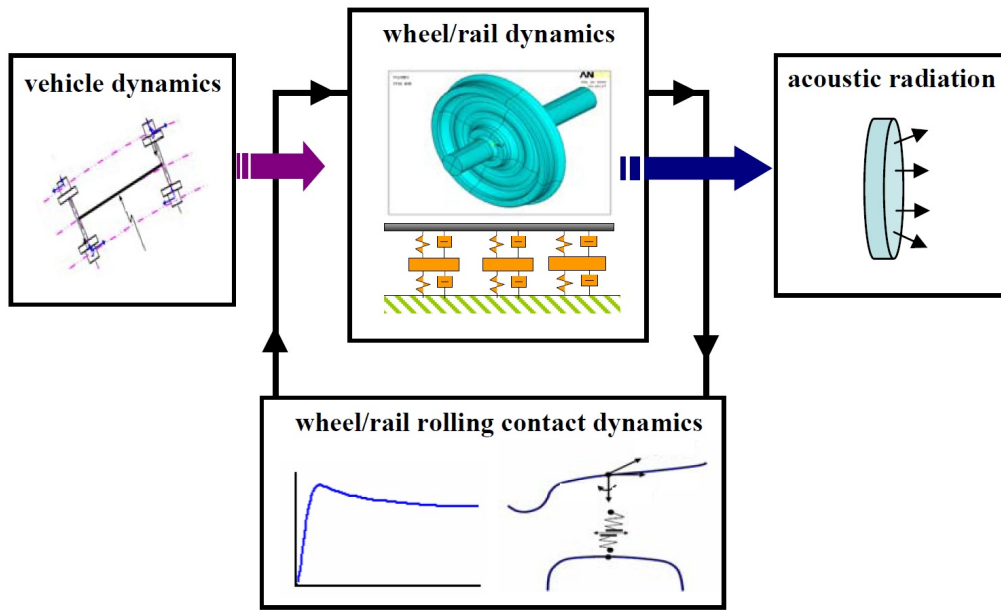


Figure 1.1: Sub-models in the general curve squeal model. Huang [3]

of the rail were adopted to describe the wheel/rail structural dynamics. Furthermore, since squealing takes place under some specified curving conditions, a vehicle dynamics model was required to provide necessary parameters related with steady-state curving behaviour. Finally, an acoustic radiation module was adopted to predict the noise level. Thus, this curve squeal model contains four sub-models: wheel and rail structural dynamics, wheel/rail rolling contact dy-

namics including the friction, vehicle dynamics, and acoustic radiation. These sub-models together constitute a loop, as shown in Figure 1.1.

Chapter 2

Squeal noise measurements

This chapter describes the two available measurement campaigns that will be used as terms of comparisons for the numerical models described later in Chapters 6 and 7. The first set of measurements was performed in Milan (Italy) between 2010 and 2011 and was aimed at characterising squeal noise of a city tramcar negotiating sharp curves (18 m radius) [4]. Experimental modal analysis was performed on the resilient wheel of the tram and rail vibration, wheel vibration and noise were simultaneously measured during curving. Noise at 1.5 m from the track centre showed that the dominant frequency was around 1550 Hz and L_{Fmax} levels could reach 120 dBA. The second available case is from the mid-1980s and deals with British Rail Class 150 Sprinter diesel multiple-unit trains (DMUs) producing high squeal noise levels when curving on 200 m radius curves in North Wales [7]. In this case the frequency dominating the noise was around 3.6 kHz and maximum recorded levels were 140 dB.

2.1 Sirio tram in Milan (Italy)

This tram was designed for the local transport service company and is fitted with independently rotating resilient wheels that contain 24 rubber elements positioned between the web and the tyre. It is available in four or seven coach configurations and in both cases bogies are rigidly connected to the body of the vehicle. Figure 2.1 shows the Sirio tram.



Figure 2.1: Photo of a Sirio tram. Reproduced from <http://www.milanotrasporti.org/>

2.1.1 Experimental modal analysis of the wheel

An experimental modal analysis campaign, performed in order to characterize the mode shapes of the wheel, was carried out twice: once with the wheel suspended and then with the wheel laid down on the rail (see Figure 2.2(a)). In both cases the wheel was mounted on a bogie frame through its own bearings. The measuring grid was formed of two concentric circles, one on the tyre and the other on the web, divided in 24 arcs that subtend angles of 15° , for a total of 48 points (see Figure 2.2(b)). For each point, five different impacts were given by means of a dynamic impact hammer, then the signals were post-processed and averaged to obtain the frequency response function (FRF), complex ratio between output

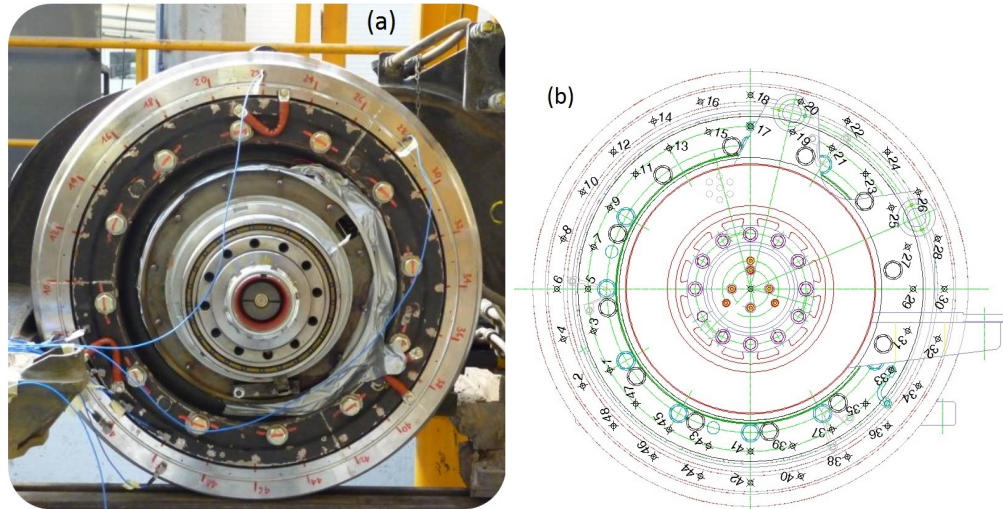


Figure 2.2: (a) Experimental modal analysis set-up, (b) The 48 measuring points on the wheel, [4].

(acceleration) and input (force) of the system. Results in this Chapter are referred to the suspended configuration and represented in terms of receptance (complex ratio between displacement and force); it was shown that FRF difference between suspended and laid-on-track configurations was negligible [4]. Figure 2.3 shows the axial receptance on the tyre for an axial input at the same point, Figure 2.4 shows the axial receptance on the web. Finally, to better understand the radial behaviour, an accelerometer was positioned on the tread and the receptance is shown in Figure 2.5; the clear presence in the radial receptance of the same peaks depicted in the axial one demonstrates how in-plane (radial) and out-of-plane (axial) modes are strongly coupled.

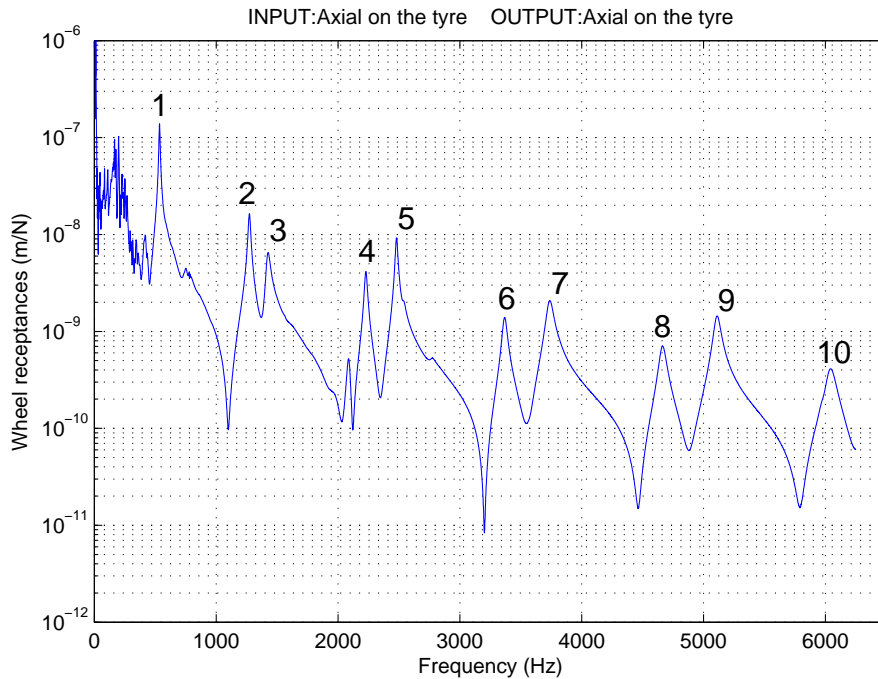


Figure 2.3: Axial receptance measured at the tyre point 2 for an axial input at the same point on the suspended wheel.

In Figures 2.3 and 2.4 a unique number is given to each mode to facilitate vibration modes representation. By using an experimental modal analysis software developed within the Mechanical Engineering Department at Polimi these modes were identified in terms of natural frequencies, damping ratios and mode shapes (axial component only). The idea of the algorithm is to identify first the poles of the system through the so called Least Squares Complex Exponential method (LSQE) and then to refine the corresponding natural frequencies and damping ratios and to identify the mode shapes by means of a curve fitting procedure in the frequency domain. At the time the experimental campaign was performed only seven vibration modes were identified according to this procedure, while in the present work the modal identification procedure has been extended to all the modes numbered in the Figures and depicted from Figure 2.6 to 2.22.

The mode shapes that involve the tyre vibration are shown in Figures 2.6 to 2.15, the outer black dots represent the measuring point on the tyre while the inner ones the measuring point on the web. These identified modes are described as out-of-plane or in-plane vibration depending on the direction of the highest vibration

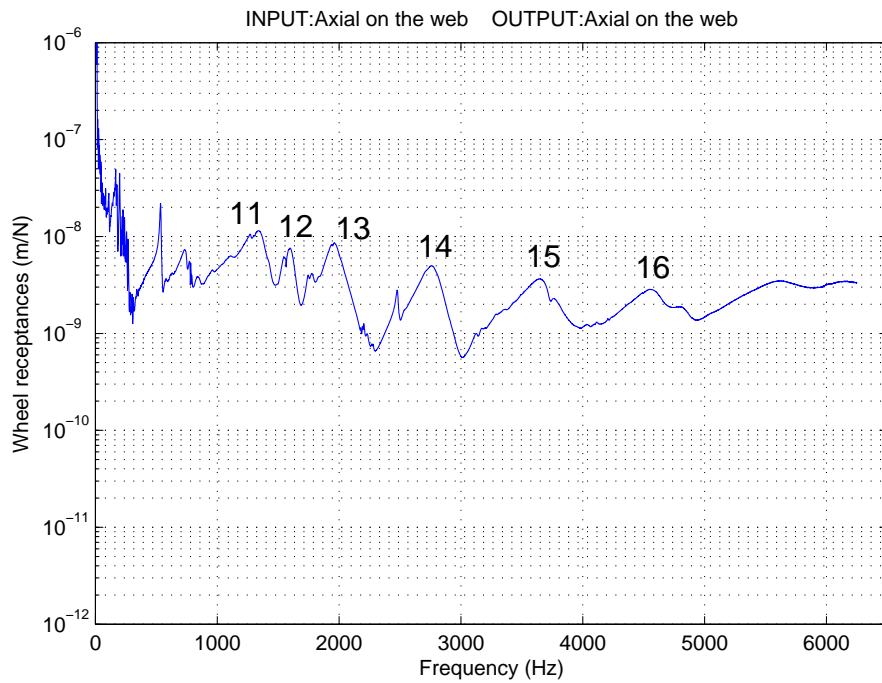


Figure 2.4: Axial receptance measured at the web point 1 for an axial input at the same point on the suspended wheel.

amplitude. This means that a pure radial, or axial, mode does not exist because due to the characteristics of the resilient wheel, the in-plane (radial) vibration is always coupled with the out-of-plane (axial) one and vice versa. For this reason, each type of motion always occurs together with the other one. The identified damping ratio (named h in these figures) is shown in the figure title along with the identified natural frequency.

Finally, Figures 2.16 to 2.22 show the mode shapes that predominantly involve the web flexure.

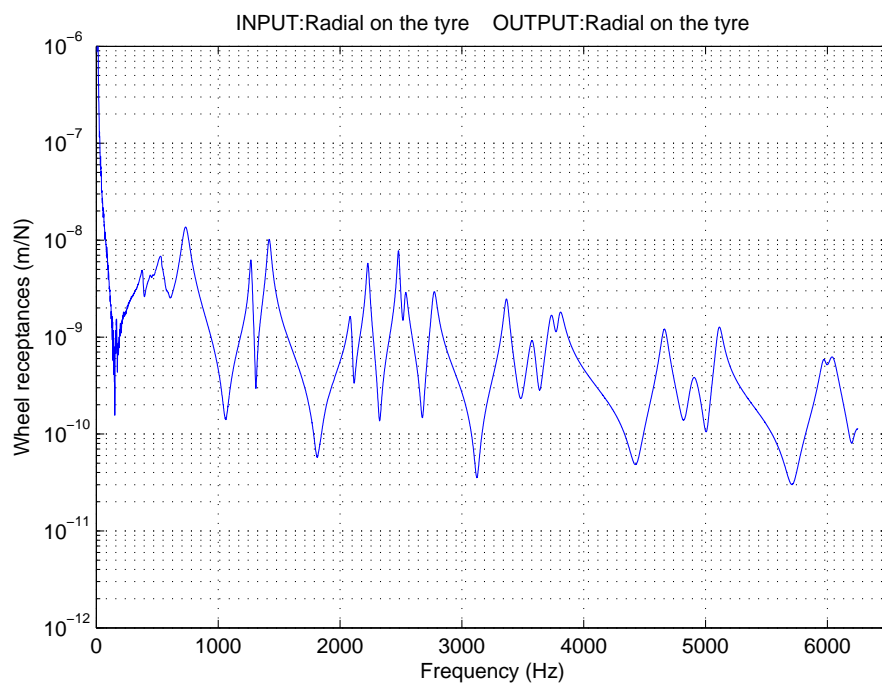


Figure 2.5: Radial receptance measured at a point on the tyre tread for a radial input at the same point on the suspended wheel.

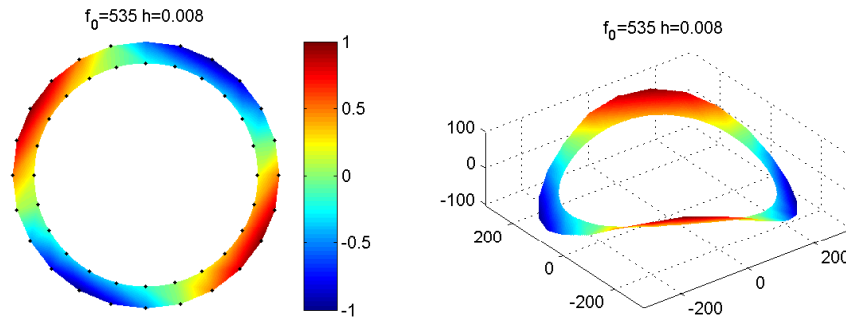


Figure 2.6: 1st peak 535 Hz, out-of-plane mode with 2 nodal diameters

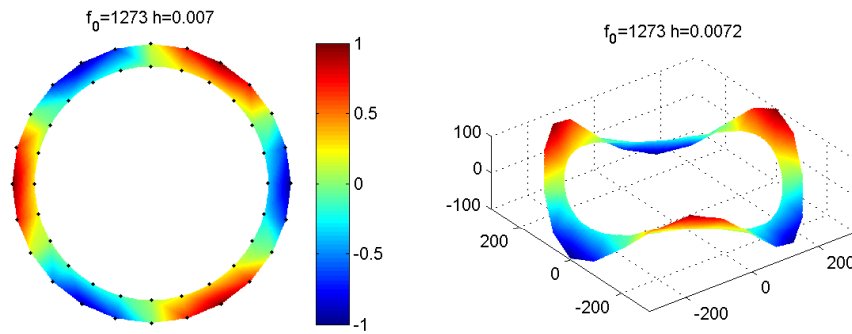


Figure 2.7: 2nd peak 1273 Hz, out-of-plane mode with 3 nodal diameters

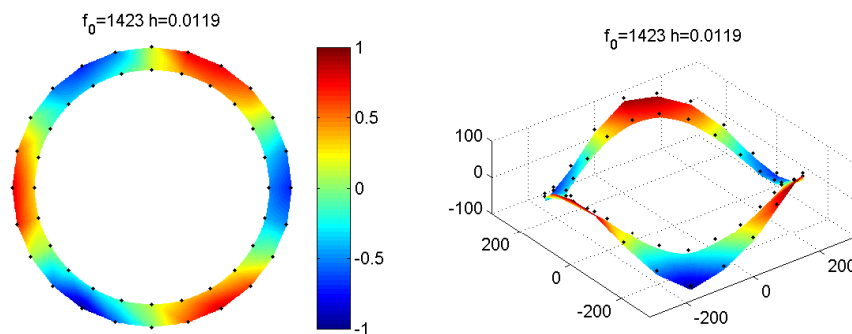


Figure 2.8: 3rd peak 1423 Hz, in-plane mode with 3 nodal diameters

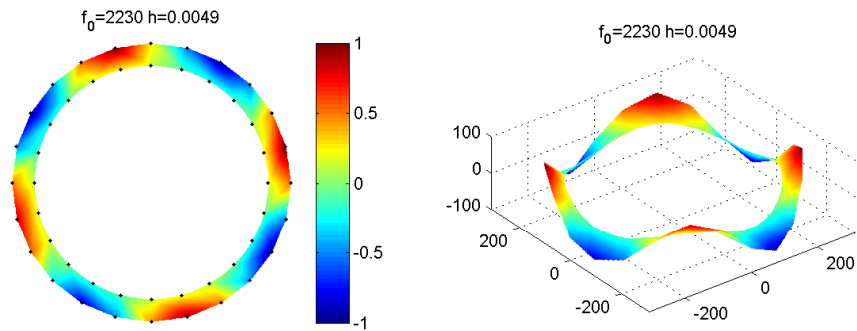


Figure 2.9: 4th peak 2230 Hz, in-plane mode with 4 nodal diameters

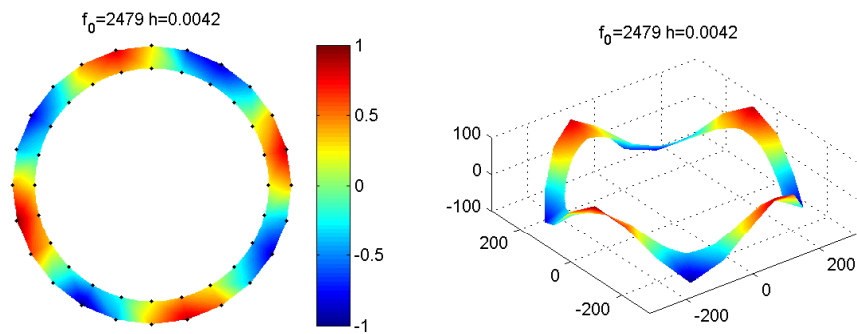


Figure 2.10: 5th peak 2479 Hz, out-of-plane mode with 4 nodal diameters

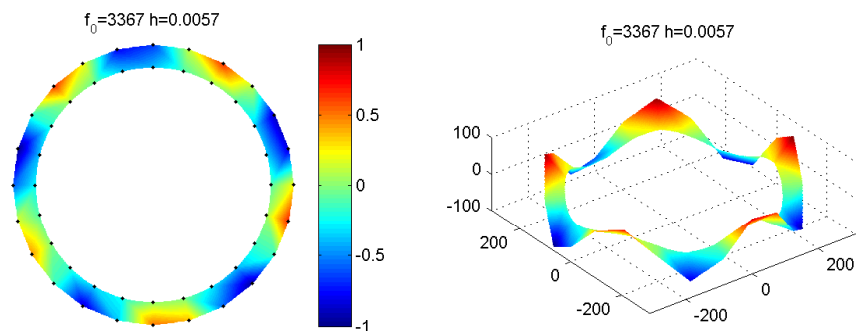


Figure 2.11: 6th peak 3367 Hz, in-plane mode with 5 nodal diameters

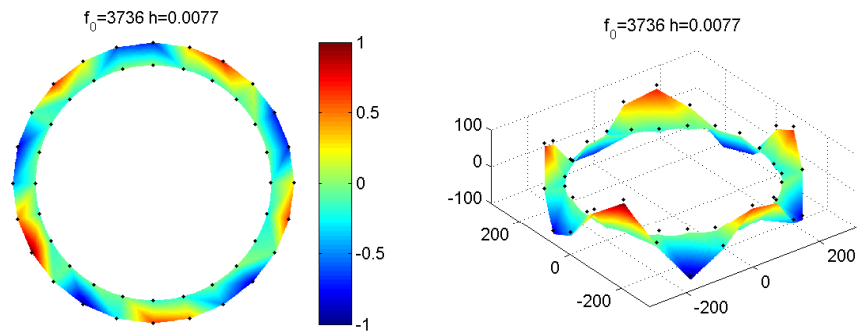


Figure 2.12: 7th peak 3736 Hz, out-of-plane mode with 5 nodal diameters

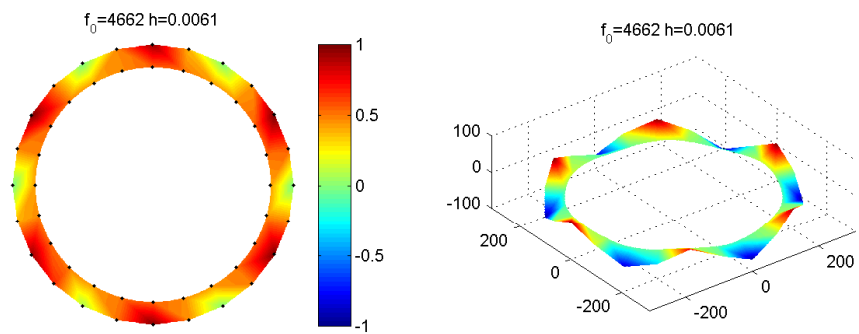


Figure 2.13: 8th peak 4662 Hz, in-plane mode with 6 nodal diameters

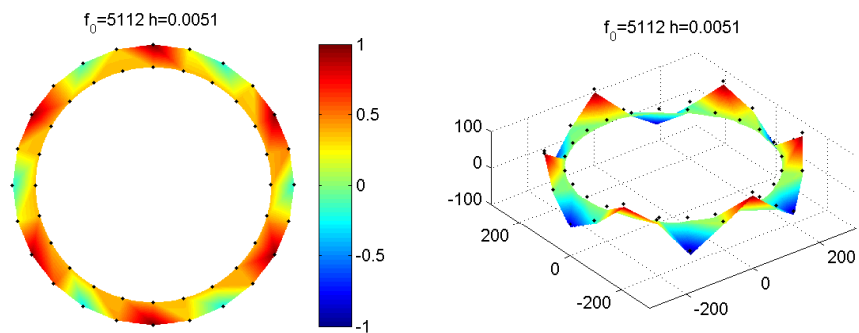


Figure 2.14: 9th peak 5112 Hz, out-of-plane mode with 6 nodal diameters

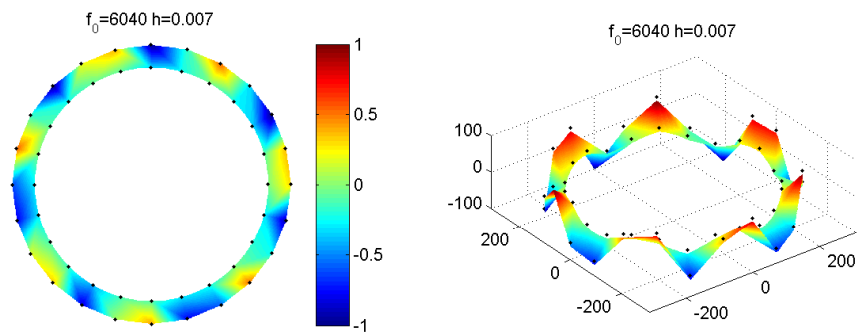


Figure 2.15: 10th peak 6040 Hz, in-plane mode with 7 nodal diameters

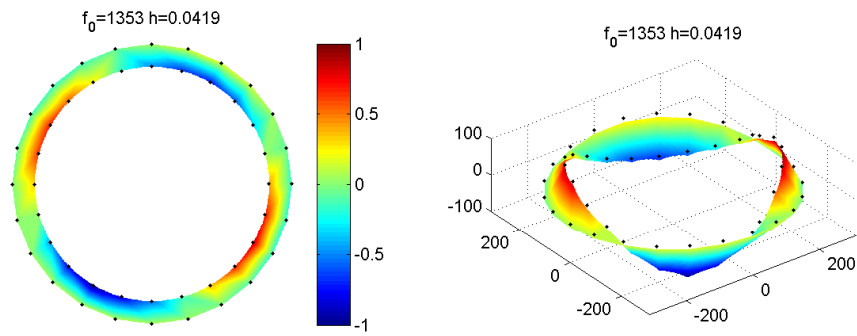


Figure 2.16: 11th peak 1353 Hz, web flexural mode with 2 nodal diameters

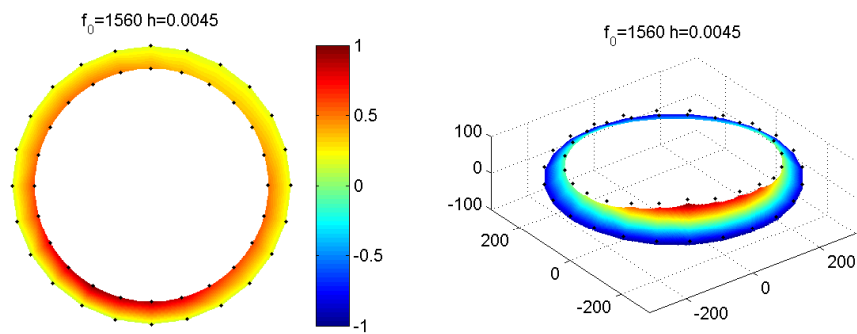


Figure 2.17: 12th(a) peak 1560 Hz, web flexural mode with 0 nodal diameters

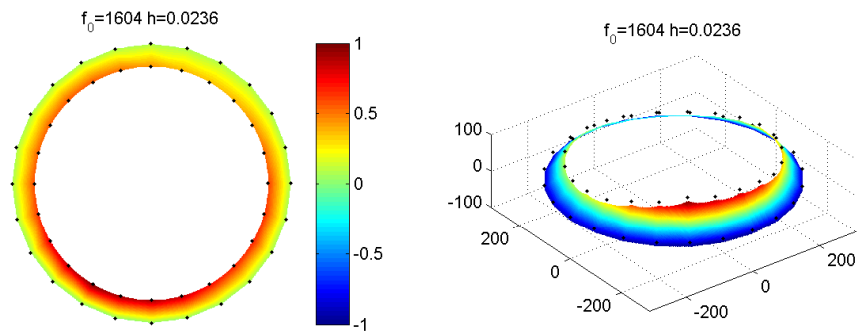


Figure 2.18: 12th(b) peak 1604 Hz, web flexural mode with 0 nodal diameters

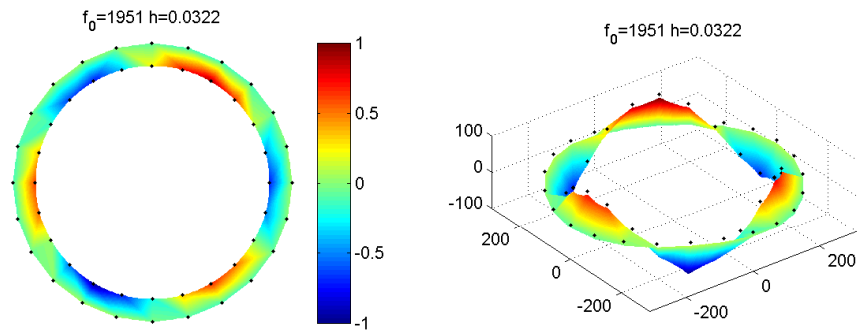


Figure 2.19: 13th 1951 Hz, web flexural mode with 3 nodal diameters

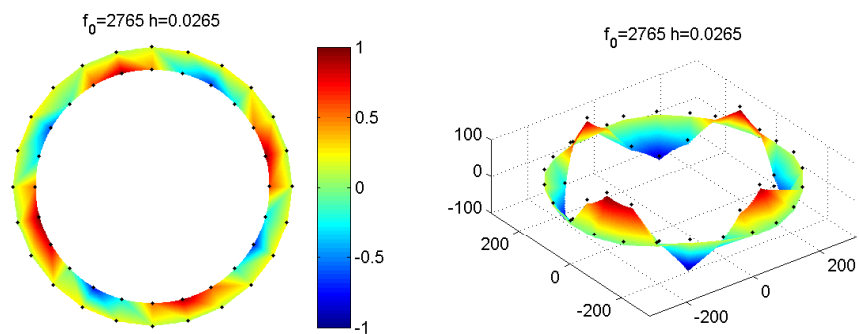


Figure 2.20: 14th peak 2765 Hz, web flexural mode with 4 nodal diameters

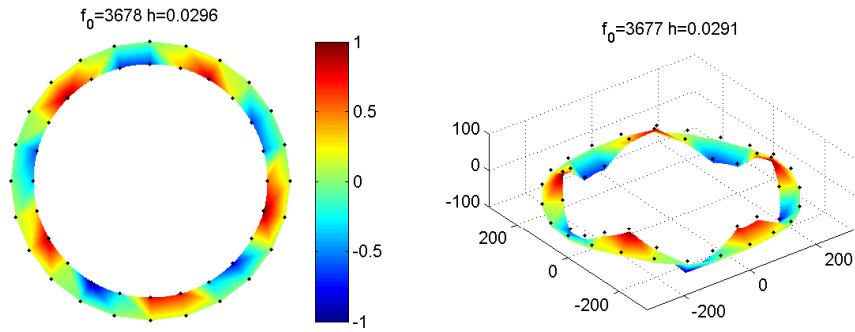


Figure 2.21: 15th peak 3678 Hz, web flexural mode with 5 nodal diameters

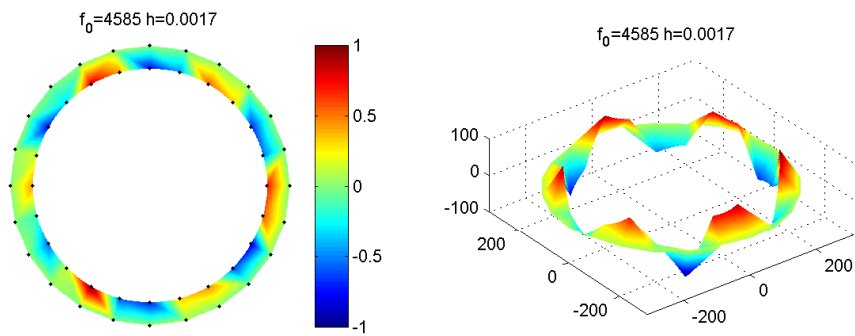


Figure 2.22: 16th peak 4585 Hz, web flexural mode with 6 nodal diameters

Finally, in a later stage of the measurement campaign, some FRFs of the wheel assembled on the tram were recorded with the vehicle in standstill condition on the track. The idea was to observe any possible difference in terms of natural frequency due to the load of the vehicle on the resilient wheel. Figure 2.23 shows the receptances of the suspended wheel (as described above) compared with those measured on the fully loaded wheel. It can be observed that in the frequency region up to 6000 Hz the two curves, although different, do not present a significant shift of the natural frequencies.

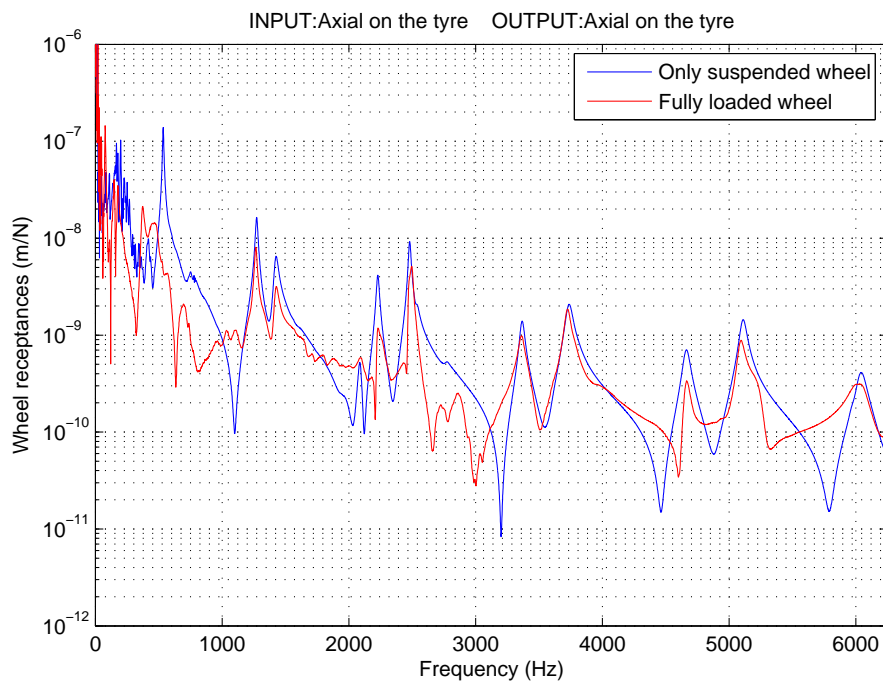


Figure 2.23: Blue curve: axial receptance measured at the tyre point 2 for an axial input at the same point considering only the suspended wheel. Red line: axial receptance measured at the tyre point 4 for an axial input at the tyre point 22 considering the whole tram with the wheel resting on the rail.

2.1.2 Noise and vibration measurements

An experimental campaign was performed to characterize the squeal noise phenomenon when the tramcar negotiates curved track. This was performed in the curve shown in Figure 2.24. On this curve, two different sections 8 metres from each other were instrumented (see Figure 2.25).

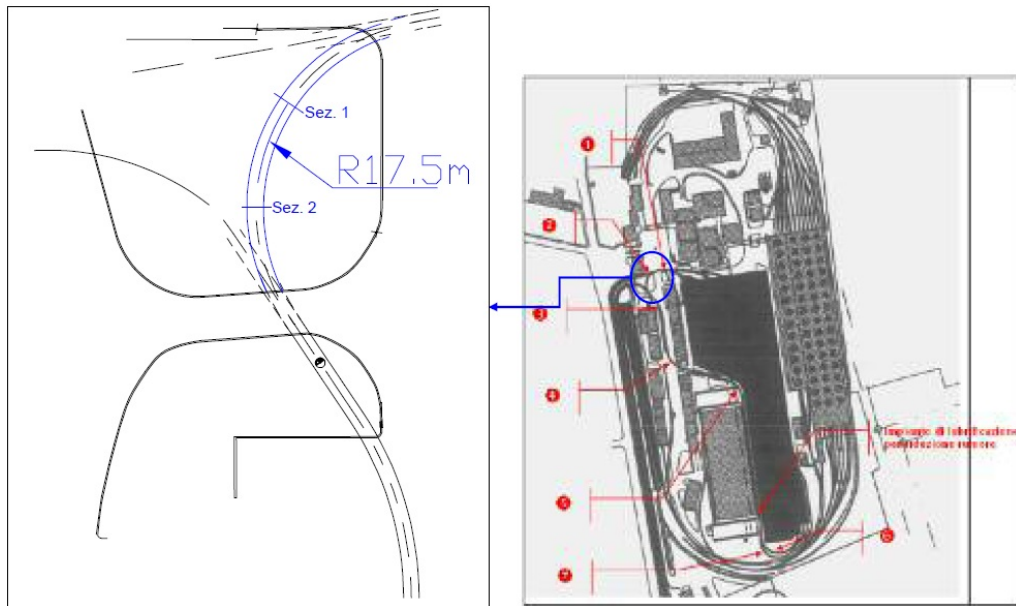


Figure 2.24: Curve used to perform the line test, [4].



Figure 2.25: The tramcar during line test, [4].

During the test, two different measurement systems, one on-board and the other on the ground, were employed to record the measurements of two different groups of transducers. Thus, two separate acquisition systems were used.

In the case of the on-board system, different transducers were used and in particular six accelerometers mounted on each wheel in turn of the front axle of the second bogie were used to measure the wheel vibration. These accelerometers (named WA) were positioned at precise locations as shown in Figure 2.26(a). Four accelerometers were located on the tyre covering a quarter of the wheel and measuring in the axial direction, one was mounted on the web (axial direction) and finally one was used to measure the radial acceleration of the tyre.

Regarding the ground system, two transducer types were adopted: accelerometers and microphones. The accelerometers (named RA) were placed on the rails to measure their vibration. Both the inner and the outer rails were instrumented with three accelerometers: one on the flange, one on the grooved head and one on the rail web, as shown in Figure 2.26(b). Four microphones (named M) were located on the tested curve as shown in Figure 2.26(c). The microphones were moved to the outer part of the curve (their position is mirrored to respect of the axis of the rail) when the instrumented wheel faced this side.

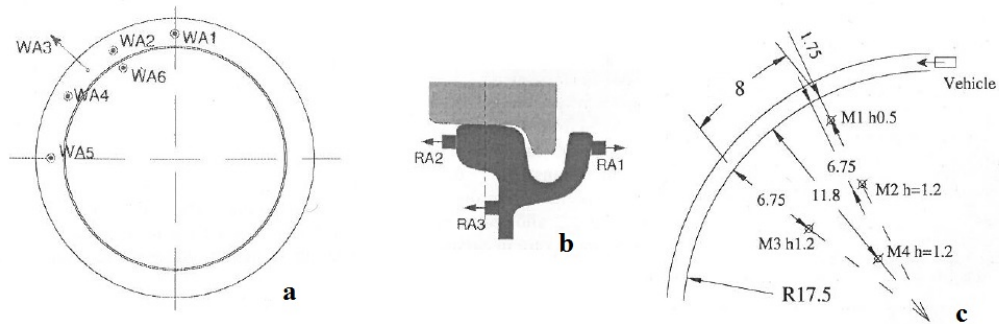


Figure 2.26: (a) Position and sensing direction of the wheel accelerometers, (b) Position and sensing direction of the rail accelerometers, (c) Location and height of the microphones, instrumented wheel on the left side. Dimensions in metres, [4].

Two different test sessions were carried out with the tram running along the left sided curve at 10 km/h. The first one considered the instrumented wheel mounted on the left bogie, front axle, inner side. In this case the flange back of the wheel was possibly in contact with the rail grooved head. The second one referred to the configuration with the instrumented wheel facing outward, in this condition there could be a contact between the flange and the running head. This nature of the wheel/rail contact was suggested by the highly worn condition of the rail head and of the grooved head.

Some of the measurements obtained from WA2, WA3 and R1 sensors are reported below along with an example of pass-by noise from microphone M1. In particular the time history of the acceleration signals, the harmonic and spectrogram analysis of particular time ranges and the time evolution of the vibration levels restricted to 1/3 octave frequency bands are shown in order to characterize the phenomenon. Note that the microphones registered the sound pressures generated from all the wheels and the rail, but only one of the 16 wheels was instrumented and only the vibration signals of this one are reported. Therefore it is difficult to draw exhaustive conclusions on the phenomenon by simply correlating the vibration of the instrumented wheel with the measurements obtained from the microphones. In this sense, a clearer indication of the tones involved in squeal is given by the wheel vibration and it is better to focus on this signal if a comparison with possible unstable frequencies from a numerical model is to be made. However an example of a pass-by noise level is presented to show the most important tonal components recorded in the campaign.

Before presenting a summary of the post-processing of the measurements it is important to observe that at the time of the measurements the rail was showing a very high level of wear indicating in particular that the back of the flange of the inner wheel was consistently in contact with the grooved head while, as typically happens, the flange of the outer wheel was in contact with the rail head.

In Figures 2.27 to 2.39 the post-processed signals obtained from the WA2, WA3, R1 and M1 sensors are shown in terms of time histories, spectra, spectrogram and rms levels per 1/3 octave band. The amplitude of the spectra is normalized in such a way that a unit amplitude sinusoidal signal in the time domain would have an amplitude one in frequency domain.

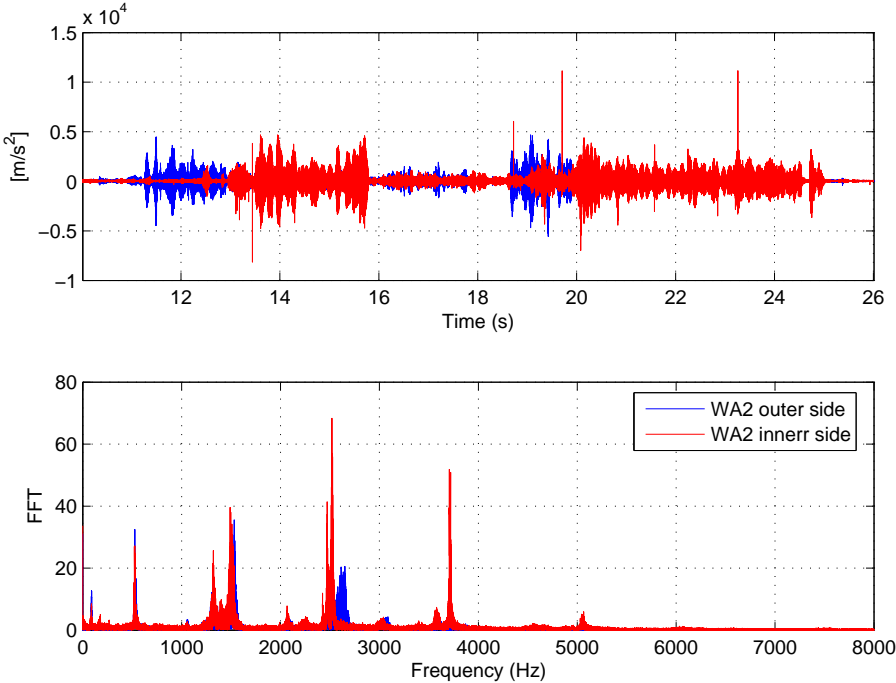


Figure 2.27: Time history and harmonic analysis of the acceleration signals obtained from the inner and outer WA2 sensor (axial direction).

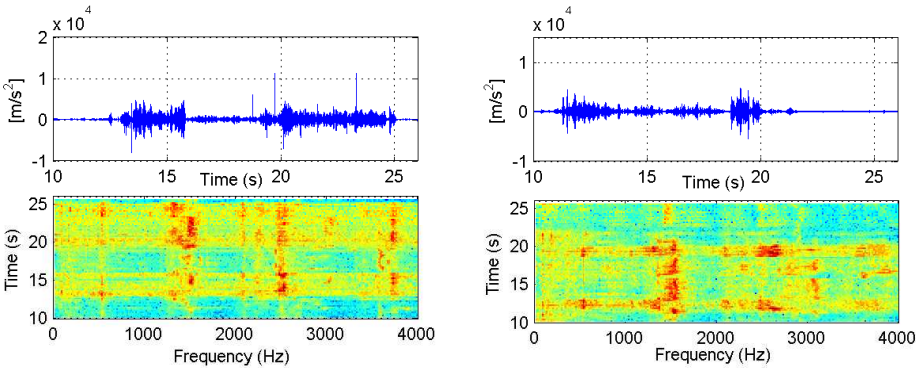


Figure 2.28: Time-frequency analysis of the acceleration signals obtained from the inner (left Figure) and outer (right Figure) WA2 sensor (axial direction).

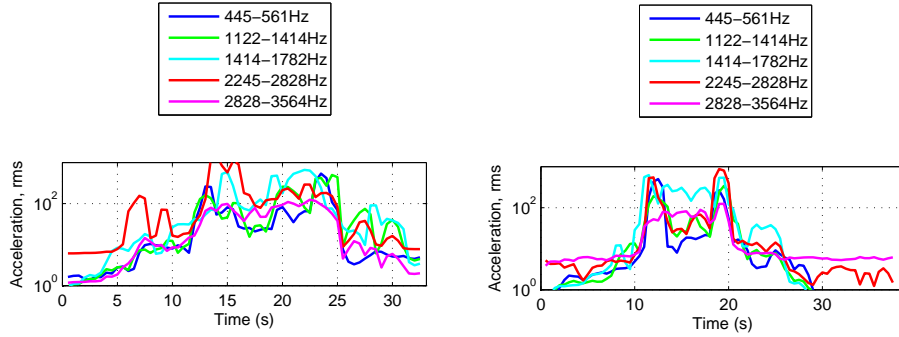


Figure 2.29: Vibration levels of the acceleration signals obtained from the inner (left Figure) and outer (right Figure) WA2 sensor (axial direction).

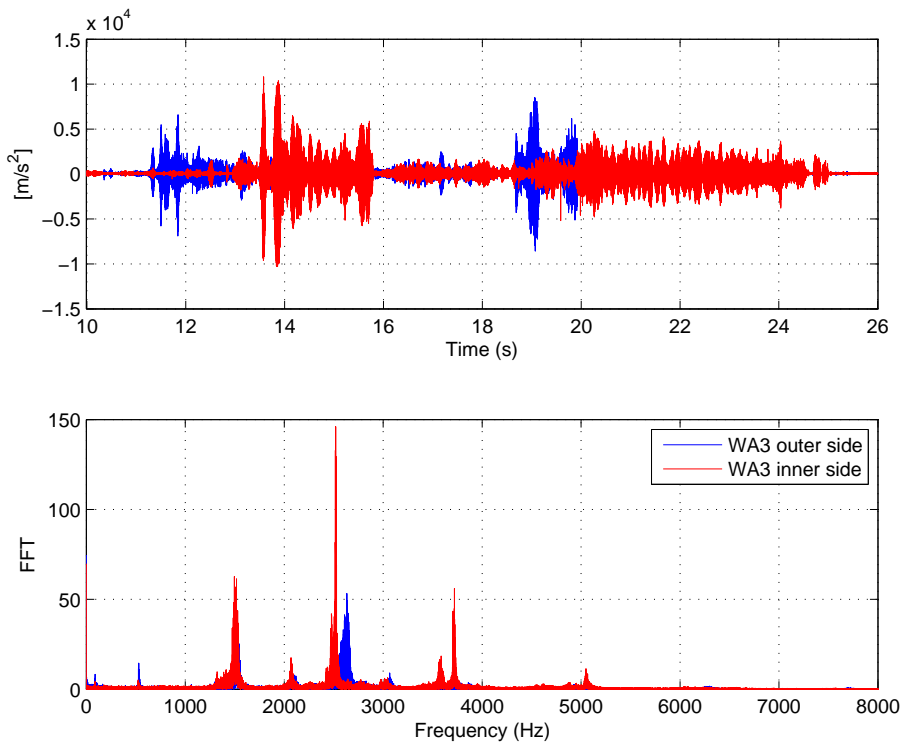


Figure 2.30: Time history and harmonic analysis of the acceleration signals obtained from the inner and outer WA3 sensor (radial direction).

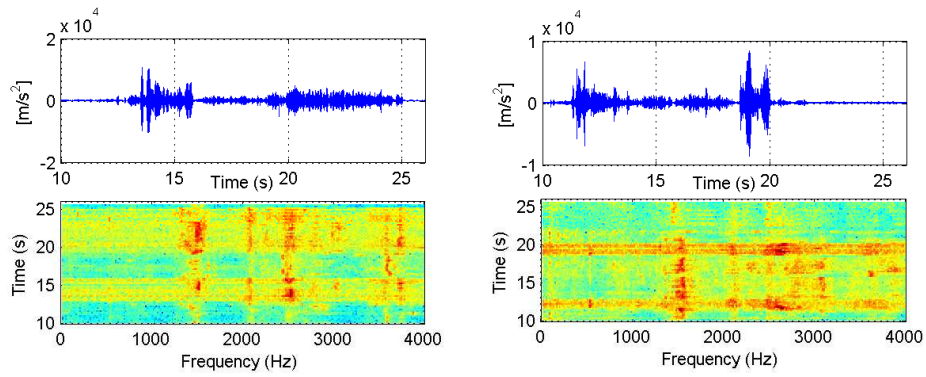


Figure 2.31: Time-frequency analysis of the acceleration signals obtained from the inner (left Figure) and outer (right Figure) WA3 sensor (radial direction).

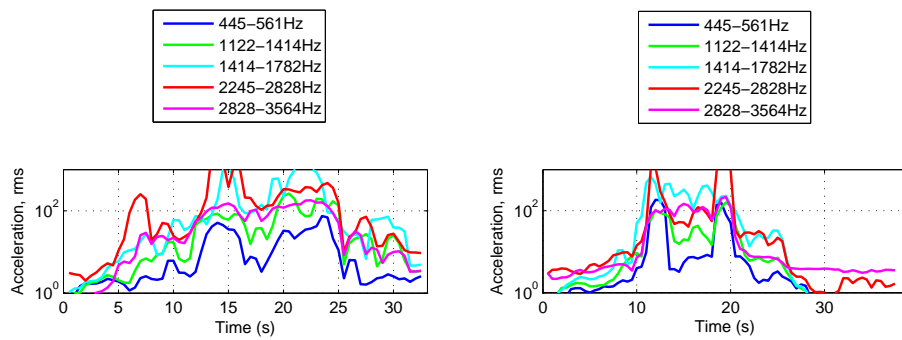


Figure 2.32: Vibration levels of the acceleration signals obtained from the inner (left Figure) and outer (right Figure) WA3 sensor (radial direction).

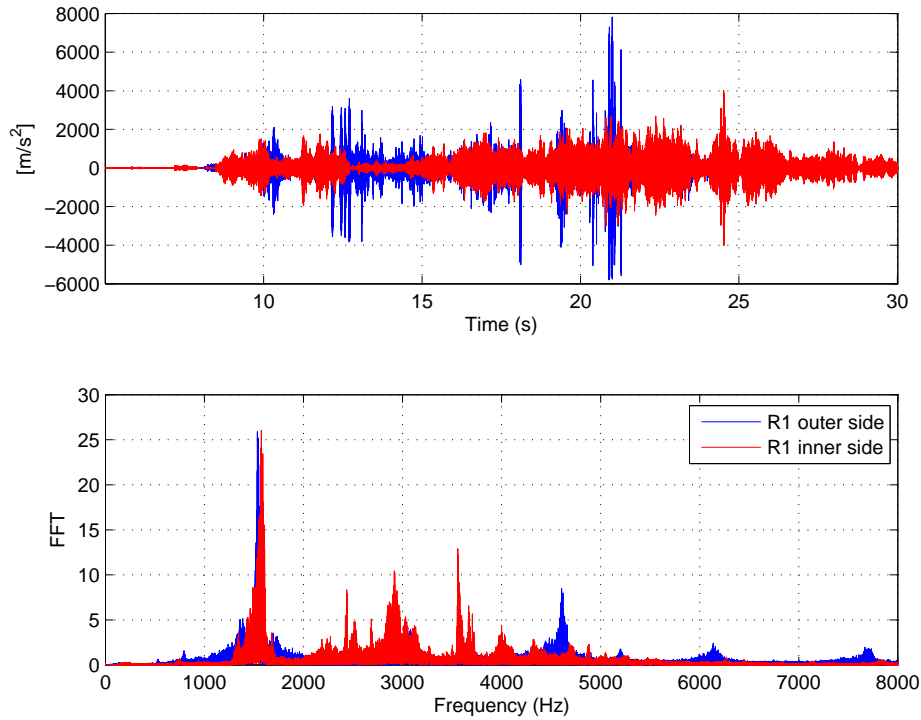


Figure 2.33: Time history and harmonic analysis of the acceleration signals obtained from the inner and outer R1 sensor.

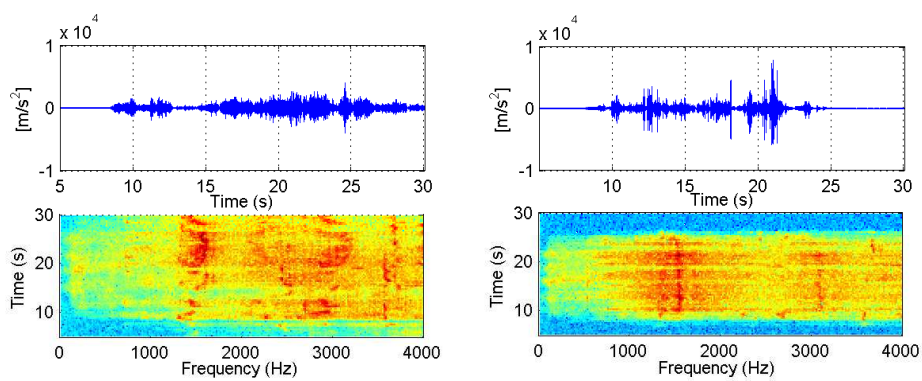


Figure 2.34: Time-frequency analysis of the acceleration signals obtained from the inner (left Figure) and outer (right Figure) R1 sensor.

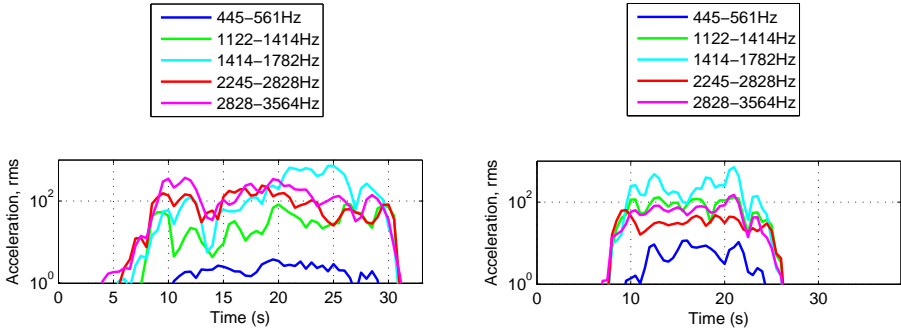


Figure 2.35: Vibration levels of the acceleration signals obtained from the inner (left Figure) and outer (right Figure) R1 sensor.

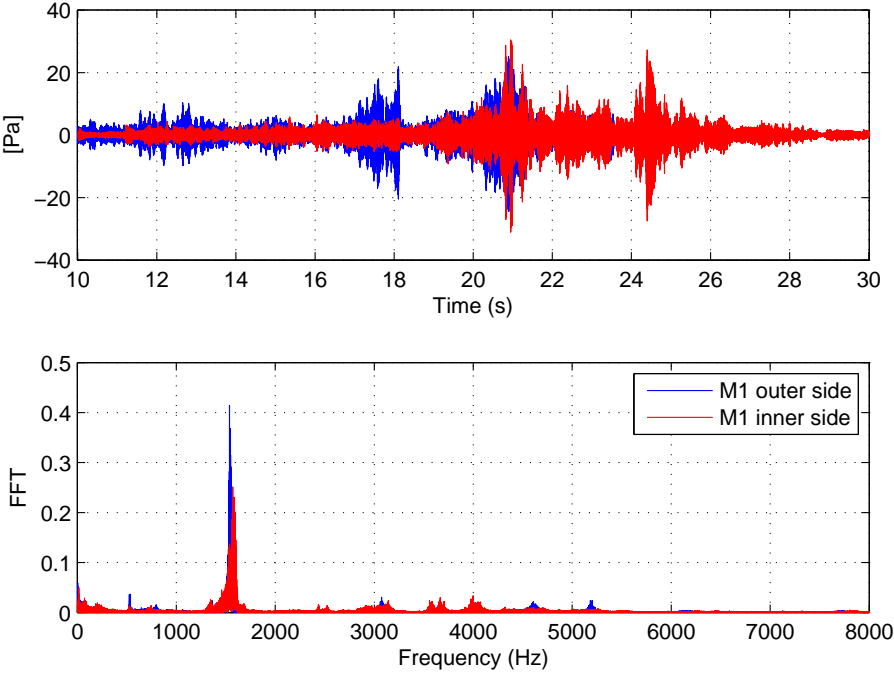


Figure 2.36: Time history and harmonic analysis of the microphone signals obtained from the inner and outer M1 sensor.

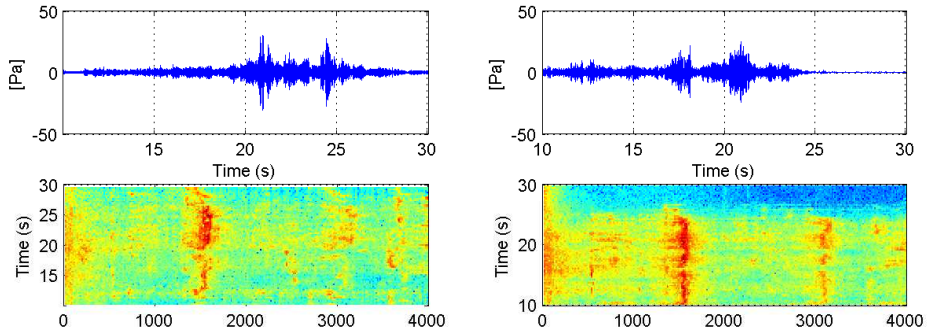


Figure 2.37: Time-frequency analysis of the microphone signals obtained from the inner (left Figure) and outer (right Figure) M1 sensor.

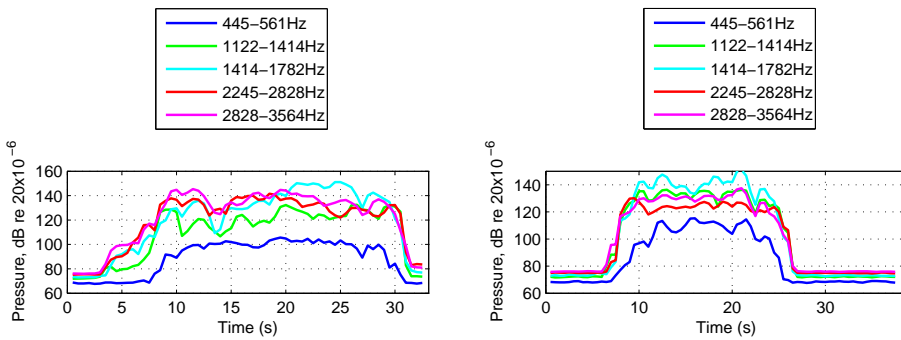


Figure 2.38: Sound pressure levels obtained from the inner (left Figure) and outer (right Figure) M1 sensor.

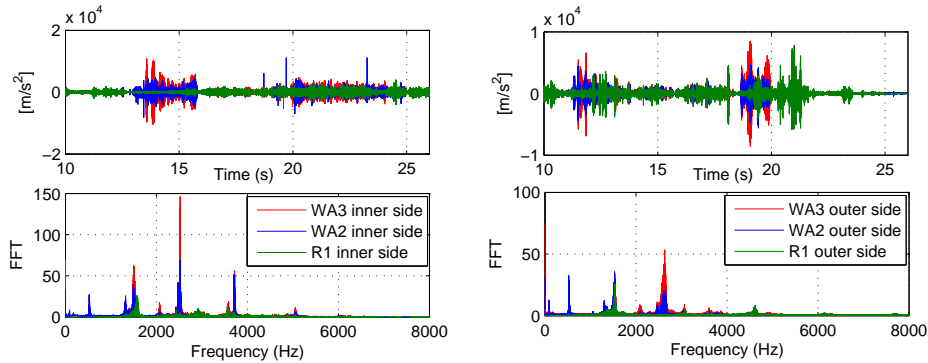


Figure 2.39: Time history and harmonic analysis of the acceleration signals obtained from the WA3, WA2 and R1 sensors. Left Figure: inner side. Right Figure: outer side.

By observing Figures 2.29 and 2.32 it is evident that there are some frequency bands that dominate the response (i. e. 1414-1728 Hz, 2245-2828 and 2828-3564 Hz). This suggests that there are at least three wheel natural frequencies that may be involved in squeal, however a closer look at the spectra and spectrogram (see Figures 2.27, 2.28, 2.30 and 2.31) indicate that several wheel modes are likely to be involved. According to curve squeal theory each tone recorded during the vehicle passage is expected to be related to a wheel mode. In this case this is not always straightforward. In fact, it is peculiar to observe that the modes at 1270 Hz and 1420 Hz seem to generate squeal at higher frequencies (1330 Hz and 1550 Hz) and the mode at 2480 Hz has a similar behaviour. It is unlikely that the modes dominated by wheel web deflections (like mode 12 in Figure 2.4) are the reason for the squeal due to their high damping levels. Rail vibration confirms that one of the most important frequencies involved in the phenomenon is in fact at 1550 Hz (see Figure 2.33, 2.34 and 2.35) and the sound pressure level shown in Figure 2.38 is entirely dominated by the same frequency. In order to better understand this behaviour, harmonic analyses focused on some short interval ranges are shown in Figures 2.40 to 2.44. All the Figures are related to the inner front wheel.

$T = 13.74 - 13.86 \text{ s}$

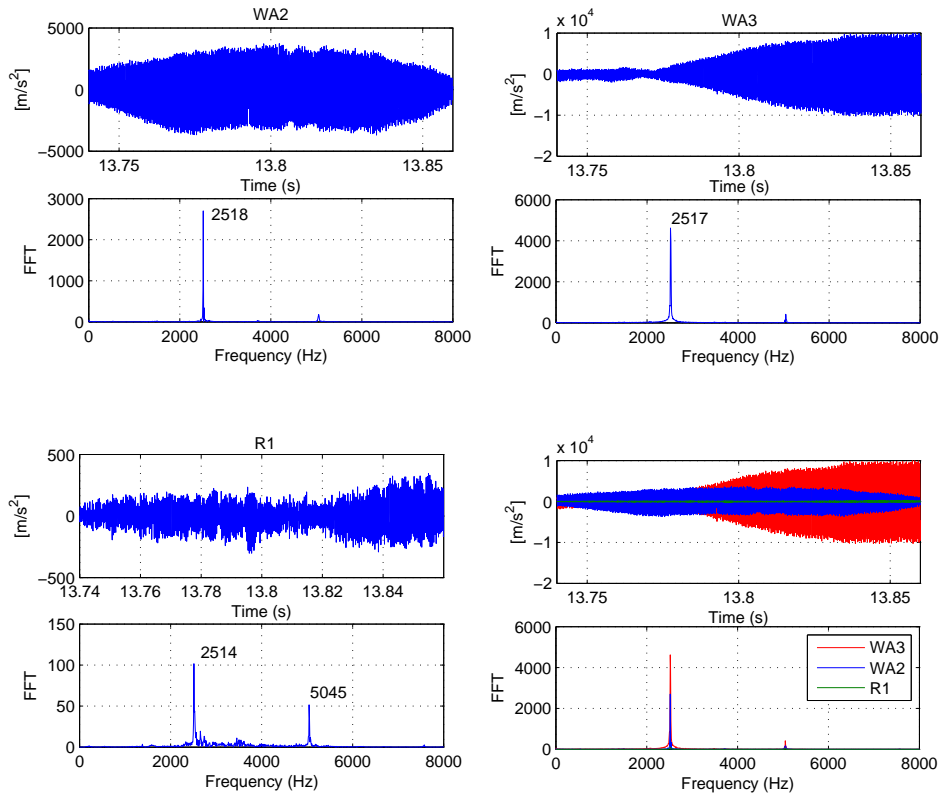


Figure 2.40: Time history and harmonic analysis of the acceleration signals in the range 13.74 - 13.86 s. The last Figure represent the comparison between them.

$T = 14.68 - 14.8 \text{ s}$

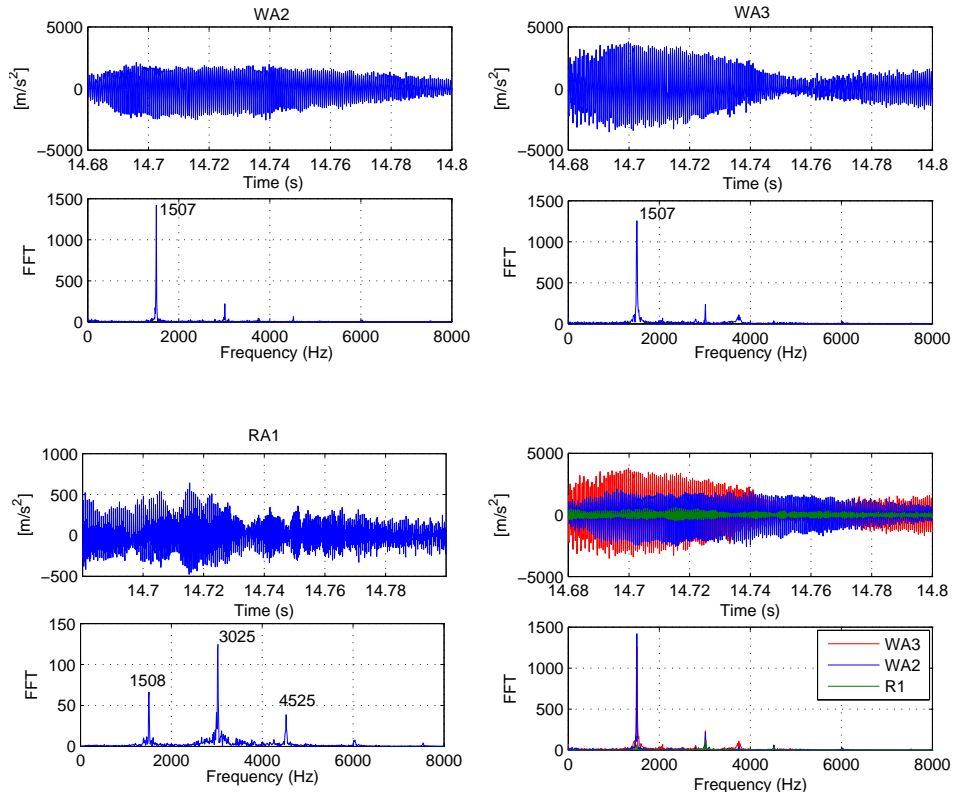


Figure 2.41: Time history and harmonic analysis of the acceleration signals in the range 14.68 - 14.8 s. The last Figure represent the comparison between them.

$T = 20.12 - 20.18 \text{ s}$

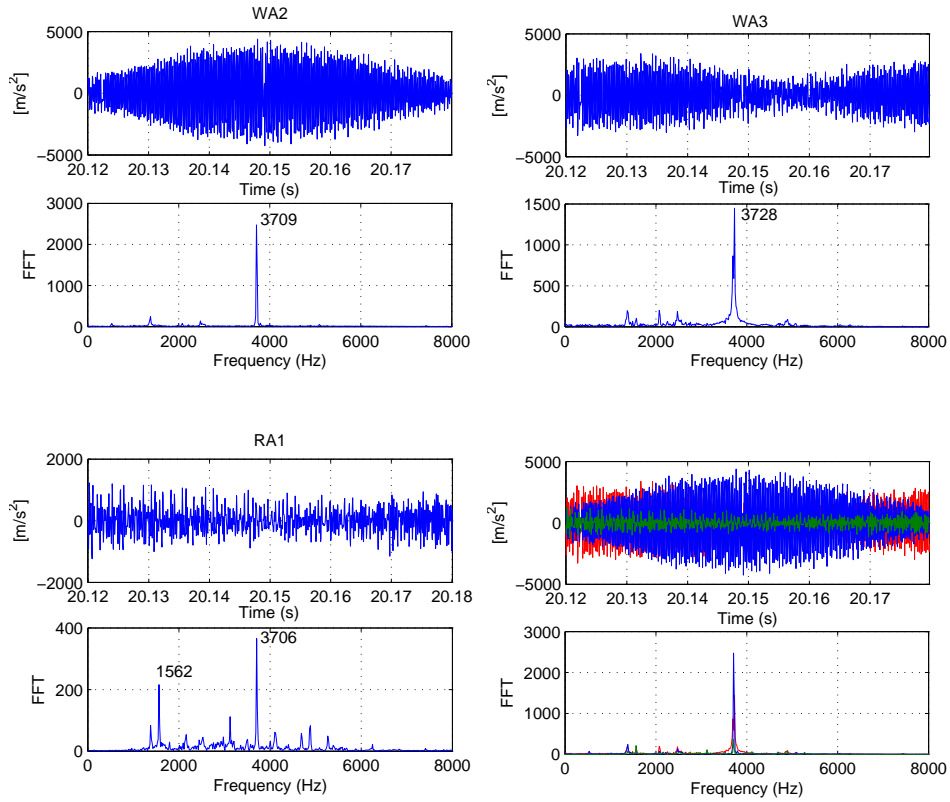


Figure 2.42: Time history and harmonic analysis of the acceleration signals in the range 20.12 - 20.18 s. The last Figure represent the comparison between them.

$T = 23.4 - 23.6$ s

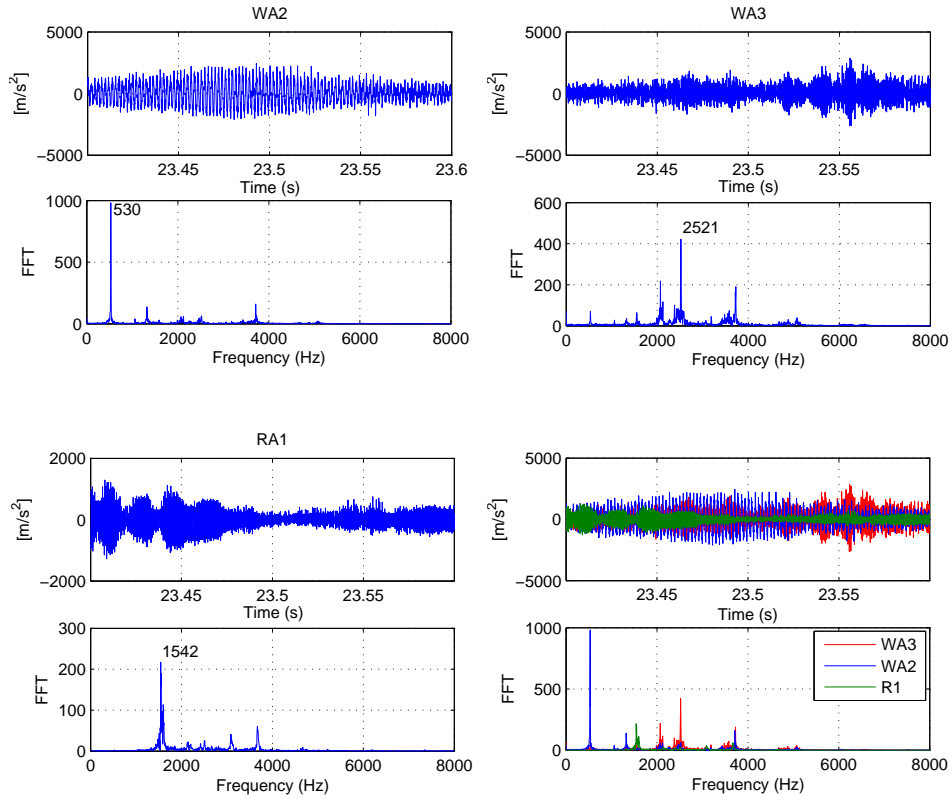


Figure 2.43: Time history and harmonic analysis of the acceleration signals in the range 23.4 - 23.6 s. The last Figure represent the comparison between them.

$T = 24.5 - 24.54$ s

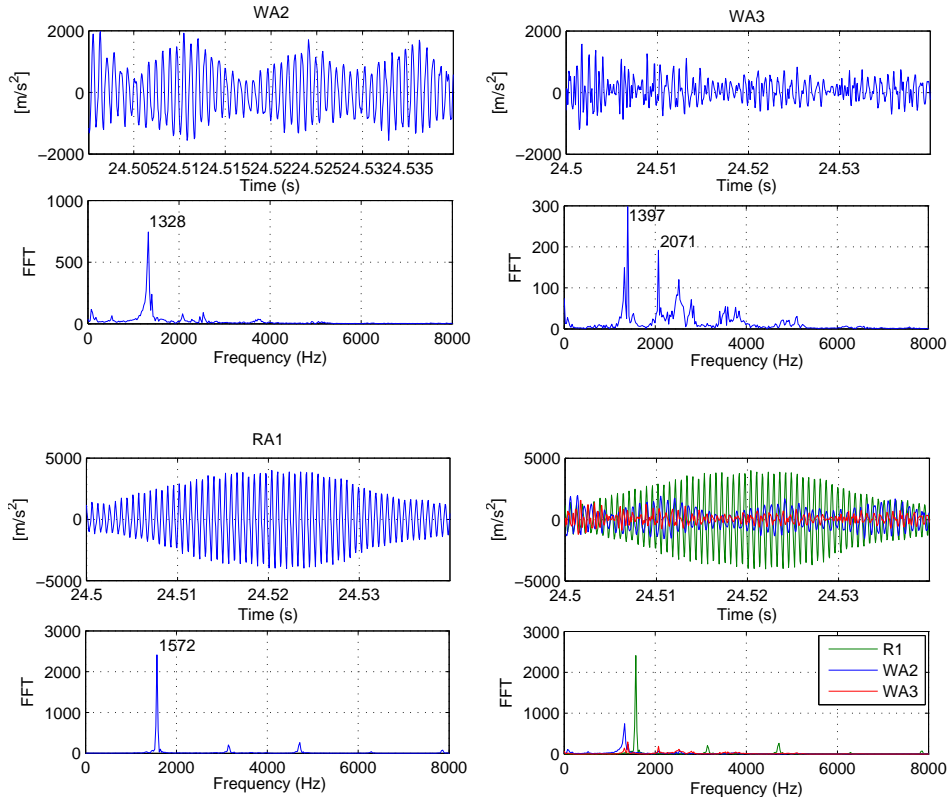


Figure 2.44: Time history and harmonic analysis of the acceleration signals in the range 24.5 - 24.54 s. The last Figure represent the comparison between them.

Despite the microphone being often dominated by noise at 1550 Hz, Figures 2.40 to 2.44 have shown that the mode(s) involved vary with time and all the frequencies listed in Tables 2.1 and 2.2 have been observed.

It is important to note that the microphone was fixed at a certain position along the curve and it is sensitive to all the tram wheels and the rail. Therefore, in order to compare measured data with a numerical model (see Chapters 6 and 7) it is better to use the information contained in the wheel vibration.

	WA2 (Ax. tyre)			WA3 (Rad. tyre)			WA6 (Ax. web)		
12 - 13.5 sec	522	1324	2520	2072	2535		538	1321	2637
13.5 - 14.5 sec	2478	2519		2520			2478	2520	
14.5 - 16 sec	527	1503	2472	1503	2479	2519	1503	2472	2515
	2518	3718		3725			3716		
19 - 20 sec	1475	1526	2467	1475	1537	2475	1485	1538	2477
20 - 21 sec	1306	1400	1489	1389	1489	1534	1364	1489	1537
	2467	3707	3720	2546	3706	3720	2487	3707	3720
21 - 22 sec	1315	1491	3717	1490	1525	2518	525	1311	1486
				3728			1528	3717	
22 - 23 sec	1516	2528	3716	1494	1517	2527	1493	1516	2530
				3724					
23 - 24 sec	527	1321	1462	1319	1465	1512	523	1322	1462
	1500	2070	2468	2070	2459	2521	1506	2461	
24 - 25 sec	90	1337	2533	1334	2068	2531	90	1312	2674

Table 2.1: Experimental frequencies involved in squeal phenomenon observed from the WA2, WA3 and WA6 sensors of the inner front wheel for different time ranges. Values in Hz.

	WA2 (Ax. tyre)			WA3 (Rad. tyre)			WA6 (Ax. web)		
11 - 12 sec	90	527	1353	532	1530	2581	528	1354	1535
	1537	2472	2652	2645			2471	2600	2644
12 - 13 sec	526	1056	1310	530	1537	2118	527	2464	
	2118	2474	2557	2466	2556				
13 - 15 sec	1357	1505	1551	1362	1548	3084	1478	1505	1549
	3085								
15 - 17 sec	1355	1487	1537	1537	3066	3605	1355	1481	1535
	3053	3605							
17 - 18 sec	1534	3060		1535	3065		1537		
18 - 19 sec	528	1543	2460	532	1552	2100	528	1553	2504
	2574	2660		2458	2575	2659	2581	2653	
19 - 20 sec	527	1303	1512	1301	1514	2083	1303	1512	2482
	2610	2634		2507	2608	2634	2629		

Table 2.2: Experimental frequencies involved in squeal phenomenon observed from the WA2, WA3 and WA6 sensors of the outer front wheel for different time ranges. Values in Hz.

2.2 British Rail Class 150 Sprinter in North Wales

In the mid-1980s new Class 150 Sprinter diesel multiple units (see Figure 2.45) were introduced onto a wide variety of routes, replacing 1950s designs. A severe squeal noise problem occurred on some curving routes, with high amplitude sustained tones in the region 2 to 5 kHz. Particular problems arose on the Llandudno to Blaenau Ffestiniog line in North Wales. The 14 km section from Betws-y-Coed to Ffestiniog tunnel has many reverse curves of radius 160 to 240 m with no transition curves. For safety reasons the track on these curves was fitted with check rails. BR Research was asked to investigate these problems. A measure-



Figure 2.45: Photo of the Class 150 Sprinter diesel multiple unit train. Reproduced from <http://en.wikipedia.org/>

ment programme was performed in May 1987 in which microphones were placed adjacent to each wheel of the leading bogie of a Class 150 unit [7]. The train ran in normal passenger operation on the Llandudno to Blaenau Ffestiniog route and measurements were taken over the course of several trips over the route. A member of the team also rode in the cab to identify location and curve direction.

Very high noise levels were recorded adjacent to the wheels as shown in Figure 2.46, in some cases as high as 140 dB. Frequency analysis showed that squeal occurred in the radial modes of the wheels. This is in contrast to the usual situation in curve squeal where axial modes are excited by lateral forces at the running surface. In a given curve a single radial mode was excited and this sustained a constant noise level. The radial modes with 2, 3, 4, 5 and 8 nodal diameters were found to occur, with the mode with 4 nodal diameters at 3.6 kHz being the most commonly found. These modes have natural frequencies between 2 and 8 kHz [7].

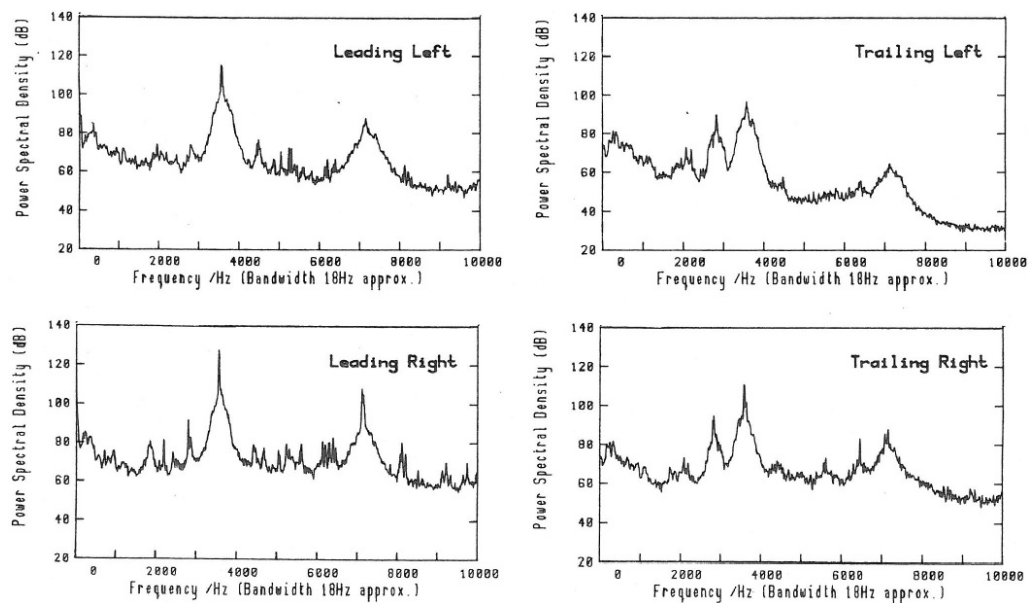


Figure 2.46: Example of noise spectra measured at each wheel right hand curve of 240 m [7].

The cause of this particular squeal problem was believed to be due to vertical stick/slip forces acting between the check rail and the wheel flange. The validity of this hypothesis was reinforced observing the mode shapes of this type of wheel as will be described in section 3.2. The radial modes present a large radial component of motion at the back of the flange and a small radial component at the tread near the field side. They could therefore be readily excited by the check rail while not being restrained or damped by the contact with the running rail. Moreover, the wheel flange backs were observed to be shiny, indicating sustained contact with the check rails.

In order to eliminate the curve squeal, a damping treatment was recommended.

After laboratory testing at BR Research in Derby a constrained layer damping treatment was designed and approval was obtained from DMEE for fitting this to the vehicles. A trial took place in 1988 in which a unit fitted with these dampers was run over the branch line and shown not to squeal. Since then all Class 150, 153 and 156 vehicles were fitted with these dampers.

In 2011, as part of same work for the vehicle owner, the mode shapes and damping of the Class 15x wheels with and without dampers were studied ¹. Here the case of the Class 15x wheels without dampers is described.

Measurements of wheel frequency response functions were carried out at Pullmans in Cardiff on 7 September 2011.

The wheelset was suspended from its axle so that the wheels were clear of the ground (see Figure 2.47). The wheel was excited using an instrumented hammer at four positions on the tread as shown in Figure 2.48. Position 2 was located at the nominal running position, 70 mm from the flange-back, while position 3 was approximately 20 mm from the field side.



Figure 2.47: Photograph of the test set-up at Pullmans, Cardiff.

¹Measurements were performed under contract and results are here reported after personal communication with D. J. Thompson

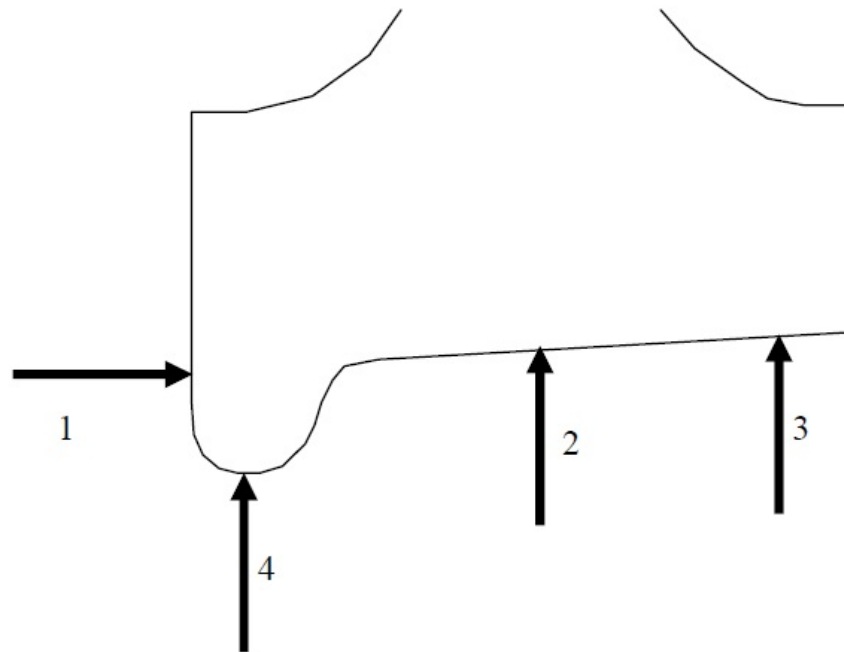


Figure 2.48: Diagram of measurement positions.

The response was measured using an accelerometer at positions adjacent to the excitation point in each case. Due to the light damping of the wheels, the analysis time had to be chosen to be long enough to avoid truncation of the signals.

The measured frequency response functions at each of the four positions are shown in Figures 2.49 and 2.50, while the modal damping and natural frequencies identified using a circle fitting technique are listed in Table 2.3. Finally, in Table 2.4, the measured modal damping and natural frequencies of damped Class 15x wheel are reported.

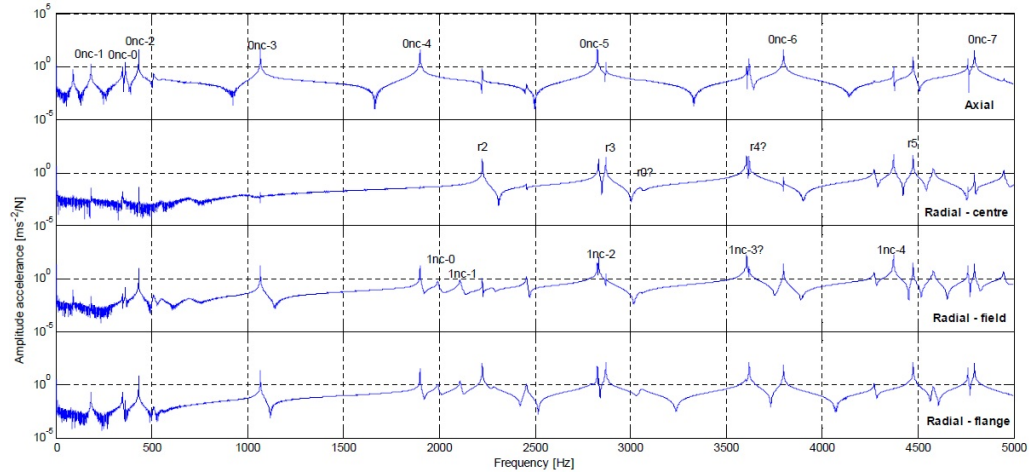


Figure 2.49: Modal identification for undamped Class 15x wheel (0-5 kHz).

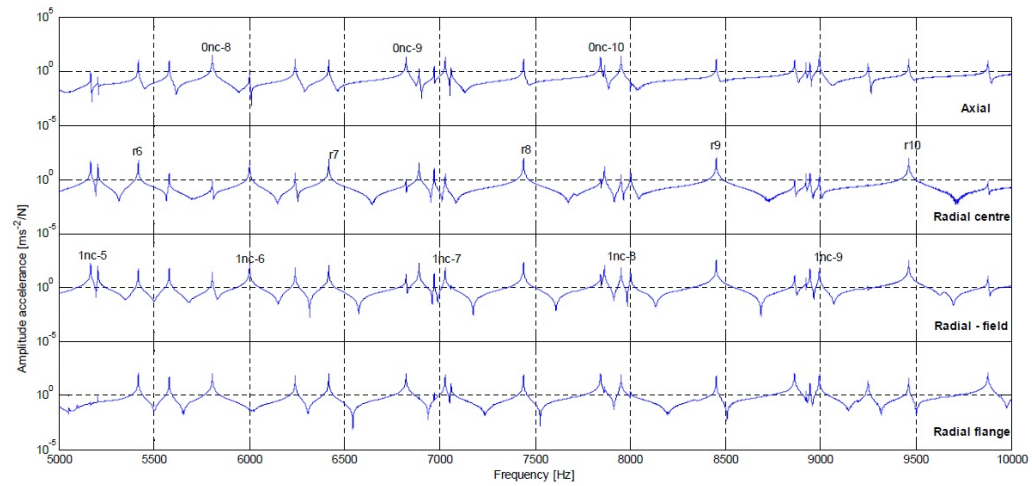


Figure 2.50: Modal identification for undamped Class 15x wheel (5-10 kHz).

n	Natural frequency (Hz)			Damping ratio ($\times 10^{-4}$)		
	0-n-c	radial	1-n-c	0-n-c	radial	1-n-c
0	362.4		1992.9	5.14		14.8
1	181.9		2109.5	16.0		15.5
2	431.1	2225.5	2831.7	0.642	0.907	1.08
3	1067.0	2870.0	3605.8	0.810	0.757	0.595
4	1900.3	3619.3	4372.2	0.891	0.644	0.595
5	2826.0	4474.9	5204.9	0.933	0.548	0.587
6	3798.5	5416.4	6000.4	0.787	0.472	0.523
7	4795.3	6416.4	7027.5	0.677	0.462	0.495
8	5805.6	7438.3	7951.8	0.633	0.445	0.483
9	6823.4	8451.6	8992.1	0.766	0.441	0.443
10	7843.9	9462.1		0.754	0.441	

Average: 0.643

Table 2.3: Measured natural frequencies and damping ratios of undamped Class 15x wheel.

n	Natural frequency (Hz)			Damping ratio ($\times 10^{-4}$)		
	0-n-c	radial	1-n-c	0-n-c	radial	1-n-c
0	362.4		1992.9	5.82		14.5
1	181.7		2109.5	20.8		15.1
2	433.4	2228.3	2834.0	2.74	8.80	2.19
3	1070.3	2875.9	3613.3	7.02	11.5	16.3
4	1905.6	3613.0	4384.1	2.27	34.5	12.1
5	2834.0	4487.6	5183.4	2.02	9.48	8.84
6	3809.6	5434.2	6020.9	1.32	9.81	9.51
7	4809.6	6441.5	7055.2	1.09	5.95	6.68
8	5823.2	7470.4	7979.4	1.05	3.79	5.34
9	6844.0	8489.7	9019.3	1.10	2.09	4.33
10	7868.0	9504.4		1.01	1.44	

Average: 6.67

Table 2.4: Measured natural frequencies and damping ratios of damped Class 15x wheel.

Chapter 3

Wheel finite element modelling

Referring to the measurement campaigns described in Chapter 2 the finite element models of the two respective wheels are described here. Particular attention is given to the resilient wheel of the Sirio tram whose model has been developed within this thesis work. In this sense, in order to improve accuracy, several iterative attempts have been made. To reduce computational time an axi-symmetric representation of the wheel has been adopted and measured FRFs have been used to tune and update model parameters.

A finite element model of the Class 150 wheel was already available; it is summarised in section 3.2.

3.1 Resilient wheel of Sirio tram

3.1.1 Procedure to determine the rubber parameters for the FE model

To understand the squeal noise phenomenon better, an accurate finite element model of the wheel is needed. The fundamental characteristics to consider in developing the FE model of this wheel are: the correct geometry of the wheel and parameters for the steel and rubber (Young's moduli, Poisson's ratios and densities). The geometry, steel parameters, and density of the rubber are available. Regarding the density of the rubber, from measurements, this value was found to be around $1957\text{kg}/\text{m}^3$. However in the FE model this value of density for the rubber as to be adjusted because the wheel in the experimental modal analysis has 24 rubber elements that fill the half of the total space available between the web and the tyre, while the axi-symmetric FE model considers the rubber element

as an elastic ring that fills all the space available. So, the model has to adopt an equivalent density of the rubber to maintain the total mass of the rubber and the value used is $1000\text{kg}/\text{m}^3$. In addition the Young's modulus and Poisson's ratio of the rubber are unknown and have to be 'tuned' so that the numerical natural frequencies of the model are close to the experimental ones. To assign appropriate rubber parameters, a very simple equation is used that calculates the mean square error, in terms of natural frequencies, between the FE model and experimental data:

$$e(E, \nu)_i = (f_n(E, \nu) - f_e)_i^2. \quad (3.1)$$

where $e(E, \nu)$ and $f_n(E, \nu)$ indicate the mean square error and the numerical natural frequencies that depend on the Young's modulus and Poisson's ratio of the rubber, f_e indicates the experimental natural frequencies while the index i indicates the considered mode. Below, an example is performed to explain how Eq.(3.1) can be use to tune the rubber parameters.

First of all, the natural frequencies to be considered and a degree of detail of the wheel geometry have to be chosen. Then, by varying the rubber parameters, a modal analysis is performed up to 6000 Hz for each combination of Young's modulus and Poisson's ratio of the rubber. In this way, for each natural frequency considered, a matrix composed of the natural frequencies calculated for each combination of Young's modulus and Poisson's ratio is determined. To simplify the example, only one natural frequency is considered here, in particular the out-of-plane mode with 2 nodal diameters at 535 Hz (the mode labeled '1' in Figure 2.3). Figure 3.1 indicates the wheel geometry of the model considered to study this example while matrix (3.2) shows the natural frequencies of the out-of-plane mode with 2 nodal diameters for different rubber parameters values. Each column of the matrix represent results for a fixed Poisson's ratio while Young's modulus is spanned within the interval of Eq.(3.3). Eq.(3.4) shows Poisson's ratio range considered.

$$F_1 = \begin{bmatrix} 535.21 & 535.59 & 535.97 & 536.34 & 536.70 & 537.06 \\ 536.31 & 536.68 & 537.05 & 537.42 & 537.78 & 538.13 \\ 537.52 & 537.89 & 538.25 & 538.61 & 538.97 & 539.32 \\ 538.85 & 539.22 & 539.58 & 539.93 & 540.28 & 540.63 \\ 540.34 & 540.70 & 541.05 & 541.37 & 541.71 & 542.05 \\ 541.99 & 542.34 & 542.69 & 543.00 & 543.34 & 543.67 \\ 543.84 & 544.18 & 544.52 & 544.82 & 545.15 & 545.47 \end{bmatrix}, \quad (3.2)$$

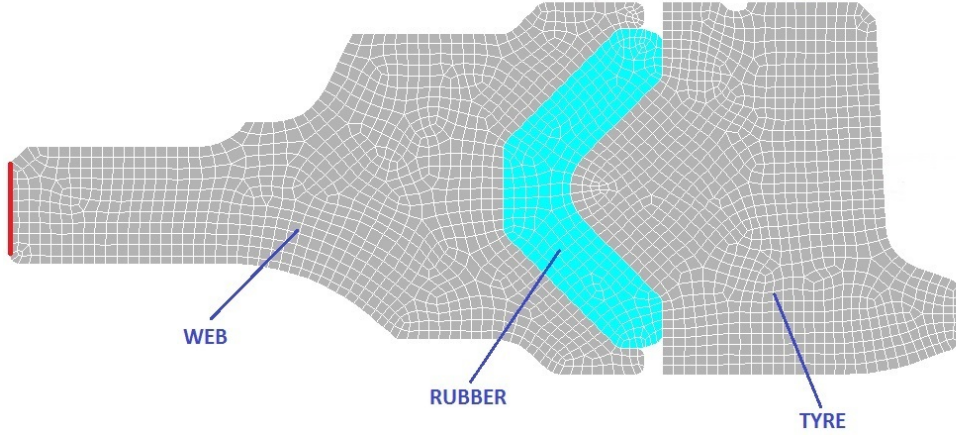


Figure 3.1: Wheel geometry of the model considered to study this example.

$$E = [92 : 1 : 97] \text{ MPa}, \quad (3.3)$$

$$\nu = [0.36 : 0.01 : 0.42]. \quad (3.4)$$

where the subscript of F (1 in this case) indicates the mode number given in Figures 2.3 and 2.4.

Then, by means of Eq.(3.1) with $i = 1$, the mean square error between each natural frequency described in matrix (3.2) and the experimental natural frequency can be calculated obtaining the matrix of the mean square errors related to this mode:

$$e_1 = \begin{bmatrix} 0.04 & 0.34 & 0.94 & 1.79 & 2.89 & 4.24 \\ 1.71 & 2.82 & 4.20 & 5.85 & 7.72 & 9.79 \\ 6.35 & 8.35 & 10.56 & 13.03 & 15.76 & 18.66 \\ 14.82 & 17.80 & 20.97 & 24.30 & 27.87 & 31.69 \\ 28.51 & 32.49 & 36.60 & 40.57 & 45.02 & 49.70 \\ 48.86 & 53.87 & 59.13 & 64.00 & 69.55 & 75.16 \\ 78.14 & 84.27 & 90.63 & 96.43 & 103.02 & 109.62 \end{bmatrix}. \quad (3.5)$$

From matrix (3.5) it can be noted that for rubber parameters equal to:

$$E = 92 \text{ MPa},$$

$$\nu = 0.36.$$

the mean square error between numerical and experimental natural frequency is

minimum.

Considering more than one mode in the tuning algorithm leads Eq.(3.1) to be modified as:

$$e(E, \nu)_{tot} = \sum_i (f_n(E, \nu) - f_e)_i^2, \quad i = 1, 2, 3, \quad (3.6)$$

and the matrix of the total mean square error is:

$$e_{tot} = \begin{bmatrix} 318.62 & 282.47 & 244.98 & 213.49 & 184.85 & 157.24 \\ 213.41 & 182.19 & 156.61 & 131.69 & 110.28 & 91.60 \\ 122.71 & 102.20 & 84.88 & 70.80 & 59.81 & 50.87 \\ 60.07 & 50.85 & 45.22 & \mathbf{43.84} & 45.19 & 49.38 \\ 45.08 & 51.62 & 61.69 & 75.02 & 91.47 & 112.39 \\ 113.86 & 140.20 & 170.65 & 203.06 & 239.33 & 283.32 \\ 329.10 & 380.12 & 437.92 & 493.88 & 560.23 & 628.10 \end{bmatrix}. \quad (3.7)$$

Observing this last matrix, the rubber parameters that minimize the mean square error between numerical and experimental natural frequencies change, in fact the values are:

$$E = 95 \text{ MPa},$$

$$\nu = 0.39.$$

Note it is more sensitive to E than it is to ν .

In order to understand if a good calibration has been done, a modal model is needed to allow a comparison between numerical and experimental receptances. In this way, the matching of the curves and the correspondence between numerical and experimental peaks can be checked and evaluations regarding new updates can be done. This modal model contains the modal frequencies, modal masses and mode shapes obtained from the structural dynamics of the wheel calculated from the FE model but it also allows the modal damping of each mode to be considered. To perform this comparison a software produced for the Franco-German project STARDAMP has been adopted [27], see Figures 3.2 for screenshot example. The software calculates the wheel receptances at the nominal contact point (in the three directions and rotations around the three axes) and the lateral receptance at six selected points on the web. Finally, by means of the comparison between numerical and experimental receptance, the modal damping of each mode can be manually 'tuned.'

Mode type	Number of nodal diameters										Frequency (Hz)	invr 2011/12
	0	1	2	3	4	5	6	7	8	9	10	
0 nodal circle	367.83	316.7	537.76	1267.4	2213.2							
1 nodal circle	1419.6	1341.9	1430.3	2098.3	3157.3	4341.6	5493.8		6466.6			
2 nodal circles	5402.3	5629.6	6282.5									
3 nodal circles												
Radial	2758.1	503.74	743.3	1409								
Circumferential	298.6											
Other 1	2118.3	2559.2	3592.9	4952.2	2457.2	3347.8	4618.2	5945.6	6348			
Other 2	2793.6	3779.1	5763.1	6175.3	6119.5	3697.5	5049.1	6267.4				
Other 3	6197.1	4035.2	5869.9	6584.6	6211.8	6249.6	6299.2	6336.7				
Other 4		6201.2	6226.2		6619.4	6527.3	6571.5	6557.1				

wheel_prime_0t wheel_prime_0t_wheel_modes

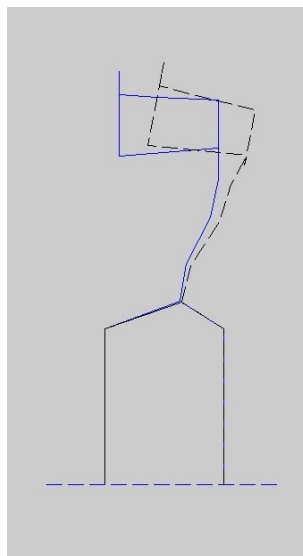


Figure 3.2: Example of screenshot of the software [27].

3.1.2 First model

The first model attempted considers only the wheel. Figure 3.3 shows the CAD model of the Sirio wheel and it can be noticed that the web is composed of two parts assembled by means of a bolted connection. Figure 3.4 shows the FE model of the Sirio wheel obtained using the ANSYS software. The rubber is constrained between the web and tyre, and the web is composed of a single part. Looking at Figure 3.4 the red line indicates the presence of a rigid constraint, while the red and blue vectors identify the positions where the FRFs have been calculated.

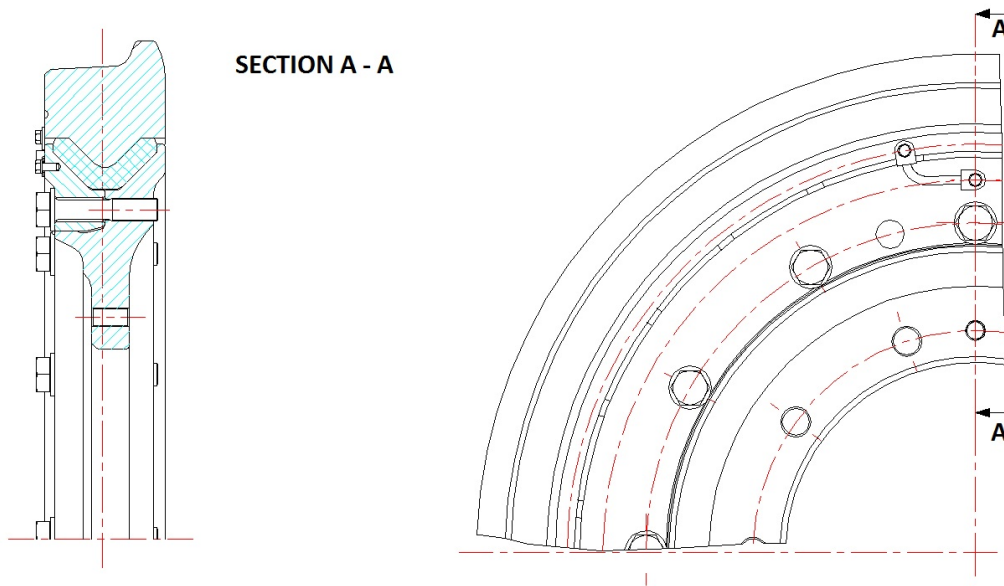


Figure 3.3: CAD model of the Sirio wheel

In order to have the numerical natural frequency very close to the experimental ones, the rubber parameters have been identified as described in section 3.1.1. Six experimental natural frequencies related to six tyre modes have been taken into account. The mode shapes of the first five natural frequencies are shown in Figures 2.6, 2.7, 2.8, 2.9, 2.10 while the sixth is a mode obtained by means of the comparison between the peak at 733 Hz in the radial experimental receptance in Figure 2.5 and the corresponding numerical natural frequency found close to experimental one. This numerical mode shape describes an in-plane mode with 2 nodal diameters. The experimental mode shape of this radial mode could not be identified due to a lack of accelerometer positions in the radial direction. So, considering these six natural frequencies to calibrate the rubber parameters,

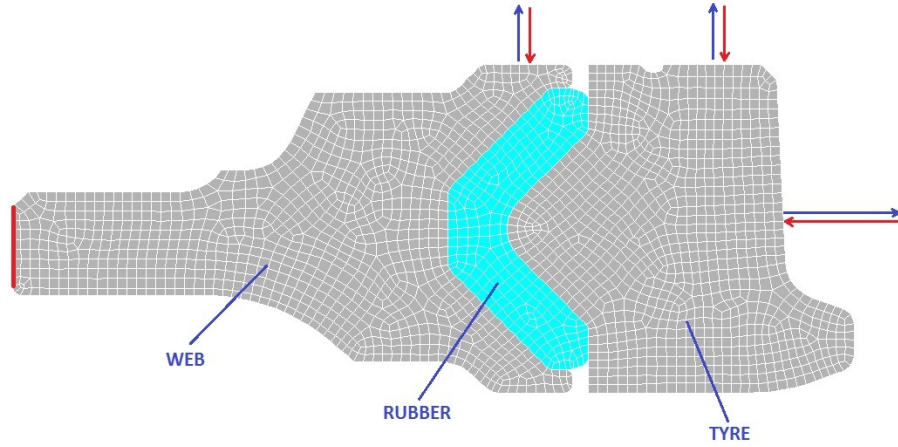


Figure 3.4: FE model of the Sirio wheel: axi-symmetric model. The coloured vectors indicate the positions where the FRFs are calculated.

modal analysis is performed up to 6000 Hz while the Young's modulus and Poisson's ratio of the rubber are chosen in the following range:

$$E = [92 : 1 : 97],$$

$$\nu = [0.36 : 0.01 : 0.42].$$

These values are coherent with the parameters of the resilient wheel model used by Jones and Thompson to study rolling noise generated by railway wheels with visco-elastic layers [28].

The rubber parameters obtained are:

$$E = 96MPa, \nu = 0.37.$$

The comparison between experimental and numerical wheel receptance at the considered points (see Figure 3.4) are shown in Figures 3.5, 3.6 and 3.7. When available, experimentally identified damping ratios have been used, the best fitting ones have been adopted otherwise.

Figures 3.5 and 3.6 are related to the wheel tyre and they show that the numerical FRF is very close to the experimental one while Figure 3.7 (web) shows that the two curves are distant from one another. In this last curve, the modal damping is not modified in order to show clearly the correspondence between numerical and experimental peaks (black arrows).

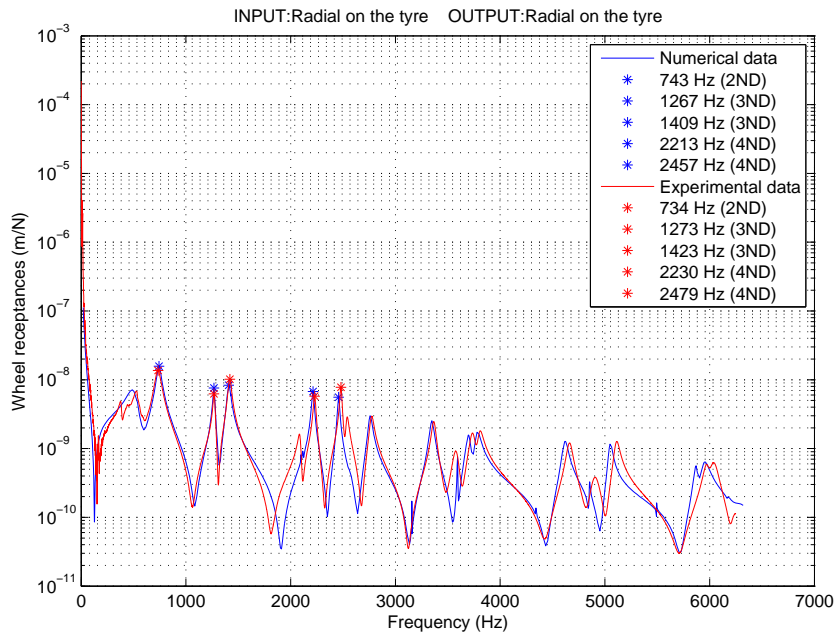


Figure 3.5: Radial receptance at a point on the tyre tread for a radial input at the same point.

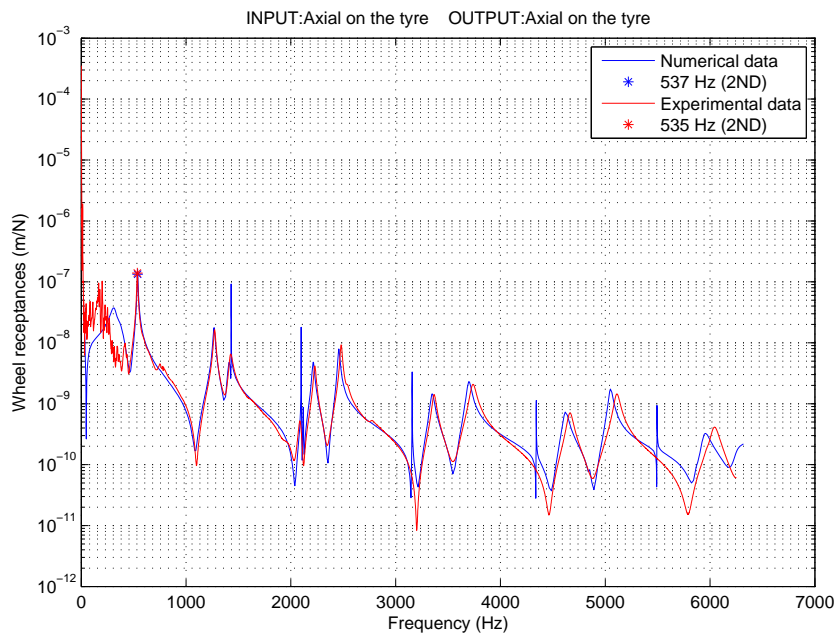


Figure 3.6: Axial receptance at a tyre point for an axial input at the same point.

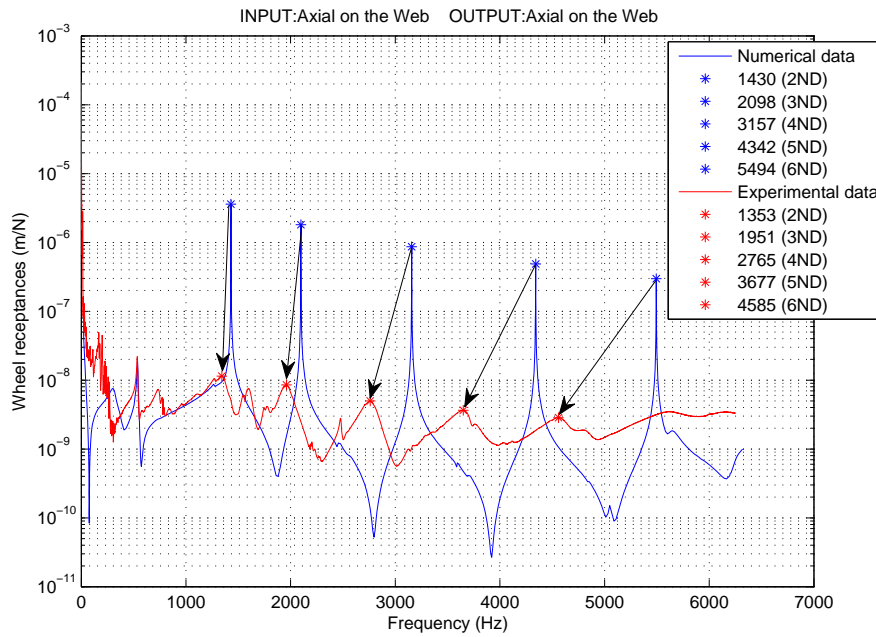


Figure 3.7: Axial receptance at a web point for an axial input at the same point.

3.1.3 Second model

The second model attempted has the aim to reproduce the wheel with all the details that can observe in reality. In this sense, the new model considers not only the wheel but also other components such as hollow axle, axle and bearings (see Figure 3.8).

Figure 3.9 shows the CAD model of the complete Sirio wheel. The lower web and the hollow axle are linked by means of bolted connections, while two tapered roller bearings are positioned between the axle and the hollow axle to allow the rotation of the wheel around the axle. The FE model, shown in Figure 3.8, corresponds to the CAD model. Both sides of the lower web are constrained at the hollow axle (see the green lines), while the tapered roller bearings are constrained at the hollow axle and the axle. The red line indicates the presence of a rigid constraint on the axle.

The modal analysis is performed with the same rubber parameters used in the first model. The radial and the axial receptances remain similar to those obtained from the first model, therefore they are not shown here, while the axial receptance on the web is shown in Figure 3.10. In this last Figure, the modal damping is not

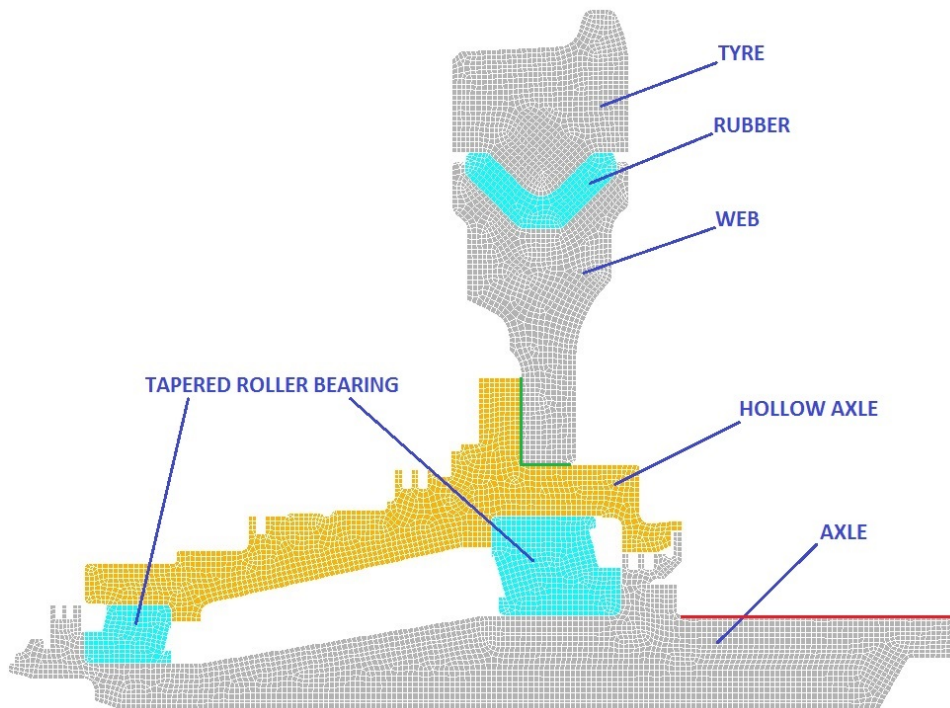


Figure 3.8: FE model of the complete Sirio wheel: axi-symmetric model.

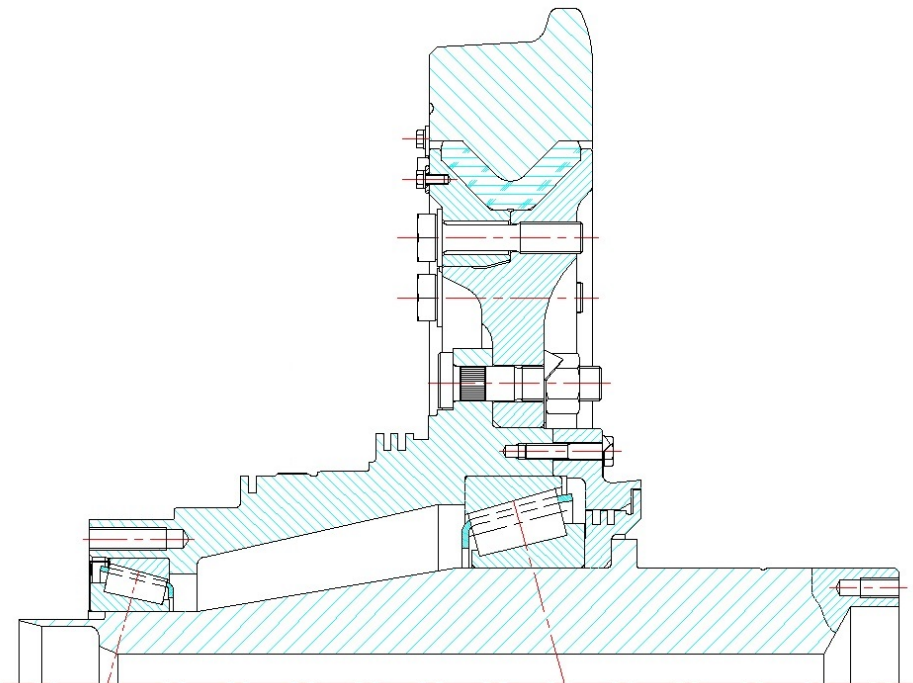


Figure 3.9: CAD model of the complete Sirio wheel

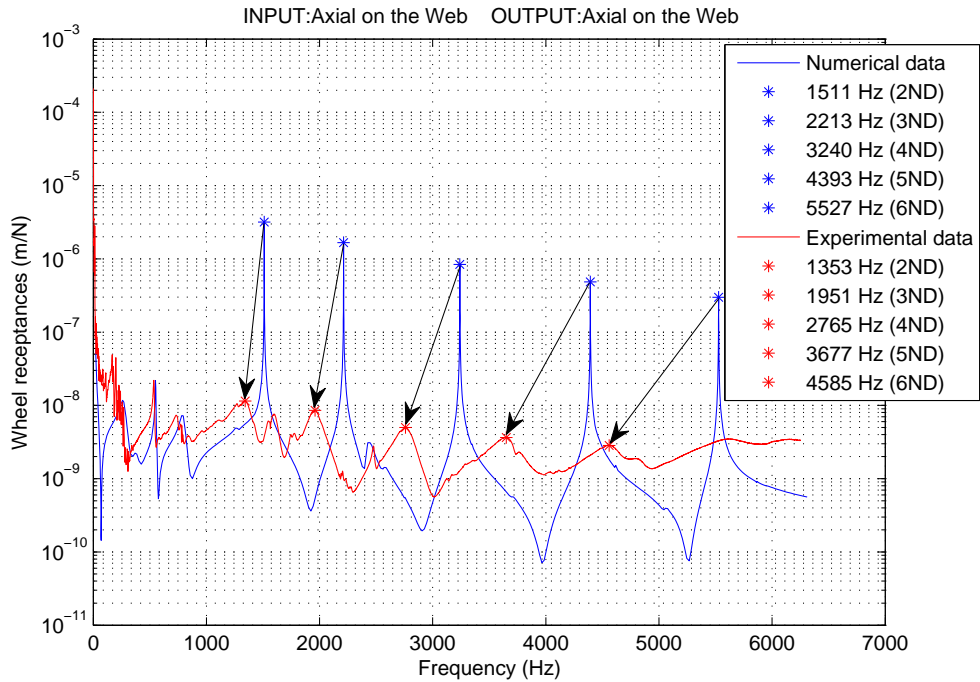


Figure 3.10: Axial receptance at a web point for an axial input at the same point.

modified and the black arrows indicate the correspondence between the numerical and experimental peaks. This receptance is similar to the receptance obtained from the first model, rather, the natural frequencies have increased slightly. The constraint between the web and the hollow axle is therefore too stiff.

For this reason the second model is modified considering a less stiff constraint between the axle and the hollow axle. The red line, in Figure 3.11, shows that the constraint between the two parts takes place where the bolt is located (see Figure 3.9).

The rubber parameters are again those from the first model. The radial and the axial receptances do not change, therefore they are not shown here, while the axial receptance on the web, in Figure 3.12, shows that the natural frequencies are slightly lowered.

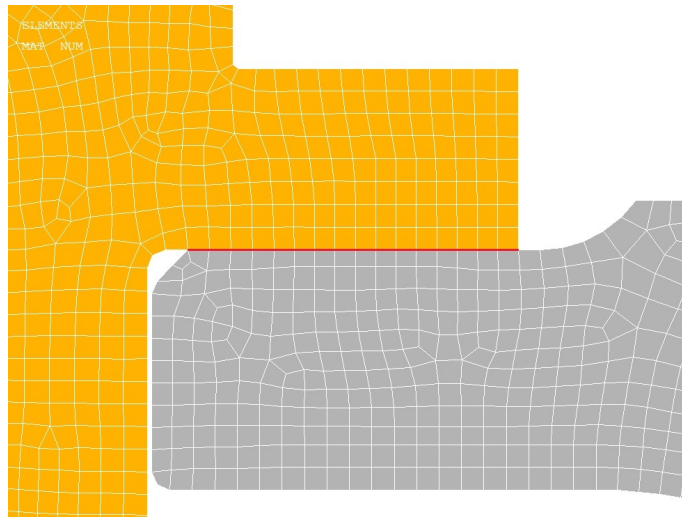


Figure 3.11: Bond between the hollow axle and the axle.

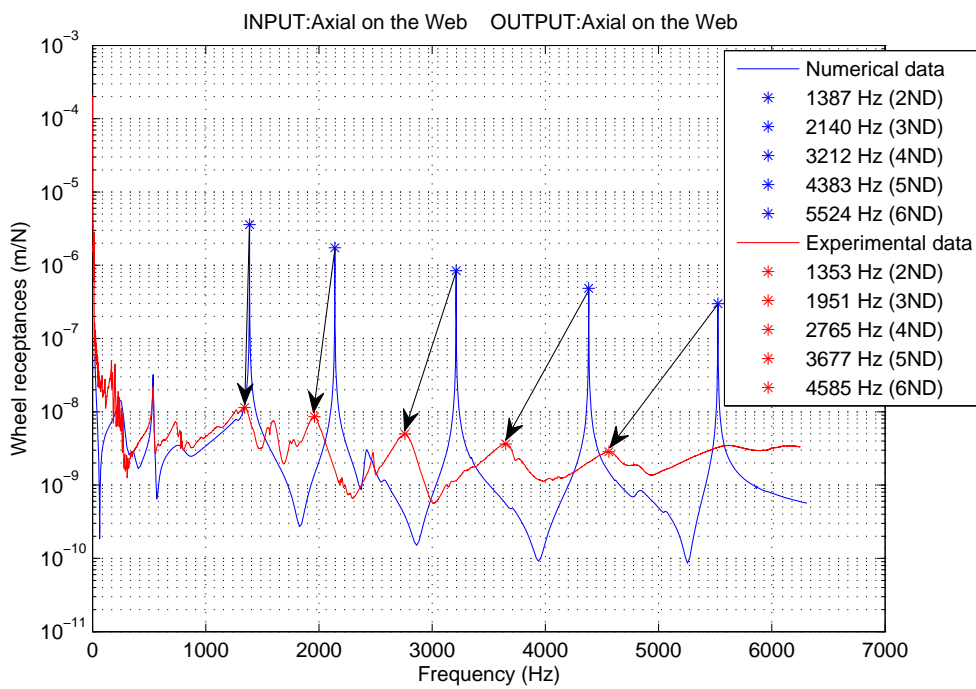


Figure 3.12: Axial receptance at a web point for an axial input at the same point.

3.1.4 Third model

In order to investigate the effect of a possible modification of stiffness connection, the model in Figure 3.13 is considered. The web is linked to the hollow axle in the same way as shown in the last model developed. Then, the hollow axle is not constrained at the axle, but is free. This is the case in which the stiffness of the bearing is neglected.

By comparing the natural frequencies of this model with the natural frequencies of the same model rigidly constrained at the bearings, it has been observed that (results not shown here) the frequencies related to the web modes do not change. Particularly, they do not vary for modes with two or more nodal diameters.

Observing the web modes from the FE model, these modes involve only the web movements. The axle, hollow axle and bearing movements seem to be involved for modes at low frequencies (0 or 1 nodal diameter).

In conclusion, the rubber parameters should be the reason of the low correspondence between the experimental and numerical web modes.

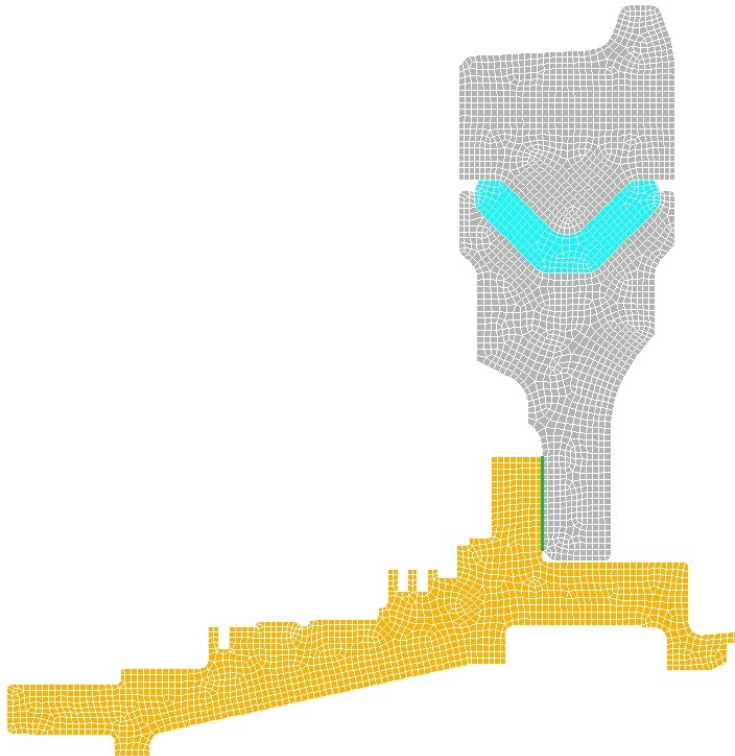


Figure 3.13: FE model of the wheel with hollow axle.

3.1.5 Fourth model

The second model with the reduced stiffness constraint between axle and hollow axle is adopted and the rubber parameters are calibrated considering not only the six natural frequencies considered in the first model but also five web modes with nodal diameters from 2 to 6. In this case values obtained for the rubber are:

$$E = 36MPa, \nu = 0.475.$$

Corresponding receptances are shown in Figures 3.14, 3.15 and 3.16.

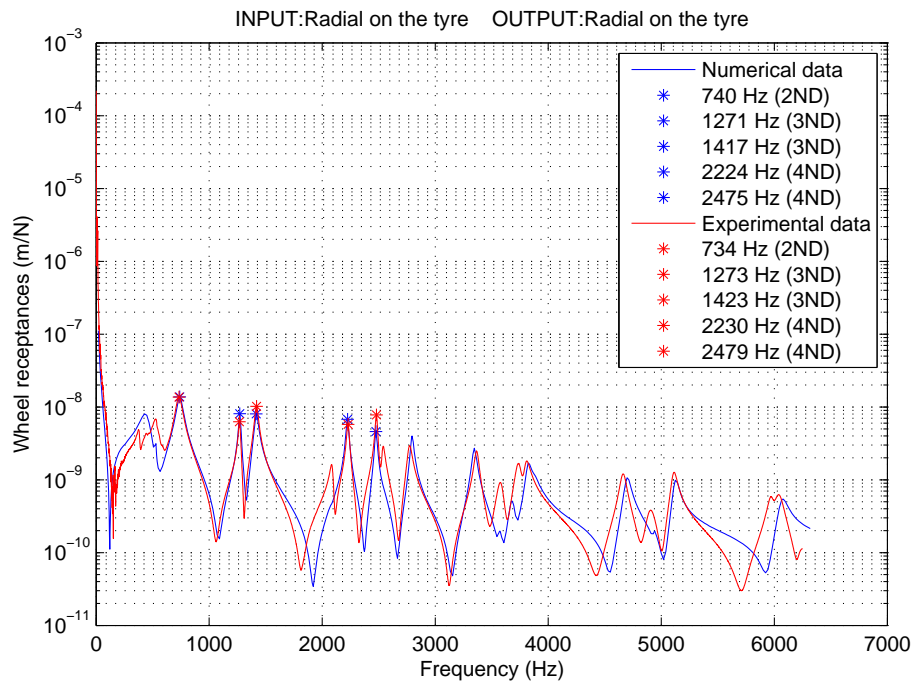


Figure 3.14: Radial receptance at a point on tyre tread for a radial input at the same point.

The radial and axial receptances on the tyre show a good correspondence between the experimental and numerical natural frequencies, while the axial receptance on the web shows that the correspondence of frequencies is improved but the curves do not present a good match. Observing these Figures it can be noted that if the rubber parameters change, the web receptance changes much more than the tyre receptance. Therefore, the rubber parameters remain difficult to obtain and the model developed up to now is not sufficient to describe correctly the axial

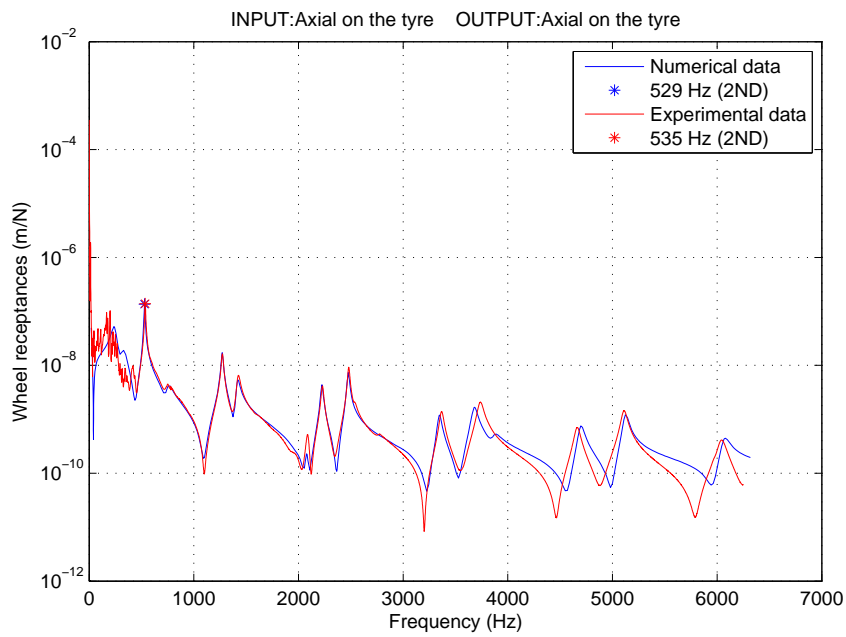


Figure 3.15: Axial receptance in a tyre point for an axial input in the same point.

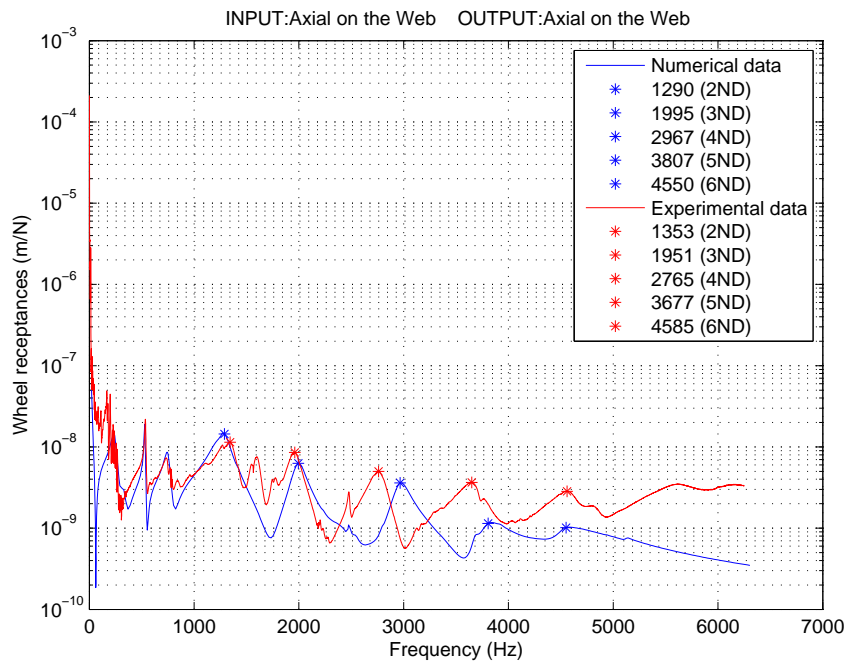
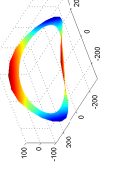
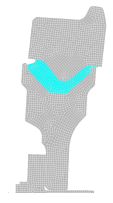
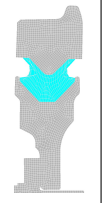
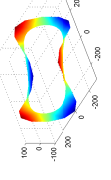
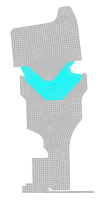
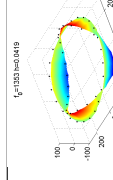
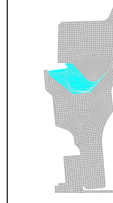
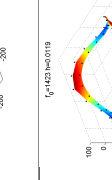
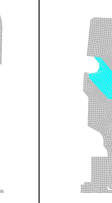
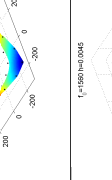


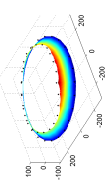
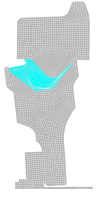
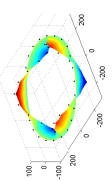
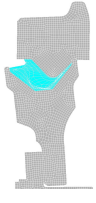
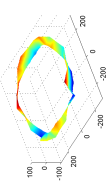
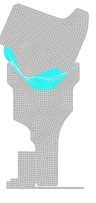
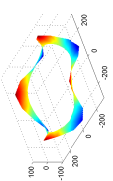

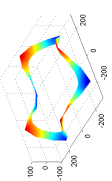
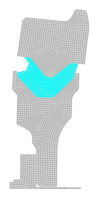
Figure 3.16: Axial receptance at a web point for an axial input at the same point.

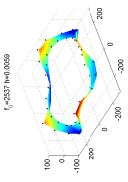
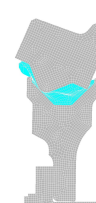
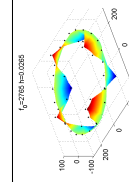
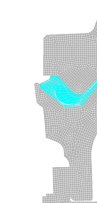
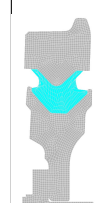
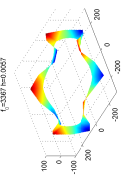
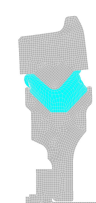
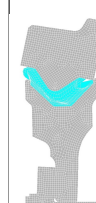
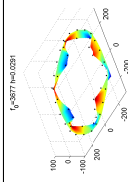
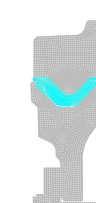
behaviour on the web. It is possible that a 3D model of the wheel along with more sophisticated model updating algorithm can give better results at the web. However this is beyond the scope of the thesis. In fact, the web modes are unlikely to be responsible for squeal due to their high damping levels and a correct description of the tyre is assumed to be sufficient at this stage of the research.

In Table 3.1 the experimental natural frequencies, damping ratios and mode shapes of the wheel are summarized and compared with the numerical ones. The Table is composed of four columns: the first gives the number of nodal diameters of each mode, the second one the experimental data in terms of natural frequencies and damping ratio while the third, in the same way, the numerical data. The last column shows the experimental and numerical mode shapes. Observing this Table, it can be noted that some numerical or experimental modes cannot be identified and in some cases both. When the damping ratio is written in red, it means that the numerical damping ratio is taken from experiments.

This last model is used to study the unstable frequencies of the wheel/rail system, therefore, the modal model is used to generate a text file [27] that will be the most important input of the Huang model [3]. This file contains the modal frequencies, modal mass and mode shapes of the FE model and the selected damping ratios.

ND	Experimental data		Numerical data		Mode shape	
	Frequency (Hz)	Damping ratio (%)	Frequency (Hz)	Damping ratio (%)	Experimental	Numerical
2	535	0.8	529	0.8		
2	734		740	3.5		
3	1273	0.72	1271	0.72		
2	1353	4.19	1290	4.19		
3	1423	1.19	1417	1.19		
0	1560	0.45				

ND	Experimental data		Numerical data		Mode shape	
	Frequency (Hz)	Damping ratio (%)	Frequency (Hz)	Damping ratio (%)	Experimental	Numerical
0	1604	2.36				
3	1951	3.22	1995	3.22		
0	2089	0.77	2078	0.77		
4	2230	0.5	2224	0.5		
4	2479	0.42	2475	0.42		

ND	Experimental data		Numerical data		Mode shape	
	Frequency (Hz)	Damping ratio (%)	Frequency (Hz)	Damping ratio (%)	Experimental	Numerical
1	2537	0.59	2536	0.59		
4	2765	2.65	2967	2.65		
0	2774		2795	0.5		
5	3367	0.57	3346	0.57		
2	3575		3569	0.5		
5	3678	2.96	3807	2.96		

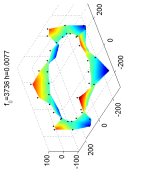
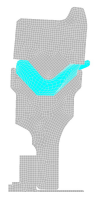
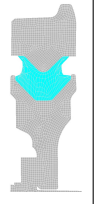
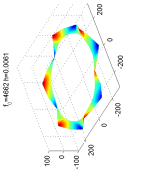
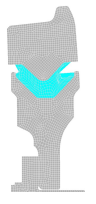
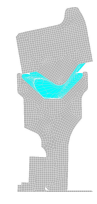
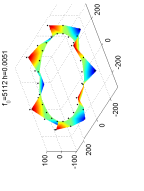
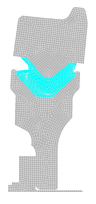
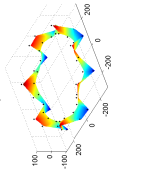
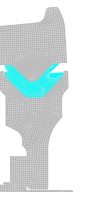
ND	Experimental data		Numerical data		Mode shape	
	Frequency (Hz)	Damping ratio (%)	Frequency (Hz)	Damping ratio (%)	Experimental	Numerical
5	3736	0.78	3680	0.78		
1	3810		3825	0.7		
6	4662	0.61	4697	0.61		
3	4907		4934	0.3		
6	5112	0.51	5123	0.51		
	5971					
7	6040	0.7	6065	0.7		

Table 3.1: Experimental natural frequencies, damping ratio and mode shapes of the wheel in comparison with the numerical ones.

3.2 Class 15x wheel

After the 1987 tests it was hypothesised by BR Research that the radial modes of the Class 15x wheel, as discussed in section 2.2, were largely unaffected by contact with the running rail. They therefore had very light damping and could be easily excited by the check rail contact. The damping treatment applied on this wheel increased the damping of the radial and 1-nodal-circle modes and this was sufficient to eliminate the squeal problem.

In 2011, as discussed in section 2.2, the mode shapes and damping of the Class 15x wheels with and without dampers were studied. Moreover, finite element analysis of the wheel was performed and used to produce a model of the frequency response behaviour. Here the finite element model of the undamped 15x Class wheel is described ¹.

To reduce the computation time, an axi-symmetric representation, shown in Figure 3.17, was adopted. Example of mode shapes of Class 15x wheel obtained by means of the modal analysis are shown in Figure 3.18 while all the calculated natural frequencies are listed in Table 3.2. Moreover, Table 3.3 lists the percentage differences between the measured and predicted natural frequencies. It can be seen that the predictions for the wheels are close to the measured results.

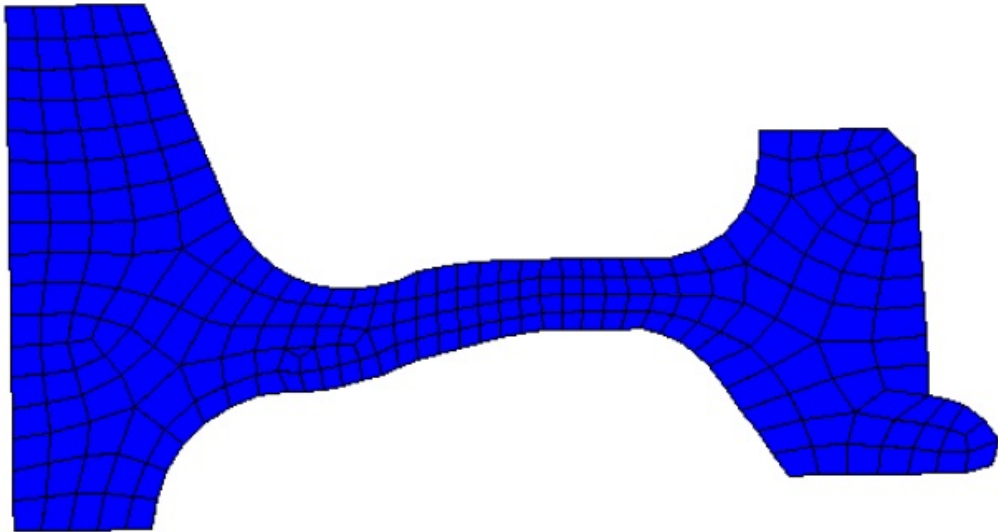
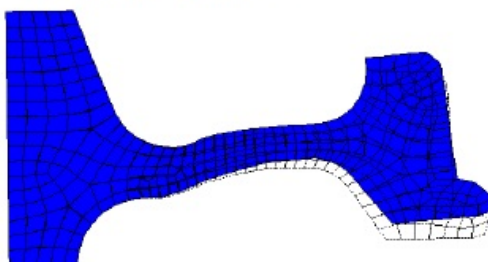


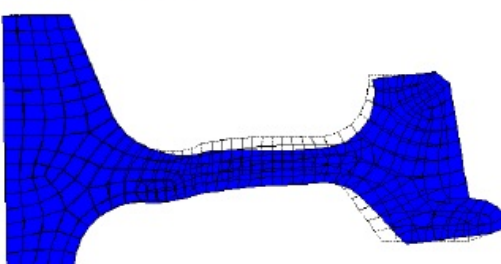
Figure 3.17: FE model of cross-section of the Class 15x wheel.

¹Measurements were performed under contract and results are here reported after personal communication with D. J. Thompson

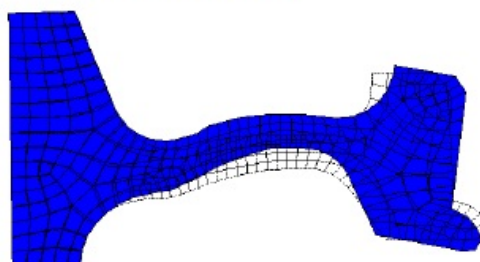
(a) 0-nodal-circle mode 462.96 Hz



(b) Radial mode, 2220.0 Hz



(c) 1-nodal-circle mode, 2901.4 Hz

Figure 3.18: Example of mode shapes of Class 15x wheel with $n=2$.

n	0-n-c	radial	1-n-c	2-n-c	Circum	3-n-c	Other
0	393.77	3551.3	1995.5	4943.8	721.20	8148.0	6431.7
1	306.62	1520.5	2275.0	4983.7	3753.8	8245.8	
2	462.96	2220.0	2901.4	5267.8	4947.8	8892.6	9600.8
3	1124.4	2879.7	3627.2	5777.5	6747.7	9984.9	
4	1997.4	3645.3	4438.0	6495.3	8641.7		
5	2979.4	4517.0	5311.5	7456.7			
6	4019.4	5475.7	6247.8	8335.5			
7	5086.8	6499.9	7252.4	9404.2			
8	6161.7	7571.6	8325.7				
9	7229.9	8678.4	9462.1				
10	8280.3	9812.4					

Table 3.2: Calculated natural frequencies of Class 15x wheel.

n	Wheel		
	0-n-c	radial	1-n-c
2	7.4%	-0.2%	2.5%
3	5.4%	0.3%	0.6%
4	5.1%	0.7%	1.5%
5	5.4%	0.9%	2.0%
6	5.8%	1.1%	4.1%
7	6.1%	1.3%	3.2%
8	6.1%	1.8%	4.7%
9	6.0%	2.7%	5.2%
10	5.6%	3.7%	
average	5.9%	1.4%	3.0%

Table 3.3: Differences between measured and predicted natural frequencies of Class 15x wheel.

In order to assess the propensity to squeal due to excitation at the flange-back, a simple calculation was performed. The wheel was assumed to be excited by a harmonic force at the flange-back in the radial direction while it is connected to the running rail. The connection to the rail was assumed to be in the vertical direction through a contact spring at a position 15 mm from the field side of the wheel tread. This is shown schematically in Figure 3.19.

Figure 3.20 shows the frequency response predicted for a Class 15x wheel with and without the connection to the running rail. The locations of the radial modes are shown as vertical dotted lines. It can be seen that the modes at 2.2, 2.9 and 3.6 kHz (radial modes with 2, 3 and 4 nodal diameters) experience very little additional damping due to connection with the running rail. These modes are therefore likely to be susceptible to squeal. This agrees qualitatively with the results in [7] where radial modes with 2, 3, 4, 5 and 8 nodal diameters were found to squeal.

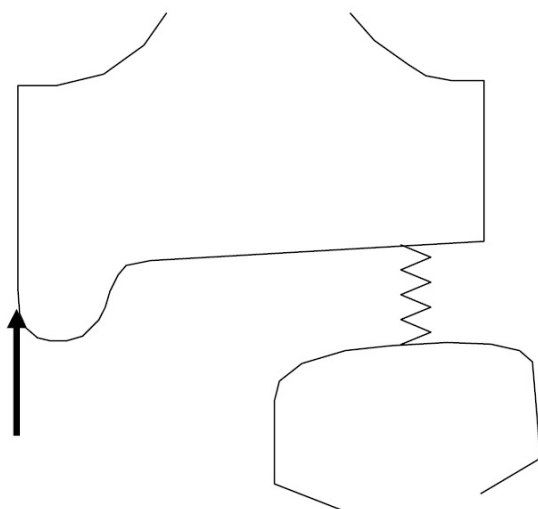


Figure 3.19: Diagram of calculation model showing radial excitation at flange-back and running rail connected through contact spring at wheel tread.

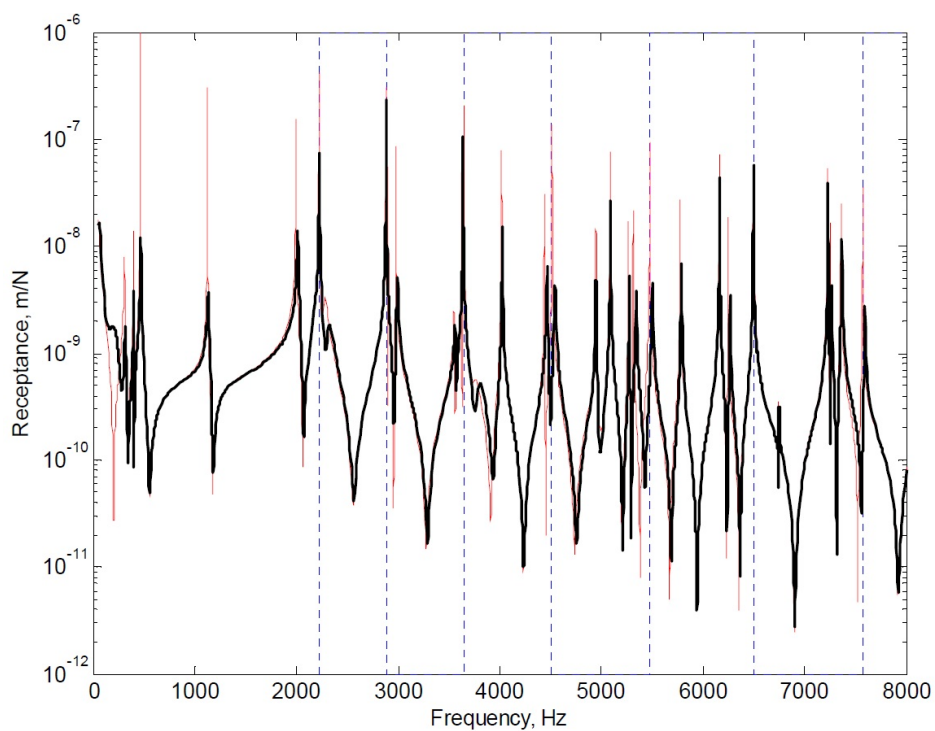


Figure 3.20: Calculated radial receptance of undamped Class 15x wheel at flange-back. (red line) free wheel, (black line) wheel coupled to rail, (blue dotted lines) natural frequencies of radial modes.

Chapter 4

Numerical model for tramcar vehicle dynamics simulation

Urban rail vehicles, especially tramcars, are characterized by structural configuration and design solutions (e.g., articulated bogie frames, independently rotating wheels) which can significantly differ from those of traditional rail vehicles. Moreover, the operating conditions in tramways present peculiar characteristics, different from those typical of railways: low radius curves, frequent departures/stops, and low operational speed. For these reasons, a numerical model (named Monstram), specific for urban vehicles, was developed at Politecnico di Milano [5], [6] to reproduce the vehicle dynamic behaviour during the curve in terms of steady-state and transient behaviour. In particular, it comprises a detailed contact force schematization that takes into account the out of plane contacts which occur as a consequence of the non-negligible wheel-rail yaw angle in low radius curves and accounts for combined longitudinal, lateral and vertical vehicle dynamics.

In the curve squeal phenomenon modelled by Huang [3], some steady-state curving parameters, such as creepages, contact positions and normal contact forces, are required. The dedicated steady-state curving model developed by Politecnico di Milano can provide these parameters. This Chapter describes the Monstram software and shows the results obtained for the specific case relating to the Sirio tram measurement campaign described in Chapter 2.

4.1 The vehicle model

All the results presented in this Chapter are carried out by means of a multi-body mathematical model of the vehicle [5], [29]; large displacement schematization and kinematic non-linearities are considered. This allows the dynamic behaviour of a tramcar to be analyzed, running in tangent and curved track with variable speed, in terms of steady-state and transient behaviour.

The most common configurations of modern tramcars can be reproduced by the combination of two types of basic modules:

- Module A, which is made up of one car body and one bogie.
- Module B, which is a single car body, suspended between two type A modules.

The modules are implemented in the simulation software adopting the following sequence: A-B-A-B-A-B-A (see Figure 4.1).

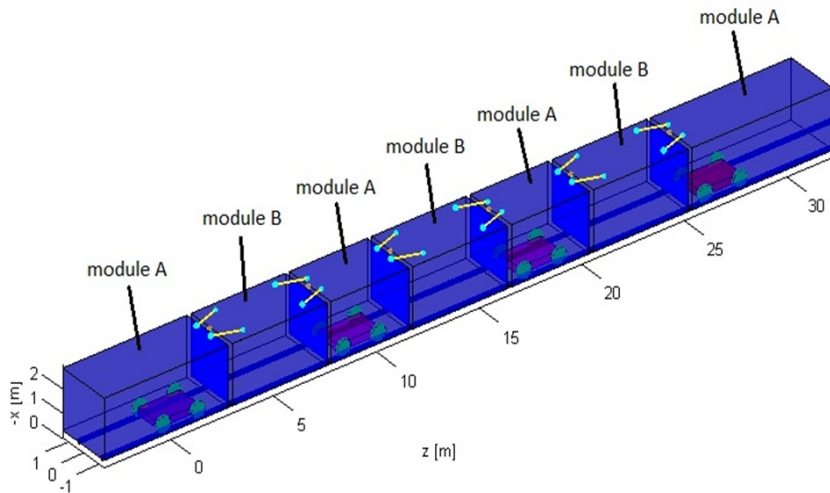


Figure 4.1: Low-floor articulated tramcar (four type A modules and three type B modules). [6]

These different modules are linked to one another by means of kinematic constraints and/or elastic and viscous elements, which reproduce the actual connections between car bodies. The equations of motion are written using different frames of reference: the ideal track centreline is defined with respect to a fixed global coordinate system, while different auxiliary frames of reference are considered to describe the motion of A and B modules.

The equations of motion of each type B module are written by considering the gross motion of a car body coordinate system with respect to the global coordinate system. The origin of the car body coordinate system is rigidly attached to the centre of gravity and its axes are the car body principal axes (see Figure 4.2(a)).

The equations of motion of each A module are written with respect to an auxiliary moving frame of reference (track frame of reference), travelling with variable speed along the ideal track centreline and following the car body centre of gravity (see Figure 4.2 (b)). The second and third A modules present the carbody centre of gravity in the same place as the bogie centre of gravity, but in the first and last this is not the case, therefore this leads to have a different dynamic behaviour if compared with the dynamic behaviour of the second and third A modules. The relative motion of the A module components (carbody, bogie and wheelsets) with respect to this moving reference frame is described through the modal superposition approach: the equations of motion are written in terms of the generalized coordinates corresponding to the rigid and flexible natural modes of each module component (car body, bogie, and wheelset), considered free from any mutual/global constraint. Finally, the total motion of each A module is obtained by superimposing the small displacements of the single components on the gross motion of the overall module, as it results from the motion of the track frame of reference.

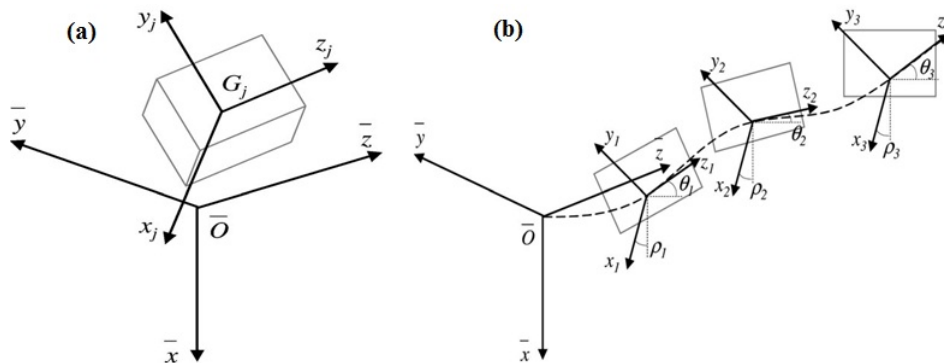


Figure 4.2: (a) Frames of reference adopted for each type B module. (b) Frames of reference adopted for each type A module. [6]

4.2 Wheel-rail contact model

The contact model adopted for the calculation of the forces acting at the wheel-rail interface is suitable for reproducing the contact phenomena which are typical of tramcar operation. In particular, it is designed to account for the out of plane contacts which occur as a consequence of the non negligible wheel-rail yaw angle in low radius curves, as well as the presence of multiple contact points on the tread and the flange, and also in the case of the presence of an edge rail.

The normal forces are evaluated through a multi-Hertzian model [30], while Shen-Hedrick-Elkins [31] formulation is used to calculate those forces acting in the tangential plane. This choice allows a limited number of contact parameters to be considered, without influencing the accuracy of the results. Contact parameters are evaluated beforehand outside the simulation procedure. Therefore, as a preliminary step, a geometrical analysis is carried out in order to obtain the contact parameters which are necessary to solve the contact problem.

The inputs to the geometrical analysis are wheel and rail profiles, which are defined through discrete points, thus allowing measured profiles to be considered as well as theoretical ones. The profiles are then coupled, for given values of relative lateral displacement and yaw angle between wheel and rail, in order to find the geometrical contact points. When a contact point is found, it is possible to determine its longitudinal position with respect to the wheel centre. The final results of the geometrical analysis are multidimensional tables which contain contact parameters for each potential contact point, as a function of both the relative lateral displacement and the yaw angle between the wheel and rail.

Then, at each integration step during time domain dynamic simulation, the actual relative lateral displacement and yaw angle between the generic wheel and the rail are derived from the system state variables, thus allowing the interpolation of the precalculated contact tables, so that the actual contact parameters as well as the number of the actual potential contact points can be obtained.

Finally, by means the multi-Hertzian model, for each contact point the Hertz problem is solved and the normal contact forces are calculated. Then, by means of the longitudinal and lateral creepages at each contact area, the lateral and longitudinal contact forces are determined through the heuristic Shen-Hedrick-Elkins contact model.

4.3 Steady-state behaviour

Before showing the results of time domain multibody simulations, some preliminary considerations concerning the typical behaviour of tramway bogies in a curve are introduced.

Considering the tram in steady-state full curving condition (see Figure 4.3), each of the two axles will show a certain yaw angle with respect to the curve radial direction. This yaw angle is the result of two different contributions. The first one is the 'geometric' contribution σ_g (see Figure 4.3(a)); by indicating with $2p$ the bogie wheelbase and with R the curve radius, it follows that:

$$\sigma_g = \frac{p}{R}. \quad (4.1)$$

Note that the angles σ_g on the two axles have opposite signs and this results in the front axle being understeered, while the rear one is oversteered. For this reason, each wheel velocity is formed not only by the longitudinal component, but also by the transverse velocity (see the red arrows in Figure 4.3(a)). This last component is the origin of the transverse creepage on each wheel and therefore the transverse creep forces occur, which are directed outwards on the front axle and inwards on the rear axle (see the blue arrows in Figure 4.3(a)). As a consequence, a counter-steering yaw moment arises which makes the bogie rotate until the front outer wheel reaches flange contact condition and a flange contact force takes place, which tends to balance the effect of the creep forces mentioned above (see the blue and black arrows in Figure 4.3(b)). It is worth remarking that, in sharp curves, the flange contact condition can be reached also on the rear inner wheel. The mechanism described is responsible for the second contribution to the axle-track relative yaw angle, that will be labelled the 'clearance' contribution σ_c (see Figure 4.3(b)). Since the maximum wheel-rail relative displacement is that corresponding to the lateral clearance ($\pm c$) between the wheelset and the track, if both the front outer wheel and the rear inner wheel reach flange contact condition, the angle σ_c is given by:

$$\sigma_c = \frac{c}{p}. \quad (4.2)$$

While the overall axle-track relative yaw angle on the front axle is given by the sum of σ_g and σ_c , in the case of the rear axle the two contributions subtract. In sharp curves, typical of urban tramways, the curve radius is small, therefore the

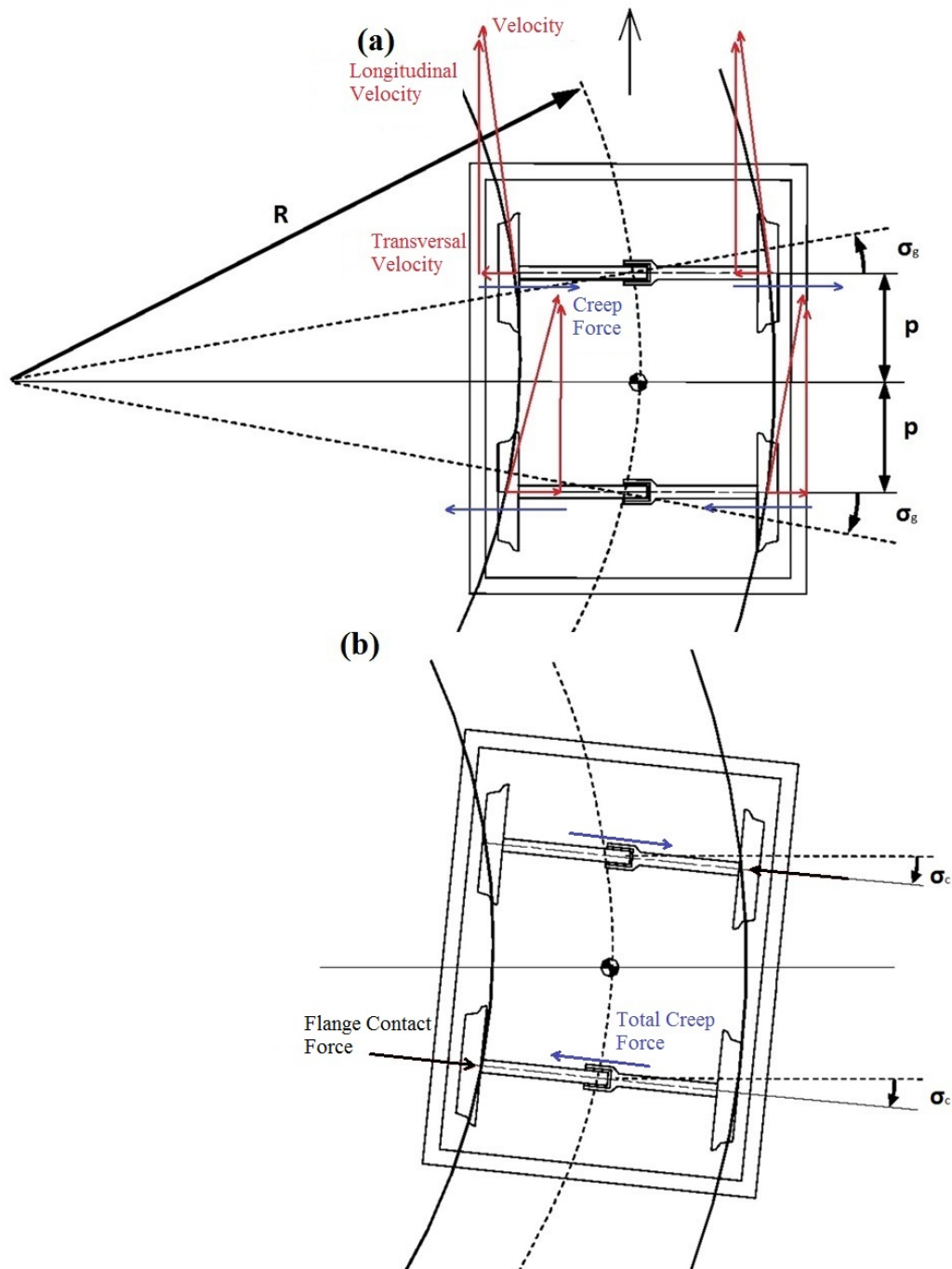


Figure 4.3: Yaw angles of the two axes of a tramway bogie with respect to the track: (a) 'geometric contribution' associated with the ratio between wheelbase and curve radius; (b) 'clearance' contribution corresponding to the lateral clearance ($\pm c$) between the wheelset and the track [32].

‘geometric’ contribution is predominant over the ‘clearance’ one and the rear axle turns out to be oversteered.

The final outcome is that, when dealing with sharp curves, the wheel-rail lateral contact forces on the four wheels of a tramway bogie are typically directed as shown in Figure 4.4(a), no matter what the bogie architecture is (solid axles or independently rotating wheels).

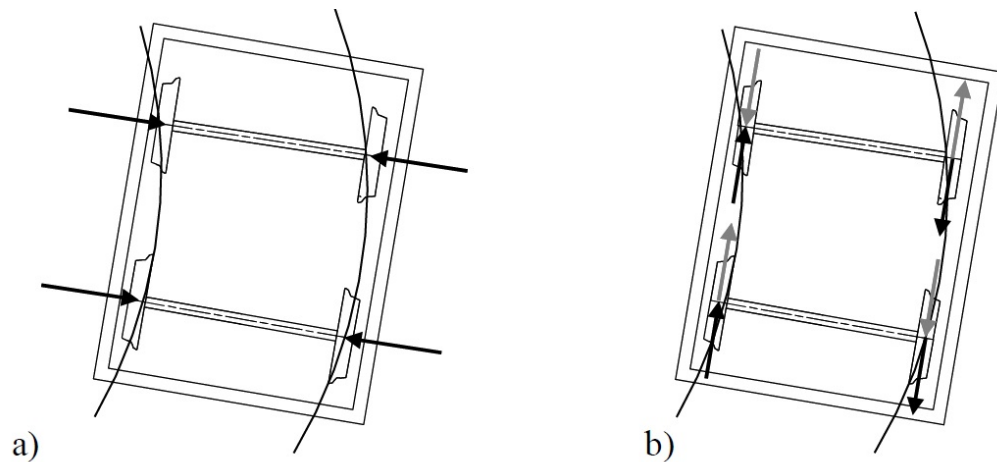


Figure 4.4: (a) Typical distribution of the lateral contact forces on the four wheels of a tramway bogie. (b) Longitudinal contact forces on a bogie with solid axles: the forces indicated in black and in grey respectively correspond to the effect of the inner rail radius being smaller than that of the outer one and to the effect of a wheelset lateral displacement (with respect to the centred position) [32].

While in the case of independently rotating wheels longitudinal forces are nearly absent, in the case of a bogie equipped with solid axles longitudinal creep forces (see Figure 4.4(b)) are added to the lateral ones (see Figure 4.4(a)).

Longitudinal forces occur because of the solid axle, which imposes the angular speed of the two wheels to be equal, and they are a consequence of two different mechanisms. First, the radius of the inner rail is smaller than the outer one and, consequently, the inner wheel travels at a speed lower than the outer wheel (see black arrows in Figure 4.4(b)). Second, whenever the wheelset is displaced from the centred position, the rolling radii on the two wheels become different (see grey arrows in Figure 4.4(b)). Both these effects lead to opposite creepages and consequently opposite longitudinal forces on the two wheels of an axle (see Figure 4.4(b)).

4.4 Numerical results - Simulation with gauge of 1445 mm

The analysis, reported here, refers to the second module A because this presents a symmetric geometry, therefore the dynamic behaviour is easier to study. A tram with independently rotating wheels is analyzed in a steady-state left curve with track gauge 1445 mm. The curve radius is set to be 17.5m, the curve length 32m and the tramway velocity 10km/h, while all the outputs will be shown considering the system of reference adopted for each module, as shown in Figure 4.2.

4.4.1 Lateral displacements

When the bogie enters the curve, the front axle moves to the right, while the rear one moves to the left and both the outer front and the inner rear wheel remain in flange contact during the whole curve. The relative wheel-rail lateral displacement on each wheel are shown in Figure 4.5.

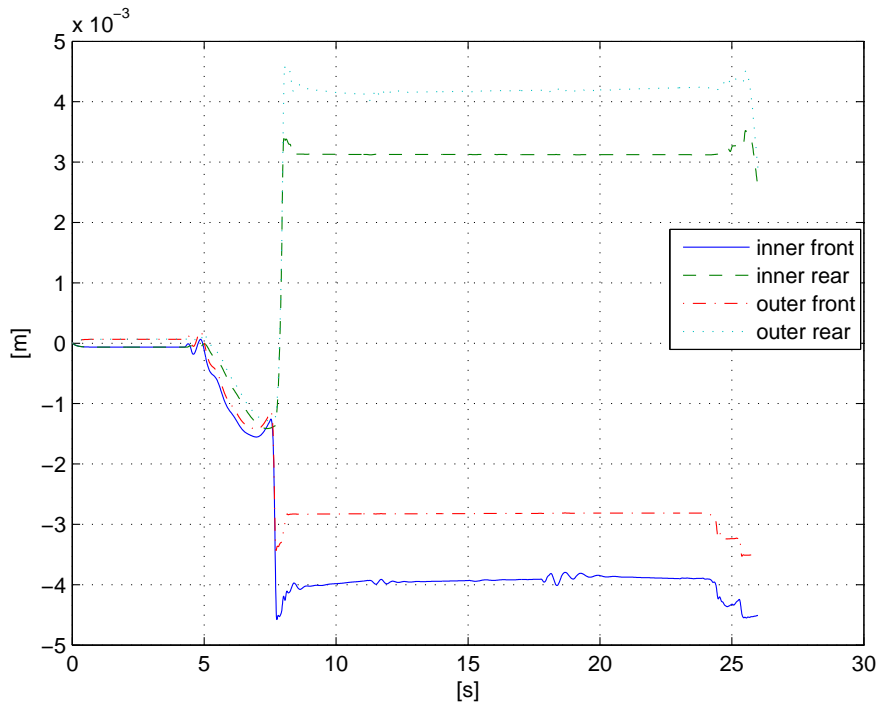


Figure 4.5: Relative wheel-rail lateral displacement of the second module A.

Considering the adopted reference system, the displacement has positive sign if

directed towards the left. Observing Figure 4.5, when the bogie fully enters the curve, the lateral displacement signs are coherent with the adopted reference system: the outer and inner front wheel have negative sign as the front axle moves to the right, while the outer and inner rear wheel, which move to the left, have positive sign. It can also be observed that the flanging wheel displacement is smaller than the opposite one because elastic deformation of the resilient wheel occurs.

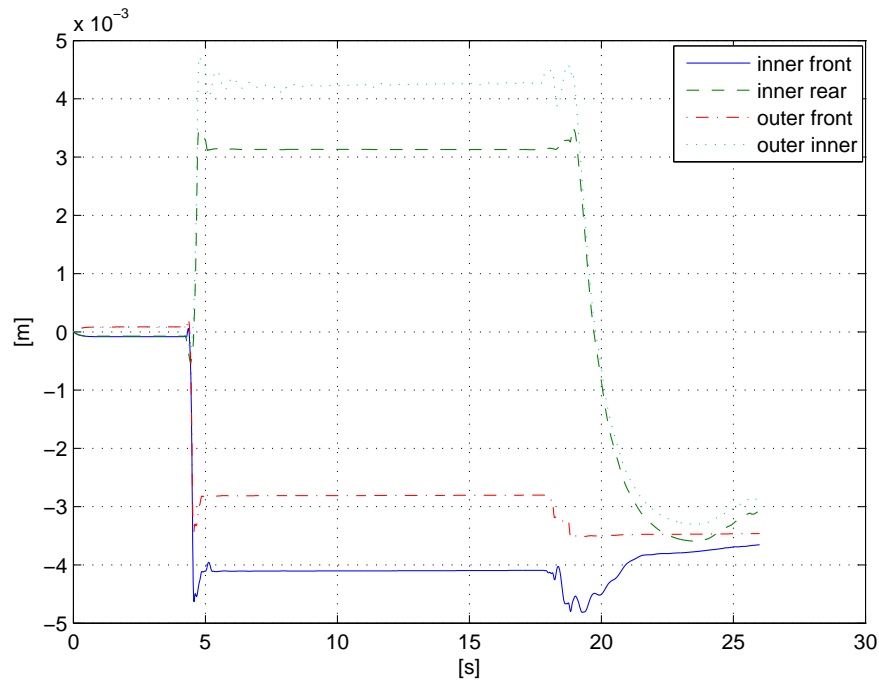


Figure 4.6: Relative wheel-rail lateral displacement of the first module A.

Considering Figure 4.6 about the relative wheel-rail displacement of the first module A, it can be noted that, when the curve is finished, the bogie does not go back to the centred position due to the fact that in the case of independently rotating wheels no self-aligning yaw moment acts on the axle.

4.4.2 Vertical forces

The vertical forces on each wheel are distributed as shown in Figure 4.7. Observing this Figure the vertical loads on each wheel are partially transferred from the inner to the outer wheels. For example, the outer front wheel is more loaded than the opposite one. In addition, transient oscillations take place during entrance and

exit of the curve, which are governed by the carbody natural modes. Finally, the input axle loads are coherent with the output of the simulation before entering the curve.

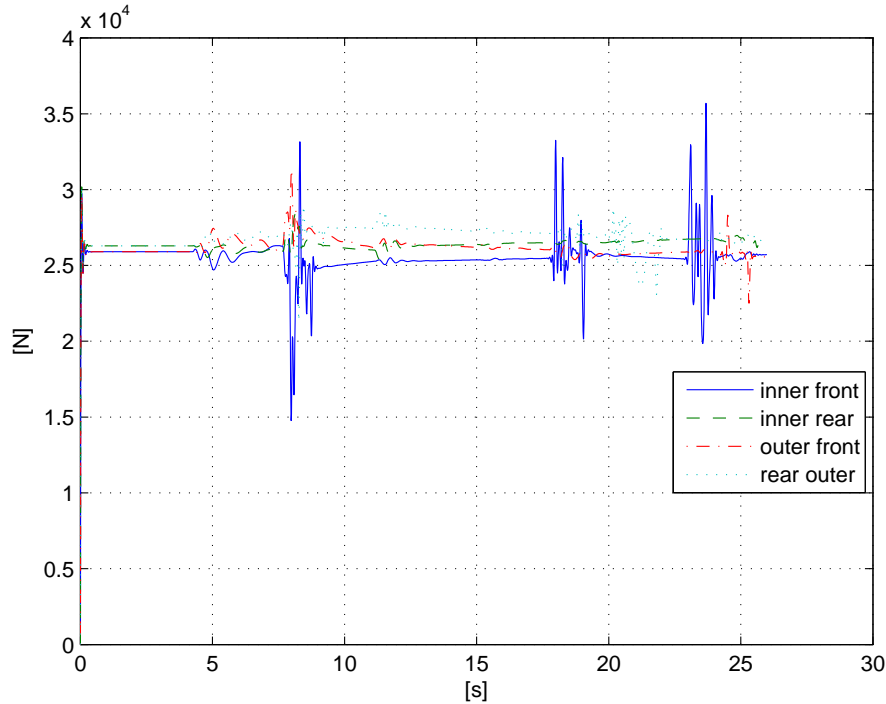


Figure 4.7: Vertical forces on each wheel of the second module A.

4.4.3 Lateral forces

Considering the creep forces and the flange contact forces, the lateral forces on each wheel are distributed as shown in Figure 4.8.

The curves show that the outer front wheel presents a positive lateral force because the flange contact force, directed to the left, is bigger than the creep force that is directed to the right. The same thing occurs for the inner rear wheel which is in flange contact condition, but presents a negative lateral force. In contrast, the inner front and outer rear wheel do not present the flange contact condition and therefore the lateral forces are caused mainly from creep forces. The inner front wheel presents a negative force while the outer rear one a positive force. Figure 4.4(a) shows the distribution of the lateral contact forces on the four wheels mentioned above.

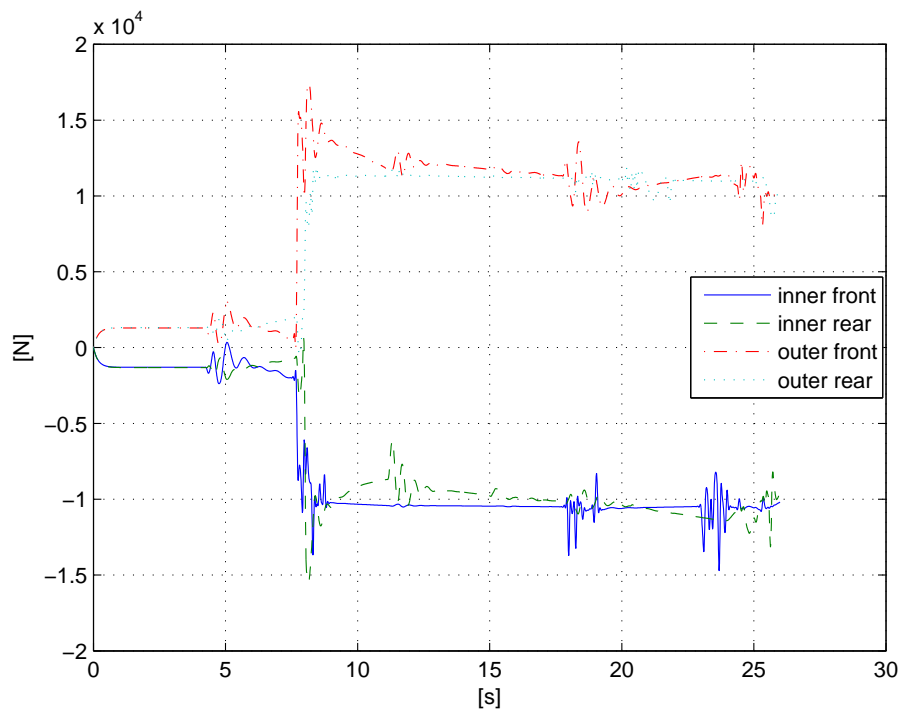


Figure 4.8: Lateral forces on each wheel of the second module A.

4.4.4 Longitudinal forces

The longitudinal forces on each wheel are distributed as shown in Figure 4.9. The loads are very small and negligible if compared with the lateral and vertical loads because independently rotating wheels are used. The only longitudinal forces

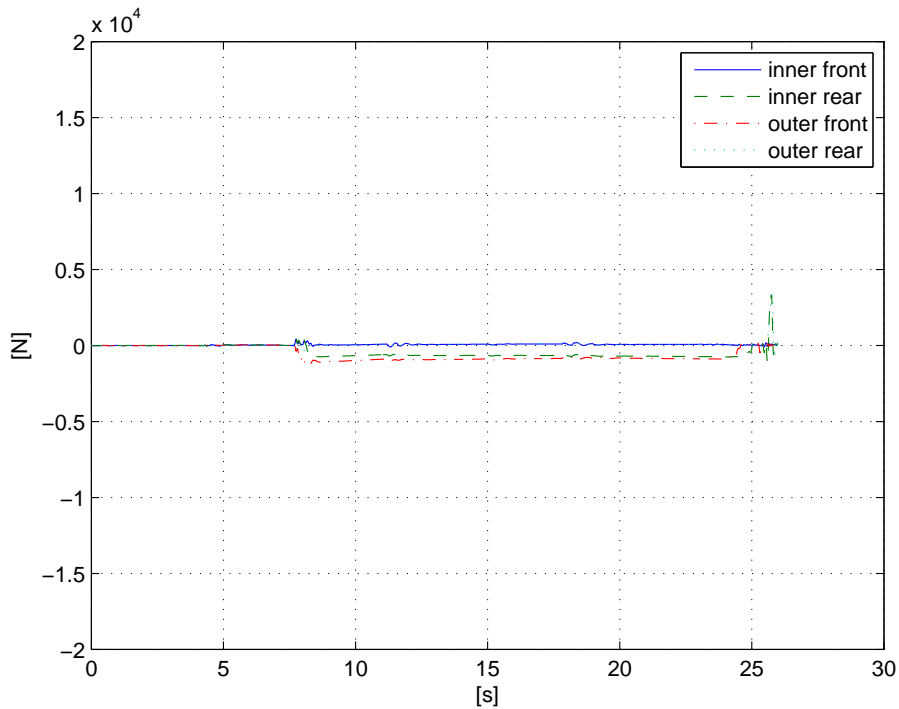


Figure 4.9: Longitudinal forces on each wheel of the second module A.

different from zero are the loads in flange contact condition. These forces are generated from creepage phenomena that occur because there are two different contact points and therefore two different rolling radii.

4.4.5 Numerical results at the contact points

Although wheel and rail profiles are considered rigid in the geometrical analysis, besides the geometrical contact points, 'potential' contact points are also taken into account. Contact may occur at these points as a consequence of the local deformation of the profiles under load. In this case, the simulation takes into account six 'potential' contact points.

The results will show that for the outer front and inner rear wheels a contact

occurs on the tread and between the flange and the rail running head while for the inner front and outer rear wheels only a contact on the tread occurs.

All the outputs will be represented considering the system of reference for each contact point as shown in Figure 4.10 for the nominal contact point.

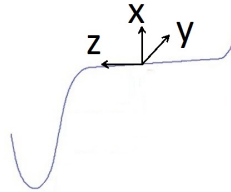


Figure 4.10: System of reference adopted in the nominal contact.

Tangents at the contact points

The tangents at the contact points, as shown in Figure 4.11, are fundamental to understand if the forces are on the tread or on the flange. Observing this Figure, the ‘potential’ contact points identified on the outer front and inner rear wheels, are on the tread (green curve) and between the flange and the rail running head (red curve). Instead, in the case of inner front and outer rear wheels, there is one identified on the tread (green curve) and another between the flange back and the rail grooved head (blue curve).

Normal, transverse and longitudinal contact forces

The normal contact forces are shown in Figure 4.12. The curves of this Figure show that for the outer front and inner rear wheels a contact point occurs on the tread and between the flange and the rail running head while for the inner front and outer rear wheels only a contact on the tread occurs and no contact between the flange back and rail grooved head happens, in fact the normal contact force in that point is equal to zero (blue line).

The transverse contact forces are shown in Figure 4.13, while Figure 4.14 represents the normal and transverse contact forces on the front wheelset at 15 seconds into the simulation. It can be seen that the lateral and vertical forces from the decomposition are equal to the lateral and vertical forces obtained from the simulation (see Figures 4.8 and 4.7).

Finally, the longitudinal contact forces are shown in Figure 4.15.

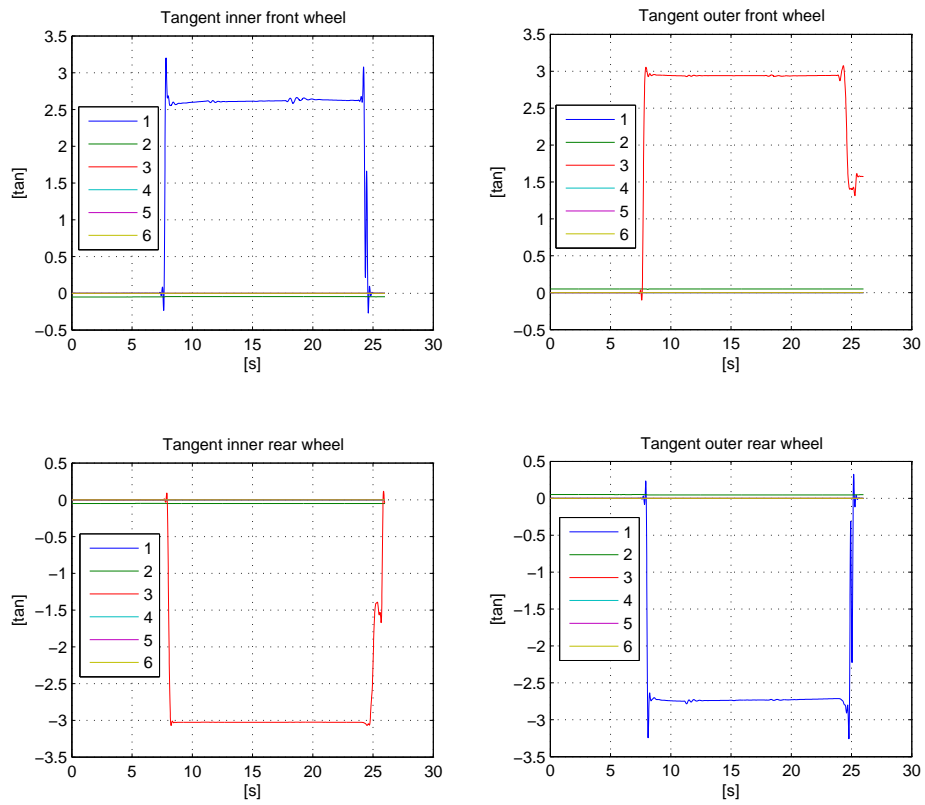


Figure 4.11: Tangents at the contact points of the second module A.

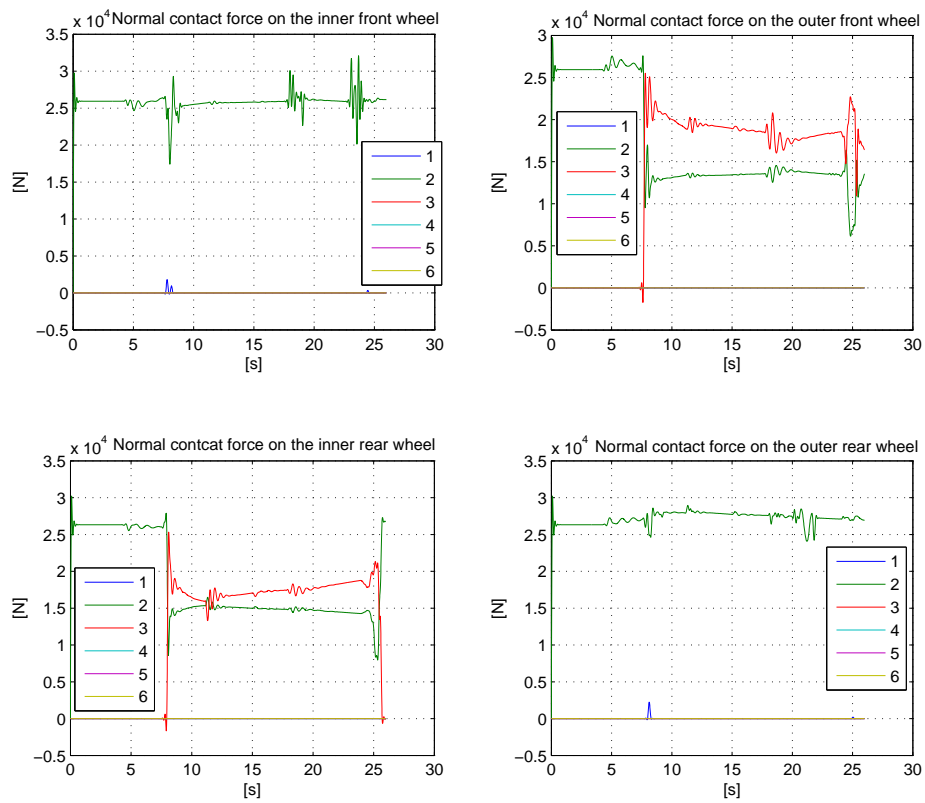


Figure 4.12: Normal contact forces on the wheels of the second module A.

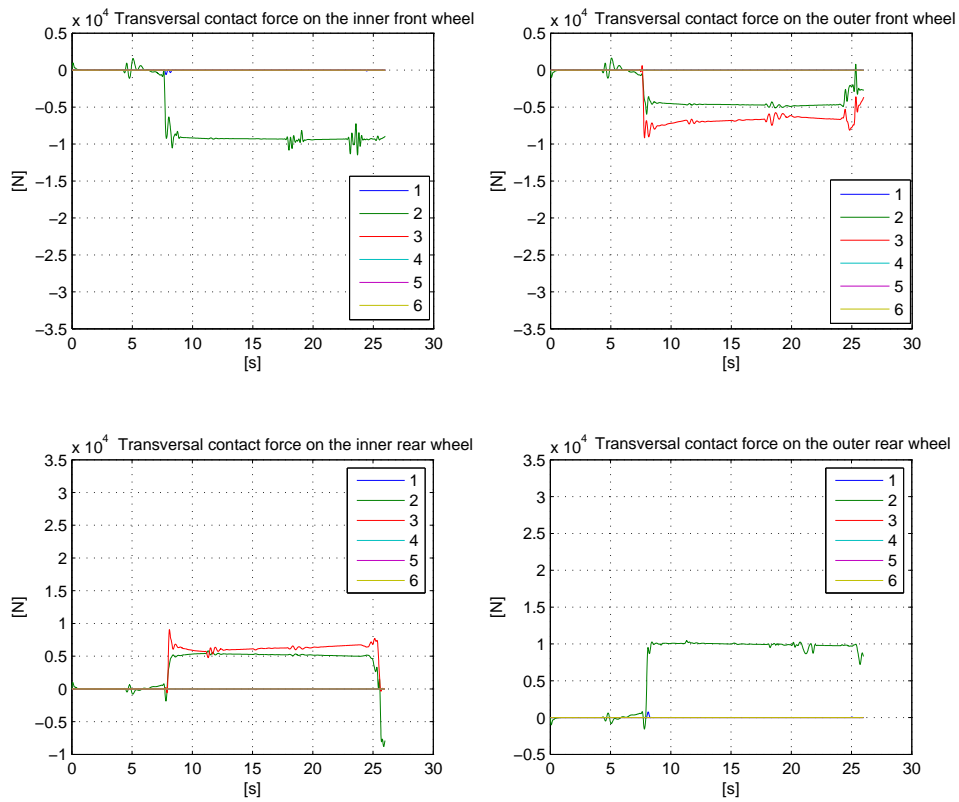


Figure 4.13: Transverse contact forces on the wheels of the second module A.

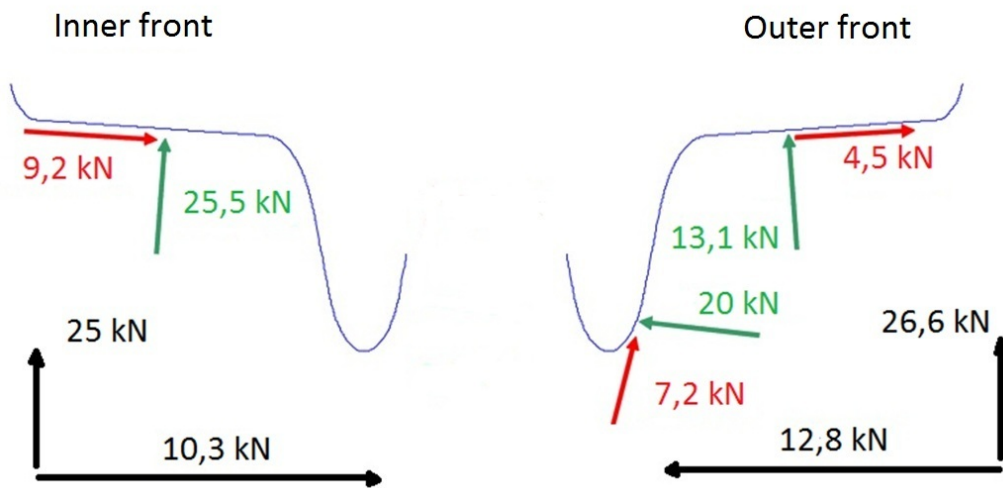


Figure 4.14: Distribution of the normal and transverse contact forces on the front wheelset of the second module A at 15 seconds into the simulation.

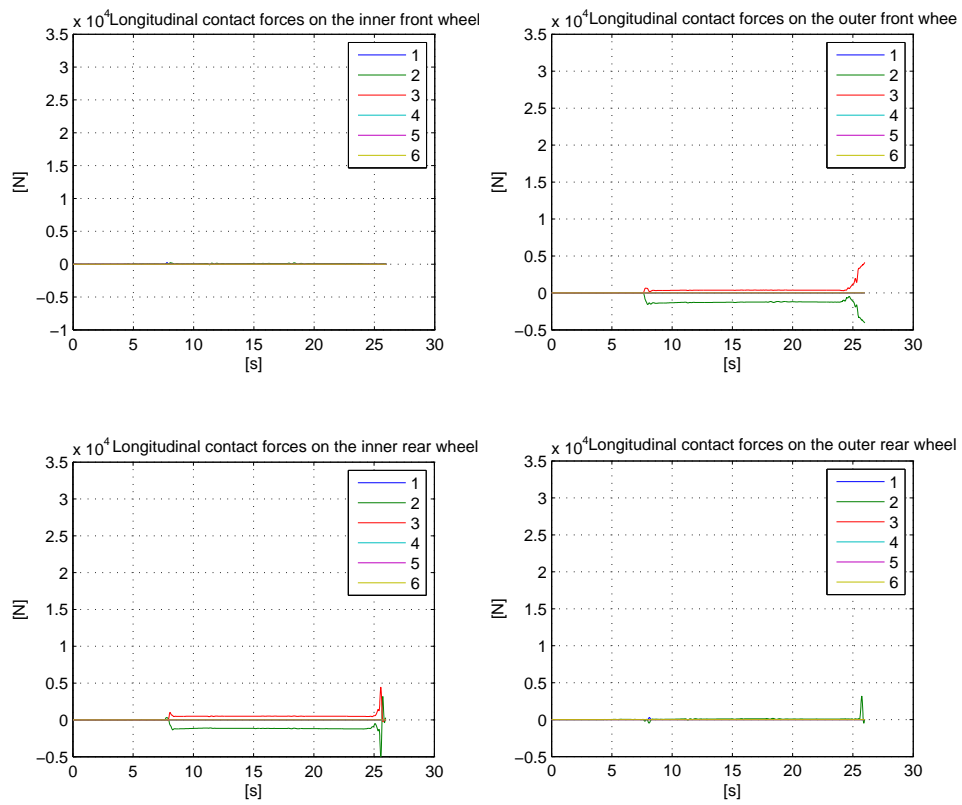


Figure 4.15: Longitudinal contact forces on the wheels of the second module A.

Longitudinal, transverse and spin creepages

In Figures 4.16 and 4.17 are shown the longitudinal and transverse creepages. The longitudinal ones, as seen with longitudinal forces, are nearly absent.

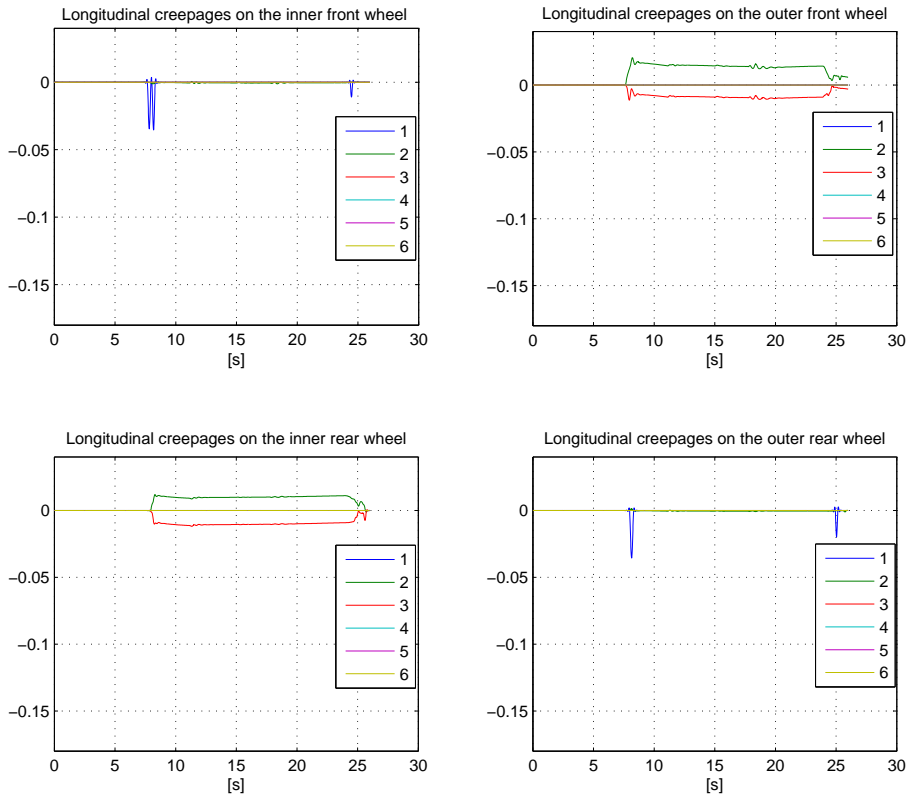


Figure 4.16: Longitudinal creepages on the wheels of the second module A.

The results of the spin creepages in time domain are not reported here. To have an idea of this value the spin creepages at the contact points of the inner and outer front wheel at 15 seconds into the simulation are calculated as:

$$\gamma_{60} = \frac{\sin(\theta)}{R_w}. \quad (4.3)$$

where θ is the angle of the tangent in the contact point while R_w is the radius of the wheel. The values are reported in Table 4.1.

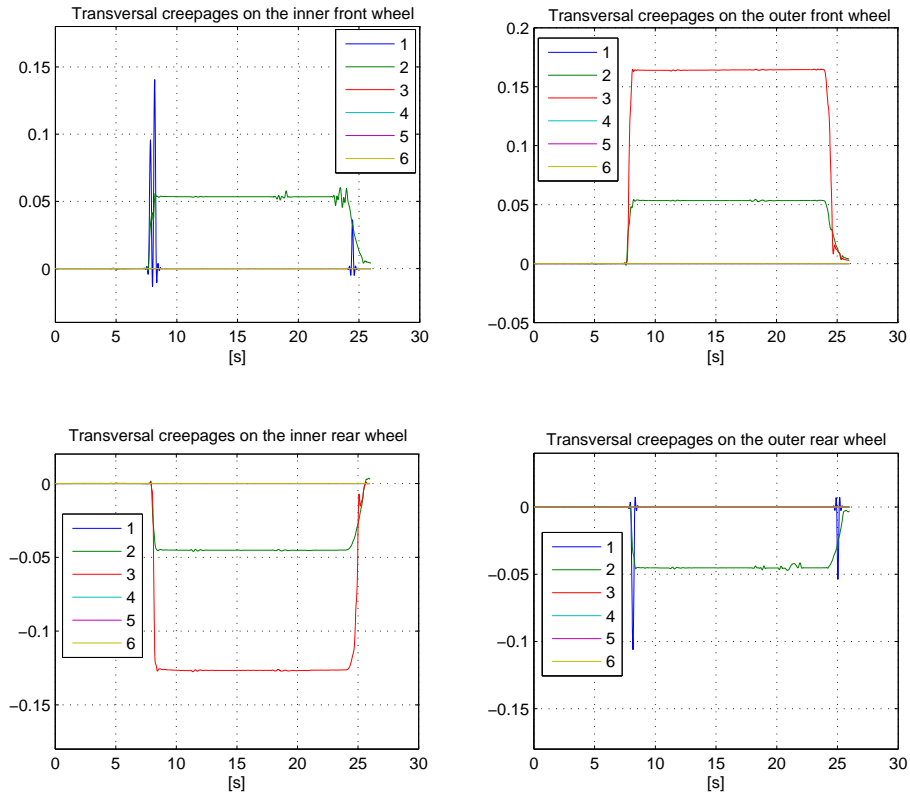


Figure 4.17: Transverse creepages on the wheels of the second module A.

Wheel	Contact point	Name	Unit	Value
Outer front wheel	Contact on the tread	γ_{60}	[1/m]	0.16
Outer front wheel	Contact on the flange	γ_{60}	[1/m]	2.95
Inner front wheel	Contact on the tread	γ_{60}	[1/m]	-0.13

Table 4.1: Spin creepages at the contact points of the inner and outer front wheel at 15 seconds into the simulation.

Contact point positions

Figure 4.18 shows the difference in radius between the nominal contact point and the new contact point of each wheel. In this way the vertical position with respect to the nominal contact point can be determined but not the lateral position. For this reason the lateral position with respect to the nominal contact point is needed. This result is not reported here, but the lateral position at 15 seconds into the simulation is obtained and reported in Figure 4.19.

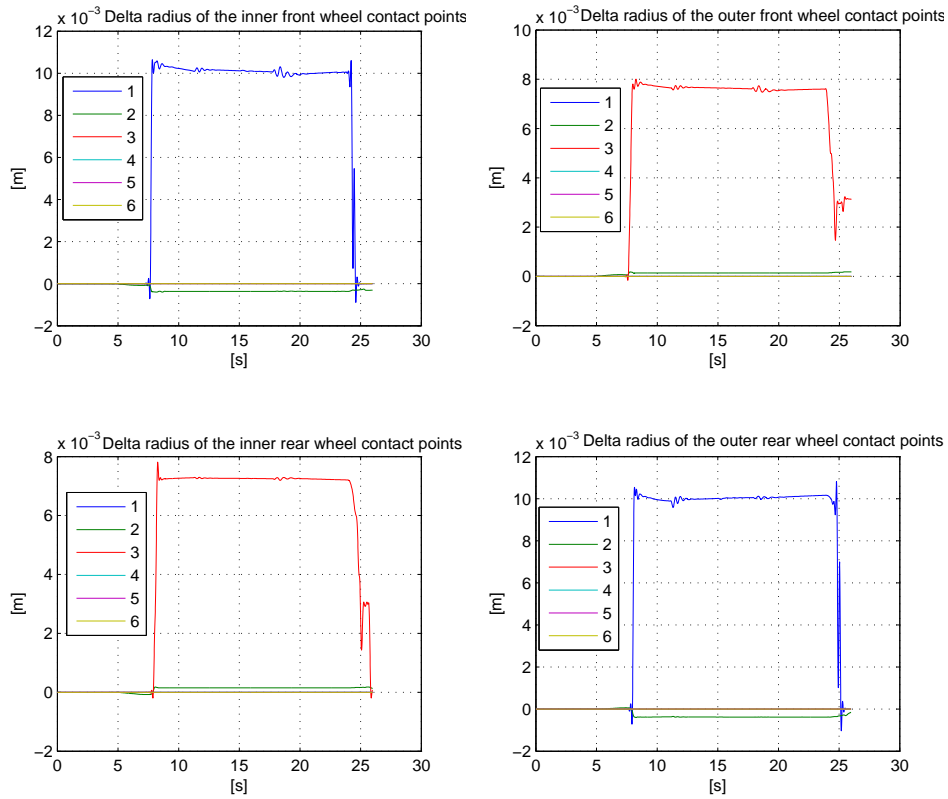


Figure 4.18: Difference in radius of the wheel contact points.

Considering the frame of reference at the nominal contact point, as shown in Figure 4.19, the contact point positions of the inner and outer front wheel with respect to the nominal contact point are shown in Figure 4.19 and reported in Table 4.2.

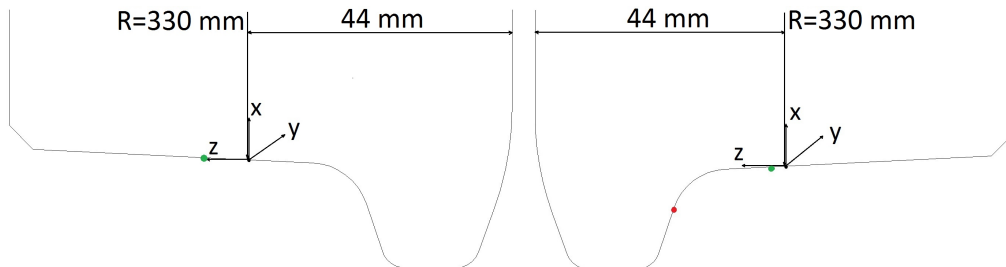


Figure 4.19: Contact point positions on the front wheelset of the second module A at 15 seconds into the simulation.

Wheel	Contact point	Name	Unit	Value
Outer front wheel	Contact on the tread	$[x \ y \ z]$	[mm]	[-0.15 0 2.8]
Outer front wheel	Contact on the flange	$[x \ y \ z]$	[mm]	[-7.65 50.65 19.8]
Inner front wheel	Contact on the tread	$[x \ y \ z]$	[mm]	[0.35 0 7.45]

Table 4.2: Contact point positions of the inner and outer front wheel at 15 seconds into the simulation

Finally, using the geometry of the rail in Figure 4.20 and the contact points on the wheels shown in Figure 4.19 the contact points on the rails with respect to the system of reference shown in Figure 4.21 are visually estimated. They are shown in Figure 4.21 and listed in Table 4.3.

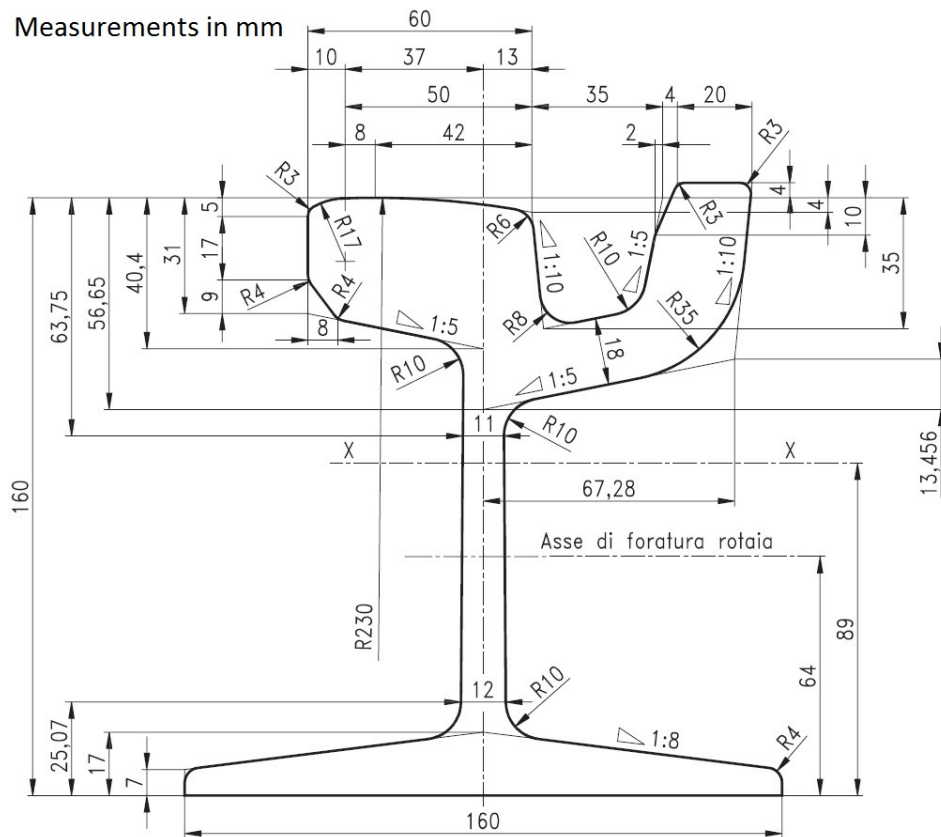


Figure 4.20: Geometry of the rail (grooved rail Ic UNI 3142) adopted for the experimental campaign [33].

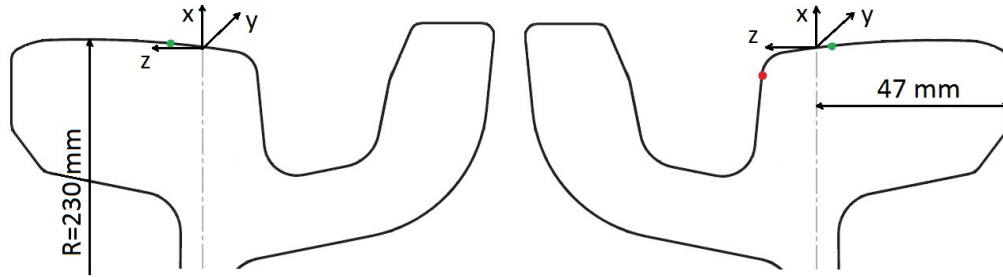


Figure 4.21: Contact point positions on the rails at 15 seconds into the simulation.

Rail	Contact point	Name	Unit	Values
Outer rail	Contact on the tread	$[x \ y \ z]$	[mm]	[0.5 0 -3.5]
Outer rail	Contact on the flange	$[x \ y \ z]$	[mm]	[-7 50.65 13]
Inner rail	Contact on the tread	$[x \ y \ z]$	[mm]	[1.5 0 8]

Table 4.3: Contact point positions of the inner and outer rail at 15 seconds into the simulation

4.5 Numerical results - Simulation with gauge of 1447 mm

Since, in the previous simulation, only contact points on tread and between the flange and the rail running head occur, a simulation with a widened track gauge has been performed in order to obtain contact points between the flange back and rail grooved head. For this reason, a simulation with the same input parameters mentioned before and gauge of 1447 mm have been investigated.

4.5.1 Numerical results at the contact points

In this case only the numerical results regarding the contact points of the inner and outer front wheels have been taken into account. All the outputs will be represented considering the system of reference for each contact point as shown in Figure 4.10 for the nominal contact point.

Tangents and normal, transverse and longitudinal forces at the contact points

By looking at Figures 4.22 and 4.23, the results show that, for the inner front wheel, a contact point occurs on the tread (green line) and between the flange back and rail grooved head (blue line). For the outer front wheel, a contact point

occurs on the tread (green line) and between the flange and rail running head (red line).

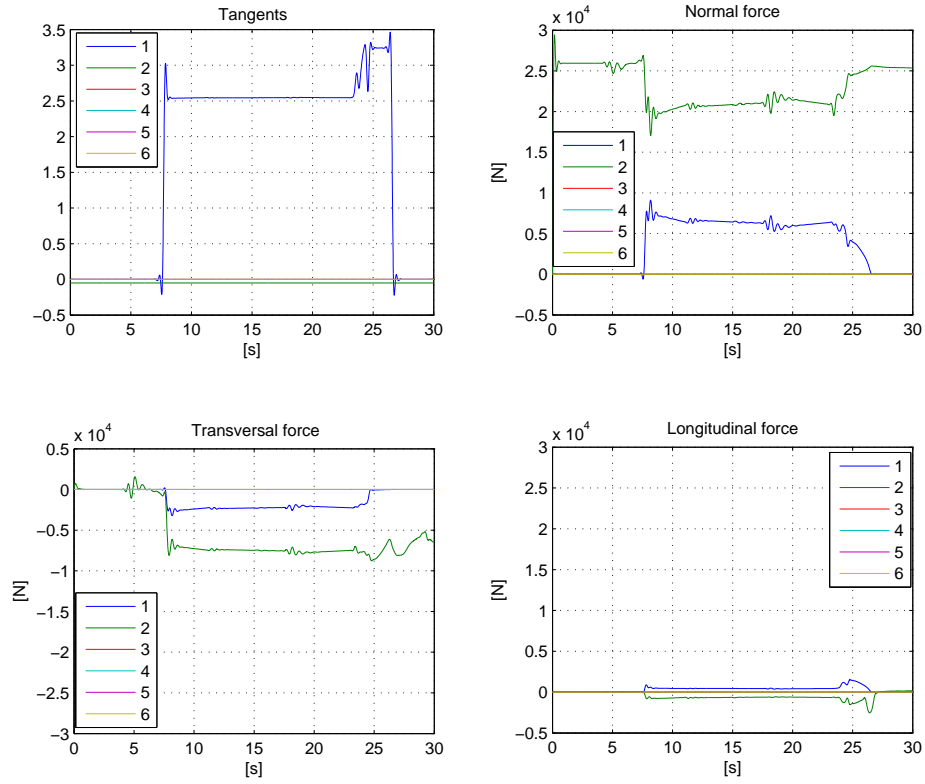


Figure 4.22: Tangents and normal, transverse and longitudinal forces at the contact points of the inner front wheel.

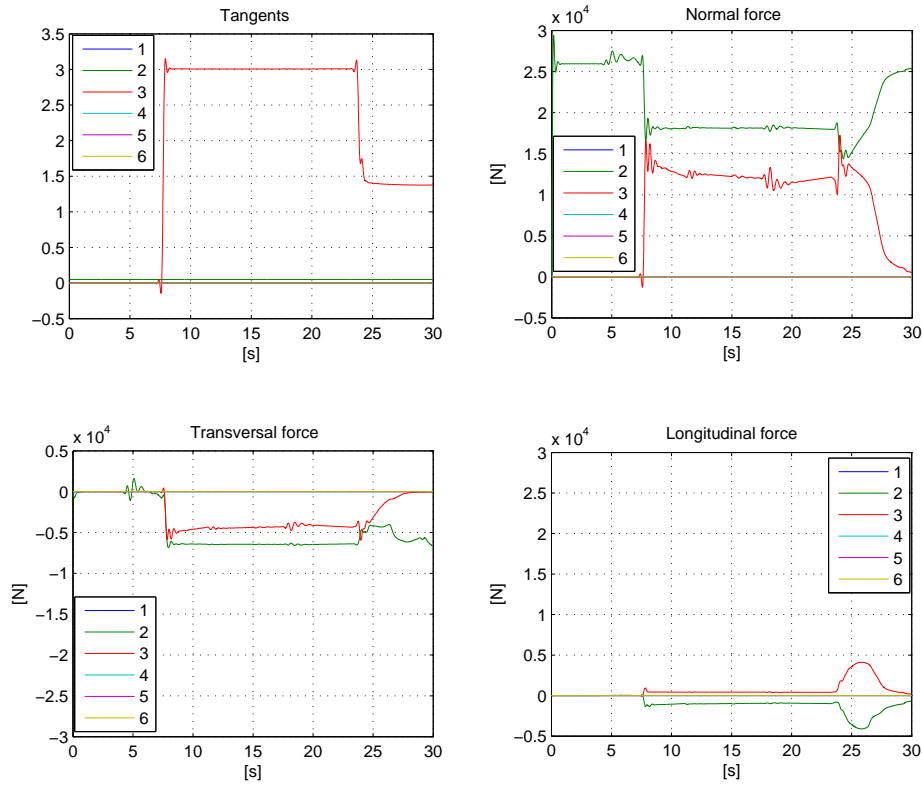


Figure 4.23: Tangents and normal, transverse and longitudinal forces at the contact points of the outer front wheel.

Longitudinal, transverse and spin creepages

In Figure 4.24 the longitudinal and transverse creepages at the contact points of the inner and outer front wheels are shown. The longitudinal ones, as seen with the longitudinal force, are nearly absent.

Then, the value of the spin creepages at 15 seconds into the simulation are calculated by means of Eq.(4.3) and reported in Table 4.4.

Wheel	Contact point	Name	Unit	Values
Inner front wheel	Contact on the tread	γ_{60}	[1/m]	-0.15
Inner front wheel	Contact on the flange back	γ_{60}	[1/m]	2.82
Outer front wheel	Contact on the tread	γ_{60}	[1/m]	0.15
Outer front wheel	Contact on the flange	γ_{60}	[1/m]	2.87

Table 4.4: Spin creepage at the contact points of the inner and outer front wheel at 15 seconds into the simulation.

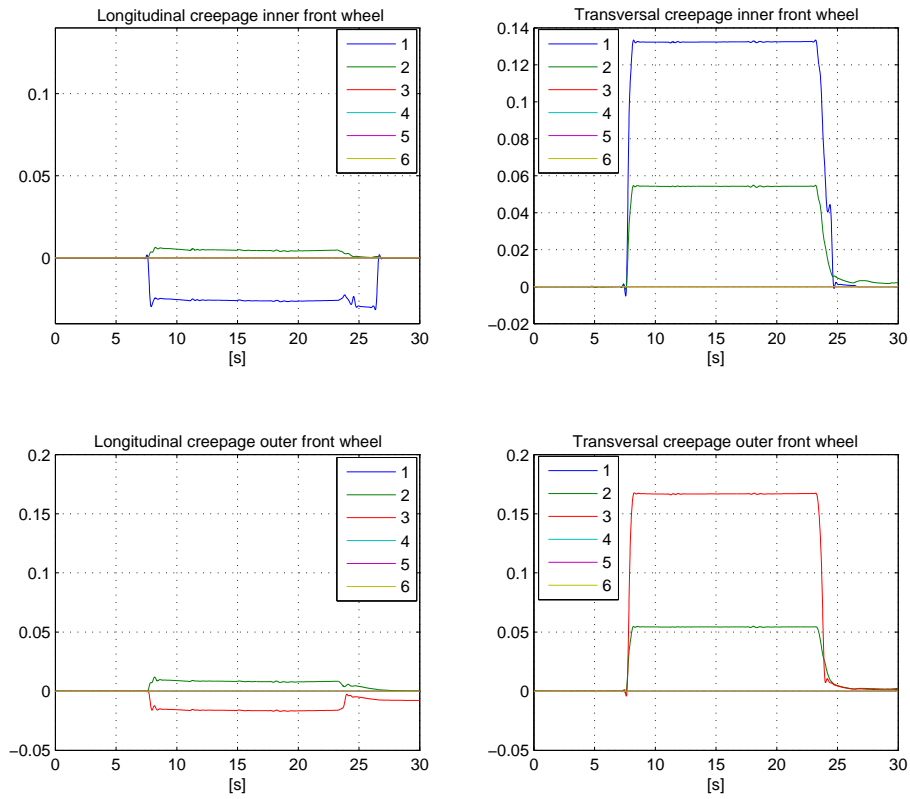


Figure 4.24: Longitudinal and transverse creepages at the contact points of the inner and outer front wheels.

Contact point positions

Finally, considering the frame of reference at the nominal contact point, as shown in Figure 4.25, the contact point positions of the inner and outer front wheels and inner and outer rails with respect to the nominal contact point are shown in Figure 4.25 and reported in Table 4.5.

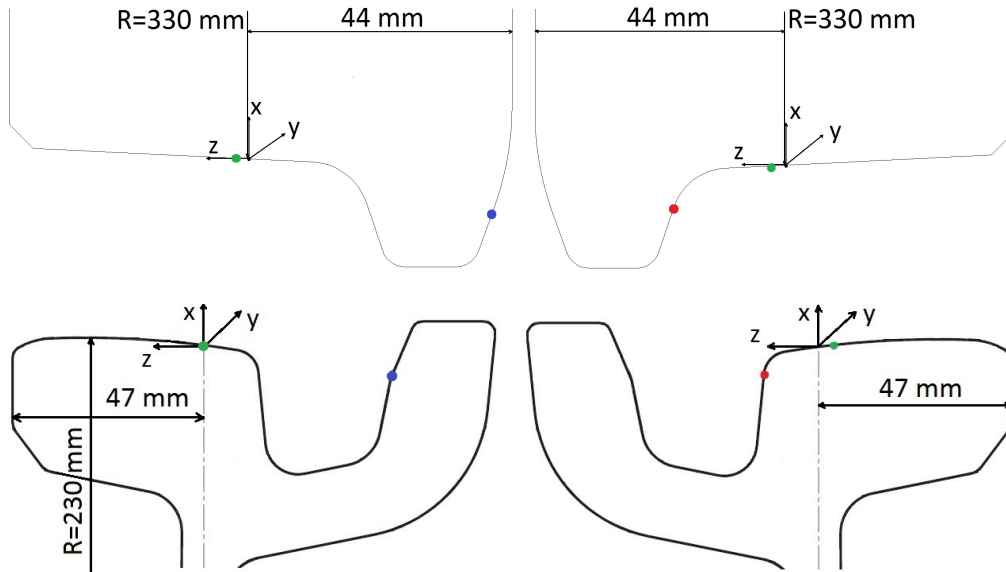


Figure 4.25: Contact point positions on the inner and outer front wheels and inner and outer rails.

4.6 Numerical results - Simulation with gauge of 1450 mm

The last simulation analyzed has 1450 mm track gauge. In this case the contact point between the flange back and rail grooved head remains but the contact point between the flange and the rail running head disappears.

4.6.1 Numerical results at the contact points

Only the numerical results regarding the contact points of the inner and outer front wheels have been taken into account. All the outputs will be represented considering the system of reference for each contact point as shown in Figure 4.10 for the nominal contact point.

Tangents and normal, transverse and longitudinal forces at the contact points

By looking at Figures 4.26 and 4.27, the results show that, for the inner front wheel, a contact point occurs on the tread (green line) and between the flange back and rail grooved head (blue line). For the outer front wheel, a contact point occurs only on the tread (green line).

Wheel/Rail	Contact point	Name	Unit	Values
Inner wheel	Contact on the tread	$[x \ y \ z]$	[mm]	[0.22 0 4.5]
Inner wheel	Contact on the flange back	$[x \ y \ z]$	[mm]	[-10.4 50.65 -40.2]
Inner rail	Contact on the tread	$[x \ y \ z]$	[mm]	[0 0 0]
Inner rail	Contact on the flange back	$[x \ y \ z]$	[mm]	[-10 50.65 -48]
Outer wheel	Contact on the tread	$[x \ y \ z]$	[mm]	[-0.2 0 4.1]
Outer wheel	Contact on the flange	$[x \ y \ z]$	[mm]	[-8 50.65 19.9]
Outer rail	Contact on the tread	$[x \ y \ z]$	[mm]	[0.5 0 -3.5]
Outer rail	Contact on the flange	$[x \ y \ z]$	[mm]	[-7 50.65 13]

Table 4.5: Contact point positions of the inner and outer front wheels and inner and outer rails at 15 seconds into the simulation.

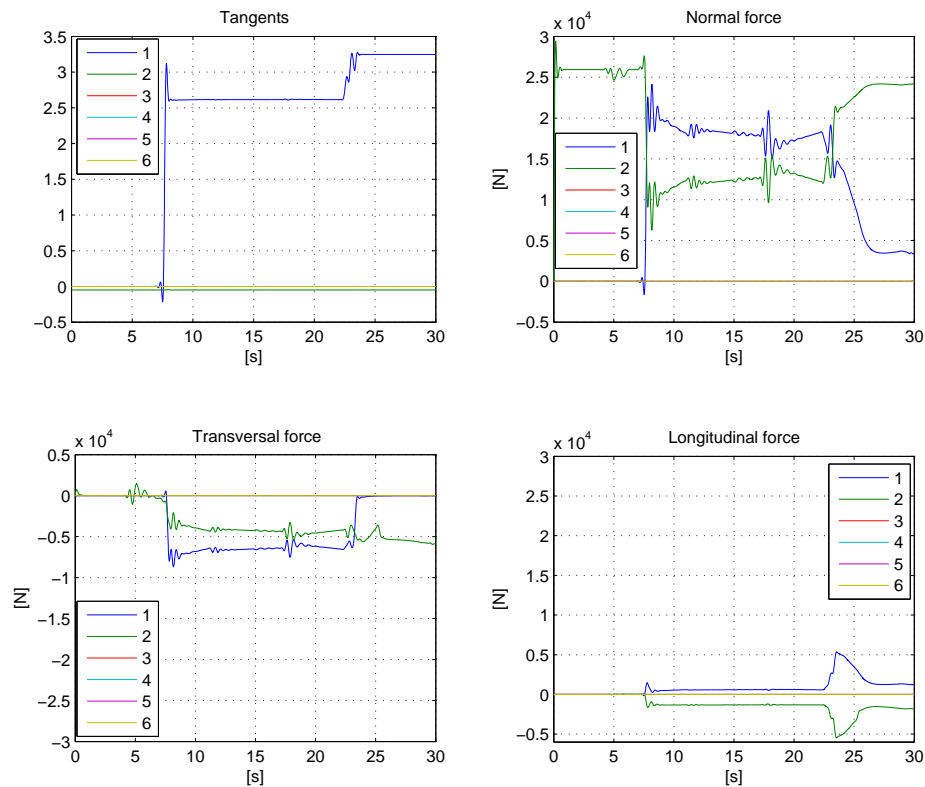


Figure 4.26: Tangents and normal, transverse and longitudinal forces at the contact points of the inner front wheel.

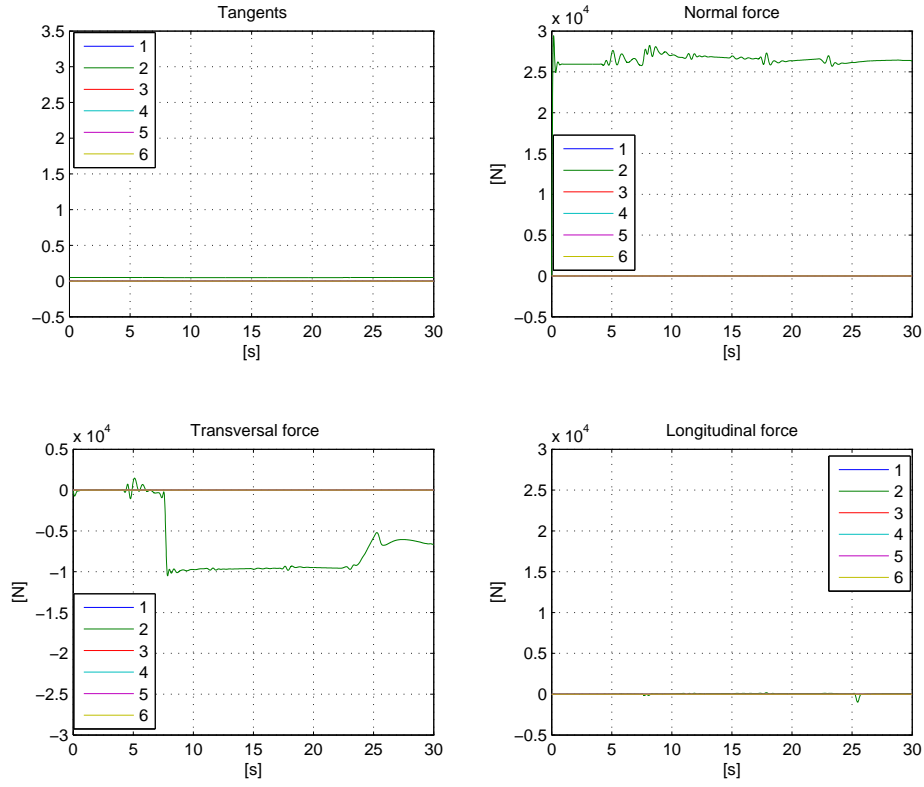


Figure 4.27: Tangents and normal, transverse and longitudinal forces at the contact points of the outer front wheel.

Longitudinal, transverse and spin creepages

In Figure 4.28 the longitudinal and transverse creepages at the contact points of the inner and outer front wheel are shown. The longitudinal ones, as seen with longitudinal force, are nearly absent.

Then, the value of the spin creepages at 15 seconds into the simulation are calculated by means of Eq.(4.3) and reported in Table 4.6.

Wheel	Contact point	Name	Unit	Values
Inner front wheel	Contact on the tread	γ_{60}	[1/m]	-0.15
Inner front wheel	Contact on the flange back	γ_{60}	[1/m]	2.83
Outer front wheel	Contact on the tread	γ_{60}	[1/m]	0.147

Table 4.6: Spin creepage at the contact points of the inner and outer front wheel at 15 seconds into the simulation.

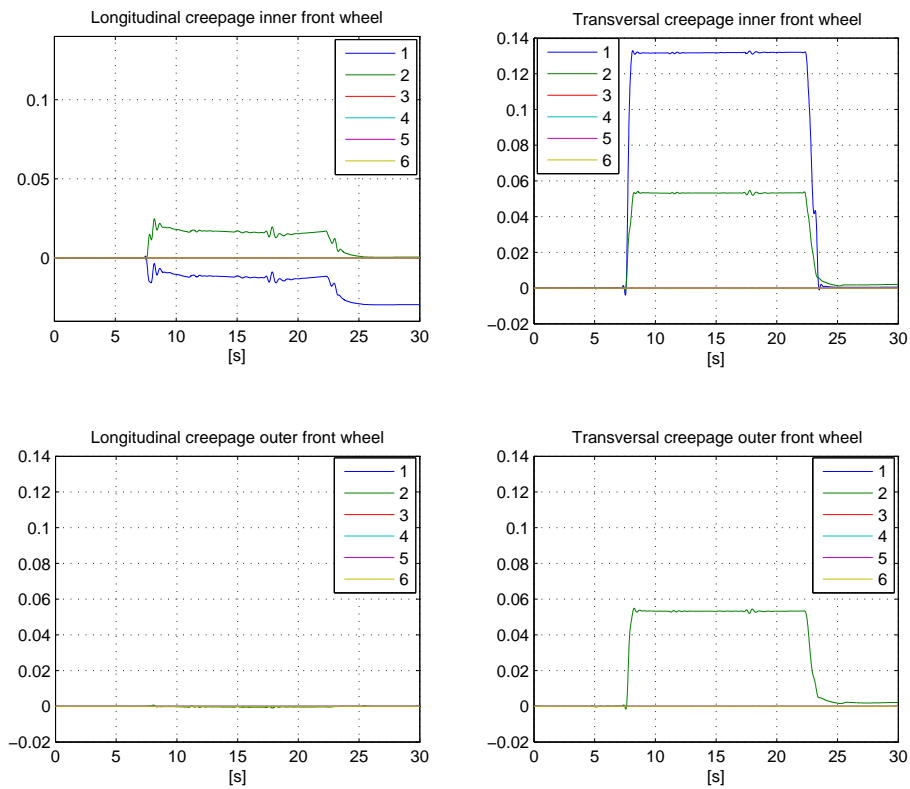


Figure 4.28: Longitudinal and transverse creepages at the contact points of the inner and outer front wheel.

Contact point positions

Finally, considering the frame of reference at the nominal contact point, as shown in Figure 4.29, the contact point positions of the inner and outer front wheel and inner and outer rail with respect to the nominal contact point are shown in Figure 4.29 and reported in Table 4.7.

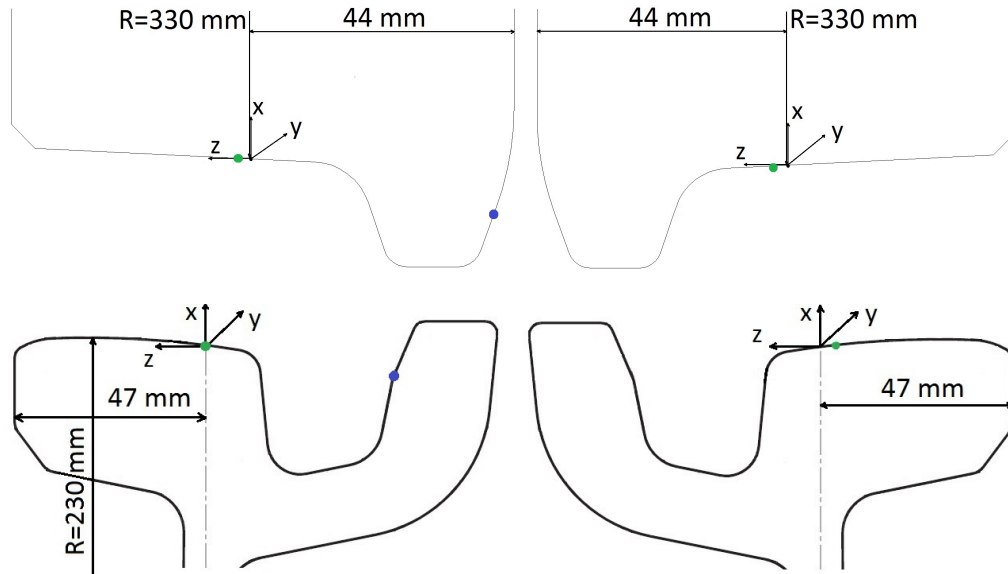


Figure 4.29: Contact point positions on the inner and outer front wheel and inner and outer rail.

Wheel/Rail	Contact point	Name	Unit	Values
Inner wheel	Contact on the tread	$[x \ y \ z]$	[mm]	[0.13 0 2.66]
Inner wheel	Contact on the flange back	$[x \ y \ z]$	[mm]	[-9.9 50.65 -40.3]
Inner rail	Contact on the tread	$[x \ y \ z]$	[mm]	[0 0 0]
Inner rail	Contact on the flange back	$[x \ y \ z]$	[mm]	[-10 50.65 -48]
Outer wheel	Contact on the tread	$[x \ y \ z]$	[mm]	[-0.16 0 3.3]
Outer rail	Contact on the tread	$[x \ y \ z]$	[mm]	[0.5 0 -3.5]

Table 4.7: Contact point positions of the inner front wheel and inner rail at 15 seconds into the simulation.

4.7 Conclusion

For the squeal noise analysis, the results obtained from the inner front wheel with a gauge of 1445 mm and the outer front wheel with a gauge of 1450 mm that present a contact point on the tread will be used as input parameters to analyze the squeal noise phenomenon by means of the model with one contact point.

The case with a gauge of 1447 mm, for which the inner and outer front wheels have two contact points, is closer to the reality and the results will be used as input parameters to analyze the squeal noise phenomenon by means of the model with two contact points.

However it is important to remark that the contact conditions are variable along

the curve and a deterministic approach may be not fully representative of the phenomenon. Therefore, in the following, a certain degree of variability will be added to some of the parameters calculated here.

Chapter 5

Rolling friction model and self-excited vibration

The curve squeal noise generated by the tramcar during curve negotiation is described as a form of self-excited vibration of the wheels due to the stick/slip phenomenon generated at the contact points between wheels and rail. This stick/slip mechanism is described by a negative damping coefficient that varies with vibration amplitude and that can be related with the negative slope of the friction characteristics at large sliding velocity. Rudd [9] was the first to suggest this theory applied to this topic, then, many other authors, such as De Beer et al. [20], Huang [3] and Koch et al. [24], confirmed this hypothesis performing experiments on a scale test rig with dry contact conditions, changing the yaw angle between wheel and rail from negative to positive to produce the corresponding lateral creepage. The first two observed that the squeal occurs when the friction forces decrease at large lateral creepages, while the third also observed the occurrence of the squeal at large sliding velocities but the friction force curve did not show any region of negative slope.

Despite this last conflicting result, for the curve squeal model, only a friction coefficient decreasing with increasing creepage is able to destabilize the system and induce wheel vibration. Therefore, for the application of squeal analysis, the phenomenon of falling friction in sliding had to be considered in the friction model.

In the first part of this chapter the friction model adopted in Huang's model is described, while in the second part an idealized mass-on-moving-belt model

is established to provide an interpretation of the possible self-excited vibration due to the stick/slip phenomenon generated in the wheel/rail contact system. McMillan [34] was one of many authors that studied this simple system.

5.1 Rolling friction model

5.1.1 Friction curve

The schematic diagram of the friction curve in Figure 5.1 relates the friction force and sliding velocity. This relation is involved in steady-state rolling contact. For small sliding velocity, the friction force increases linearly from zero, until it saturates at the Coulomb friction limit. This is the adhering zone where microslip occurs in part of the contact. After this zone, the rolling contact is under gross sliding. For most cases, the friction force is a function of sliding velocity. Often, the friction curve slopes down from the Coulomb friction limit and then may reach a constant value. In Figure 5.1 (b) the influence of the normal force is eliminated, while the sliding velocity is changed in to creepage. So, Figure 5.1 (a) is changed into a curve in terms of non-dimensional friction force and creepage. The non-dimensional friction force μ_i , $i = 1, 2, 6$, represents the non-dimensional ratio between the friction force (moment) in the i direction and the nominal force. Figure 5.1 (b), indicates also that the direction of the friction force is opposite to the sliding velocity.

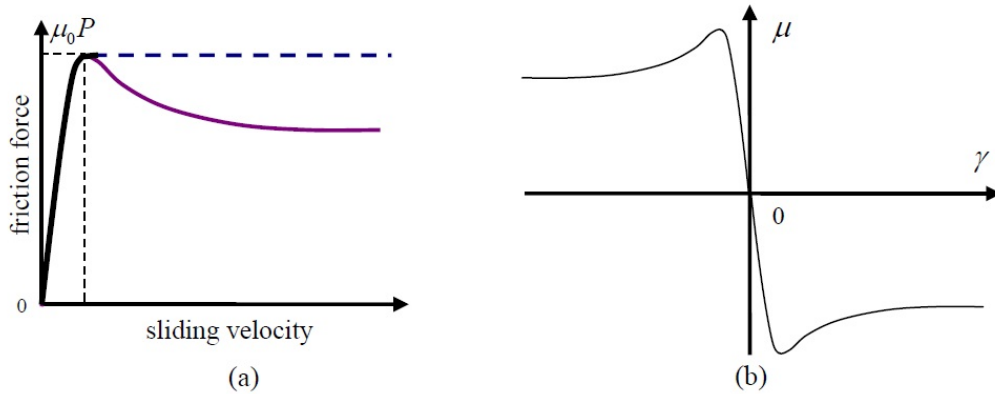


Figure 5.1: Schematic diagram of friction curve, (a) friction force with respect to the sliding velocity, (b) non-dimensional friction force with respect to the creepage. Huang [3]

5.1.2 Theoretical model adopted for the friction curve in adhering

To describe the friction curve in the adhering zone two methods can be adopted. For cases with creepages and spin, Kalker's FASTSIM algorithm [35] can provide good computational speed with small cost in terms of accuracy. The Shen-Hendrick-Elkins formula [31] is an appropriate analytical model for cases with creepages and small spin.

Kalker's FASTSIM algorithm is adopted in Huang's model. Since this algorithm needs the dimensions of the contact area to determine the relation between the friction force and sliding velocity, Hertz's theory [36] is adopted to calculate this quantity. Hertz showed that two curved solids in contact touch initially at a single point, then, under the action of the lightest load, they deform in the vicinity of their point of first contact with the consequence that they touch over an area. This theory allows the dimensions of the contact area and the distribution of the normal contact pressure to be obtained.

Kalker's FASTSIM algorithm allows the determination, from given Coulomb friction coefficient μ_0 , of creepages, spin, Kalker's coefficients and dimensions of the contact area, the surface condition (stick or slip at any contact point) and the local Coulomb friction. It also allows the total tangential forces to be calculated in the steady-state rolling contact problem.

The results from FASTSIM show that the spin may not influence the longitudinal friction, but it can have a large influence on the lateral friction. Considering the lateral friction curve, the adhering zone can be influenced by the sign and magnitude of the spin.

5.1.3 Heuristic formula for falling friction in sliding

The friction curve in gross sliding can only be partly explained in terms of tribology. To describe the falling region, a heuristic approach is adopted in Huang's model, which was first proposed by Kraft [10]. The falling function used in Huang's model is slightly different:

$$\tau(\gamma) = 1 - \lambda e^{\left(\frac{-\kappa}{|\gamma|}\right)}, \quad (5.1)$$

where λ is termed falling ratio, defined as:

$$\lambda \equiv \frac{\mu_0 - |\mu_k(\gamma)|}{\mu_0}, \quad \gamma \rightarrow \infty, \quad (5.2)$$

and κ is the saturation coefficient which determines how quickly the friction falls and indirectly this affects the point of saturation. The results from the heuristic formula show that the falling ratio λ influences the friction curve at large creepages, while the saturation coefficient κ mainly influences the friction curve at small creepages, close to the saturation zone.

5.1.4 Hertz contact spring

When any fluctuation of the two contacting bodies takes place in the normal direction, they will approach each other in the direction normal to the contact surface without penetration. Due to the stiffness of the material, an additional normal force will be generated and added to the nominal load. The relation between the normal force $P > 0$ and the normal approach $\delta_H > 0$ can be represented by the stiffness of the Hertz spring k_H which is non-linear but a linearised form is used in the Huang's model.

5.2 Self-excited vibration

5.2.1 Equations of motion

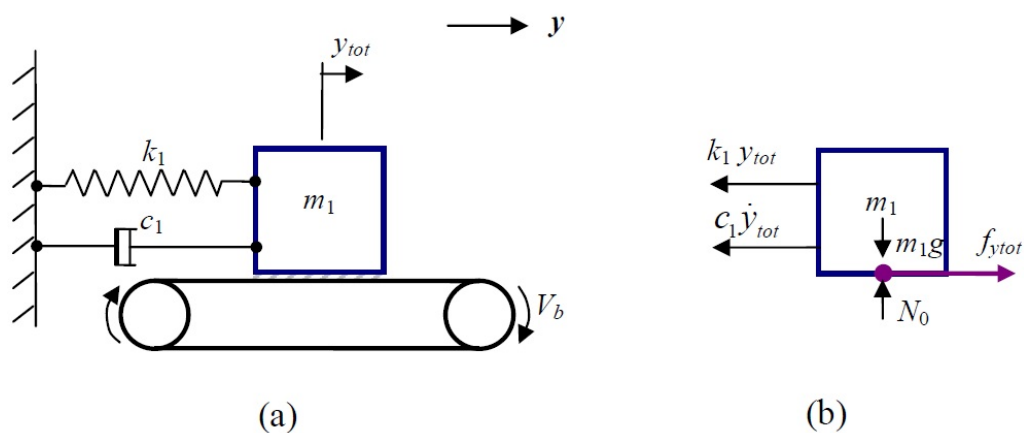


Figure 5.2: Mass-on-moving-belt system, (a) friction driven mass-spring-damper system, (b) schematic diagram of the forces acting on the mass. Huang [3]

In the mass-spring-damper system shown in Figure 5.2 the belt is assumed to move with a constant speed V_b . The mass m_1 has a velocity of \dot{y}_{tot} . So, the sliding velocity between the mass and belt is:

$$v_{ytot}^s \equiv \dot{y}_{tot} - V_b. \quad (5.3)$$

If the normal contact force N_0 is known, the sliding friction force acting on the mass can be obtained:

$$f_{ytot} = N_0 \mu(v_{ytot}^s), \quad (5.4)$$

where the non-dimensional friction force μ includes a sign opposite to that of the sliding velocity.

If the system is under equilibrium conditions, the mass m_1 has a velocity of $\dot{y}_{tot} = 0$. Thus, the equilibrium sliding velocity v_{y0}^s , given from Eq.(5.3), becomes related only to the velocity of moving belt:

$$v_{y0}^s = -V_b. \quad (5.5)$$

Consequently, the equilibrium friction force f_{y0} given from Eq.(5.4) is:

$$f_{y0} = N_0 \mu(v_{y0}^s). \quad (5.6)$$

In these conditions, to balance the equilibrium friction force f_{y0} , the spring k_1 must stretch an equilibrium length $y_{tot} = y_0$ from its relaxed position, giving:

$$f_{y0} = N_0 \mu(v_{y0}^s) = k_1 y_0. \quad (5.7)$$

If a transient force moves the mass from its steady-state position, the mass will start to oscillate. The displacement of the mass can be written as the sum of an equilibrium part y_0 and a dynamic part y :

$$y_{tot} \equiv y_0 + y, \quad (5.8)$$

and the velocity and acceleration are:

$$\dot{y}_{tot} = \dot{y}, \quad (5.9)$$

$$\ddot{y}_{tot} = \ddot{y}, \quad (5.10)$$

Considering Eqs.(5.9) and (5.5), the sliding velocity, given from Eq.(5.3), can be rewritten as a sum of an equilibrium part v_{y0}^s and a dynamic part \dot{y} :

$$v_{ytot}^s = v_{y0}^s + \dot{y}. \quad (5.11)$$

The friction force f_{ytot} can also be written as the sum of an equilibrium part f_{y0} and a dynamic part f_y :

$$f_{ytot} \equiv f_{y0} + f_y. \quad (5.12)$$

The governing equation of this mass-spring-damper system is:

$$m_1 \ddot{y}_{tot} + c_1 \dot{y}_{tot} + k_1 y_{tot} = f_{ytot}. \quad (5.13)$$

Combining Eqs.(5.7), (5.8), (5.9), (5.10) and (5.12) the equilibrium part in Eq.(5.13) can be eliminated giving:

$$m_1 \ddot{y} + c_1 \dot{y} + k_1 y = f_y. \quad (5.14)$$

Substituting Eqs.(5.11), (5.4) and (5.6) into Eq.(5.12) the dynamic friction force can be related to the vibration of the mass, \dot{y} :

$$f_y = f_{ytot} - f_{y0} = N_0(\mu(\dot{y} + v_{y0}^s) - \mu(v_{y0}^s)). \quad (5.15)$$

Thus, the equation of motion, considering the friction force in Eq.(5.15), can be rewritten as:

$$m_1 \ddot{y} + c_1 \dot{y} + k_1 y = N_0(\mu(\dot{y} + v_{y0}^s) - \mu(v_{y0}^s)). \quad (5.16)$$

5.2.2 Self-excited vibration

The equation of motion (5.16) describes the interaction between the sliding velocity and the friction force in the mass-on-moving-belt system. This interaction can also be described as a positive feedback loop, see Figure 5.3. The input of the loop is a disturbance, while the output is the vibration of the mass. The block in the forward route is a linear mass-spring-damper system. The block in the feedback route can be considered as a generator for the friction force.

To study the stability of the mass-on-moving-belt system at one possible equilibrium sliding velocity v_{y0}^s , the linearized system around this equilibrium point can be considered. Eq.(5.16) shows that only the dynamic friction force f_y is

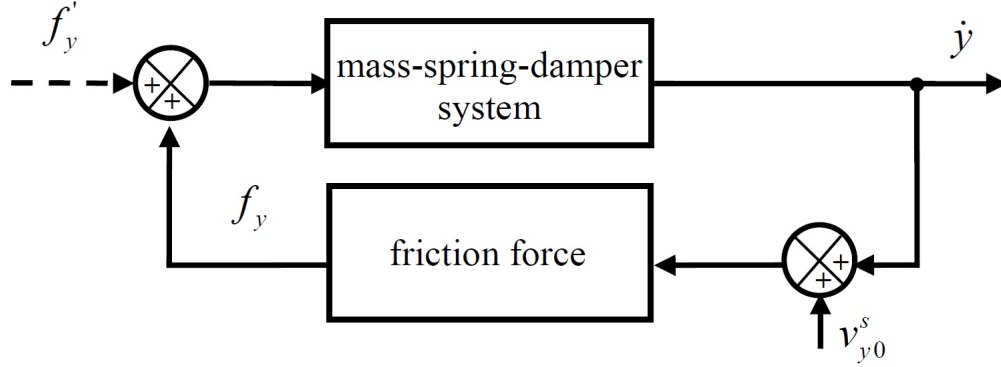


Figure 5.3: Feedback loop of the mass-on-moving-belt system. Huang [3]

non-linear:

$$f_y(\dot{y}) = f_{ytot} - f_{y0} = N_0(\mu(\dot{y} + v_{y0}^s) - \mu(v_{y0}^s)). \quad (5.17)$$

Thus, the dynamic friction force evaluated in the equilibrium point, given from the first order Taylor series approximation, is:

$$f_y \approx \dot{y} \left. \frac{\partial f_y}{\partial \dot{y}} \right|_{v_{y0}^s} = \dot{y} N_0 \left. \frac{\partial \mu}{\partial \dot{y}} \right|_{v_{y0}^s}. \quad (5.18)$$

Since the derivative of the dynamic friction force with respect to the dynamic sliding velocity is similar to the definition of viscous damping, an equivalent damping coefficient about v_{y0}^s can be defined as follows:

$$c_e(v_{y0}^s) = - \dot{y} \left. \frac{\partial f_y}{\partial \dot{y}} \right|_{v_{y0}^s}. \quad (5.19)$$

Therefore the dynamic friction force can be written as:

$$f_y = -c_e \dot{y}. \quad (5.20)$$

The linearized equation of motion can be obtained substituting Eq.(5.20) into Eq.(5.14):

$$m_1 \ddot{y} + (c_e + c_1) \dot{y} + k_1 y = 0. \quad (5.21)$$

Thus, the stability of the mass-on-moving-belt system is judged by the following

criterion:

$$\begin{cases} c_1 \geq 0, & \text{for } c_e > 0 \\ c_1 > |c_e|, & \text{for } c_e \leq 0 \end{cases}, \quad (5.22)$$

which means the structural damping can keep the system stable if the equivalent damping of the friction force is not negative, or the structural damping should be greater than the value of the negative equivalent damping. In Figure 5.4, two

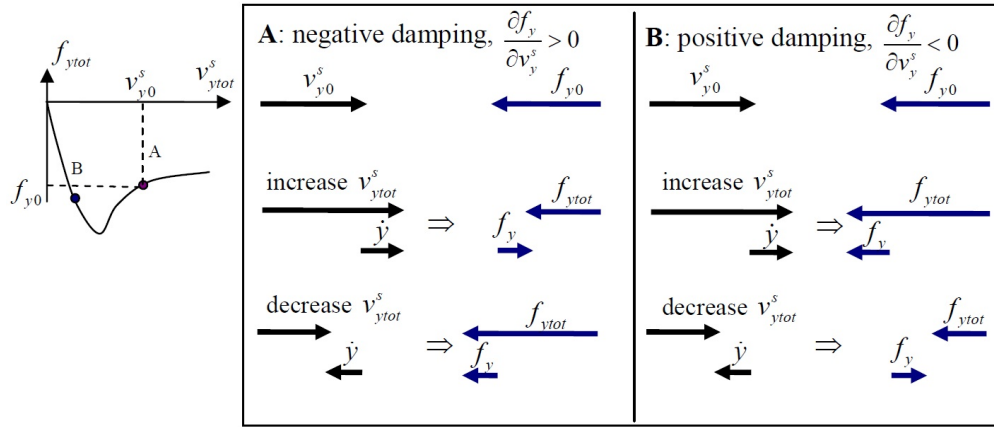


Figure 5.4: Equivalent damping effects of the friction force. Huang [3]

possible equilibrium points, **A** and **B**, are chosen on a friction curve with falling zone. At point **A**, the friction curve has a negative c_e . It is found that the dynamic friction force $f_y = f_{ytot} - f_{y0}$ is always in the same direction as the increment of dynamic sliding velocity $\dot{y} = v_{ytot}^s - v_{y0}^s$. This will tend to increase the amplitude of vibration and in turn increase the friction force. Therefore, the system may be unstable at point **A**. However, at point **B**, the friction force has a positive c_e . In this case, the direction of dynamic friction force f_y is always opposite to that of the increment of dynamic sliding velocity \dot{y} . Thus, the dynamic friction force will tend to decrease the vibration and maintain the system at the equilibrium point **B**.

5.2.3 Self-excited vibration in a single-mode wheel

The mass-on-moving-belt model can be used directly to simulate the self-excited behaviour of one of the modes of a curving wheel sliding on a rigid rail in one direction. So, the mass-damper-spring system can be adopted to represent the wheel with one mode. The rail with rigid surface is represented by the belt. The

possible equilibrium lateral sliding velocity between the wheel and rail can be represented by the belt velocity V_b .

As the rail is assumed to be motionless, the equilibrium sliding velocity v_{y0}^s corresponds to the lateral component of rolling speed of the wheel, which is evaluated from its creepage. The total lateral creepage is defined as:

$$\gamma_{2tot} = \frac{v_{ytot}^s}{V_0}. \quad (5.23)$$

The lateral creepage in steady-state curving is quasi-static. Hence, the possible equilibrium sliding velocity can be expressed in terms of the steady-state lateral creepage:

$$v_{y0}^s = \gamma_{20} V_0. \quad (5.24)$$

Substituting Eq.(5.24) into Eq.(5.18) gives:

$$f_y \approx \dot{y} N_0 \left. \frac{d\mu}{d\dot{y}} \right|_{v_{y0}^s} = \dot{y} \frac{N_0}{V_0} \left. \frac{d\mu}{d(\dot{y}/V_0)} \right|_{v_{y0}^s/V_0} = \dot{y} \frac{N_0}{V_0} \left. \frac{d\mu}{d\gamma} \right|_{\gamma_{20}} = \dot{y} \frac{N_0}{V_0} \mu'(\gamma_{y0}). \quad (5.25)$$

The equivalent damping coefficient defined in Eq.(5.19) can thus be expressed as:

$$c_e(\gamma_{y0}) = -\frac{N_0}{V_0} \mu'(\gamma_{20}). \quad (5.26)$$

Since the curve of non-dimensional friction force is non-linear, the minimum damping ratio needed to make the unstable wheel into a stable one is dependent on the steady-state creepage and the friction curve. To ensure the stability of the wheel, a damping coefficient is required that is as large as the maximum value of the equivalent damping coefficient of the friction force:

$$c_c = \frac{N_0}{V_0} |\mu'(\gamma_p)|, \quad (5.27)$$

where the peak value of the derivative of friction force is at the creepage of γ_p .

Chapter 6

Squeal model for single wheel/rail contact

The mass-on-moving-belt model, as discussed in Chapter 5, can explain well the phenomenon of self-excited vibration of a single-mode wheel/rail system where the excitation force (friction) sustaining the vibration is determined by the vibration (sliding velocity) itself. This self-excited vibration loop can provide important insights into the squeal noise phenomenon in terms of falling friction force that can be considered as a negative equivalent damping, which may result in instability of the contact system if it is greater than the structural damping. However, the mass-on-moving-belt model is too simple to describe the squeal analysis in the practical wheel/rail rolling contact system, therefore, a new model that considers more than one degree of freedom is needed.

In this chapter Huang's model [3] is described. A general self-excited vibration loop is established by including models of the wheel/rail rolling contact dynamics and wheel and rail structural dynamics in state-space form. This will allow the stability of the self-excited vibration loop to be calculated in the frequencies domain that can show which wheel modes are prone to squeal, while an analysis in the time domain allows vibration and noise levels to be estimated.

6.1 Wheel/rail rolling contact dynamics

6.1.1 Wheel/rail rolling contact dynamics in the time domain

The general wheel/rail rolling contact system is shown in Figure 6.1.

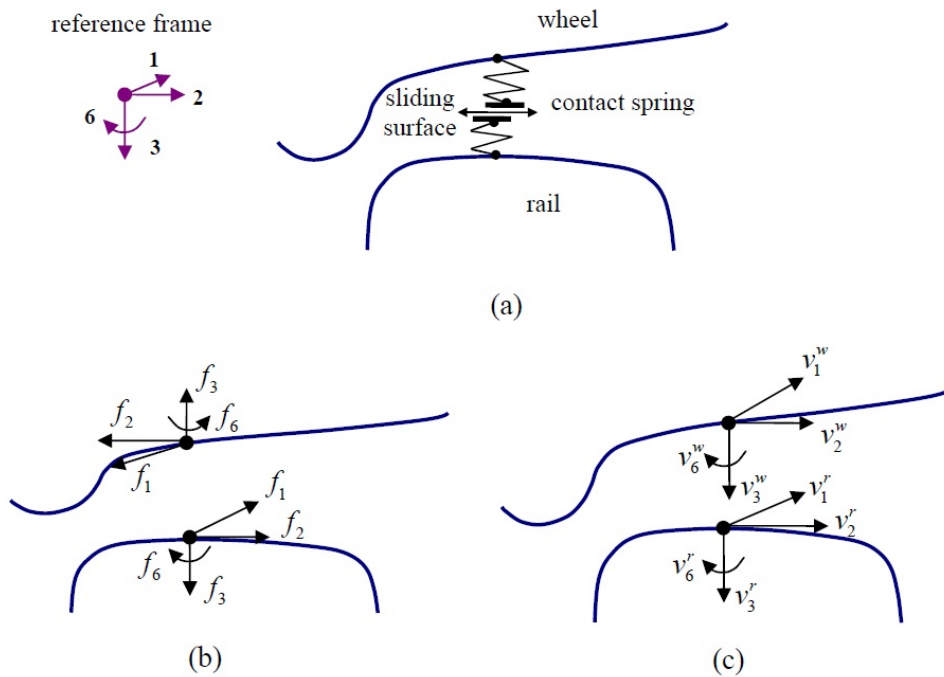


Figure 6.1: Forces and velocities of the wheel/rail contact system: (a) schematic diagram of the wheel/rail contact system, (b) forces acting on the wheel and rail in the contact area, (c) velocities of the wheel and rail. Huang [3]

The reference frame, given in Figure 6.1, shows that there are four degrees of freedom. The longitudinal and lateral directions (with index 1 and 2) are located in the contact plane. The vertical direction (with index 3) is normal to the contact plane. The spin (with index 6) rotates around the vertical direction. The massless Hertz contact spring is adopted to represent local dynamic behaviour of the contact zone in the normal direction. Figures 6.1(b) and 6.1(c) show the dynamic contact forces and the dynamic velocities.

The dynamic contact forces are the dynamic part of the friction forces. They can

be represented in vector form as:

$$\bar{f} \equiv \{f_1 \quad f_2 \quad f_3 \quad f_6\}^T. \quad (6.1)$$

Wheel and rail forces have opposite direction and equal magnitude. Therefore:

$$\bar{f}^w \equiv -\bar{f}, \quad (6.2)$$

$$\bar{f}^r \equiv \bar{f}. \quad (6.3)$$

The dynamic velocity vectors of wheel \bar{v}^w and rail \bar{v}^r are represented as:

$$\bar{v}^w \equiv \{v_1^w \quad v_2^w \quad v_3^w \quad v_6^w\}^T, \quad (6.4)$$

$$\bar{v}^r \equiv \{v_1^r \quad v_2^r \quad v_3^r \quad v_6^r\}^T. \quad (6.5)$$

The relation between the dynamic sliding velocities and dynamic friction forces at the contact point is formulated as follows.

In the vertical direction, sliding does not exist because the wheel and the rail maintain contact due to the vertical load. The local behaviour of the contact zone can be described as the compression of the contact spring:

$$d_3^c \equiv -(d_3^r - d_3^w) = -\int_0^t (v_3^r - v_3^w) dt, \quad (6.6)$$

where the compression of the contact spring is assumed to be positive. Consequently, the relative velocity of the contact spring is:

$$v_3^c \equiv -(v_3^r - v_3^w). \quad (6.7)$$

From Eq.(6.8), the vertical sliding velocity can then be determined, and must be equal to zero:

$$v_3^s \equiv (v_3^r - v_3^w) + v_3^c = 0. \quad (6.8)$$

In the longitudinal, lateral and spin directions, the dynamic sliding velocities exist

and are defined as the relative velocities between wheel and rail:

$$\begin{pmatrix} v_1^s \\ v_2^s \\ v_3^s \\ v_6^s \end{pmatrix} \equiv \begin{pmatrix} v_1^r \\ v_2^r \\ v_3^r \\ v_6^r \end{pmatrix} - \begin{pmatrix} v_1^w \\ v_2^w \\ v_3^w \\ v_6^w \end{pmatrix} + \begin{pmatrix} 0 \\ 0 \\ v_3^c \\ 0 \end{pmatrix}. \quad (6.9)$$

For a general situation, during steady-state curving for a rolling speed V_0 , the longitudinal sliding v_{1tot}^s , lateral sliding v_{2tot}^s and spin v_{6tot}^s are present simultaneously.

The spin sliding velocity is the component of the wheel rotation vector in the direction normal to the contact patch:

$$v_{6tot}^s = \frac{V_0}{r_0} \sin \theta, \quad (6.10)$$

where θ is the angle between the plane of the contact and the ground plane and r_0 is the nominal radius of the wheel. The sliding velocities are normally evaluated in terms of the creepages:

$$\begin{pmatrix} \gamma_{1tot} \\ \gamma_{2tot} \\ \gamma_{6tot} \end{pmatrix} \equiv \frac{1}{V_0} \begin{pmatrix} v_{1tot}^s \\ v_{2tot}^s \\ v_{6tot}^s \end{pmatrix}, \quad (6.11)$$

where γ_{1tot} , γ_{2tot} , γ_{6tot} are the longitudinal, lateral, and spin creepages. These sliding velocities and corresponding creepages can be split into a steady-state component and a dynamic component:

$$\begin{pmatrix} \gamma_{1tot} \\ \gamma_{2tot} \\ \gamma_{6tot} \end{pmatrix} \equiv \frac{1}{V_0} \begin{pmatrix} v_{10}^s + v_1^s \\ v_{20}^s + v_2^s \\ v_{60}^s + v_6^s \end{pmatrix} = \begin{pmatrix} \gamma_{10} + \frac{v_1^s}{V_0} \\ \gamma_{20} + \frac{v_2^s}{V_0} \\ \gamma_{60} + \frac{v_6^s}{V_0} \end{pmatrix}. \quad (6.12)$$

The steady-state components are determined by the steady-state curving behaviour. The dynamic components are determined by the dynamic sliding velocities of the wheel and the rail at the contact patch, as given in Eq.(6.9)

The longitudinal and lateral friction force and the spin moment can be written

as the product of the normal contact force and corresponding non-dimensional friction forces:

$$\begin{Bmatrix} f_{1tot} \\ f_{2tot} \\ f_{6tot} \end{Bmatrix} = \begin{Bmatrix} \mu_1(\gamma_{1tot}, \gamma_{2tot}, \gamma_{6tot}, f_{3tot}) \\ \mu_2(\gamma_{1tot}, \gamma_{2tot}, \gamma_{6tot}, f_{3tot}) \\ \mu_6(\gamma_{1tot}, \gamma_{2tot}, \gamma_{6tot}, f_{3tot}) \end{Bmatrix} f_{3tot}, \quad (6.13)$$

where the non-dimensional friction forces are non-linear functions of all three creepages and the normal contact force. These creepages can be calculated using Kalker's FASTSIM algorithm [35]. The contact spring compresses and extends. Therefore, the normal contact force fluctuates and can be considered as the sum of a nominal contact force and a dynamic vertical force:

$$f_{3tot} \equiv N_0 + f_3. \quad (6.14)$$

The stiffness of the contact spring k_H is a non-linear function of the normal contact force f_{3tot} . It can be linearised around the steady-state point d_{30}^c due to normal load N_0 . So, for small vertical fluctuations around this point, the dynamic vertical force is:

$$f_3 = k_H d_3^c = -k_H \int_0^t v_3^s dt. \quad (6.15)$$

Using Eq.(6.13), the friction forces and spin moment at the steady-state point can be expressed as:

$$\begin{Bmatrix} f_{10} \\ f_{20} \\ f_{60} \end{Bmatrix} = \begin{Bmatrix} \mu_1(\gamma_{10}, \gamma_{20}, \gamma_{60}, N_0) \\ \mu_2(\gamma_{10}, \gamma_{20}, \gamma_{60}, N_0) \\ \mu_6(\gamma_{10}, \gamma_{20}, \gamma_{60}, N_0) \end{Bmatrix} N_0. \quad (6.16)$$

These steady-state components of friction forces and moment are balanced by the vehicle suspension forces, which means only the dynamic components are directly related to squealing. Considering Eq.(6.13) and Eq.(6.16) the dynamic friction forces can be written as:

$$\begin{Bmatrix} f_1 \\ f_2 \\ f_6 \end{Bmatrix} = \begin{Bmatrix} f_{1tot} \\ f_{2tot} \\ f_{6tot} \end{Bmatrix} - \begin{Bmatrix} f_{10} \\ f_{20} \\ f_{60} \end{Bmatrix} =$$

$$\begin{aligned}
&= \left\{ \begin{array}{l} \mu_1 \left(\gamma_{10} + \frac{v_1^s}{V_0}, \gamma_{20} + \frac{v_2^s}{V_0}, \gamma_{60} + \frac{v_6^s}{V_0}, N_0 + f_3 \right) \\ \mu_2 \left(\gamma_{10} + \frac{v_1^s}{V_0}, \gamma_{20} + \frac{v_2^s}{V_0}, \gamma_{60} + \frac{v_6^s}{V_0}, N_0 + f_3 \right) \\ \mu_6 \left(\gamma_{10} + \frac{v_1^s}{V_0}, \gamma_{20} + \frac{v_2^s}{V_0}, \gamma_{60} + \frac{v_6^s}{V_0}, N_0 + f_3 \right) \end{array} \right\} (N_0 + f_3) - \\
&\quad + \left\{ \begin{array}{l} \mu_1 (\gamma_{10}, \gamma_{20}, \gamma_{60}, N_0) \\ \mu_2 (\gamma_{10}, \gamma_{20}, \gamma_{60}, N_0) \\ \mu_6 (\gamma_{10}, \gamma_{20}, \gamma_{60}, N_0) \end{array} \right\} N_0. \tag{6.17}
\end{aligned}$$

These non-linear friction equations are used in the state-space wheel and rail models.

6.1.2 Wheel/rail rolling contact dynamics in the frequency domain

In the quasi-steady condition, the dynamic forces and velocities can be converted into the frequency response by assuming they are harmonically oscillating at frequency ω :

$$f_i = F_i e^{j\omega t}, v_i^w = V_i^w e^{j\omega t}, v_i^r = V_i^r e^{j\omega t}, v_3^c = V_3^c e^{j\omega t}, v_i^s = V_i^s e^{j\omega t} \tag{6.18}$$

$$i = 1, 2, 3, 6.$$

In the frequency domain, the ratio between the velocity amplitude V_i at a location i and the force amplitude F_k at a location k is called mobility $Y_{ik}(\omega)$. Hence, the dynamic velocities and the dynamic forces can be connected by the mobility matrix.

Wheel/rail mobilities are first calculated at the nominal contact point while a rigid translation and rotation at the actual contact point is performed in a subsequent stage.

For the wheel this gives:

$$\begin{Bmatrix} V_1^w \\ V_2^w \\ V_3^w \\ V_6^w \end{Bmatrix} = - \begin{bmatrix} Y_{11}^w & Y_{12}^w & Y_{13}^w & Y_{16}^w \\ Y_{21}^w & Y_{22}^w & Y_{23}^w & Y_{26}^w \\ Y_{31}^w & Y_{32}^w & Y_{33}^w & Y_{36}^w \\ Y_{61}^w & Y_{62}^w & Y_{63}^w & Y_{66}^w \end{bmatrix} \begin{Bmatrix} F_1 \\ F_2 \\ F_3 \\ F_6 \end{Bmatrix}. \quad (6.19)$$

In this case, the mobilities can be calculated adopting the modal parameters obtained by the FE model of the wheel (see chapter 3) as a sum of the response at each mode [37]:

$$Y_{ik}^w(\omega) = \sum_n \frac{j\omega\phi_{in}\phi_{kn}}{m_n(\omega_n^2 - \omega^2 + 2j\zeta_n\omega\omega_n)}, \quad (6.20)$$

$$i = 1, 2, 3, 6,$$

$$k = 1, 2, 3, 6,$$

where ϕ_{in} and ϕ_{kn} are the mode shape amplitudes of mode n in direction i and k , m_n is the modal mass, ζ_n is the modal damping ratio and ω_n is the natural circular-frequency.

For the rail, Eq.(6.19) can be rewritten as:

$$\begin{Bmatrix} V_1^r \\ V_2^r \\ V_3^r \\ V_6^r \end{Bmatrix} = \begin{bmatrix} Y_{11}^r & Y_{12}^r & Y_{13}^r & Y_{16}^r \\ Y_{21}^r & Y_{22}^r & Y_{23}^r & Y_{26}^r \\ Y_{31}^r & Y_{32}^r & Y_{33}^r & Y_{36}^r \\ Y_{61}^r & Y_{62}^r & Y_{63}^r & Y_{66}^r \end{bmatrix} \begin{Bmatrix} F_1 \\ F_2 \\ F_3 \\ F_6 \end{Bmatrix}. \quad (6.21)$$

In this case, the railway track is reasonably represented by an infinite structure, so an FE model is not straightforward to be adopted. Therefore analytical models are preferred. These can also represent different kinds of tracks simply by changing a small number of parameters and largely reduce computational time.

The vertical mobility Y_{33}^r can be calculated using two types of beams: Euler-Bernoulli beam [38] or Timoshenko beam on double elastic layer [38]. The first one is based on the assumption that plane sections of the beam remain plane and perpendicular to the neutral axis and can be adopted for low frequencies. In the rail, when the frequencies are above 500 Hz, shear deformation and rotational inertia play a role and should be included in the description of the beam. Therefore,

to consider these effects, the Timoshenko beam model is adopted.

The lateral mobility Y_{22}^r , the torsional mobility around x-axis Y_{44}^r and the cross-lateral mobility Y_{24}^r are obtained using a multiple-beam model [39], [40], [41]. In this model the whole rail is divided into three parts as shown in Figure 6.2: the head and the foot are represented by two infinite Timoshenko beams, and the web is replaced by numerous beams which connect the head and foot. This configuration allows account to be taken of the cross-sectional deformations which become significant for the lateral vibration of a rail at high frequencies.

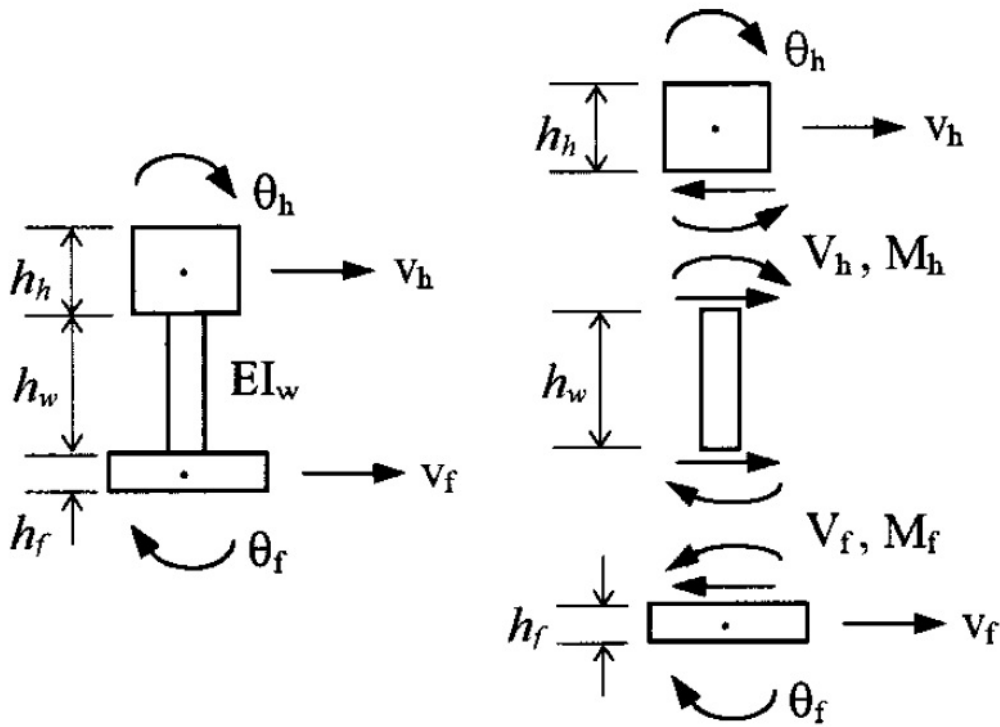


Figure 6.2: Multiple beam model for lateral and torsional vibration of rail [39].

The spin mobility Y_{66}^r , around the vertical direction, is calculated using the Timoshenko beam or the Euler-Bernoulli beam [3], while the Lurcock's investigation [42] regarding the longitudinal vibration properties of a railway track is taken into account to calculate the longitudinal mobility Y_{11}^r . The other mobilities are considered equal to zero.

For the contact spring the vertical velocity can be expressed as:

$$V_3^c = Y_{33}^c F_3, \quad (6.22)$$

where the mobility of vertical contact spring Y_{33}^c is:

$$Y_{33}^c = \frac{j\omega}{k_H}. \quad (6.23)$$

According to Eq.(6.9), the amplitudes of the sliding velocities are:

$$\begin{Bmatrix} V_1^s \\ V_2^s \\ V_3^s \\ V_6^s \end{Bmatrix} \equiv \begin{Bmatrix} V_1^r \\ V_2^r \\ V_3^r \\ V_6^r \end{Bmatrix} - \begin{Bmatrix} V_1^w \\ V_2^w \\ V_3^w \\ V_6^w \end{Bmatrix} + \begin{Bmatrix} 0 \\ 0 \\ V_3^c \\ 0 \end{Bmatrix}. \quad (6.24)$$

Substituting Eq.(6.19), Eq.(6.21) and Eq.(6.22) into Eq.(6.24), the relation between the dynamic sliding velocities and the dynamic forces is:

$$\begin{Bmatrix} V_1^s \\ V_2^s \\ V_3^s \\ V_6^s \end{Bmatrix} = \begin{bmatrix} Y_{11} & Y_{12} & Y_{13} & Y_{16} \\ Y_{21} & Y_{22} & Y_{23} & Y_{26} \\ Y_{31} & Y_{32} & Y_{33} & Y_{36} \\ Y_{61} & Y_{62} & Y_{63} & Y_{66} \end{bmatrix} \begin{Bmatrix} F_1 \\ F_2 \\ F_3 \\ F_6 \end{Bmatrix}, \quad (6.25)$$

where $Y_{ik} = Y_{ik}^w + Y_{ik}^r + Y_{ik}^c$ is the sum of mobilities of wheel, rail, and contact spring.

Rigid translation and rotation are performed to consider mobilities of wheel and rail separately at the actual contact point as:

$$[Y_{ik}^w] = [T_{tot}^w][Y_{ik}^w]_0 [T_{tot}^w]^T, \quad (6.26)$$

$$[Y_{ik}^r] = [T_{tot}^r][Y_{ik}^r]_0 [T_{tot}^r]^T. \quad (6.27)$$

The rotation and translation matrices and the validity of this approach are described in Appendix A.

Considering Eq.(6.25), the vertical sliding velocity is equal to zero:

$$V_3^s = Y_{31}F_1 + Y_{32}F_2 + Y_{33}F_3 + Y_{36}F_6 = 0. \quad (6.28)$$

Therefore, the vertical dynamic force can be expressed in terms of the other three dynamic friction forces:

$$F_3 = - \left\{ \begin{array}{ccc} Y_{31} & Y_{32} & Y_{36} \\ Y_{33} & Y_{33} & Y_{33} \end{array} \right\} \left\{ \begin{array}{c} F_1 \\ F_2 \\ F_6 \end{array} \right\}. \quad (6.29)$$

This allows V_3^s to be eliminated from Eq.(6.25):

$$\left\{ \begin{array}{c} V_1^s \\ V_2^s \\ V_6^s \end{array} \right\} = \begin{bmatrix} Y_{11} & Y_{12} & Y_{16} \\ Y_{21} & Y_{22} & Y_{26} \\ Y_{61} & Y_{62} & Y_{66} \end{bmatrix} \left\{ \begin{array}{c} F_1 \\ F_2 \\ F_6 \end{array} \right\} + \left\{ \begin{array}{c} Y_{13} \\ Y_{23} \\ Y_{63} \end{array} \right\} F_3. \quad (6.30)$$

Substituting Eq.(6.29) into Eq.(6.30) gives:

$$\left\{ \begin{array}{c} V_1^s \\ V_2^s \\ V_6^s \end{array} \right\} = \begin{bmatrix} Y_{11} - \frac{Y_{13}Y_{31}}{Y_{33}} & Y_{12} - \frac{Y_{13}Y_{32}}{Y_{33}} & Y_{16} - \frac{Y_{13}Y_{36}}{Y_{33}} \\ Y_{21} - \frac{Y_{23}Y_{31}}{Y_{33}} & Y_{22} - \frac{Y_{23}Y_{32}}{Y_{33}} & Y_{26} - \frac{Y_{23}Y_{36}}{Y_{33}} \\ Y_{61} - \frac{Y_{63}Y_{31}}{Y_{33}} & Y_{62} - \frac{Y_{63}Y_{32}}{Y_{33}} & Y_{66} - \frac{Y_{63}Y_{36}}{Y_{33}} \end{bmatrix} \left\{ \begin{array}{c} F_1 \\ F_2 \\ F_6 \end{array} \right\}. \quad (6.31)$$

So the dynamic relationship of the wheel/rail contact system can be written as:

$$\bar{V}^s = [G]\bar{F}^f, \quad (6.32)$$

where the vector of dynamic sliding velocities is:

$$\bar{V}^s \equiv \left\{ V_1^s \quad V_2^s \quad V_6^s \right\}, \quad (6.33)$$

the vector of dynamic friction forces is:

$$\bar{F}^f \equiv \left\{ F_1 \quad F_2 \quad F_6 \right\}, \quad (6.34)$$

and the mobility matrix is:

$$[G] = \begin{bmatrix} Y_{11} - \frac{Y_{13}Y_{31}}{Y_{33}} & Y_{12} - \frac{Y_{13}Y_{32}}{Y_{33}} & Y_{16} - \frac{Y_{13}Y_{36}}{Y_{33}} \\ Y_{21} - \frac{Y_{23}Y_{31}}{Y_{33}} & Y_{22} - \frac{Y_{23}Y_{32}}{Y_{33}} & Y_{26} - \frac{Y_{23}Y_{36}}{Y_{33}} \\ Y_{61} - \frac{Y_{63}Y_{31}}{Y_{33}} & Y_{62} - \frac{Y_{63}Y_{32}}{Y_{33}} & Y_{66} - \frac{Y_{63}Y_{36}}{Y_{33}} \end{bmatrix}. \quad (6.35)$$

The friction equation in Eq.(6.17) can be linearized relative to the steady-state point $(\gamma_{10}, \gamma_{20}, \gamma_{60}, N_0)$ by assuming that the dynamic quantities are small and ignoring terms of second order in small quantities:

$$\begin{Bmatrix} f_1 \\ f_2 \\ f_6 \end{Bmatrix} = \frac{N_0}{V_0} \begin{bmatrix} \frac{\partial \mu_1}{\partial \gamma_1} & \frac{\partial \mu_1}{\partial \gamma_2} & \frac{\partial \mu_1}{\partial \gamma_6} & \frac{\partial \mu_1}{\partial f_3} \\ \frac{\partial \mu_2}{\partial \gamma_1} & \frac{\partial \mu_2}{\partial \gamma_2} & \frac{\partial \mu_2}{\partial \gamma_6} & \frac{\partial \mu_2}{\partial f_3} \\ \frac{\partial \mu_6}{\partial \gamma_1} & \frac{\partial \mu_6}{\partial \gamma_2} & \frac{\partial \mu_6}{\partial \gamma_6} & \frac{\partial \mu_6}{\partial f_3} \end{bmatrix} \begin{Bmatrix} v_1^s \\ v_2^s \\ v_6^s \\ V_0 f_3 \end{Bmatrix} + \begin{Bmatrix} \mu_1 \\ \mu_2 \\ \mu_6 \end{Bmatrix} f_3. \quad (6.36)$$

To convert the last relationship into the frequency domain, the dynamic forces and dynamic sliding velocities are assumed to be in harmonic form. So, Eq.(6.36) can be rewritten as:

$$\begin{Bmatrix} F_1 \\ F_2 \\ F_6 \end{Bmatrix} = \frac{N_0}{V_0} \begin{bmatrix} \frac{\partial \mu_1}{\partial \gamma_1} & \frac{\partial \mu_1}{\partial \gamma_2} & \frac{\partial \mu_1}{\partial \gamma_6} & \frac{\partial \mu_1}{\partial f_3} \\ \frac{\partial \mu_2}{\partial \gamma_1} & \frac{\partial \mu_2}{\partial \gamma_2} & \frac{\partial \mu_2}{\partial \gamma_6} & \frac{\partial \mu_2}{\partial f_3} \\ \frac{\partial \mu_6}{\partial \gamma_1} & \frac{\partial \mu_6}{\partial \gamma_2} & \frac{\partial \mu_6}{\partial \gamma_6} & \frac{\partial \mu_6}{\partial f_3} \end{bmatrix} \begin{Bmatrix} V_1^s \\ V_2^s \\ V_6^s \\ V_0 F_3 \end{Bmatrix} + \begin{Bmatrix} \mu_1 \\ \mu_2 \\ \mu_6 \end{Bmatrix} F_3. \quad (6.37)$$

The terms related to F_3 can be collected together to give:

$$\begin{Bmatrix} F_1 \\ F_2 \\ F_6 \end{Bmatrix} = \frac{N_0}{V_0} \begin{bmatrix} \frac{\partial \mu_1}{\partial \gamma_1} & \frac{\partial \mu_1}{\partial \gamma_2} & \frac{\partial \mu_1}{\partial \gamma_6} \\ \frac{\partial \mu_2}{\partial \gamma_1} & \frac{\partial \mu_2}{\partial \gamma_2} & \frac{\partial \mu_2}{\partial \gamma_6} \\ \frac{\partial \mu_6}{\partial \gamma_1} & \frac{\partial \mu_6}{\partial \gamma_2} & \frac{\partial \mu_6}{\partial \gamma_6} \end{bmatrix} \begin{Bmatrix} V_1^s \\ V_2^s \\ V_6^s \end{Bmatrix} + \begin{Bmatrix} \mu_1 + N_0 \frac{\partial \mu_1}{\partial f_3} \\ \mu_2 + N_0 \frac{\partial \mu_2}{\partial f_3} \\ \mu_6 + N_0 \frac{\partial \mu_6}{\partial f_3} \end{Bmatrix} F_3. \quad (6.38)$$

Substituting Eq.(6.29) into this last equation, the dynamic friction forces can be rewritten as:

$$\begin{Bmatrix} F_1 \\ F_2 \\ F_6 \end{Bmatrix} = \frac{N_0}{V_0} \begin{bmatrix} \frac{\partial \mu_1}{\partial \gamma_1} & \frac{\partial \mu_1}{\partial \gamma_2} & \frac{\partial \mu_1}{\partial \gamma_6} \\ \frac{\partial \mu_2}{\partial \gamma_1} & \frac{\partial \mu_2}{\partial \gamma_2} & \frac{\partial \mu_2}{\partial \gamma_6} \\ \frac{\partial \mu_6}{\partial \gamma_1} & \frac{\partial \mu_6}{\partial \gamma_2} & \frac{\partial \mu_6}{\partial \gamma_6} \end{bmatrix} \begin{Bmatrix} V_1^s \\ V_2^s \\ V_6^s \end{Bmatrix} - \begin{Bmatrix} \mu_1 + N_0 \frac{\partial \mu_1}{\partial f_3} \\ \mu_2 + N_0 \frac{\partial \mu_2}{\partial f_3} \\ \mu_6 + N_0 \frac{\partial \mu_6}{\partial f_3} \end{Bmatrix} \begin{Bmatrix} Y_{31} & Y_{32} & Y_{36} \\ Y_{33} & Y_{33} & Y_{33} \end{Bmatrix} \begin{Bmatrix} F_1 \\ F_2 \\ F_6 \end{Bmatrix}. \quad (6.39)$$

This relationship between the dynamic friction forces and dynamic sliding velocities can be written as:

$$\bar{F}^f = [H_1] \bar{V}^s + [H_2] \bar{F}^f, \quad (6.40)$$

where the frictional impedance matrix $[H_1]$ is formed from the derivatives of non-dimensional friction force with respect to creepages:

$$[H_1] = \frac{N_0}{V_0} \begin{bmatrix} \frac{\partial \mu_1}{\partial \gamma_1} & \frac{\partial \mu_1}{\partial \gamma_2} & \frac{\partial \mu_1}{\partial \gamma_6} \\ \frac{\partial \mu_2}{\partial \gamma_1} & \frac{\partial \mu_2}{\partial \gamma_2} & \frac{\partial \mu_2}{\partial \gamma_6} \\ \frac{\partial \mu_6}{\partial \gamma_1} & \frac{\partial \mu_6}{\partial \gamma_2} & \frac{\partial \mu_6}{\partial \gamma_6} \end{bmatrix} = \begin{bmatrix} \frac{\partial f_1}{\partial v_1^s} & \frac{\partial f_1}{\partial v_2^s} & \frac{\partial f_1}{\partial v_6^s} \\ \frac{\partial f_2}{\partial v_1^s} & \frac{\partial f_2}{\partial v_2^s} & \frac{\partial f_2}{\partial v_6^s} \\ \frac{\partial f_6}{\partial v_1^s} & \frac{\partial f_6}{\partial v_2^s} & \frac{\partial f_6}{\partial v_6^s} \end{bmatrix}, \quad (6.41)$$

and the matrix $[H_2]$ determines the influence from the fluctuation of the vertical force on the friction forces:

$$[H_2] = - \begin{Bmatrix} \mu_1 + N_0 \frac{\partial \mu_1}{\partial f_3} \\ \mu_2 + N_0 \frac{\partial \mu_2}{\partial f_3} \\ \mu_6 + N_0 \frac{\partial \mu_6}{\partial f_3} \end{Bmatrix} \begin{Bmatrix} Y_{31} & Y_{32} & Y_{36} \\ Y_{33} & Y_{33} & Y_{33} \end{Bmatrix}. \quad (6.42)$$

6.2 Self-excited vibration loop in the frequency domain

From Eq.(6.32), the wheel/rail dynamic equation gives the relationship between the dynamic friction forces and the dynamic sliding velocities:

$$\bar{V}^s = [G]\bar{F}^f, \quad (6.43)$$

where \bar{F}^f is formed of the friction forces and spin moment, and \bar{V}^s includes the dynamic sliding velocities in the longitudinal, lateral and spin directions.

Similarly, the linearized dynamic friction forces in Eq.(6.40) give the relationship between the dynamic sliding velocities and the dynamic friction forces:

$$\bar{F}^f = [H_1]\bar{V}^s + [H_2]\bar{F}^f. \quad (6.44)$$

These two relationships can establish a MIMO (Multi-Input Multi-Output) system, as shown in figure 6.3. Substituting Eq.(6.43) into Eq.(6.44), the relation-

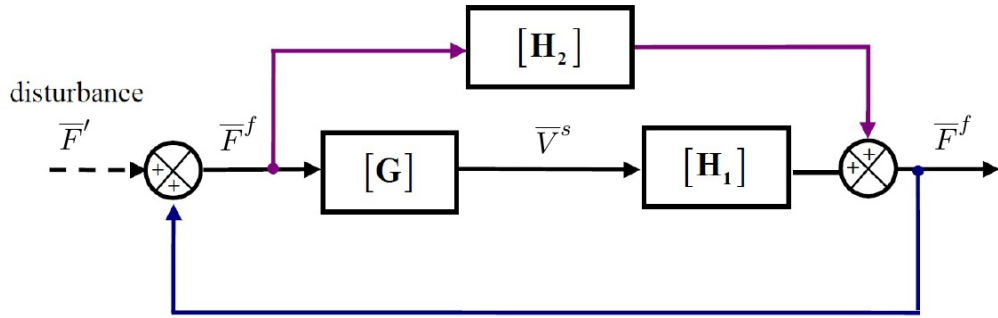


Figure 6.3: Frequency-domain self-excited vibration loop of the wheel/rail contact system. Huang [3]

ship between the dynamic sliding velocities and the dynamic friction forces can be rewritten as:

$$\bar{F}^f = ([H_1][G] + [H_2])\bar{F}^f. \quad (6.45)$$

Thus, the open-loop transfer function is:

$$\bar{F}^f = [Q]\bar{F}^f, \quad (6.46)$$

where $[Q] = [H_1][G] + [H_2]$ is the open-loop transfer function matrix (TFM).

6.3 Stability analysis for the frequency domain loop

6.3.1 Stability analysis for the lateral motion

If the input to a linear system is sinusoidal, the output is sinusoidal with the same frequency but with a different amplitude and phase. Therefore, in a SISO (Single-Input Single-Output) linear system, the open-loop response to a sinusoidal input at varying frequencies is represented by a transfer function with respect to the frequency. The open-loop transfer function can be used to predict the behaviour of the closed-loop system via classic frequency-domain techniques, e.g. Nyquist stability criterion, Bode plot and root locus.

For a case where only lateral creepage is of interest the wheel/rail dynamic equation from Eq.(6.31) can be rewritten as:

$$V_2^s = \left(Y_{22} - \frac{Y_{23}Y_{32}}{Y_{33}} \right) F_2 = GF_2, \quad (6.47)$$

and the linearized friction force from Eq.(6.39) is:

$$F_2 = \frac{N_0}{V_0} \frac{\partial \mu_2}{\partial \gamma_2} V_2^s - \left(\mu_2 + N_0 \frac{\partial \mu_2}{\partial f_3} \right) \frac{Y_{32}}{Y_{33}} F_2 = H_1 V_2^s + H_2 F_2. \quad (6.48)$$

In this case, the general system described in Figure 6.3 is reduced to a SISO system with open loop:

$$F_2 = (H_1 G + H_2) F_2, \quad (6.49)$$

where the open-loop transfer function is:

$$Q = H_1 G + H_2. \quad (6.50)$$

If a system is stable, the response of the system to a disturbance will asymptotically tend to the equilibrium. For a SISO system, if an open-loop system is stable, the stability analysis of its closed-loop system can be considered using its open-loop Bode plot. The Bode plot is introduced here to illustrate the conditions for instability of the corresponding closed feedback loop. According to the Nyquist criterion, instability occurs in the closed loop system if the polar plot of the open loop frequency response crosses the real axis beyond the critical point $(-1/k, j0)$, where for a positive feedback, $k = -1$. This means, in the Bode plot, if the amplitude of the open loop transfer function $H_1 G + H_2$ exceeds unity when

the phase angle is 0° , the positive feedback loop is unstable.

The physical meaning can be explained intuitively as follow. Only if the feedback signals are in phase with the reference input, will the output amplitude increase steadily.

Thus, the closed loop of the positive feedback system in Figure 6.3 will be unstable if the open loop frequency response has a gain $q(\omega)$ greater than unity at the frequency giving an open loop phase of 0° . Therefore, the unstable frequencies must satisfy the following condition:

$$\text{Re}\{q(\omega)\} > 1, \quad (6.51)$$

$$\text{Im}\{q(\omega)\} = 0. \quad (6.52)$$

6.3.2 Stability analysis for the general system

For a general MIMO loop, the open-loop responses are represented by a transfer function matrix (TFM) (see section 6.2). So, the techniques for the SISO system may not be appropriate and need to be generalized for MIMO problems. The Nyquist stability criterion was developed using eigenloci of the open-loop TFM [43][44][45][46].

The system will be closed-loop stable if and only if the net sum of anti-clockwise encirclements of the critical point $(-1/k + j0)$ by the set of eigenloci of the open-loop TFM is equal to the total number of right-half plane poles of the TFM, where for a positive feedback $k = -1$. Thus, the eigenloci of the open-loop TFM must not encircle the critical point $(1+j0)$ to make sure the closed-loop system is stable, when the frequency is varied from zero to infinity.

However, although this mathematical generalization of the classic Nyquist stability criterion is possible, the application of this method has some limitations. So, for predicting the possible unstable frequencies in the squeal loop, only the eigenvalue with maximum modulus at each frequency is chosen to judge the stability by means of Eqs.(6.51) and (6.52).

6.4 Wheel/rail structural dynamics for time domain model

In modelling squeal, the wheel and the rail are assumed to have linear dynamics, but the excitation forces acting on them are non-linear. Thus, the method of step-

by-step integration in the time domain is appropriate. This requires the dynamic properties of the wheel and rail to be described in the state-space form.

6.4.1 Wheel structural dynamics

The Sirio wheel modelled by finite element analysis (see Chapter 3) provides the modal parameters (damping ratios, natural frequencies and mode shapes).

For the step-by-step simulation, the modal analysis method can be adopted to describe the state-space response of the wheel and is built as follows.

Consider a wheel with n modes, four input dynamic forces $\bar{f}^w = \{f_1^w, f_2^w, f_3^w, f_6^w\}^T$ and four output dynamic velocities $\bar{v}^w = \{v_1^w, v_2^w, v_3^w, v_6^w\}^T$ defined in longitudinal, lateral, vertical and spin direction. This can be represented by a state equation, Eq.(6.53), and an output equation, Eq.(6.54):

$$\dot{\bar{w}} = [A^w]\bar{w} + [B^w]\bar{f}^w, \quad (6.53)$$

$$\bar{v}^w = [C^w]\bar{w}, \quad (6.54)$$

where the $2n$ -order state-variable vector consists of the modal velocity \dot{q}_r and the modal displacement q_r of modes r (1 to n):

$$\bar{w} = \left\{ \dot{q}_1 \quad \dot{q}_2 \quad \dots \quad \dot{q}_n \quad q_1 \quad q_2 \quad \dots \quad q_n \right\}^T = \left\{ w_1 \quad w_2 \quad \dots \quad w_{2n} \right\}^T. \quad (6.55)$$

The system matrix $[A^w]$ is:

$$[A^w] = \left[\begin{array}{cccc|cccc} -2\zeta_1\omega_1 & & & & -\omega_1^2 & & & \\ & -2\zeta_2\omega_2 & & & & -\omega_2^2 & & \\ & & -2\zeta_3\omega_3 & & & & -\omega_3^2 & \\ & & & \ddots & & & & \ddots \\ & & & & -2\zeta_n\omega_n & & & -\omega_n^2 \\ \hline & 1 & & & & & & \\ & & 1 & & & & & \\ & & & 1 & & & & \\ & & & & \ddots & & & \\ & & & & & 1 & & \\ & & & & & & & [0] \end{array} \right], \quad (6.56)$$

where ζ_r is the damping ratio of mode r (1 to n) and ω_r is the natural frequency (in radians/sec) of mode r . The input matrix $[B^w]$ transforms external forces into

modal forces for each mode, while the output matrix $[C^w]$ sums modal velocities of each mode into external velocities. Both matrices are formed of the mode shape displacements at the contact point of the wheel:

$$[B^w] = \begin{bmatrix} \phi_{11} & \phi_{12} & \dots & \phi_{1n} & 0 & 0 & \dots & 0 \\ \phi_{21} & \phi_{22} & \dots & \phi_{2n} & 0 & 0 & \dots & 0 \\ \vdots & \vdots & \ddots & \vdots & \vdots & \vdots & \ddots & \vdots \\ \phi_{k1} & \phi_{k2} & \dots & \phi_{kn} & 0 & 0 & \dots & 0 \end{bmatrix}^T, \quad (6.57)$$

$k = 1, 2, 3, 6$

$$[C^w] = \begin{bmatrix} \phi_{11} & \phi_{12} & \dots & \phi_{1n} & 0 & 0 & \dots & 0 \\ \phi_{21} & \phi_{22} & \dots & \phi_{2n} & 0 & 0 & \dots & 0 \\ \vdots & \vdots & \ddots & \vdots & \vdots & \vdots & \ddots & \vdots \\ \phi_{i1} & \phi_{i2} & \dots & \phi_{in} & 0 & 0 & \dots & 0 \end{bmatrix}, \quad (6.58)$$

$i = 1, 2, 3, 6,$

where ϕ_{ir} and ϕ_{kr} are the mass-normalized mode shapes of mode r in the i and k directions.

6.4.2 Rail structural dynamics

The point mobility curves (with force and response at the same point) of the track in the longitudinal, lateral, vertical and spin directions are available (see section 6.1.2). For each mobility curve, it is possible to find an equivalent system with a transfer function expressed in the form of a ratio of two polynomials:

$$H(s) \equiv \frac{B(s)}{A(s)} = \frac{b_1 s^{m-1} + b_2 s^{m-2} + \dots + b_m}{s^m + a_1 s^{m-1} + a_2 s^{m-2} + \dots + a_m}, \quad (6.59)$$

where the order of the denominator is one order higher than that of numerator. Determining the coefficients in this transfer function is actually a process of system identification. These coefficients are not unique but depend on how much error is allowed in the application. Normally, the higher the order of the equivalent system assumed, the less is the error of the system identification results. However, if the order of the system is very high, the performance of the equivalent system is sensitive to the coefficients and may be unstable. To seek appropriate coefficients, the *'invfreqs'* function provided by the Signal Processing

Toolbox of MATLAB [47] can be adopted.

For any particular input force f_k^r and output response v_i^r , their dynamic relationship can be described in the frequency domain by a mobility function Y_{ik}^r . A corresponding equivalent system with the form in Eq.(6.59) can be calculated, with coefficients $a_{ik,j}$ and $b_{ik,j}$, $j = 1, \dots, m$. Then, the state-space model can be written as:

$$\dot{\bar{r}}_{ik} = [A_{ik}^r]\bar{r}_{ik} + [B_{ik}^r]f_k, \quad (6.60)$$

$$v_i^r = [C_{ik}^r]\bar{r}_{ik} + [D_{ik}^r]f_k, \quad (6.61)$$

where the vector of state variables is:

$$\bar{r}_{ik} \equiv \left\{ r_{ik,1} \quad r_{ik,2} \quad \dots \quad r_{ik,m} \right\}^T. \quad (6.62)$$

The system matrix is:

$$[A_{ik}^r] \equiv \begin{bmatrix} -a_{ik,1} & -a_{ik,2} & \dots & \dots & -a_{ik,m} \\ 1 & 0 & \dots & \dots & 0 \\ 0 & 1 & & \dots & 0 \\ \vdots & & \ddots & \vdots & \vdots \\ 0 & 0 & \dots & 1 & 0 \end{bmatrix}, \quad (6.63)$$

the input matrix is:

$$[B_{ik}^r] \equiv [1 \quad 0 \quad \dots \quad 0]^T, \quad (6.64)$$

and the output matrix is:

$$[C_{ik}^r] \equiv [b_{ik,1} \quad b_{ik,2} \quad \dots \quad b_{ik,m}]. \quad (6.65)$$

The direct output matrix is zero:

$$[D_{ik}^r] = 0. \quad (6.66)$$

The whole rail model is a multiple-input, multiple-output (MIMO) system. The sub-models corresponding to each force input and each velocity output can be assembled to give the complete state-space model. It is not necessary to include all the possible FRFs, because the rail is normally much more damped than the wheel and consequently has much lower response than it. Four point FRFs and no cross FRF are retained to describe the dynamic properties at the contact point.

These FRFs are longitudinal, lateral, vertical and spin, Y_{ik}^r , $i = k = 1, 2, 3, 6$.

The complete state-space model of the rail, with four input forces

$\bar{f}^r = \{f_1^r, f_2^r, f_3^r, f_6^r\}^T$ and four output velocities $\bar{v}^r = \{v_1^r, v_2^r, v_3^r, v_6^r\}^T$, is obtained by assembling these sub-models as follows:

$$\dot{\bar{r}} = [A^r]\bar{r} + [B^r]\bar{f}^r, \quad (6.67)$$

$$\bar{v}^r = [C^r]\bar{r}, \quad (6.68)$$

where the vector of state variables is:

$$\bar{r} \equiv \left\{ \bar{r}_{11} \quad \bar{r}_{22} \quad \dots \quad \bar{r}_{66} \right\}^T, \quad (6.69)$$

the system matrix is:

$$[A^r] \equiv \begin{bmatrix} [A_{11}^r] & & & \\ & [A_{22}^r] & & \\ & & [A_{33}^r] & \\ & & & [A_{66}^r] \end{bmatrix}, \quad (6.70)$$

the input matrix is:

$$[B^r] \equiv \begin{bmatrix} [B_{11}^r] & & & \\ & [B_{22}^r] & & \\ & & [B_{33}^r] & \\ & & & [B_{66}^r] \end{bmatrix}, \quad (6.71)$$

and the output matrix is:

$$[C^r] \equiv \begin{bmatrix} [C_{11}^r] & & & \\ & [C_{22}^r] & & \\ & & [C_{33}^r] & \\ & & & [C_{66}^r] \end{bmatrix}. \quad (6.72)$$

6.5 Self-excited vibration loop in the time domain

A general self-excited vibration model can be developed by combining wheel/rail structural models and the wheel/rail rolling contact model in a loop as shown in Figure 6.4. This loop is running on a set of steady-state conditions. If some small

transient disturbances \bar{f}' are introduced, the wheel and rail will produce dynamic responses \bar{v}^w and \bar{v}^r , which can give dynamic sliding velocities \bar{v}^s and the dynamic velocity of the contact spring v_3^c . In the contact area, the dynamic friction forces may be produced due to either the dynamic sliding velocities or the normal fluctuating force. Consequently, the contact forces \bar{f} , including friction forces and normal fluctuating force, are updated and fed back to the wheel and rail system. For the simulation in the time domain, the general loop can be realized in state space, as shown in Figure 6.5.

In the state-space model of the wheel, the state variables \bar{w} are the dynamic displacement and velocity of each mode. For the wheel, according to the definition of wheel forces \bar{f}^w in Eq.(6.2), the contact forces \bar{f} are reversed in sign and applied to the wheel. To obtain the sliding velocities \bar{v}^s defined in Eq.(6.9), the velocities of the wheel \bar{v}^w need to be reversed again. Hence, these negative signs can be eliminated.

In the state-space model of the rail, the state variables \bar{r} are derived from the coefficients of equivalent systems, so they have no clear physical meaning. According to the definition in Eq.(6.3), the forces acting on the rail are the same as the contact forces \bar{f} . The velocities of rail \bar{v}^r can be used directly to calculate the sliding velocities \bar{v}^s , as given in Eq.(6.9).

The dynamic friction forces f_1, f_2, f_6 can be calculated in Eq.(6.17), with creepage-dependent non-dimensional friction forces μ_1, μ_2, μ_6 and steady-state conditions $\gamma_{10}, \gamma_{20}, \gamma_{60}, N_0, V_0, k_H$. The vertical fluctuating force f_3 is updated by the dynamic vertical approach velocity v_3^c , as given in Eq.(6.15).

The whole state-space feedback loop includes the non-linear relationship between the sliding velocities and the friction forces as well as the linear relationships in the wheel/rail contact system. The time domain simulation is implemented by the step-by-step integration from any small disturbance \bar{f}' .

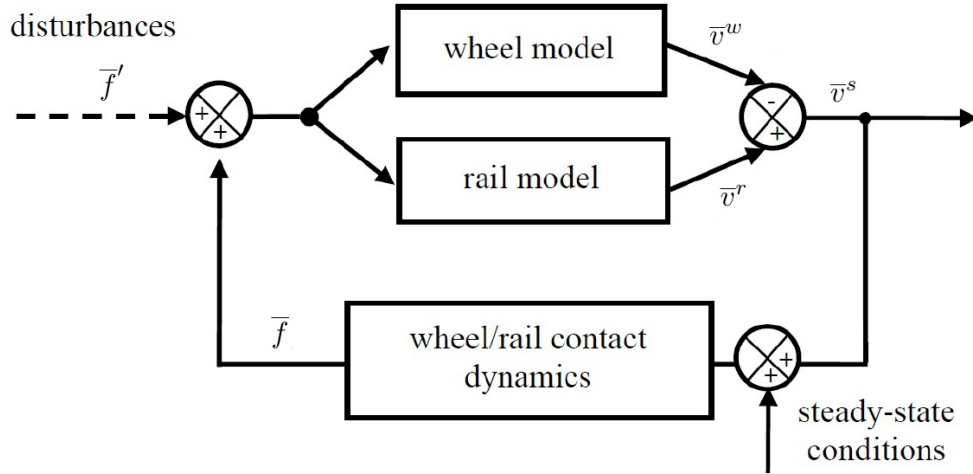


Figure 6.4: General self-excited vibration loop of the wheel/rail contact system. Huang [3]

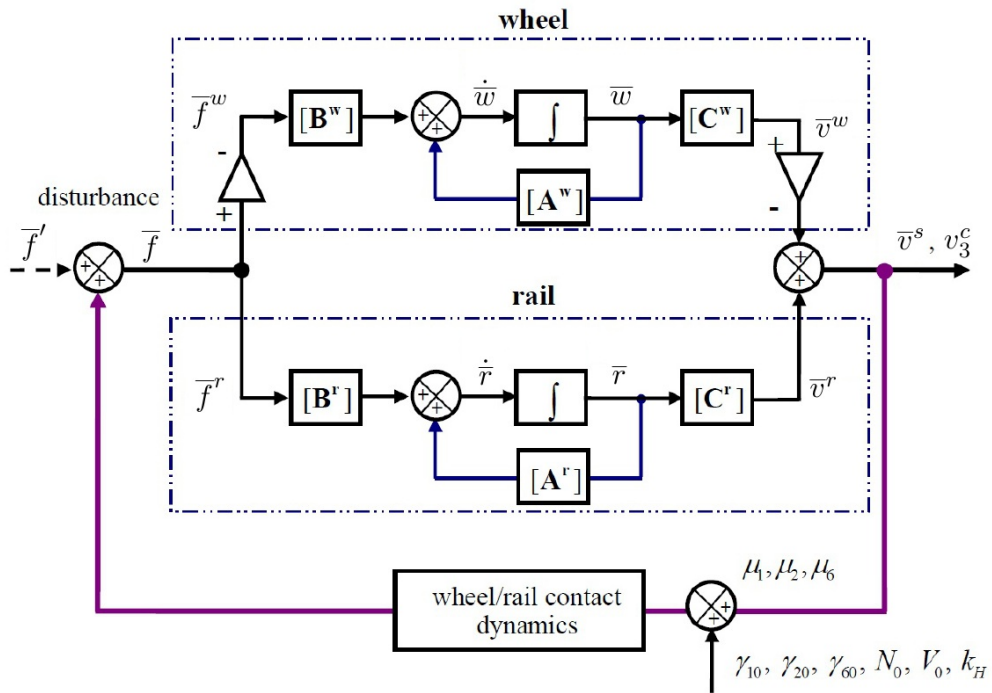


Figure 6.5: State-space self-excited vibration loop of the wheel/rail contact system. Huang [3]

6.6 Results

The stick/slip phenomenon generated at the contact points between wheels and rail, as discussed in this Chapter, is the reason for the self-excited vibration of the wheels and therefore of the squeal noise generation. This stick/slip mechanism is described by a negative damping coefficient that varies with vibration amplitude and that can be related to the negative slope of the friction characteristics at large sliding velocities. For the curve squeal model, only a negative slope of the friction coefficient is able to destabilize the system and induce wheel vibration, therefore, the parameters that describe this falling region are very important in order to provoke the squeal noise. Unfortunately, the detailed description of the friction curves are not available from the experimental campaign performed in Milan and they are also very difficult to estimate and discover in the literature. For this reason, considering part of the outputs obtained from the numerical model simulation of the bogie during the curve, a parametric study of these values has been performed in order to find parameters values that can induce squeal noise.

Moreover, it is known that curve squeal noise is far from being deterministic and parameters like temperature, humidity and even dirt and particles on the rail can have a strong effect on curve squeal occurrence. For this reason in the frequency domain model presented hereafter, parameters of friction characteristics and other input parameters have been defined as uncertain variables and, as a result, the model is used to give the frequency values of possible unstable eigenvalues of the system while the range of uncertain parameters is randomly spanned.

Finally, to have an idea of which frequencies are really involved in the squeal phenomenon and estimate noise levels, a time domain simulation has been performed. In this case, since the time domain simulation is much longer than the frequency domain one, only one combination of input parameters has been selected.

Despite the rail having a negligible effect in generating squeal noise, the analytical model of the rail has been modified considering the geometric properties of the cross section of the grooved rail for modelling the urban track case.

6.6.1 Friction curve

Before showing the results, the lateral friction coefficient versus lateral creepage is shown in order to explain how the parameters κ and λ influence the falling region. As discussed in Chapter 5 the equation that describes this region can be

written as:

$$\tau(\gamma) = 1 - \lambda e^{\left(\frac{-\kappa}{|\gamma|}\right)}, \quad (6.73)$$

where λ is the falling ratio while κ is the saturation coefficient.

In Figure 6.6 friction curves are plotted for different values of κ and λ . In the first one, κ is fixed at 0.05 while λ is varied between 0.1 and 1. In the second one the chosen value of λ is 0.5 and κ is varied between 0.005 and 1.

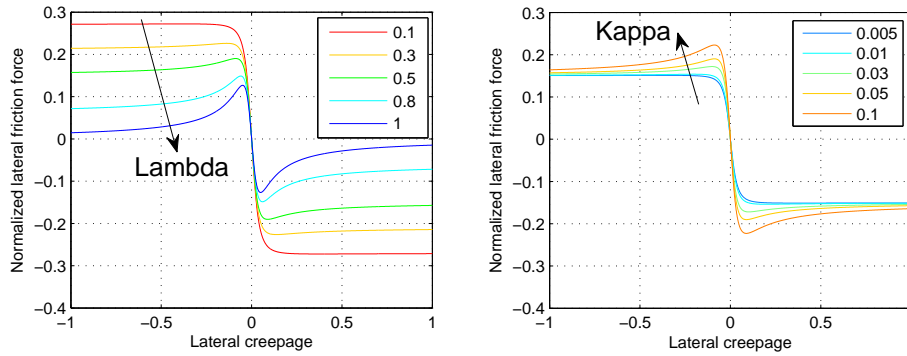


Figure 6.6: Lateral friction coefficient versus lateral creepage for different value of λ and κ . In the first graph, the κ value is fixed at 0.05. In the second graph the λ value is fixed at 0.5.

The results of the heuristic formula show that the falling ratio λ influences the friction curve at large creepages while the saturation coefficient κ mainly influences the friction curve at small creepages, close to the saturation zone. In this case the friction characteristics in longitudinal and spin directions are not shown or taken into account because they do not have a great contribution in squeal generation, rather the falling zone of the friction curve is attenuated or even eliminated if these values are large enough, and therefore, the squeal noise could be attenuated.

6.6.2 Analysis in frequency domain

Analysis of the inner front wheel - case with gauge of 1445 mm

The outputs obtained simulating a left curve with a track gauge of 1445 mm, for the inner front wheel, show a contact point on the tread. In Table 6.1, the results obtained at 15 seconds into the simulation and other parameters are listed and converted considering the frames of reference shown in Figure 6.7. By looking

at this Table, most of the values are defined in a range of values with a uniform distribution (U) to make, as discussed before, the input parameters for the squeal model non-deterministic. The following approximation is used for spin around direction normal to contact plane:

$$\gamma_{60} = \frac{\sin(\theta)}{R_w}, \quad (6.74)$$

where θ is the contact angle between wheel and rail, while R_w the nominal radius of the wheel. Since θ is defined in a uniform distribution, γ_{60} varies accordingly.

Description	Name	Unit	Values
Normal contact force	N_0	[kN]	$U(20.6, 31)$
Contact position on the wheel	$[x \ y \ z]$	[mm]	$[0 \ U(-12.5, -2.5) \ -0.35]$
Contact position on the rail	$[x \ y \ z]$	[mm]	$[0 \ -8 \ -1.5]$
Contact angle between wheel/rail	θ	[°]	$U(2.1, 3.1)$
Longitudinal creepage	γ_{10}	-	$U(-0.0006, -0.0004)$
Lateral creepage	γ_{20}	-	$U(-0.0642, -0.0428)$
Spin creepage	γ_{60}	[1/m]	Eq.(6.74)
Curving velocity	V	[m/s]	$U(1.9, 3.6)$
Nominal radius of the wheel	R_w	[m]	0.33
Transverse curve radius of the wheel	R_{wt}	[m]	0
Transverse curve radius of the rail	R_{rt}	[m]	0.230
Coloumb coefficient	μ_0	-	0.4
Falling ratio	λ	-	$U(0.04, 0.06)$
Saturation coefficient	κ	-	0.8

Table 6.1: Input parameters at contact point on the tread of the inner front wheel.

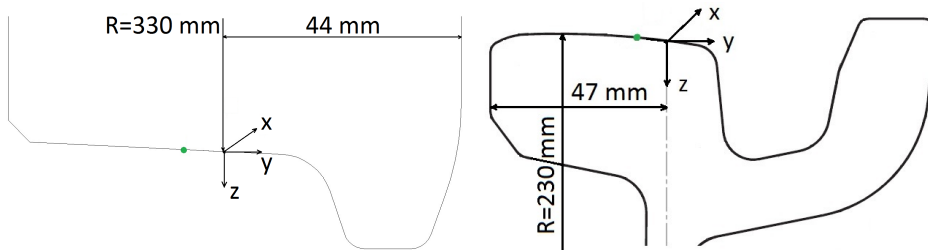


Figure 6.7: Contact point position on the inner front wheel and inner rail.

Values λ and κ have been selected to have a negative slope at the creepages considered. Figure 6.8 shows the range of friction curves range related to κ and

λ of Table 6.1.

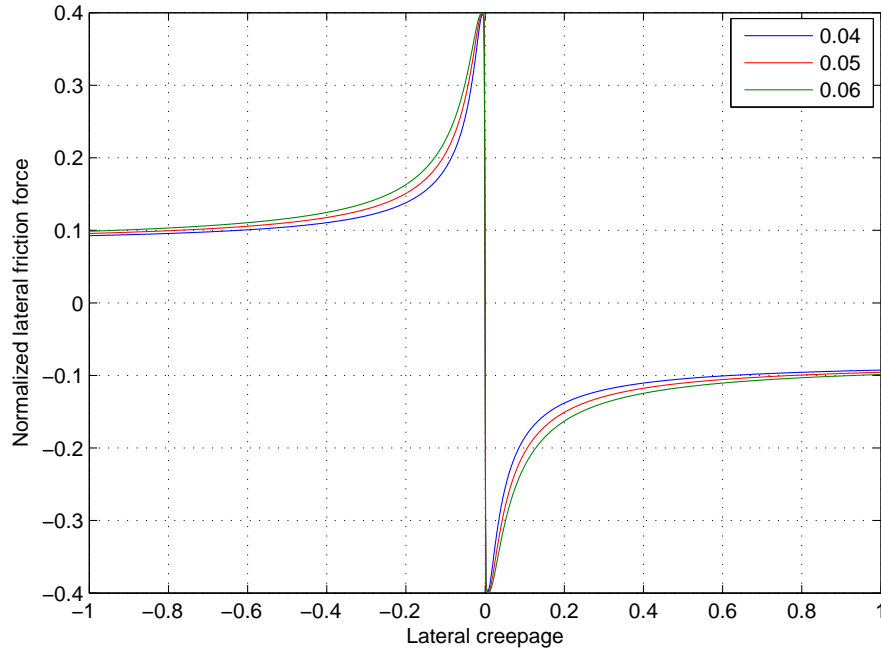


Figure 6.8: Lateral friction versus lateral creepage for λ equal to 0.8 and κ values of 0.04, 0.05 and 0.06.

In order to produce a single set of inputs and to run a single case, uncertain parameters are randomly extracted from the uniform distributions and, for each case, the eigenvalues of the open loop are calculated for all frequencies.

Figure 6.9 summarizes the results for the inner leading wheel depicting black dots at the unstable frequencies for each case run; in the background the wheel mobility at the contact point in tangential and normal directions is also shown for reference. A total of 450 cases have been calculated giving an idea of the variability of the phenomenon. The model predicts unstable frequencies that are close to measured ones, see Figure 6.10 although not all of them are present in the wheel vibration spectrograms of Figure 6.10. One of the two most important frequencies involved in squeal noise at 2550 Hz is found to be one of the more likely to be unstable in the model as well. Also other frequencies that, although present in the measurements, have less importance in terms of levels and persistence, are also found in the predictions, like 530, 1330, 2100, 2250, 3600 and 3700 Hz. Interestingly also the model finds that unstable eigenvalues can have higher

frequencies than the corresponding natural mode. For example the mode at 1271 Hz would generate squeal at around 1330 Hz. It has been verified that the mode at 1271 Hz is the one responsible for possible squeal at 1330 Hz by adding fictitious damping to it; as a consequence the unstable frequencies at around 1330 Hz disappeared. The same thing has been done for the other frequencies possibly involved in squeal noise and they are summarized in Table 6.2. Further comments and explanations for this shift between wheel natural frequencies and unstable frequencies will be given below in Section 6.6.3.

By looking at Figure 6.9 and Table 6.2, it can be noted that the predominately axial modes (528 Hz and 1271 Hz) have been predicted to be unstable with a certain persistence. This is due to the fact that the contact condition selected is such as to readily excite the axial modes as the friction force is acting on the tread in the axial direction (contact angle is in fact in between 2° and 3°). Conversely by looking at Figure 6.10 a frequency at around 1530 Hz is persistent and it is not predicted by the model. This frequency is likely to be correlated with the predominantly radial mode at 1423 Hz possibly excited by a friction force acting on the flange back; therefore, to predict this mode in the model, a contact point on the flange back may be needed as well. This will be discussed in the results obtained from the model with two contact points later in Chapter 7.

Finally, it is interesting also to observe that the predicted unstable frequencies in the range 2501-2537 Hz are connected with two modes, at 2475 Hz and 2536 Hz (see Table 6.2). In this sense, it has been verified that if one of the two is suppressed the other one is still capable of causing instabilities. On the one hand Figure 6.11 shows the curve squeal occurrences adopting a wheel modal model which does not include the mode at 2536 Hz and it is clear how the other mode, at 2475 Hz, is still responsible for possible curve squeal in this frequency range. On the other hand Figure 6.12 shows that the mode at 2536 Hz alone can give instability as well. Both these modes again have a strong axial component at the contact point.

To conclude, this example can be used to understand what are the most important factors in the appearance of unstable frequencies in the numerical model. In fact, provided that the slope of the friction curve is negative and the modal damping ratio of the wheel is relatively low, in order for unstable eigenvalues to appear these other factors need to be taken into consideration:

- mode shape at contact point in axial and radial direction;

- direction of friction force (i.e. tangent at contact point).

Only a wheel mode having an important mode shape component in the same direction as the friction force can be readily responsible for curve squeal; in fact the axial-to-radial mode shape ratio, combined with direction of friction force, will be found to be important to explain the frequency shift mentioned above (see section 6.6.3).

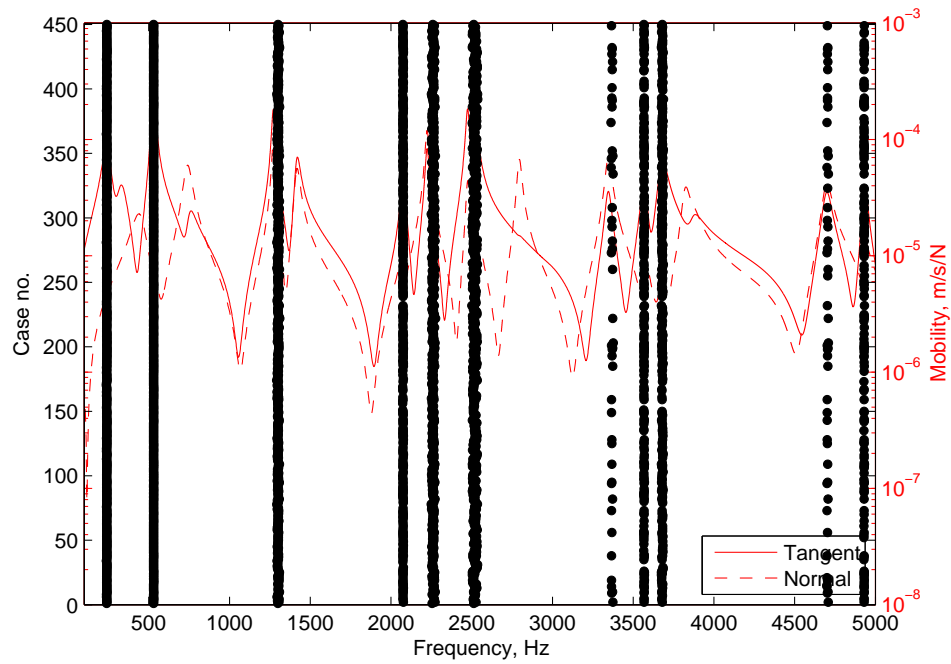


Figure 6.9: Curve squeal occurrences diagram for the inner front wheel.

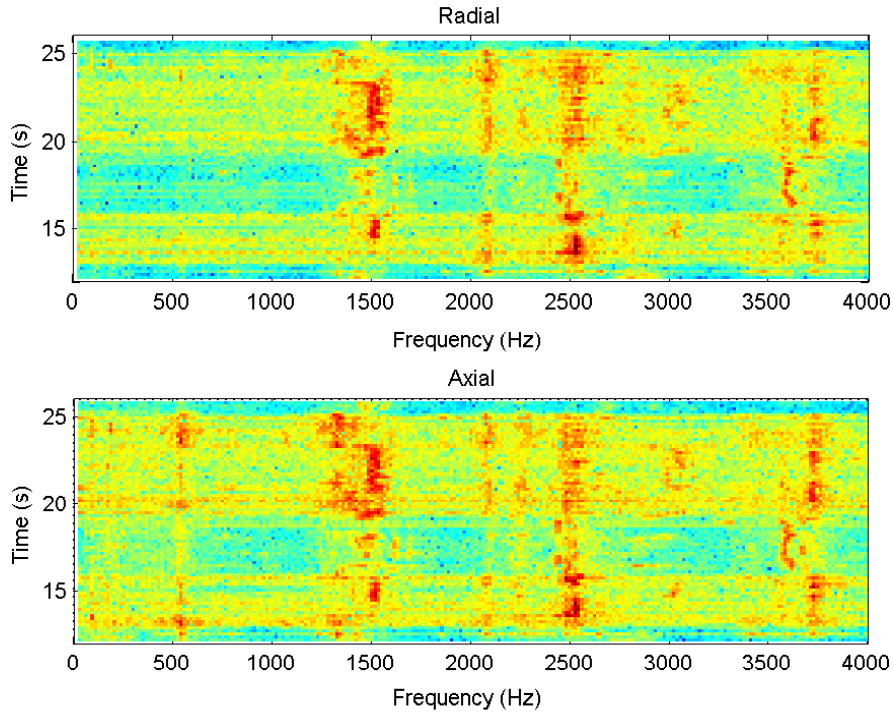


Figure 6.10: Spectrogram of inner front wheel vibration acceleration during tram pass-by.

Numerical modes involved in squeal	Frequency range predicted by model	Experimental frequencies involved in squeal
242 Hz	237 - 242 Hz	
529 Hz	529 - 531 Hz	around 530 Hz
1271 Hz	1292 - 1311 Hz	around 1330 Hz
2078 Hz	2072 - 2077 Hz	around 2100 Hz
2224 Hz	2249 - 2276 Hz	around 2250 Hz
2475 Hz, 2536 Hz	2501 - 2537 Hz	around 2550 Hz
3346 Hz	3362 - 3376 Hz	
3569 Hz	3565 - 3571 Hz	around 3600 Hz
3680 Hz	3674 - 3687 Hz	around 3700 Hz
4697 Hz	4699 - 4709 Hz	
4934 Hz	4929 - 4933 Hz	

Table 6.2: Numerical modes involved in squeal compared with the experimental frequencies involved in squeal and frequency range predicted by the model.

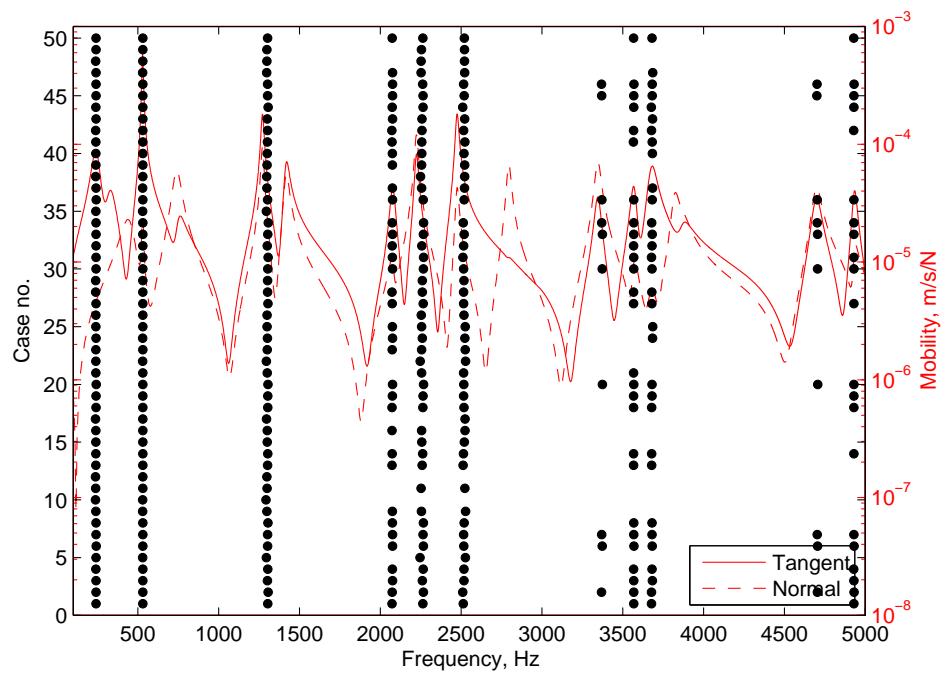


Figure 6.11: Curve squeal occurrences diagram for the inner front wheel with the mode at 2536 Hz suppressed.

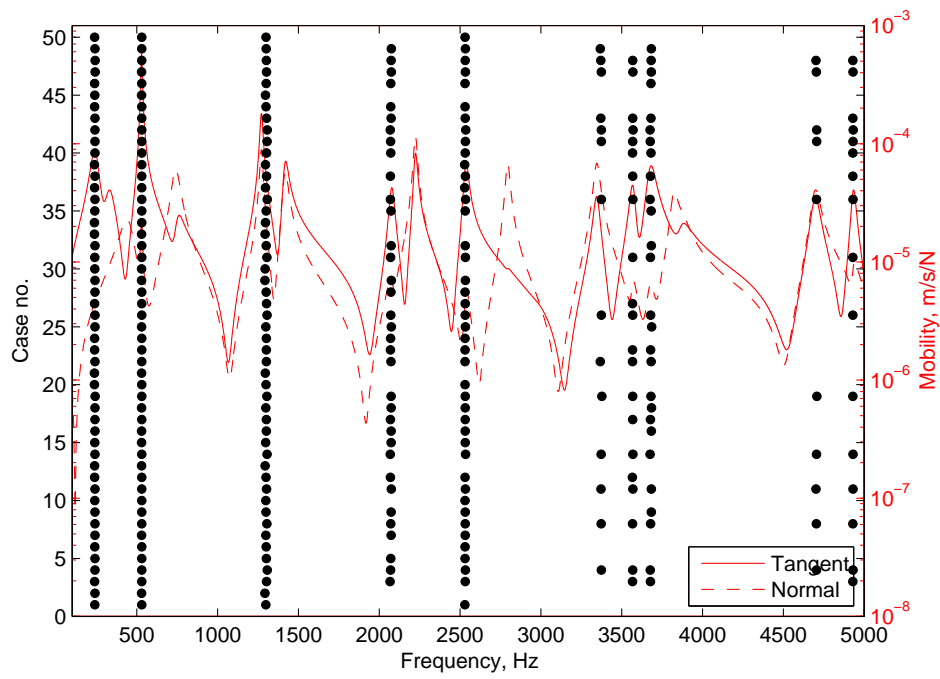


Figure 6.12: Curve squeal occurrences diagram for the inner front wheel with the mode at 2475 Hz suppressed.

Analysis of the outer front wheel - case with gauge of 1450 mm

The same analysis performed before has been done for the outer front wheel in the case of a simulation with a track gauge of 1450 mm. The results obtained from the left curve steady-state numerical simulation show a contact point occurrence on the tread; in Table 6.3 the uncertain and deterministic input parameters for the squeal model are summarized and converted considering the frames of reference shown in Figure 6.13.

Description	Name	Unit	Values
Normal contact force	N_0	[kN]	$U(21.5, 32.3)$
Curving velocity	V	[m/s]	$U(1.9, 3.6)$
Nominal radius of the wheel	Rw	[m]	0.33
Transverse curve radius of the wheel	Rwt	[m]	0
Transverse curve radius of the rail	Rrt	[m]	0.230
Contact position on the wheel	$[x \ y \ z]$	[mm]	$[0 \ U(-8.3, -1.7) \ 0.16]$
Contact position on the rail	$[x \ y \ z]$	[mm]	$[0 \ 3.5 \ -0.5]$
Contact angle between wheel/rail	θ	[°]	$U(-3.3, -2.3)$
Longitudinal creepage	γ_{10}	-	$U(-0.00025, -0.00016)$
Lateral creepage	γ_{20}	-	$U(-0.0638, -0.0425)$
Spin creepage	γ_{60}	[1/m]	Eq.(6.74)
Coloumb coefficient	μ	-	0.4
Falling ratio	λ	-	$U(0.04, 0.06)$
Saturation coefficient	κ	-	0.8

Table 6.3: Input parameters at contact point on the tread of the outer front wheel.

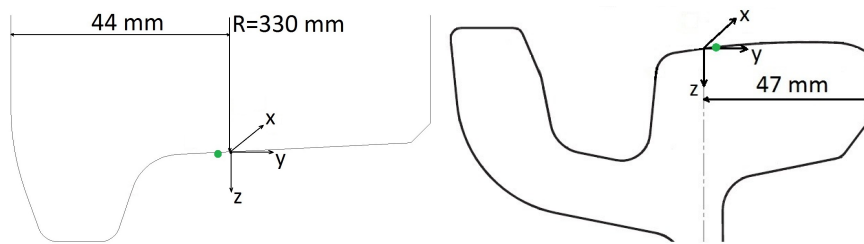


Figure 6.13: Contact point position on the outer front wheel and inner rail.

Also in this case, the model predicts unstable frequencies (see the black dots in Figure 6.14) that are close to measured ones (see Figure 6.15). The same consideration as before can be proposed again here in a similar way. The only thing that changes from before is the shift of some frequencies that is more visible.

In this sense, it is peculiar to observe that the predicted frequency range 1320-1353 Hz is correlated to the modes 1271 Hz and 1417 Hz. It has been seen that if one of the two modes is highly damped the unstable frequency still appears (see Figure 6.16 and 6.17), but if one of the two modes is suppressed the predicted frequency disappears (see Figure 6.18 and 6.19). Therefore, since the two modes are close, it is possible that it is a coupling between them that will result in unstable eigenvalues. Also this coupling between modes may play an important role in explaining the frequency shift.

Furthermore, Table 6.4 highlights the presence of two predicted unstable frequency ranges that seem not to be correlated with any mode shape (2359-2424 Hz and 3630-3634 Hz). To understand this, while considering the range 2359-2424 Hz the following tests have been done. A wheel with increased damping ratio at 2224 Hz has been first considered and the predicted frequencies are reported in Figure 6.20. It is interesting to observe that the frequency range 2303-2358 Hz related to the mode at 2224 Hz and the range 2359-2424 Hz have disappeared. Considering a wheel with increased damping ratio at 2475 Hz the predicted frequencies are reported in Figure 6.21. In this case, it is peculiar to observe that the predicted frequency range 2484-2503 Hz related to the modes 2475 and 2536 Hz is shifted to a range 2527-2542 Hz because the mode 2536 Hz persists, but that the range 2359-2424 Hz has disappeared. Therefore, this suggests that the frequency range 2359-2424 Hz occurs only if the frequencies at 2224 Hz and 2475 Hz are predicted by the model. To understand better what happens in this situation, from an eigenvalues point of view, a particular set of input parameters from Table 6.3 has been chosen and Nyquist plots of the eigenvalues of the open loop transfer function are shown in Figure 6.22. Note that since the model considers more than one degree of freedom at the contact, only the eigenvalue with highest magnitude is used to perform the Nyquist plot; the response would be dominated by this eigenvalue. The first part shows the real and imaginary part of highest magnitude eigenvalue for all the frequency steps. Red crosses indicate the possible instabilities. The second part is a zoom of the first one in a frequency range between 2200 Hz and 2500 Hz. From this last graph, it can be observed that there are three unstable points, one identified with the circle created by the mode at 2224 Hz, one identified with the circle created by the mode at 2475 Hz and the third crossing point between these two. This is the reason why there is a predicted unstable frequency in the range 2359-2424 Hz that is not correlated with any mode shape.

In the same way, it can be said that the frequencies in range 3630-3635 Hz occur only if the modes at 3569 Hz and 3680 Hz are excited.

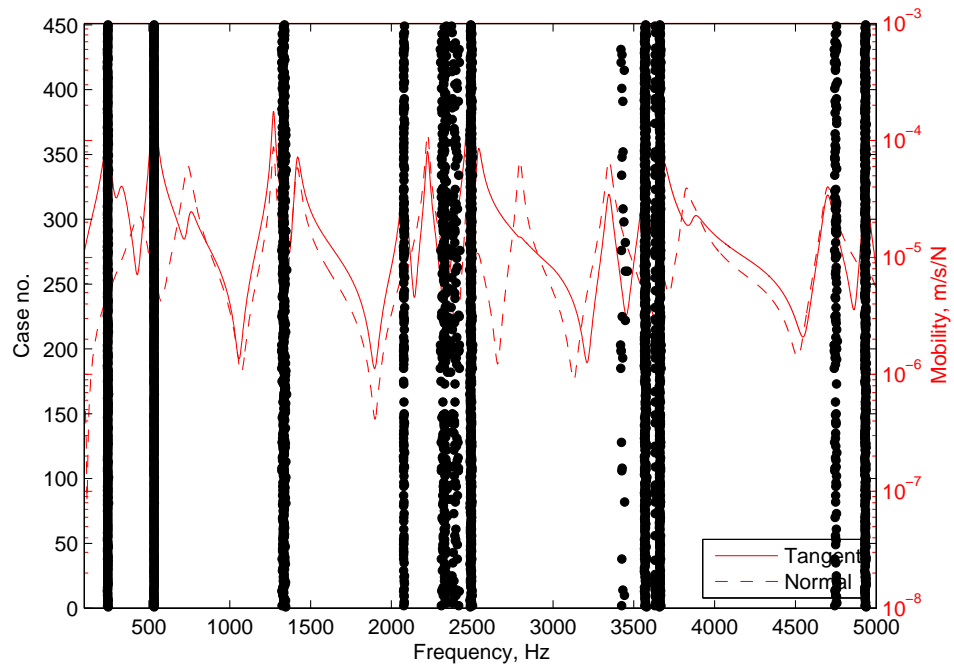


Figure 6.14: Curve squeal occurrences diagram for the outer front wheel.

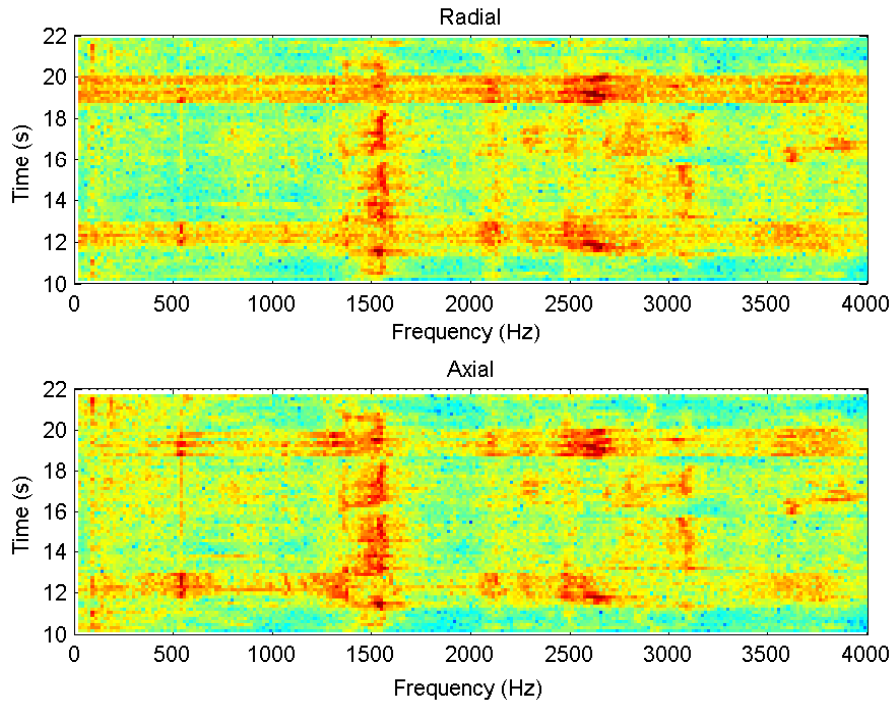


Figure 6.15: Spectrogram of outer front wheel vibration acceleration during tram pass-by.

Numerical modes involved in squeal	Frequency range predicted by model	Experimental frequencies involved in squeal
242 Hz	242 - 250 Hz	
529 Hz	530 - 534 Hz	around 530 Hz
1271 Hz, 1417 Hz	1320 - 1353 Hz	around 1330 Hz
2078 Hz	2075 - 2082 Hz	around 2100 Hz
2224 Hz	2303 - 2358 Hz	around 2300 Hz
	2359 - 2424 Hz	
2475 Hz, 2536 Hz	2484 - 2503 Hz	around 2550 Hz
3346 Hz	3418 - 3460 Hz	
3569 Hz	3565 - 3581 Hz	around 3600 Hz
	3630 - 3634 Hz	
3680 Hz	3656 - 3669 Hz	around 3700 Hz
4697 Hz	4739 - 4760 Hz	
4934 Hz	4928 - 4939 Hz	

Table 6.4: Numerical modes involved in squeal compared with the experimental frequencies involved in squeal and frequency range predicted by the model.

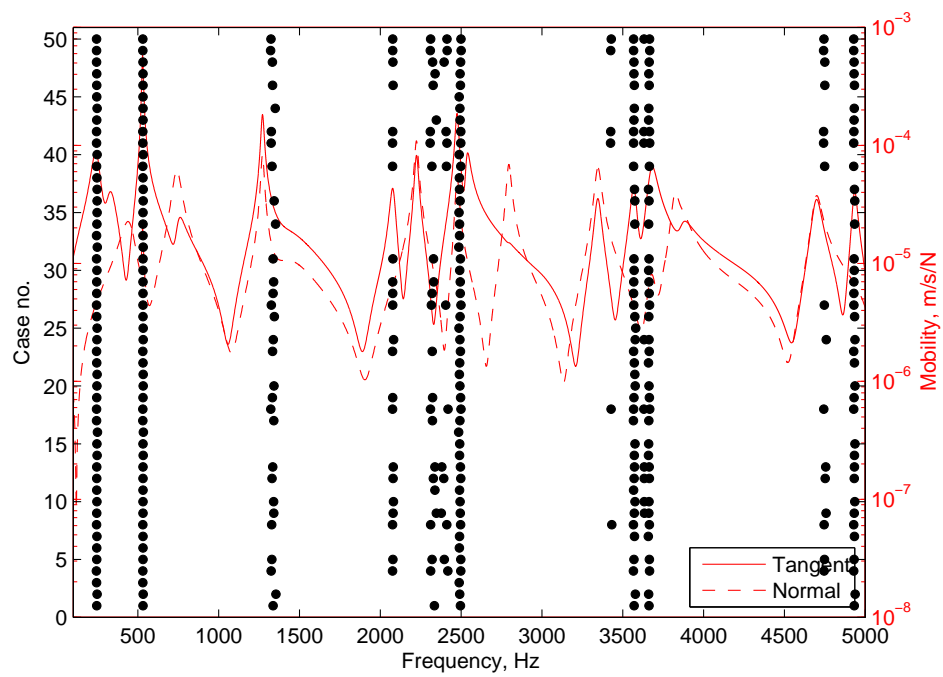


Figure 6.16: Curve squeal occurrences diagram for the outer front wheel in case with increased damping ratio at 1271 Hz.

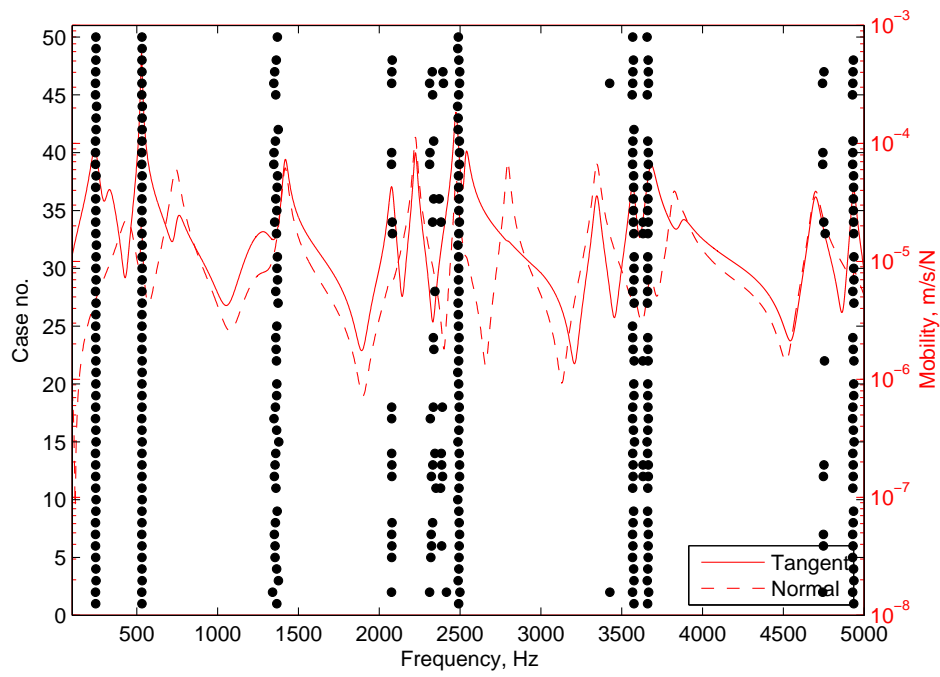


Figure 6.17: Curve squeal occurrences diagram for the outer front wheel in case with increased damping ratio at 1417 Hz.

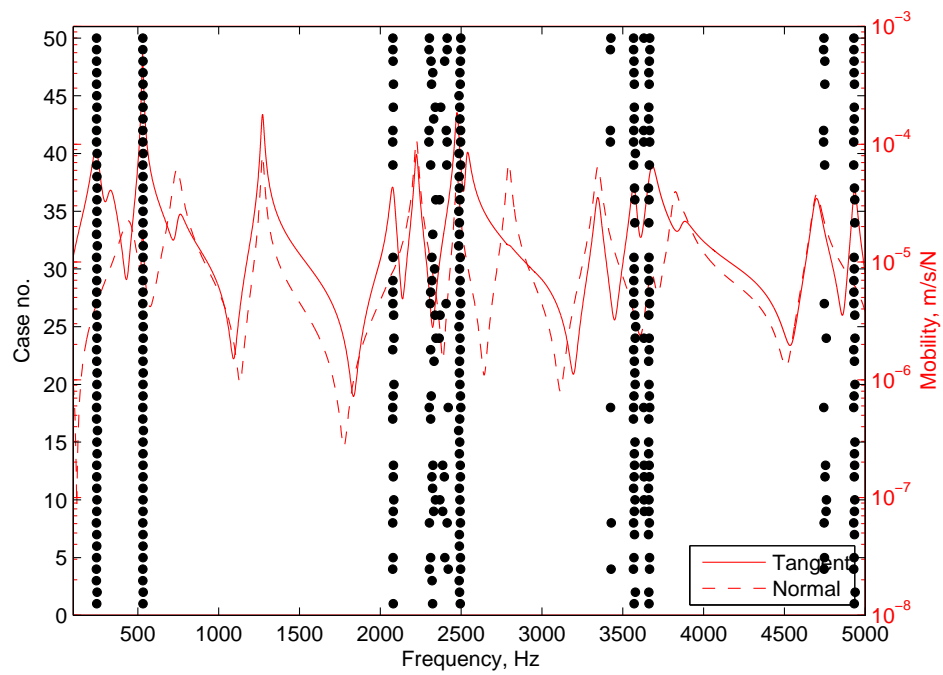


Figure 6.18: Curve squeal occurrences diagram for the outer front wheel in case with the mode at 1271 Hz suppressed.

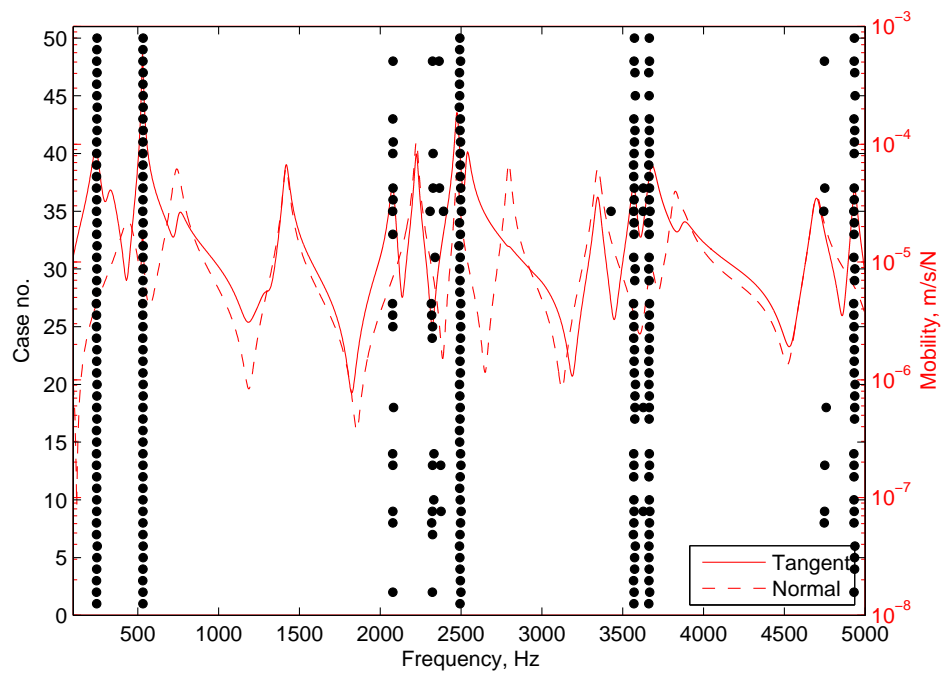


Figure 6.19: Curve squeal occurrences diagram for the outer front wheel in case with the mode at 1417 Hz suppressed.

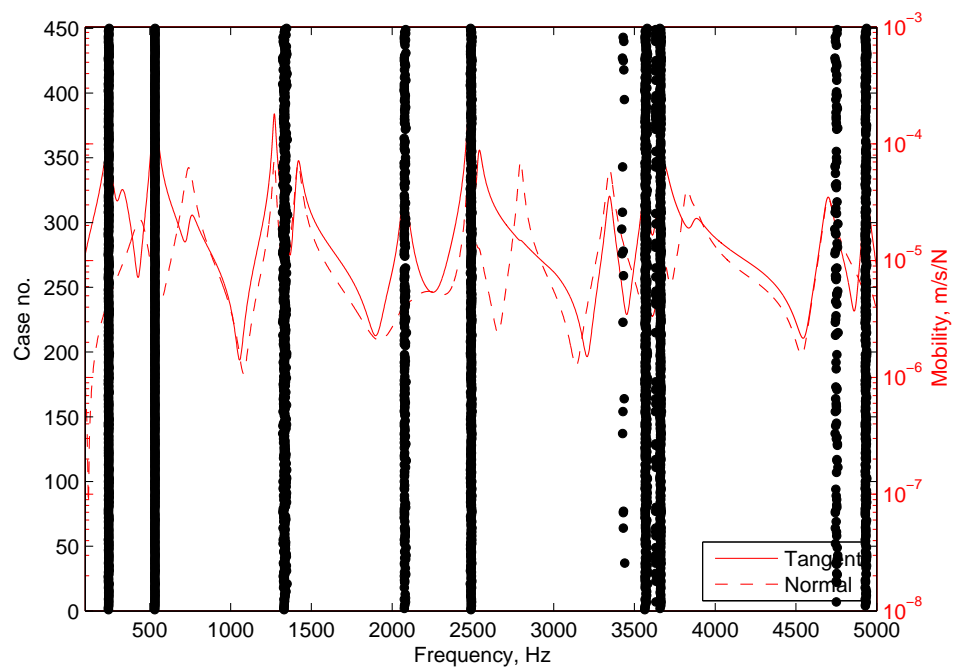


Figure 6.20: Curve squeal occurrences diagram for the outer front wheel in case with increased damping ratio at 2224 Hz.

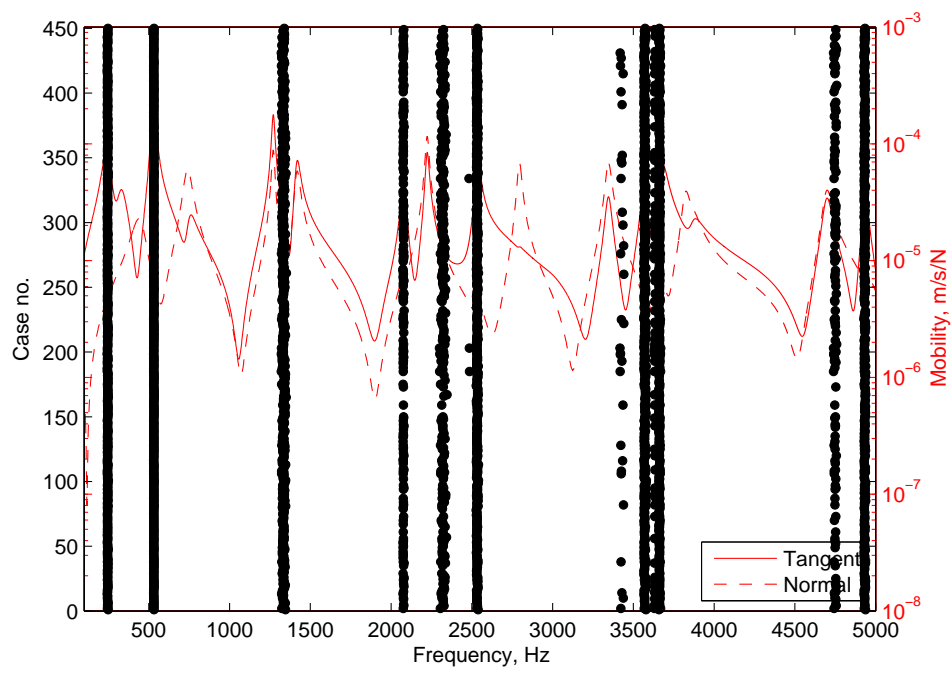


Figure 6.21: Curve squeal occurrences diagram for the outer front wheel in case with increased damping ratio at 2475 Hz.

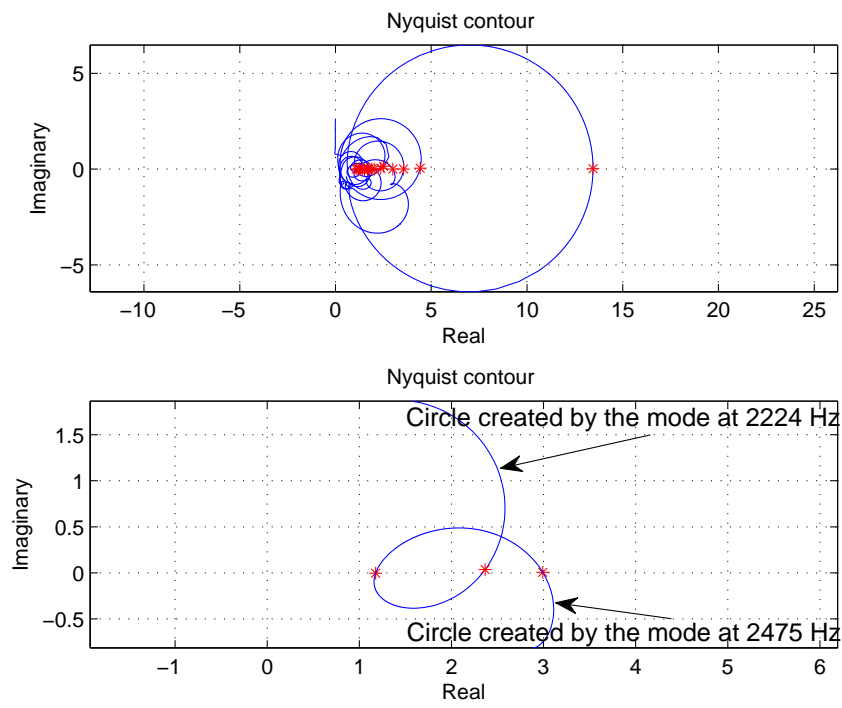


Figure 6.22: Nyquist plots of the eigenvalues.

6.6.3 On understanding the shift in frequency

In order to understand the visible shift in frequency mentioned before, it has been verified that neither the high damping values related to the resilient wheel nor the presence of the rail in the model can be considered responsible. Moreover it has also been measured that the position of the peaks in the wheel FRF is hardly influenced by the vehicle load (see Figure 2.23); therefore this also cannot explain the shift in frequency.

Focusing on the numerical results obtained from the outer front wheel of the Sirio with gauge of 1450 mm, different tests have been performed in order to understand the shift in frequency related to the mode at 1271 Hz. By looking at the results in Figure 6.14, it can be seen that the mode excited at 529 Hz does not present a shift in predicted unstable frequency. The first hypothesis to explain this it is that the displacement direction of the mode shape occurs along the same direction of the tangent at the contact point (see numerical mode at 529 Hz in Figure 6.23) along which the friction force works. For this reason, by fictitiously changing the contact angle following exactly the mode shape direction of the modes at 1417 Hz and 1271 Hz, no frequency shift is expect for those modes. Figure 6.23 reports the contact angle used to assess frequency shift for modes at 1271 Hz and 1417 Hz. The former has a ratio between radial and axial modal displacement that will result in an angle equal to 30° while the latter will give an angle of nearly -45° . It is important to note that in reality these contact angles cannot physically appear at the contact point shown in the drawings but they can be used to understand better the results shown so far.

Predicted frequencies are reported in Figures 6.24 and 6.25 for the case with contact angle at 30° and -45° , respectively. In each case only the mode displacing with the contact angle is excited and no shift in frequency appears.

By looking at Figure 6.24, it is interesting also to observe that the mode at 529 Hz remains excited but the predicted unstable frequencies vary within 536-541 Hz, slightly shifted compared with the one represented in Figure 6.14. In the same way, since the mode at 2224 Hz has a mode shape similar to the mode at 1271 Hz, it is expected that the predicted frequency range reported in Figure 6.14 becomes smaller and equal to the mode at 2224 Hz. Figure 6.24 confirms. In contrast, in Figure 6.25, the unstable frequency at 529 Hz disappears while a new predicted frequency related to a mode at 740 Hz arises. Of course this mode has a mode shape at the contact point more aligned with the direction of the contact force.

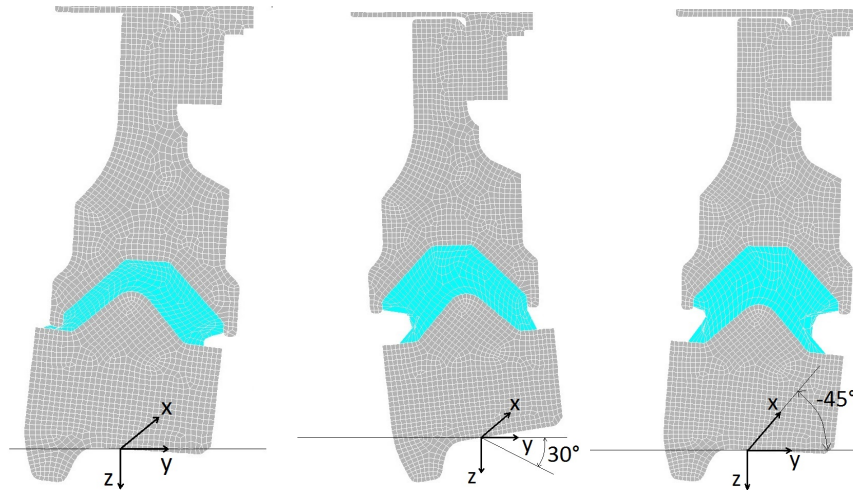


Figure 6.23: First one: numerical mode at 529 Hz. Second one: numerical mode at 1271 Hz. Third one: numerical mode at 1417 Hz.

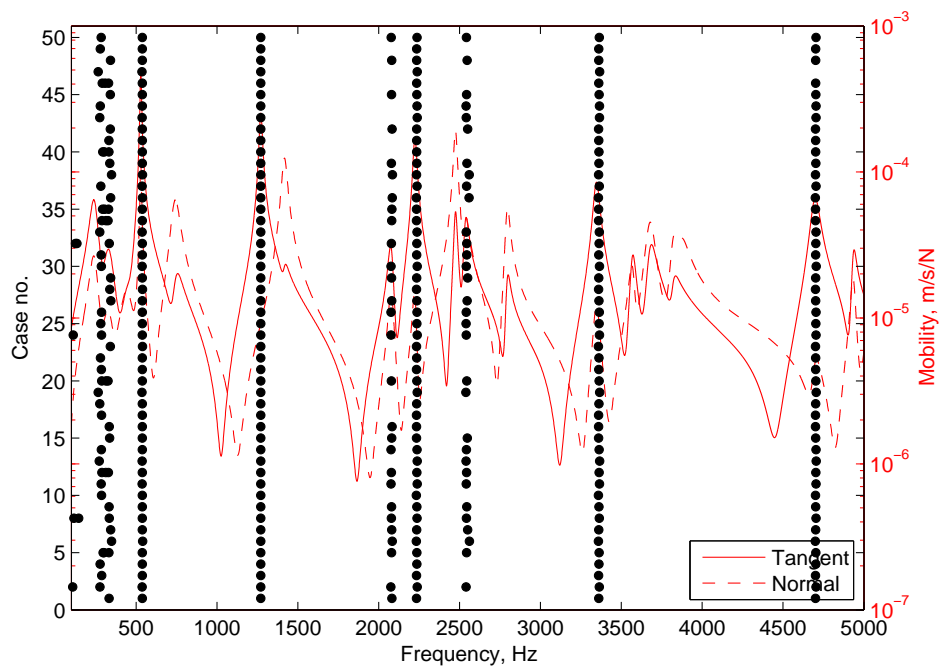


Figure 6.24: Curve squeal occurrences diagram for the outer front wheel with contact angle between wheel and rail of 30° .

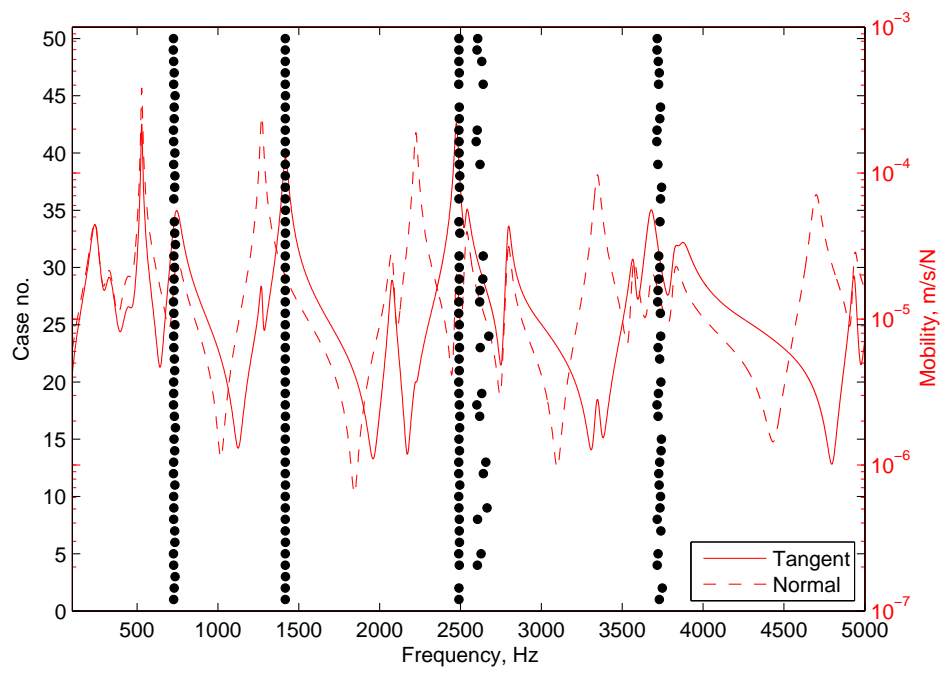


Figure 6.25: Curve squeal occurrences diagram for the outer front wheel with contact angle between wheel and rail of -45° .

The modes at 1270 Hz and at 1420 Hz are likely to be excited together, the peaks are close and the predicted unstable frequency range is due to both.

In order to understand better the shift in frequency in terms of eigenvalues, a particular set of input parameters from the Table 6.3 has been chosen and Nyquist plots of the eigenvalues of the open loop transfer function are now discussed for the three cases of Figure 6.23. Figure 6.26 refers to the case with the real contact angle between wheel and rail, while Figures 6.27 and 6.28 refer to the cases with contact angle of 30° and -45° , respectively. Each of the figures presents two Nyquist plots. The first one shows the real and imaginary part of highest magnitude eigenvalue for all frequencies. Red crosses indicate the possible instabilities. The second is a zoom of the first one in a frequency range between 1000 Hz and 2000 Hz. Only the modes at 1270 Hz and 1420 Hz are highlighted and the position of their natural frequencies is marked with green circles. The case with contact angle of -2.8° (Figure 6.26) shows that the two modes contribute to create the circle that is crossing the real axis at 1334 Hz (red cross). The shift in frequency happens because the two modes behave as coupled when the contact force acts in a direction which does not support just one specific mode. On the other hand, Figure 6.27 shows that if the direction of the contact force is meant to excite just one specific mode (1270 Hz in this case), the other mode is not contributing to modify the circle of the Nyquist plot; natural frequency and unstable frequency are very close one to another. Exactly the same happens with the mode at 1420 Hz in Figure 6.28.

Finally, Figure 6.29 shows the Nyquist plots of eigenvalues for the case with the real contact angle between wheel and rail and the mode at 1417 Hz suppressed. By looking the Figure, the circle created by the mode at 1271 Hz crosses the real axis at a frequency shifted from the real frequency of this mode (marked with green circles) because the contact force acts in a direction which does not support the mode. Moreover, since the contribution of the mode at 1417 Hz is suppressed, the mode at 1271 Hz alone is not able to be unstable, in fact the circle crosses the real axis before the real value 1.

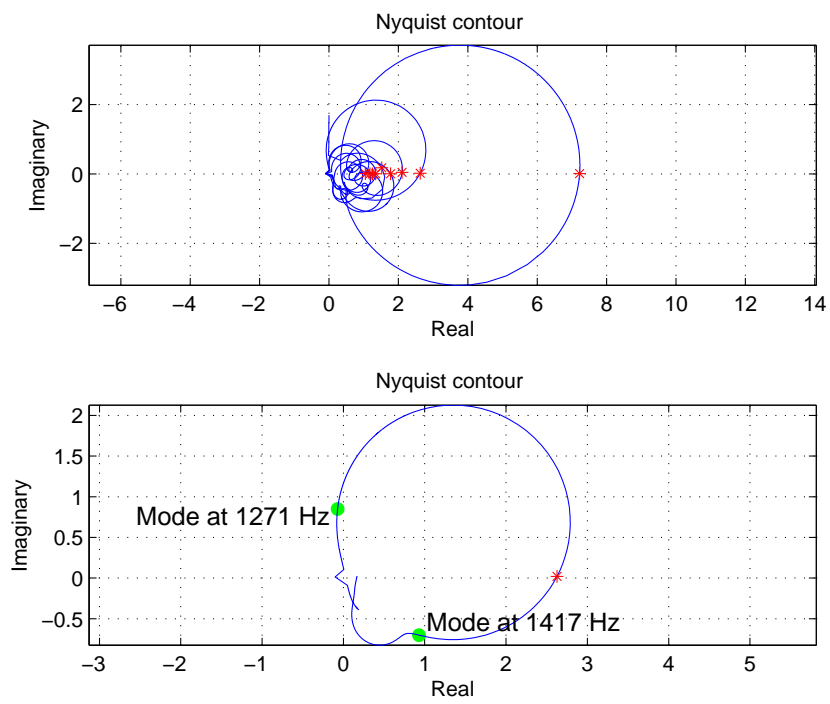


Figure 6.26: Nyquist plots of the eigenvalues in the case with the real contact angle between wheel and rail.

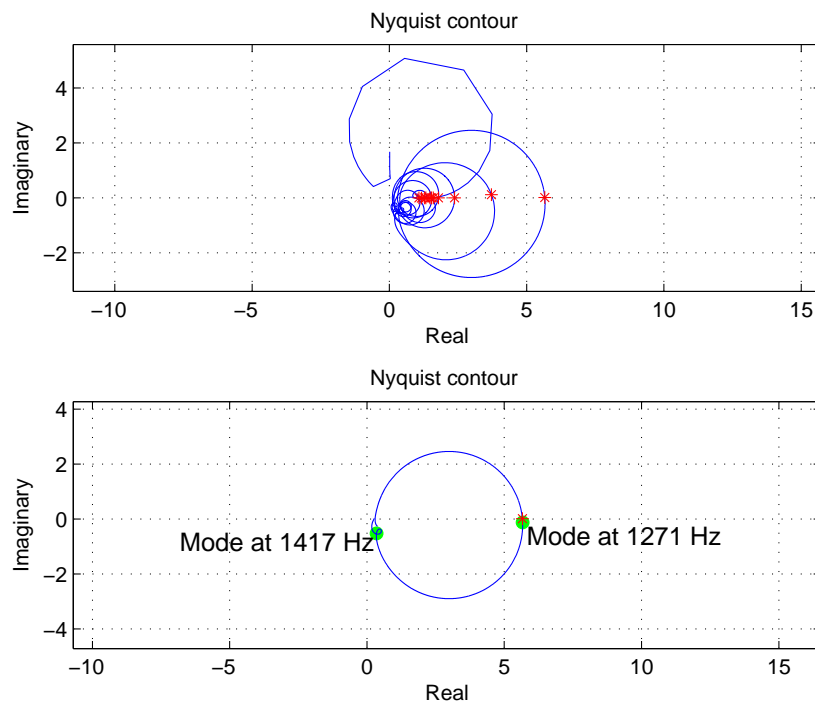


Figure 6.27: Nyquist plots of the eigenvalues in the case with contact angle of 30°

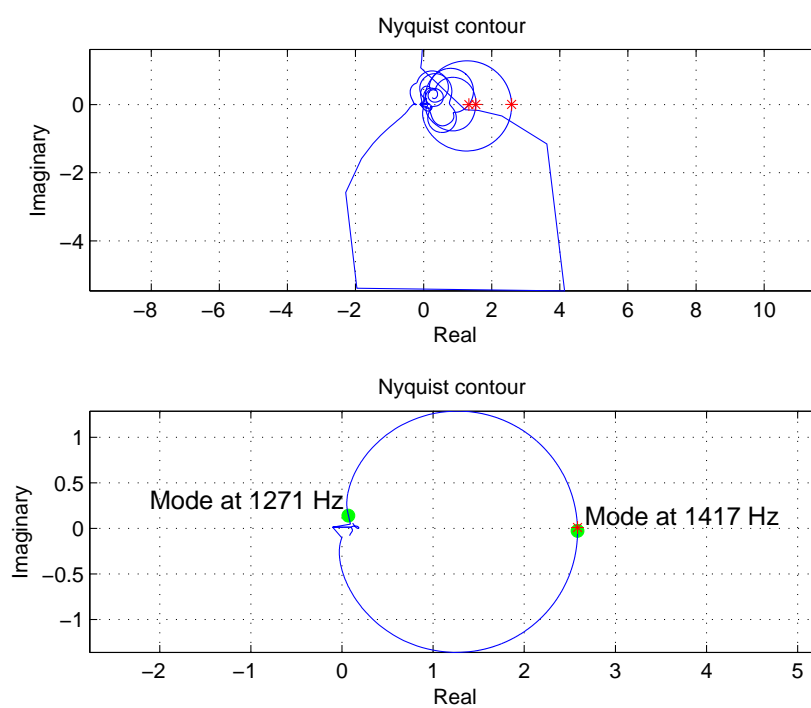


Figure 6.28: Nyquist plots of the eigenvalues in the case with contact angle of -45°

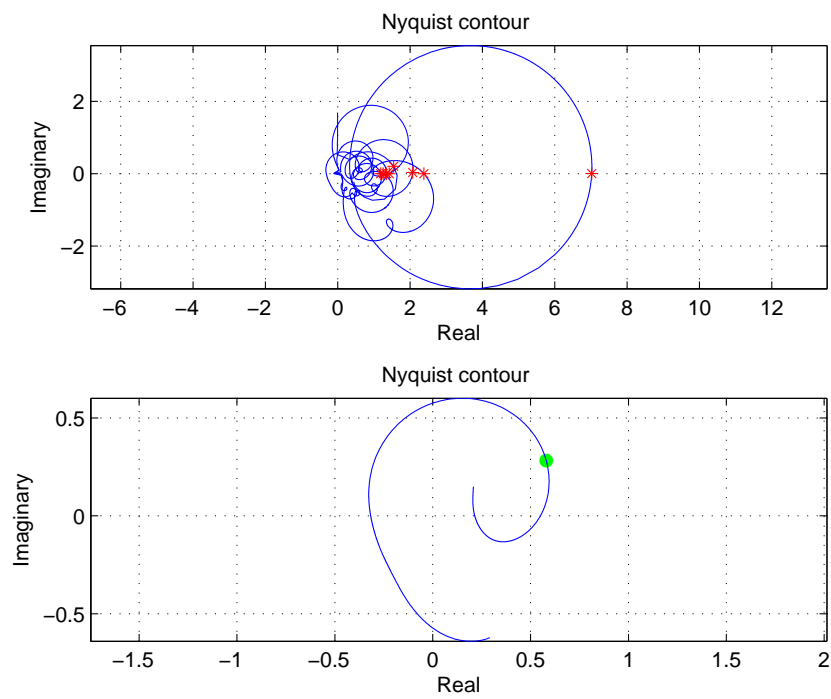


Figure 6.29: Nyquist plots of the eigenvalues in the case with the real contact angle between wheel and rail and the mode at 1417 Hz suppressed.

6.6.4 Analysis in time domain

As discussed before, since a time domain simulation needs more computation time than a frequency-domain simulation, only one case has been calculated to have an idea which frequency is really involved in the squeal phenomenon and to estimate vibration and noise levels. To perform the simulation, a set of input parameters has been chosen from the sets of parameters listed in Table 6.1 used to analyze the occurrences of squeal noise in the frequency domain for the inner front wheel of the Sirio with a gauge of 1445 mm.

In order to run a time domain simulation, the dynamic properties of the wheel and rail described in state space form are required. In particular, the state space matrices of the rail, as discussed before, have previously been determined considering only the direct terms of the mobilities (longitudinal, lateral, vertical and spin direction), but this is not consistent with the mobilities matrix of the rail used in the time domain simulation where also the cross mobilities have been taken into account. Therefore, in order to have the time and frequency domain more coherent from a coupling terms point of view, before running the simulation a small improvement has been taken into account in order to consider the effect of the cross mobilities in the state space matrix of the rail. To do that, for each mobility curve described in Eq.(6.21), it is possible, to find an equivalent system with a transfer function expressed in the form of ratio of two polynomials (see Eq.(6.59)). Then, after having collected the obtained transfer functions in matrix form:

$$[G(s)] = \begin{bmatrix} H_{11} & H_{12} & H_{13} & H_{16} \\ H_{21} & H_{22} & H_{23} & H_{26} \\ H_{31} & H_{32} & H_{33} & H_{36} \\ H_{61} & H_{62} & H_{63} & H_{66} \end{bmatrix}, \quad (6.75)$$

by means of the ‘*ss*’function of MATLAB, it is possible, from the transfer function matrix $[G(s)]$, calculate the system matrix $[A^r]$ and the input and output matrices $[B^r]$ and $[C^r]$ to represent the complete state space model of the rail.

Considering the improved state space matrices of the rail, a time domain simulation has been performed and the results are shown in Figures 6.30, 6.31 and 6.32. By looking at the first two, it is evident that the most important frequency involved in squeal noise is related to the axial mode at 529 Hz. To understand this better, the Nyquist stability analysis is reported in Figure 6.33. This Figure

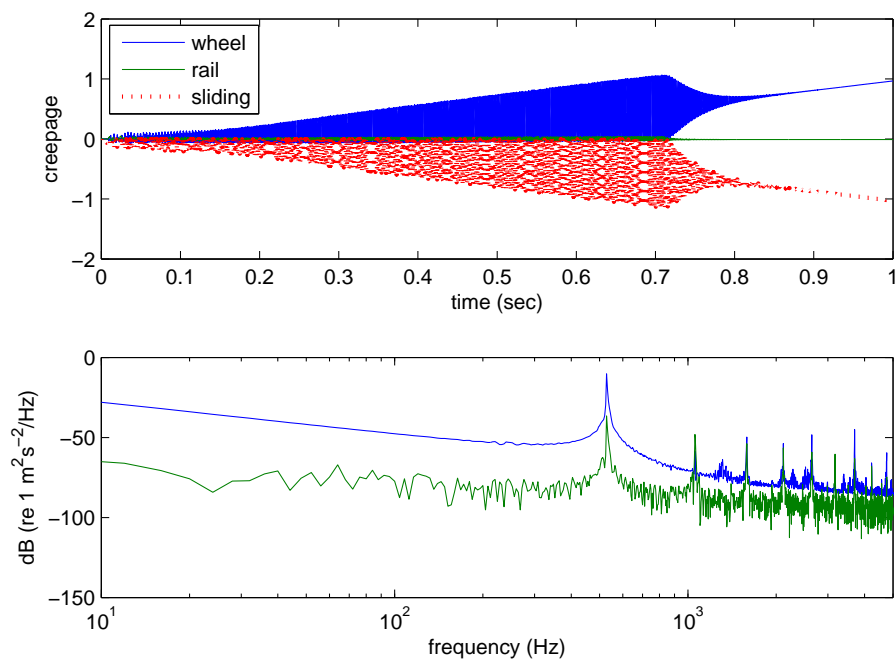


Figure 6.30: Lateral responses of the wheel and rail at the contact position, First Figure: lateral dynamic velocities of the wheel, rail and sliding velocity between wheel and rail, normalized by the vehicle speed V_0 , Second Figure: spectra of the lateral responses of the wheel and rail.

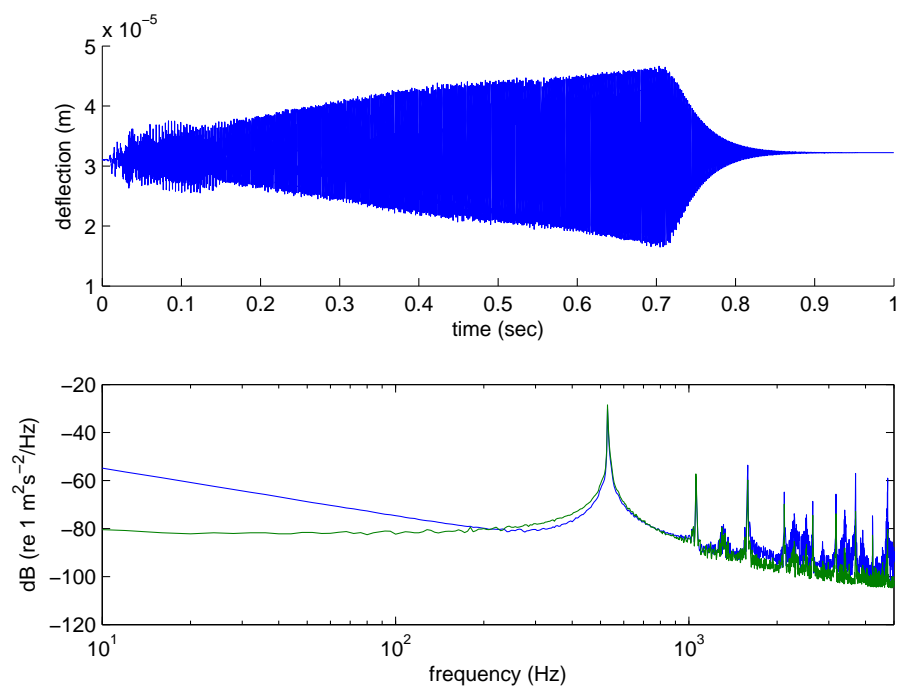


Figure 6.31: Vertical responses of the wheel and rail at the contact position, First Figure: vertical deflection between wheel and rail; Second Figure: spectra of vertical responses of the wheel and rail.

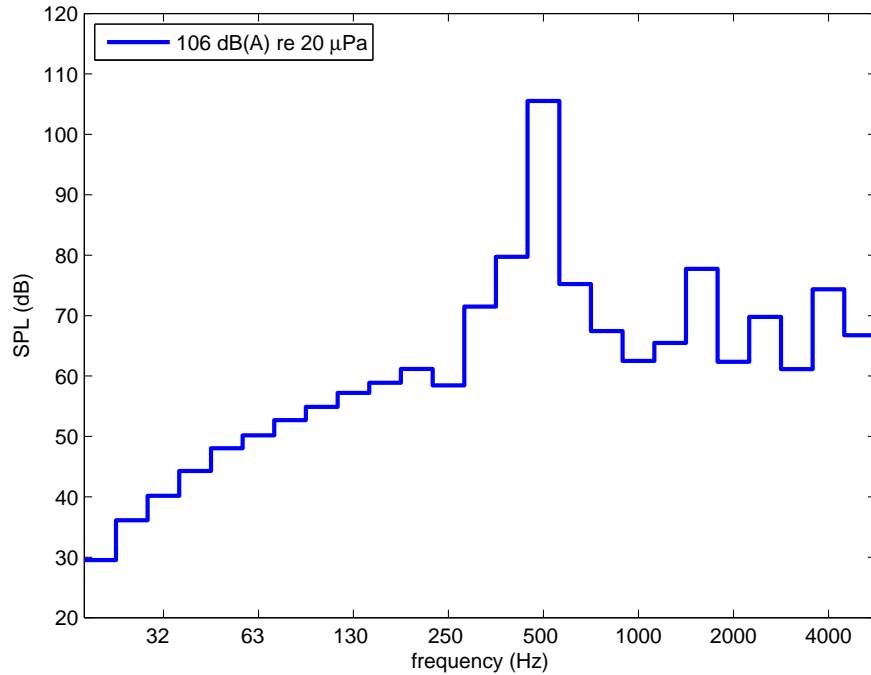


Figure 6.32: Noise radiation from the wheel: A-weighted SPL.

shows, as discussed in section 6.3.2, the Nyquist contour of eigenvalues, the maximum modulus of the eigenvalues calculated for each frequency (Bode diagram) and the predicted unstable frequencies (indicated with red points). By looking at the Figure, it is evident that the modulus of the eigenvalue related to 529 Hz is higher than the other ones; therefore, this may be the reason for the fact that the frequency at 529 Hz is dominant in the time domain simulation.

By looking at Figure 6.30, it is interesting also to observe that the other contributions at 1056, 1588, 2116, 2644, 3172 and 3700 Hz are likely to be harmonic multiples of 529 Hz which appear due to the non-linearity of the phenomenon.

The reason why the most important frequency involved in squeal noise is related to the axial mode at 529 Hz, is due to the fact that the particular contact condition of the wheel is such as to excite the axial modes. In particular, this axial mode at 529 Hz is the most likely to be excited because the displacement direction of the mode shape occurs along the same direction of the contact tangent between wheel and rail (see Figure 6.23).

The acoustic radiation of the wheel can be calculated using the method introduced by Thompson and Jones [48] as used by Huang [3]. In calculating the

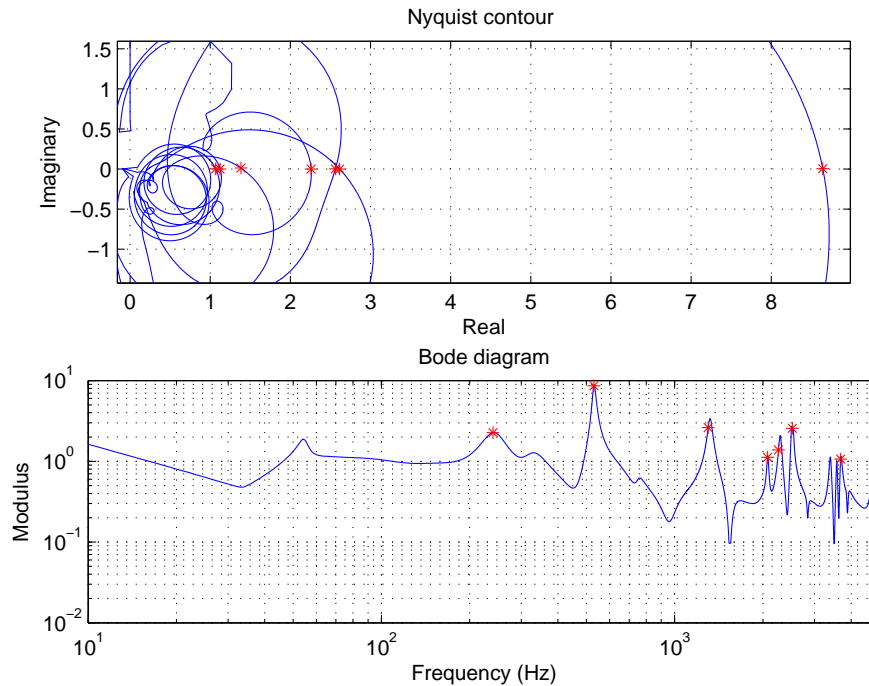


Figure 6.33: Nyquist stability analysis. First figure: Nyquist plots of the eigenvalues. Second figure: modulus of the Bode diagram of eigenvalues. Red points: unstable frequencies.

sound pressure, the wheel is assumed to be a point source and the directivity of sound radiation is not considered here. The sound pressure level (SPL) is evaluated at a position 7.5 metres from the sound source. The radiation from the rail is neglected.

The noise radiation in Figure 6.32 shows that the dominant frequency at 530 Hz determines the overall SPL.

Finally, another time domain simulation has been performed with the contact angle fictitiously changed following exactly the mode shape direction of the mode at 1271 Hz (see Figure 6.23). From the simulation, it is expected that the eigenvalue related at the predicted unstable frequency at 1271 Hz is higher than the other ones, and therefore that this frequency is dominant in the time domain results. The reason why the mainly frequency involved in squeal noise is expected to be related to the mode at 1271 Hz, is due to the fact that the displacement direction of the mode shape occurs along the same direction of the contact tangent between wheel and rail (see Figure 6.23).

Chapter 7

Squeal model for two contact points

The squeal noise phenomenon, as discussed in Chapter 6, can be described as a general self-excited vibration loop that takes into account the wheel/rail rolling contact dynamics and wheel and rail structural dynamics. Basically, it allows the squeal noise phenomenon to be predicted at two different levels: an analysis in the frequency domain studies the stability of the self-excited vibration loop identifying which wheel modes are prone to squeal, while an analysis in the time domain identifies the frequencies that are actually involved in the squeal noise generation estimating then vibration and noise levels.

The model developed by Huang [3] considers only one contact point between wheel and rail. However there are several examples where the simultaneous presence of more than one contact point happens. Typically the front outer wheel of a bogie goes into contact with the rail running head, while the flange back of the front inner wheel can be in contact with the rail grooved head (or check rail); and this can happen when the wheel tread is still in contact with the rail running head. This Chapter describes how, within the research work developed for the present thesis, the model described in Chapter 6 has been extended to consider the simultaneous presence of two contact points.

7.1 Analysis in frequency domain

In order to predict the squeal noise phenomenon the relation that defines the mobilities as the ratio between the dynamic sliding velocities and the dynamic friction forces at the considered contact point (see Eq.(6.25)) and the equation that expresses the dynamic friction force as a function of the creepages (see Eq.(6.17)) are fundamental to obtain the self-excited vibration loop necessary to analyze the stability in the frequency domain.

The mobility matrices have to be extended considering the mobilities at the second contact point and the cross-mobilities between the two contact points, while the relation between the friction forces and creepages, as described in Eq.(6.17), has to be obtained separately at the two contact points. Below the procedure to obtain the extended self-excited vibration loop is described.



Figure 7.1: Typical wheel/rail contact position: (a) nominal contact position P_0 , (b) flange (P_2) and tread (P_1) contact positions during left curve negotiation

Adopting the reference frame in the nominal contact point shown in Figure 7.1(a) and considering the wheel/rail contact condition described in Figure 7.1(b) in quasi-steady condition, the dynamic forces and velocities at these two contact points in lateral, longitudinal, vertical and spin directions can be converted into frequency responses assuming that they are harmonically oscillating at frequency ω :

$$f_{i,1} = F_{i,1} e^{j\omega t}, \quad v_{i,1}^w = V_{i,1}^w e^{j\omega t}, \quad v_{i,1}^r = V_{i,1}^r e^{j\omega t}, \quad v_{3,1}^c = V_{3,1}^c e^{j\omega t}, \quad v_{i,1}^s = V_{i,1}^s e^{j\omega t}, \quad (7.1)$$

$$f_{i,2} = F_{i,2} e^{j\omega t}, \quad v_{i,2}^w = V_{i,2}^w e^{j\omega t}, \quad v_{i,2}^r = V_{i,2}^r e^{j\omega t}, \quad v_{3,2}^c = V_{3,2}^c e^{j\omega t}, \quad v_{i,2}^s = V_{i,2}^s e^{j\omega t}, \quad (7.2)$$

$$i = 1, 2, 3, 6.$$

To describe the relation between the dynamic sliding velocities and the dynamic

friction forces at the two contact points, the mobilities of the wheel, rail and contact spring of each contact point have to be determined.

For the wheel this gives:

$$\begin{Bmatrix} \bar{V}_1^w \\ \bar{V}_2^w \end{Bmatrix} = - \begin{bmatrix} [Y_{ik,11}^w] & [Y_{ik,12}^w] \\ [Y_{ik,21}^w] & [Y_{ik,22}^w] \end{bmatrix} \begin{Bmatrix} \bar{F}_1 \\ \bar{F}_2 \end{Bmatrix}, \quad (7.3)$$

which in expanded form can be rewritten as:

$$\begin{Bmatrix} V_{1,1}^w \\ V_{2,1}^w \\ V_{3,1}^w \\ V_{6,1}^w \\ V_{1,2}^w \\ V_{2,2}^w \\ V_{3,2}^w \\ V_{6,2}^w \end{Bmatrix} = - \begin{bmatrix} Y_{11,11}^w & Y_{12,11}^w & Y_{13,11}^w & Y_{16,11}^w & Y_{11,12}^w & Y_{12,12}^w & Y_{13,12}^w & Y_{16,12}^w \\ Y_{21,11}^w & Y_{22,11}^w & Y_{23,11}^w & Y_{26,11}^w & Y_{21,12}^w & Y_{22,12}^w & Y_{23,12}^w & Y_{26,12}^w \\ Y_{31,11}^w & Y_{32,11}^w & Y_{33,11}^w & Y_{36,11}^w & Y_{31,12}^w & Y_{32,12}^w & Y_{33,12}^w & Y_{36,12}^w \\ Y_{61,11}^w & Y_{62,11}^w & Y_{63,11}^w & Y_{66,11}^w & Y_{61,12}^w & Y_{62,12}^w & Y_{63,12}^w & Y_{66,12}^w \\ Y_{11,21}^w & Y_{12,21}^w & Y_{13,21}^w & Y_{16,21}^w & Y_{11,22}^w & Y_{12,22}^w & Y_{13,22}^w & Y_{16,22}^w \\ Y_{21,21}^w & Y_{22,21}^w & Y_{23,21}^w & Y_{26,21}^w & Y_{21,22}^w & Y_{22,22}^w & Y_{23,22}^w & Y_{26,22}^w \\ Y_{31,21}^w & Y_{32,21}^w & Y_{33,21}^w & Y_{36,21}^w & Y_{31,22}^w & Y_{32,22}^w & Y_{33,22}^w & Y_{36,22}^w \\ Y_{61,21}^w & Y_{62,21}^w & Y_{63,21}^w & Y_{66,21}^w & Y_{61,22}^w & Y_{62,22}^w & Y_{63,22}^w & Y_{66,22}^w \end{bmatrix} \begin{Bmatrix} F_{1,1} \\ F_{2,1} \\ F_{3,1} \\ F_{6,1} \\ F_{1,2} \\ F_{2,2} \\ F_{3,2} \\ F_{6,2} \end{Bmatrix}, \quad (7.4)$$

where \bar{V}_1^w , \bar{V}_2^w and \bar{F}_1 , \bar{F}_2 are respectively the velocities and the friction forces at the two contact points while $[Y_{ik,11}^w]$ and $[Y_{ik,22}^w]$ are the mobilities at the two contact points and $[Y_{ik,12}^w]$ the cross-mobilities between them.

In order to obtain the mobilities that link together the dynamic sliding velocities with the dynamic friction forces, the modal matrices in the two new contact points have to be determined.

If $[\phi]_0$ is the matrix that contains the mode shapes at the nominal contact point, the two equivalent matrices $[\phi]_1$ and $[\phi]_2$ at the two actual contact points can be expressed as:

$$[\Phi]_1 = [T_{rot}]_1 [T_{off}]_1 [\Phi]_0 \equiv [T_{tot}]_1 [\Phi]_0, \quad (7.5)$$

$$[\Phi]_2 = [T_{rot}]_2 [T_{off}]_2 [\Phi]_0 \equiv [T_{tot}]_2 [\Phi]_0, \quad (7.6)$$

where the translation matrices $[T_{off}]_1$ and $[T_{off}]_2$, defined in Eq.(A.3), are the matrices that translate the modal matrix $[\Phi]_0$ at point P_0 to the new positions P_1 and P_2 . Similarly the rotation matrices $[T_{rot}]_1$ and $[T_{rot}]_2$, defined in Eq.(A.4), represent the matrices that rotate, by an angle θ_1 and θ_2 , the reference frame at the positions P_1 and P_2 around the local x_1 -axis and x_2 -axis to give the new modal

matrices $[\Phi]_1$ and $[\Phi]_2$, while the total transformation matrices are indicated as $[T_{tot}]_1$ and $[T_{tot}]_2$.

Once the mode shape amplitudes at the two contact points have been obtained, Eq.(6.20), used to calculate the wheel mobilities for the case of one contact point, can be rewritten considering two contact points as:

$$Y_{ik,ab}^w(\omega) = \sum_n \frac{j\omega\phi_{in,a}\phi_{kn,b}}{m_n(\omega_n^2 - \omega^2 + 2j\zeta_n\omega\omega_n)}, \quad (7.7)$$

$$a = 1, 2, \quad b = 1, 2,$$

$$i = 1, 2, 3, 6,$$

$$k = 1, 2, 3, 6,$$

where $\phi_{in,a}$ is the mode shape amplitude of mode n at the contact point a (1 or 2) in direction i , $\phi_{ik,b}$ is the mode shape amplitude of mode n at the contact point b (1 or 2) in direction k , m_n is the modal mass, ζ_n is the modal damping ratio and ω_n is the natural frequency.

For the rail, Eqs.(7.3) and (7.4) can be rewritten as:

$$\begin{Bmatrix} \bar{V}_1^r \\ \bar{V}_2^r \end{Bmatrix} = \begin{bmatrix} Y_{ik,11}^r & Y_{ik,12}^r \\ Y_{ik,21}^r & Y_{ik,22}^r \end{bmatrix} \begin{Bmatrix} \bar{F}_1 \\ \bar{F}_2 \end{Bmatrix}, \quad (7.8)$$

$$\begin{Bmatrix} V_{1,1}^r \\ V_{2,1}^r \\ V_{3,1}^r \\ V_{6,1}^r \\ V_{1,2}^r \\ V_{2,2}^r \\ V_{3,2}^r \\ V_{6,2}^r \end{Bmatrix} = \begin{array}{c|cccc|cccc} Y_{11,11}^r & Y_{12,11}^r & Y_{13,11}^r & Y_{16,11}^r & Y_{11,12}^r & Y_{12,12}^r & Y_{13,12}^r & Y_{16,12}^r \\ Y_{21,11}^r & Y_{22,11}^r & Y_{23,11}^r & Y_{26,11}^r & Y_{21,12}^r & Y_{22,12}^r & Y_{23,12}^r & Y_{26,12}^r \\ Y_{31,11}^r & Y_{32,11}^r & Y_{33,11}^r & Y_{36,11}^r & Y_{31,12}^r & Y_{32,12}^r & Y_{33,12}^r & Y_{36,12}^r \\ Y_{61,11}^r & Y_{62,11}^r & Y_{63,11}^r & Y_{66,11}^r & Y_{61,12}^r & Y_{62,12}^r & Y_{63,12}^r & Y_{66,12}^r \\ \hline Y_{11,21}^r & Y_{12,21}^r & Y_{13,21}^r & Y_{16,21}^r & Y_{11,22}^r & Y_{12,22}^r & Y_{13,22}^r & Y_{16,22}^r \\ Y_{21,21}^r & Y_{22,21}^r & Y_{23,21}^r & Y_{26,21}^r & Y_{21,22}^r & Y_{22,22}^r & Y_{23,22}^r & Y_{26,22}^r \\ Y_{31,21}^r & Y_{32,21}^r & Y_{33,21}^r & Y_{36,21}^r & Y_{31,22}^r & Y_{32,22}^r & Y_{33,22}^r & Y_{36,22}^r \\ Y_{61,21}^r & Y_{62,21}^r & Y_{63,21}^r & Y_{66,21}^r & Y_{61,22}^r & Y_{62,22}^r & Y_{63,22}^r & Y_{66,22}^r \end{array} \begin{Bmatrix} F_{1,1} \\ F_{2,1} \\ F_{3,1} \\ F_{6,1} \\ F_{1,2} \\ F_{2,2} \\ F_{3,2} \\ F_{6,2} \end{Bmatrix}, \quad (7.9)$$

where \bar{V}_1^r , \bar{V}_2^r and \bar{F}_1 , \bar{F}_2 are respectively the velocities and the friction forces at the two contact points while $[Y_{ik,11}^r]$ and $[Y_{ik,22}^r]$ are the mobilities at the two contact points and $[Y_{ik,12}^r]$ the cross-mobilities between them.

In this case, since only the mobilities at the nominal contact point but not the mode shapes are available, the mobilities $[Y_{ik,11}^r]$, $[Y_{ik,22}^r]$ and $[Y_{ik,12}^r]$ can only be obtained in terms of a mobility transformation.

Considering the case shown in Figure 7.1, the relation between the dynamic velocities and the dynamic friction forces at the nominal contact point P_0 can be written as:

$$\begin{Bmatrix} V_1^r \\ V_2^r \\ \vdots \\ V_6^r \end{Bmatrix}_0 = \begin{bmatrix} Y_{11}^r & Y_{12}^r & \cdots & Y_{16}^r \\ Y_{21}^r & Y_{22}^r & \cdots & Y_{26}^r \\ \vdots & \vdots & \ddots & \vdots \\ Y_{61}^r & Y_{62}^r & \cdots & Y_{66}^r \end{bmatrix}_0 \begin{Bmatrix} F_1 \\ F_2 \\ \vdots \\ F_6 \end{Bmatrix}_0, \quad (7.10)$$

$$\bar{V}_0^r = [Y_{ik,0}^r] \bar{F}_0, \quad (7.11)$$

where the matrix $[Y_{ik,0}^r]$ contains the rail mobilities at the nominal contact point P_0 . Adopting the total transformation matrices $[T_{tot}]_1$ and $[T_{tot}]_2$, obtained in Eqs.(7.5) and (7.6), the dynamic velocities and the dynamic friction forces used in Eq.(7.10) can be transformed and redefined at the two new contact points of the rail as:

$$\bar{V}_1^r = [T_{tot}]_1 \bar{V}_0^r, \quad \bar{V}_2^r = [T_{tot}]_2 \bar{V}_0^r, \quad \Rightarrow \bar{V}_0^r = [T_{tot}]_1^{-1} \bar{V}_1^r = [T_{tot}]_2^{-1} \bar{V}_2^r, \quad (7.12)$$

$$\bar{F}_1 = [T_{tot}]_1^{-T} \bar{F}_0, \quad \bar{F}_2 = [T_{tot}]_2^{-T} \bar{F}_0, \quad \Rightarrow \bar{F}_0 = [T_{tot}]_1^T \bar{F}_1 = [T_{tot}]_2^T \bar{F}_2. \quad (7.13)$$

Now, if the forces \bar{F}_1 and \bar{F}_2 at the two contact points are known, by means Eq.(7.13), the equivalent force \bar{F}_0 can be written as the sum of the transformation of \bar{F}_1 and \bar{F}_2 at the nominal contact point:

$$\bar{F}_0 = [T_{tot}]_1^T \bar{F}_1 + [T_{tot}]_2^T \bar{F}_2. \quad (7.14)$$

Substituting Eqs.(7.12) (considered one at a time) and (7.14) in Eq.(7.11), it is possible to obtain the dynamic velocities at point P_1 and P_2 considering the effect of the forces at the two contact points:

$$\bar{V}_1^r = [T_{tot}]_1 [Y_{ik}^r]_0 [T_{tot}]_1^T \bar{F}_1 + [T_{tot}]_1 [Y_{ik}^r]_0 [T_{tot}]_2^T \bar{F}_2 = [Y_{ik,11}^r] \bar{F}_1 + [Y_{ik,12}^r] \bar{F}_2, \quad (7.15)$$

$$\bar{V}_2^r = [T_{tot}]_2 [Y_{ik}^r]_0 [T_{tot}]_1^T \bar{F}_1 + [T_{tot}]_2 [Y_{ik}^r]_0 [T_{tot}]_2^T \bar{F}_2 = [Y_{ik,21}^r] \bar{F}_1 + [Y_{ik,22}^r] \bar{F}_2, \quad (7.16)$$

where the matrices $[Y_{ik,11}^r]$, $[Y_{ik,22}^r]$, $[Y_{ik,12}^r]$:

$$[Y_{ik,11}^r] = [T_{tot}]_1 [Y_{ik,0}^r] [T_{tot}]_1^T = [T_{tot}]_1 \begin{bmatrix} Y_{11}^r & Y_{12}^r & \cdots & Y_{16}^r \\ Y_{21}^r & Y_{22}^r & \cdots & Y_{26}^r \\ \vdots & \vdots & \ddots & \vdots \\ Y_{61}^r & Y_{62}^r & \cdots & Y_{66}^r \end{bmatrix}_0 [T_{tot}]_1^T, \quad (7.17)$$

$$[Y_{ik,22}^r] = [T_{tot}]_2 [Y_{ik,0}^r] [T_{tot}]_2^T = [T_{tot}]_2 \begin{bmatrix} Y_{11}^r & Y_{12}^r & \cdots & Y_{16}^r \\ Y_{21}^r & Y_{22}^r & \cdots & Y_{26}^r \\ \vdots & \vdots & \ddots & \vdots \\ Y_{61}^r & Y_{62}^r & \cdots & Y_{66}^r \end{bmatrix}_0 [T_{tot}]_2^T, \quad (7.18)$$

$$[Y_{ik,12}^r] = [Y_{ik,21}^r] = [T_{tot}]_1 [Y_{ik,0}^r] [T_{tot}]_2^T = [T_{tot}]_1 \begin{bmatrix} Y_{11}^r & Y_{12}^r & \cdots & Y_{16}^r \\ Y_{21}^r & Y_{22}^r & \cdots & Y_{26}^r \\ \vdots & \vdots & \ddots & \vdots \\ Y_{61}^r & Y_{62}^r & \cdots & Y_{66}^r \end{bmatrix}_0 [T_{tot}]_2^T, \quad (7.19)$$

indicate the mobilities at the two contact points ($[Y_{ik,11}^r]$ and $[Y_{ik,22}^r]$) and cross-mobilities between them ($[Y_{ik,12}^r]$). These matrices describe the total relation between sliding velocities and friction forces defined in Eq.(7.9).

Finally, for the contact spring the vertical velocities at the two contact points can be expressed as:

$$V_{3,1}^c = Y_{33,11}^c F_{3,1}, \quad (7.20)$$

$$V_{3,2}^c = Y_{33,22}^c F_{3,2}. \quad (7.21)$$

The mobilities of the vertical contact springs $Y_{33,11}^c$ and $Y_{33,22}^c$ can be written as:

$$Y_{33,11}^c = \frac{j\omega}{k_{H,1}}, \quad (7.22)$$

$$Y_{33,22}^c = \frac{j\omega}{k_{H,2}}, \quad (7.23)$$

where $k_{H,1}$ and $k_{H,2}$ indicate the stiffness of the two contact springs.

According to Eq.(6.24), the amplitudes of the sliding velocities considering

two contact points are:

$$\begin{pmatrix} V_{1,1}^s \\ V_{2,1}^s \\ V_{3,1}^s \\ V_{6,1}^s \\ V_{1,2}^s \\ V_{2,2}^s \\ V_{3,2}^s \\ V_{6,2}^s \end{pmatrix} \equiv \begin{pmatrix} V_{1,1}^r \\ V_{2,1}^r \\ V_{3,1}^r \\ V_{6,1}^r \\ V_{1,2}^r \\ V_{2,2}^r \\ V_{3,2}^r \\ V_{6,2}^r \end{pmatrix} - \begin{pmatrix} V_{1,1}^w \\ V_{2,1}^w \\ V_{3,1}^w \\ V_{6,1}^w \\ V_{1,2}^w \\ V_{2,2}^w \\ V_{3,2}^w \\ V_{6,2}^w \end{pmatrix} + \begin{pmatrix} 0 \\ 0 \\ V_{3,1}^c \\ 0 \\ 0 \\ 0 \\ V_{3,2}^c \\ 0 \end{pmatrix}. \quad (7.24)$$

Substituting Eqs.(7.4), (7.9), (7.20) and (7.21) into Eq.(7.24), the total relation between the dynamic sliding velocities and the dynamic forces considering two contact points can be written as:

$$\begin{Bmatrix} \bar{V}_1^s \\ \bar{V}_2^s \end{Bmatrix} = \begin{bmatrix} [Y_{ik,11}] & [Y_{ik,12}] \\ [Y_{ik,21}] & [Y_{ik,22}] \end{bmatrix} \begin{Bmatrix} \bar{F}_1 \\ \bar{F}_2 \end{Bmatrix}, \quad (7.25)$$

which in expanded form can be rewritten as:

$$\begin{pmatrix} V_{1,1}^s \\ V_{2,1}^s \\ V_{3,1}^s \\ V_{6,1}^s \\ V_{1,2}^s \\ V_{2,2}^s \\ V_{3,2}^s \\ V_{6,2}^s \end{pmatrix} = \begin{bmatrix} Y_{11,11} & Y_{12,11} & Y_{13,11} & Y_{16,11} & Y_{11,12} & Y_{12,12} & Y_{13,12} & Y_{16,12} \\ Y_{21,11} & Y_{22,11} & Y_{23,11} & Y_{26,11} & Y_{21,12} & Y_{22,12} & Y_{23,12} & Y_{26,12} \\ Y_{31,11} & Y_{32,11} & Y_{33,11} & Y_{36,11} & Y_{31,12} & Y_{32,12} & Y_{33,12} & Y_{36,12} \\ Y_{61,11} & Y_{62,11} & Y_{63,11} & Y_{66,11} & Y_{61,12} & Y_{62,12} & Y_{63,12} & Y_{66,12} \\ Y_{11,21} & Y_{12,21} & Y_{13,21} & Y_{16,21} & Y_{11,22} & Y_{12,22} & Y_{13,22} & Y_{16,22} \\ Y_{21,21} & Y_{22,21} & Y_{23,21} & Y_{26,21} & Y_{21,22} & Y_{22,22} & Y_{23,22} & Y_{26,22} \\ Y_{31,21} & Y_{32,21} & Y_{33,21} & Y_{36,21} & Y_{31,22} & Y_{32,22} & Y_{33,22} & Y_{36,22} \\ Y_{61,21} & Y_{62,21} & Y_{63,21} & Y_{66,21} & Y_{61,22} & Y_{62,22} & Y_{63,22} & Y_{66,22} \end{bmatrix} \begin{pmatrix} F_{1,1} \\ F_{2,1} \\ F_{3,1} \\ F_{6,1} \\ F_{1,2} \\ F_{2,2} \\ F_{3,2} \\ F_{6,2} \end{pmatrix}, \quad (7.26)$$

where $[Y_{ik,11}]$ and $[Y_{ik,22}]$ are the mobilities at the two contact points, $[Y_{ik,12}]$ the cross-mobilities between them while each term $Y_{ik,ab}$ of these submatrices can be described as the sum of mobilities of wheel, rail, and contact spring:

$$Y_{ik,ab} = Y_{ik,ab}^w + Y_{ik,ab}^r + Y_{ik,ab}^c,$$

$$a = 1, 2, \quad b = 1, 2.$$

\bar{V}_1^s , \bar{V}_2^s and \bar{F}_1 , \bar{F}_2 are respectively the sliding velocities and the friction forces at the two contact points.

In this relation, the vertical sliding velocities at the two contact points are equal to zero:

$$\begin{aligned} V_{3,1}^s &= Y_{31,11}F_{1,1} + Y_{32,11}F_{2,1} + Y_{33,11}F_{3,1} + Y_{36,11}F_{6,1} + \\ &+ Y_{31,12}F_{1,2} + Y_{32,12}F_{2,2} + Y_{33,12}F_{3,2} + Y_{36,12}F_{6,2} = 0, \end{aligned} \quad (7.27)$$

$$\begin{aligned} V_{3,2}^s &= Y_{31,21}F_{1,1} + Y_{32,21}F_{2,1} + Y_{33,21}F_{3,1} + Y_{36,21}F_{6,1} + \\ &+ Y_{31,22}F_{1,2} + Y_{32,22}F_{2,2} + Y_{33,22}F_{3,2} + Y_{36,22}F_{6,2} = 0, \end{aligned} \quad (7.28)$$

therefore this allows $V_{3,1}^s$ and $V_{3,2}^s$ to be eliminated from Eq.(7.26) that can be rewritten as:

$$\underbrace{\begin{pmatrix} V_{1,1}^s \\ V_{2,1}^s \\ V_{6,1}^s \\ V_{1,2}^s \\ V_{2,2}^s \\ V_{6,2}^s \end{pmatrix}}_{\bar{V}^s} = \underbrace{\begin{bmatrix} Y_{11,11} & Y_{12,11} & Y_{16,11} & Y_{11,12} & Y_{12,12} & Y_{16,12} \\ Y_{21,11} & Y_{22,11} & Y_{26,11} & Y_{21,12} & Y_{22,12} & Y_{26,12} \\ Y_{61,11} & Y_{62,11} & Y_{66,11} & Y_{61,12} & Y_{62,12} & Y_{66,12} \\ Y_{11,21} & Y_{12,21} & Y_{16,21} & Y_{11,22} & Y_{12,22} & Y_{16,22} \\ Y_{21,21} & Y_{22,21} & Y_{26,21} & Y_{21,22} & Y_{22,22} & Y_{26,22} \\ Y_{61,21} & Y_{62,21} & Y_{66,21} & Y_{61,22} & Y_{62,22} & Y_{66,22} \end{bmatrix}}_{[C]} \underbrace{\begin{pmatrix} F_{1,1} \\ F_{2,1} \\ F_{6,1} \\ F_{1,2} \\ F_{2,2} \\ F_{6,2} \end{pmatrix}}_{\bar{F}} + \underbrace{\begin{pmatrix} Y_{13,11} \\ Y_{23,11} \\ Y_{63,11} \\ Y_{13,21} \\ Y_{23,21} \\ Y_{63,21} \end{pmatrix}}_{\bar{d}_1} F_{3,1} + \underbrace{\begin{pmatrix} Y_{13,12} \\ Y_{23,12} \\ Y_{63,12} \\ Y_{13,22} \\ Y_{23,22} \\ Y_{63,22} \end{pmatrix}}_{\bar{d}_2} F_{3,2} = \quad (7.29)$$

$$= [C]\bar{F} + \bar{d}_1 F_{3,1} + \bar{d}_2 F_{3,2}. \quad (7.30)$$

From Eqs.(7.27) and (7.28) it is possible to express the vertical dynamic forces $F_{3,1}$ and $F_{3,2}$ in terms of the other six dynamic friction forces. Below, the steps to define these forces are described.

First of all, the force $F_{3,1}$ is obtained from the Eq.(7.27), while the force $F_{3,2}$ is

expressed from Eq.(7.28):

$$\begin{aligned}
 F_{3,1} &= - \underbrace{\left\{ \begin{array}{cccccc} Y_{31,11} & Y_{32,11} & Y_{36,11} & Y_{31,12} & Y_{32,12} & Y_{36,12} \\ Y_{33,11} & Y_{33,11} & Y_{33,11} & Y_{33,11} & Y_{33,11} & Y_{33,11} \end{array} \right\}}_{\bar{a}_1^T} \underbrace{\left\{ \begin{array}{c} F_{1,1} \\ F_{2,1} \\ F_{6,1} \\ F_{1,2} \\ F_{2,2} \\ F_{6,2} \end{array} \right\}}_{\bar{F}} - \frac{Y_{33,12}}{Y_{33,11}} F_{3,2} = \\
 &= -\bar{a}_1^T \bar{F} - \frac{Y_{33,12}}{Y_{33,11}} F_{3,2}, \tag{7.31}
 \end{aligned}$$

$$\begin{aligned}
 F_{3,2} &= - \underbrace{\left\{ \begin{array}{cccccc} Y_{31,21} & Y_{32,21} & Y_{36,21} & Y_{31,22} & Y_{32,22} & Y_{36,22} \\ Y_{33,22} & Y_{33,22} & Y_{33,22} & Y_{33,22} & Y_{33,22} & Y_{33,22} \end{array} \right\}}_{\bar{a}_2^T} \underbrace{\left\{ \begin{array}{c} F_{1,1} \\ F_{2,1} \\ F_{6,1} \\ F_{1,2} \\ F_{2,2} \\ F_{6,2} \end{array} \right\}}_{\bar{F}} - \frac{Y_{33,21}}{Y_{33,22}} F_{3,1} = \\
 &= -\bar{a}_2^T \bar{F} - \frac{Y_{33,21}}{Y_{33,22}} F_{3,1}. \tag{7.32}
 \end{aligned}$$

Substituting the Eq.(7.32) into Eq.(7.31), the force $F_{3,1}$ can be expressed as:

$$F_{3,1} = \underbrace{\frac{Y_{33,11} Y_{33,22}}{Y_{33,11} Y_{33,22} - Y_{33,12}^2} \left(-\bar{a}_1^T + \frac{Y_{33,12}}{Y_{33,11}} \bar{a}_2^T \right)}_{\bar{b}_1^T} \bar{F} = \bar{b}_1^T \bar{F}, \tag{7.33}$$

while substituting the Eq.(7.31) into Eq.(7.32) the force $F_{3,2}$ can be obtained:

$$F_{3,2} = \underbrace{\frac{Y_{33,11} Y_{33,22}}{Y_{33,11} Y_{33,22} - Y_{33,12}^2} \left(-\bar{a}_2^T + \frac{Y_{33,21}}{Y_{33,22}} \bar{a}_1^T \right)}_{\bar{b}_2^T} \bar{F} = \bar{b}_2^T \bar{F}. \tag{7.34}$$

Finally, substituting Eqs.(7.33) and (7.34) into Eq.(7.30) it is possible to obtain the relation between the dynamic sliding velocities and dynamic friction forces

without considering the vertical sliding velocities $V_{3,1}^s$ and $V_{3,2}^s$:

$$\begin{aligned}\bar{V}^s &= [C]\bar{F} + \bar{d}_1\bar{b}_1^T\bar{F} + \bar{d}_2\bar{b}_2^T\bar{F} = \\ &= \underbrace{([C] + \bar{d}_1\bar{b}_1^T + \bar{d}_2\bar{b}_2^T)}_{[E]}\bar{F} = [E]\bar{F},\end{aligned}\quad (7.35)$$

where \bar{F} is formed of the friction forces and spin moment at the two contact points, \bar{V}^s includes the dynamic sliding velocities in the longitudinal, lateral and spin directions at the two contact points, while $[E]$ is the mobilities matrix.

Having obtained the matrix that links together sliding velocities and friction forces, in order to obtain the extended self-excited vibration loop, the relations between the friction forces and creepages have to be taken into account separately at the two contact points.

In accordance with Eq.(6.17), the relation between friction forces and creepages at the two contact points can be written as:

$$\begin{aligned}\begin{Bmatrix} f_{1,1} \\ f_{2,1} \\ f_{6,1} \end{Bmatrix} &= \begin{Bmatrix} f_{1tot,1} \\ f_{2tot,1} \\ f_{6tot,1} \end{Bmatrix} - \begin{Bmatrix} f_{10,1} \\ f_{20,1} \\ f_{60,1} \end{Bmatrix} = \\ &= \begin{Bmatrix} \mu_{1,1} \left(\gamma_{10,1} + \frac{v_{1,1}^s}{V_0}, \gamma_{20,1} + \frac{v_{2,1}^s}{V_0}, \gamma_{60,1} + \frac{v_{6,1}^s}{V_0}, N_{0,1} + f_{3,1} \right) \\ \mu_{2,1} \left(\gamma_{10,1} + \frac{v_{1,1}^s}{V_0}, \gamma_{20,1} + \frac{v_{2,1}^s}{V_0}, \gamma_{60,1} + \frac{v_{6,1}^s}{V_0}, N_{0,1} + f_{3,1} \right) \\ \mu_{6,1} \left(\gamma_{10,1} + \frac{v_{1,1}^s}{V_0}, \gamma_{20,1} + \frac{v_{2,1}^s}{V_0}, \gamma_{60,1} + \frac{v_{6,1}^s}{V_0}, N_{0,1} + f_{3,1} \right) \end{Bmatrix} (N_{0,1} + f_{3,1}) - \\ &+ \begin{Bmatrix} \mu_{1,1} (\gamma_{10,1}, \gamma_{20,1}, \gamma_{60,1}, N_{0,1}) \\ \mu_{2,1} (\gamma_{10,1}, \gamma_{20,1}, \gamma_{60,1}, N_{0,1}) \\ \mu_{6,1} (\gamma_{10,1}, \gamma_{20,1}, \gamma_{60,1}, N_{0,1}) \end{Bmatrix} N_{0,1},\end{aligned}\quad (7.36)$$

$$\begin{Bmatrix} f_{1,2} \\ f_{2,2} \\ f_{6,2} \end{Bmatrix} = \begin{Bmatrix} f_{1tot,2} \\ f_{2tot,2} \\ f_{6tot,2} \end{Bmatrix} - \begin{Bmatrix} f_{10,2} \\ f_{20,2} \\ f_{60,2} \end{Bmatrix} =$$

$$\begin{aligned}
 &= \left\{ \begin{array}{l} \mu_{1,2} \left(\gamma_{10,2} + \frac{v_{1,2}^s}{V_0}, \gamma_{20,2} + \frac{v_{2,2}^s}{V_0}, \gamma_{60,2} + \frac{v_{6,2}^s}{V_0}, N_{0,2} + f_{3,2} \right) \\ \mu_{2,2} \left(\gamma_{10,2} + \frac{v_{1,2}^s}{V_0}, \gamma_{20,2} + \frac{v_{2,2}^s}{V_0}, \gamma_{60,2} + \frac{v_{6,2}^s}{V_0}, N_{0,2} + f_{3,2} \right) \\ \mu_{6,2} \left(\gamma_{10,2} + \frac{v_{1,2}^s}{V_0}, \gamma_{20,2} + \frac{v_{2,2}^s}{V_0}, \gamma_{60,2} + \frac{v_{6,2}^s}{V_0}, N_{0,2} + f_{3,2} \right) \end{array} \right\} (N_{0,2} + f_{3,2}) - \\
 &\quad + \left\{ \begin{array}{l} \mu_{1,2} (\gamma_{10,2}, \gamma_{20,2}, \gamma_{60,2}, N_{0,2}) \\ \mu_{2,2} (\gamma_{10,2}, \gamma_{20,2}, \gamma_{60,2}, N_{0,2}) \\ \mu_{6,2} (\gamma_{10,2}, \gamma_{20,2}, \gamma_{60,2}, N_{0,2}) \end{array} \right\} N_{0,2}, \quad (7.37)
 \end{aligned}$$

where the end of each term described in these equation is marked with the number 1 or 2 to indicate if it corresponds to the first or the second contact point. The meaning of each term is explained in section 6.1.1.

The friction equations obtained before can be linearized at the steady-state points $(\gamma_{10,1}, \gamma_{20,1}, \gamma_{60,1}, N_{0,1})$ and $(\gamma_{10,2}, \gamma_{20,2}, \gamma_{60,2}, N_{0,2})$ by assuming that the dynamic quantities are small and ignoring terms of second order in small quantities. Then assuming that the dynamic forces and dynamic sliding velocities are in harmonic form the relationships obtained can be converted into the frequency domain.

So, Eqs.(7.36) and (7.37) linearized at the steady-state points and converted into the frequency domain can be rewritten as:

$$\begin{Bmatrix} F_{1,1} \\ F_{2,1} \\ F_{6,1} \end{Bmatrix} = \frac{N_{0,1}}{V_0} \begin{bmatrix} \frac{\partial \mu_{1,1}}{\partial \gamma_{1,1}} & \frac{\partial \mu_{1,1}}{\partial \gamma_{2,1}} & \frac{\partial \mu_{1,1}}{\partial \gamma_{6,1}} & \frac{\partial \mu_{1,1}}{\partial f_{3,1}} \\ \frac{\partial \mu_{2,1}}{\partial \gamma_{1,1}} & \frac{\partial \mu_{2,1}}{\partial \gamma_{2,1}} & \frac{\partial \mu_{2,1}}{\partial \gamma_{6,1}} & \frac{\partial \mu_{2,1}}{\partial f_{3,1}} \\ \frac{\partial \mu_{6,1}}{\partial \gamma_{1,1}} & \frac{\partial \mu_{6,1}}{\partial \gamma_{2,1}} & \frac{\partial \mu_{6,1}}{\partial \gamma_{6,1}} & \frac{\partial \mu_{6,1}}{\partial f_{3,1}} \end{bmatrix} \begin{Bmatrix} V_{1,1}^s \\ V_{2,1}^s \\ V_{6,1}^s \\ V_0 F_{3,1} \end{Bmatrix} + \begin{Bmatrix} \mu_{1,1} \\ \mu_{2,1} \\ \mu_{6,1} \end{Bmatrix} F_{3,1}, \quad (7.38)$$

$$\begin{Bmatrix} F_{1,2} \\ F_{2,2} \\ F_{6,2} \end{Bmatrix} = \frac{N_{0,2}}{V_0} \begin{bmatrix} \frac{\partial \mu_{1,2}}{\partial \gamma_{1,2}} & \frac{\partial \mu_{1,2}}{\partial \gamma_{2,2}} & \frac{\partial \mu_{1,2}}{\partial \gamma_{6,2}} & \frac{\partial \mu_{1,2}}{\partial f_{3,2}} \\ \frac{\partial \mu_{2,2}}{\partial \gamma_{1,2}} & \frac{\partial \mu_{2,2}}{\partial \gamma_{2,2}} & \frac{\partial \mu_{2,2}}{\partial \gamma_{6,2}} & \frac{\partial \mu_{2,2}}{\partial f_{3,2}} \\ \frac{\partial \mu_{6,2}}{\partial \gamma_{1,2}} & \frac{\partial \mu_{6,2}}{\partial \gamma_{2,2}} & \frac{\partial \mu_{6,2}}{\partial \gamma_{6,2}} & \frac{\partial \mu_{6,2}}{\partial f_{3,2}} \end{bmatrix} \begin{Bmatrix} V_{1,2}^s \\ V_{2,2}^s \\ V_{6,2}^s \\ V_0 F_{3,2} \end{Bmatrix} + \begin{Bmatrix} \mu_{1,2} \\ \mu_{2,2} \\ \mu_{6,2} \end{Bmatrix} F_{3,2}. \quad (7.39)$$

The terms related to $F_{3,1}$ and $F_{3,2}$ can be collected together to give:

$$\begin{aligned} \begin{pmatrix} F_{1,1} \\ F_{2,1} \\ F_{6,1} \end{pmatrix} &= \frac{N_{0,1}}{V_0} \underbrace{\begin{bmatrix} \frac{\partial \mu_{1,1}}{\partial \gamma_{1,1}} & \frac{\partial \mu_{1,1}}{\partial \gamma_{2,1}} & \frac{\partial \mu_{1,1}}{\partial \gamma_{6,1}} \\ \frac{\partial \mu_{2,1}}{\partial \gamma_{1,1}} & \frac{\partial \mu_{2,1}}{\partial \gamma_{2,1}} & \frac{\partial \mu_{2,1}}{\partial \gamma_{6,1}} \\ \frac{\partial \mu_{6,1}}{\partial \gamma_{1,1}} & \frac{\partial \mu_{6,1}}{\partial \gamma_{2,1}} & \frac{\partial \mu_{6,1}}{\partial \gamma_{6,1}} \end{bmatrix}}_{[K_{1,a}]} \begin{pmatrix} V_{1,1}^s \\ V_{2,1}^s \\ V_{6,1}^s \end{pmatrix} + \underbrace{\begin{pmatrix} \mu_{1,1} + N_{0,1} \frac{\partial \mu_{1,1}}{\partial f_{3,1}} \\ \mu_{2,1} + N_{0,1} \frac{\partial \mu_{2,1}}{\partial f_{3,1}} \\ \mu_{6,1} + N_{0,1} \frac{\partial \mu_{6,1}}{\partial f_{3,1}} \end{pmatrix}}_{[K_{2,a}]} F_{3,1} = \\ &= [K_{1,a}] \begin{pmatrix} V_{1,1}^s \\ V_{2,1}^s \\ V_{6,1}^s \end{pmatrix} + [K_{2,a}] F_{3,1}, \end{aligned} \quad (7.40)$$

$$\begin{aligned} \begin{pmatrix} F_{1,2} \\ F_{2,2} \\ F_{6,2} \end{pmatrix} &= \frac{N_{0,2}}{V_0} \underbrace{\begin{bmatrix} \frac{\partial \mu_{1,2}}{\partial \gamma_{1,2}} & \frac{\partial \mu_{1,2}}{\partial \gamma_{2,2}} & \frac{\partial \mu_{1,2}}{\partial \gamma_{6,2}} \\ \frac{\partial \mu_{2,2}}{\partial \gamma_{1,2}} & \frac{\partial \mu_{2,2}}{\partial \gamma_{2,2}} & \frac{\partial \mu_{2,2}}{\partial \gamma_{6,2}} \\ \frac{\partial \mu_{6,2}}{\partial \gamma_{1,2}} & \frac{\partial \mu_{6,2}}{\partial \gamma_{2,2}} & \frac{\partial \mu_{6,2}}{\partial \gamma_{6,2}} \end{bmatrix}}_{[K_{1,b}]} \begin{pmatrix} V_{1,2}^s \\ V_{2,2}^s \\ V_{6,2}^s \end{pmatrix} + \underbrace{\begin{pmatrix} \mu_{1,2} + N_{0,2} \frac{\partial \mu_{1,2}}{\partial f_{3,2}} \\ \mu_{2,2} + N_{0,2} \frac{\partial \mu_{2,2}}{\partial f_{3,2}} \\ \mu_{6,2} + N_{0,2} \frac{\partial \mu_{6,2}}{\partial f_{3,2}} \end{pmatrix}}_{[K_{2,b}]} F_{3,2} = \\ &= [K_{1,b}] \begin{pmatrix} V_{1,2}^s \\ V_{2,2}^s \\ V_{6,2}^s \end{pmatrix} + [K_{2,b}] F_{3,2}, \end{aligned} \quad (7.41)$$

where the matrices $[K_{1,a}]$ and $[K_{1,b}]$ are formed of the derivatives of non-dimensional friction force with respect to creepages, while matrices $[K_{2,a}]$ and $[K_{2,b}]$ determine the influence from the fluctuation of vertical forces on the friction forces.

Eqs.(7.40) and (7.41) can be rewritten together in matrix form obtaining:

$$\bar{F} = \begin{pmatrix} F_{1,1} \\ F_{2,1} \\ F_{6,1} \\ F_{1,2} \\ F_{2,2} \\ F_{6,2} \end{pmatrix} = \underbrace{\begin{bmatrix} [K_{1,a}] & [0] \\ [0] & [K_{1,b}] \end{bmatrix}}_{[K_1]} \begin{pmatrix} V_{1,1}^s \\ V_{2,1}^s \\ V_{6,1}^s \\ V_{1,2}^s \\ V_{2,2}^s \\ V_{6,2}^s \end{pmatrix} + \underbrace{\begin{bmatrix} [K_{2,a}] & [0] \\ [0] & [K_{2,b}] \end{bmatrix}}_{[K_{2,c}]} \begin{pmatrix} F_{3,1} \\ F_{3,2} \end{pmatrix} = \quad (7.42)$$

$$= [K_1]\bar{V}^s + [K_{2,c}] \begin{Bmatrix} F_{3,1} \\ F_{3,2} \end{Bmatrix}. \quad (7.43)$$

Substituting Eqs.(7.33), (7.34) and (7.35) into Eq.(7.43) the relationship between the dynamic sliding velocities and dynamic friction forces can be rewritten as:

$$\bar{F} = [K_1][E]\bar{F} + [K_{2,c}] \underbrace{\begin{Bmatrix} \bar{b}_1^T \\ \bar{b}_2^T \end{Bmatrix}}_{[K_2]} \bar{F} = \quad (7.44)$$

$$= \underbrace{([K_1][E] + [K_2])}_{[R]} \bar{F} = [R]\bar{F}, \quad (7.45)$$

where $[Q] = ([K_1][E] + [K_2])$ is the new open-loop transfer function matrix of the MIMO system shown in Figure 7.2.

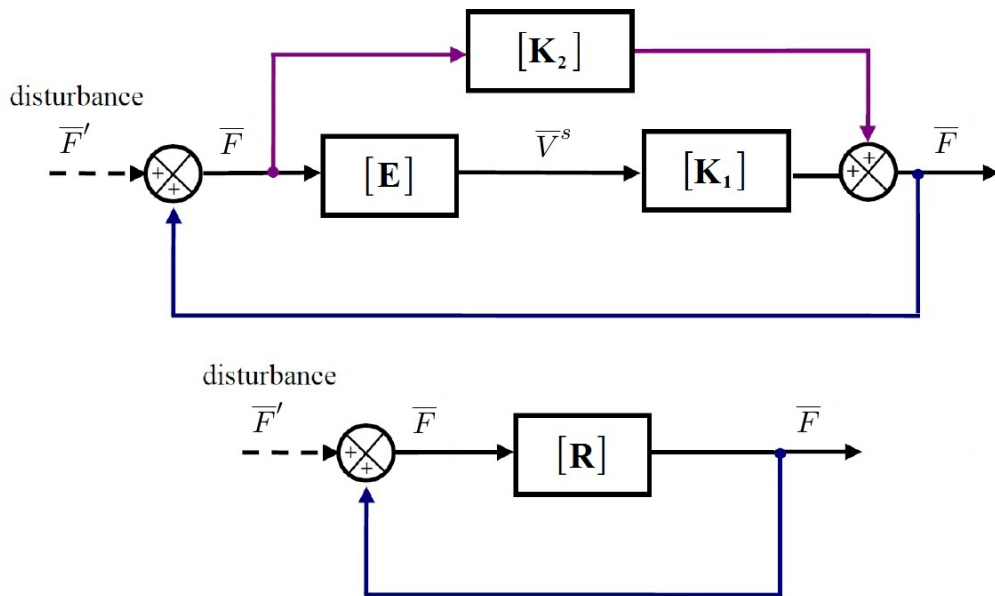


Figure 7.2: Frequency domain self-excited vibration loop of the wheel/rail contact system with two contact points.

Finally, in order to study the stability analysis in the frequency domain, the same method described in Chapter 6 is adopted.

7.2 Analysis in the time domain

During the development of the extended curve squeal software within this research work the possibility of solving the self-excited loop in the time domain has been explored and the theoretical model is described in this section. However, for the reasons explained below, a stable solution has not been found and the time domain results with two contact points cannot therefore be presented.

The method of step-by-step integration, as discussed in Chapter 6, is appropriate to study the squeal noise phenomenon in the time domain. This requires the dynamic properties of the wheel and rail to be described in state-space form.

In accordance with section 6.4.1, considering the modal parameters (damping ratio, natural frequencies and mode shapes) of the wheel obtained by means of the finite element model, the state-space model of the wheel can be determined by means of the modal analysis method. It can be represented by a state equation, Eq.(7.46), and an output equation, Eq.(7.47):

$$\dot{\bar{w}} = [A^w]\bar{w} + [B^w]\bar{f}^w, \quad (7.46)$$

$$\bar{v}^w = [C^w]\bar{w}, \quad (7.47)$$

where each term is described in section 6.4.1. The only thing that changes, if compared with the state-space model of the wheel considering only one contact point, are the input dynamic forces \bar{f}^w and the output dynamic velocities \bar{v}^w that have to be extended to consider the presence of the second contact point. Considering the longitudinal, lateral, vertical and spin directions for each contact point the new input and output vectors can be described by 8 components:

$$\bar{f}^w = \left\{ f_{1,1}^w \quad f_{2,1}^w \quad f_{3,1}^w \quad f_{6,1}^w \quad f_{1,2}^w \quad f_{2,2}^w \quad f_{3,2}^w \quad f_{6,2}^w \right\}^T, \quad (7.48)$$

$$\bar{v}^w = \left\{ v_{1,1}^w \quad v_{2,1}^w \quad v_{3,1}^w \quad v_{6,1}^w \quad v_{1,2}^w \quad v_{2,2}^w \quad v_{3,2}^w \quad v_{6,2}^w \right\}^T. \quad (7.49)$$

For this reason also the input and output matrices $[B^w]$ and $[C^w]$ have to be extended considering the mode shape displacements at the second contact point

of the wheel:

$$[B^w] = \left[\begin{array}{cccc|ccc} \phi_{11,1} & \phi_{12,1} & \dots & \phi_{1n,1} & 0 & 0 & \dots & 0 \\ \phi_{21,1} & \phi_{22,1} & \dots & \phi_{2n,1} & 0 & 0 & \dots & 0 \\ \vdots & \vdots & \ddots & \vdots & \vdots & \vdots & \ddots & \vdots \\ \phi_{k1,1} & \phi_{k2,1} & \dots & \phi_{kn,1} & 0 & 0 & \dots & 0 \\ \hline \phi_{11,2} & \phi_{12,2} & \dots & \phi_{1n,2} & 0 & 0 & \dots & 0 \\ \phi_{21,2} & \phi_{22,2} & \dots & \phi_{2n,2} & 0 & 0 & \dots & 0 \\ \vdots & \vdots & \ddots & \vdots & \vdots & \vdots & \ddots & \vdots \\ \phi_{k1,2} & \phi_{k2,2} & \dots & \phi_{kn,2} & 0 & 0 & \dots & 0 \end{array} \right]^T, \quad (7.50)$$

$$k = 1, 2, 3, 6,$$

$$[C^w] = \left[\begin{array}{cccc|ccc} \phi_{11,1} & \phi_{12,1} & \dots & \phi_{1n,1} & 0 & 0 & \dots & 0 \\ \phi_{21,1} & \phi_{22,1} & \dots & \phi_{2n,1} & 0 & 0 & \dots & 0 \\ \vdots & \vdots & \ddots & \vdots & \vdots & \vdots & \ddots & \vdots \\ \phi_{i1,1} & \phi_{i2,1} & \dots & \phi_{in,1} & 0 & 0 & \dots & 0 \\ \hline \phi_{11,2} & \phi_{12,2} & \dots & \phi_{1n,2} & 0 & 0 & \dots & 0 \\ \phi_{21,2} & \phi_{22,2} & \dots & \phi_{2n,2} & 0 & 0 & \dots & 0 \\ \vdots & \vdots & \ddots & \vdots & \vdots & \vdots & \ddots & \vdots \\ \phi_{i1,2} & \phi_{i2,2} & \dots & \phi_{in,2} & 0 & 0 & \dots & 0 \end{array} \right], \quad (7.51)$$

$$i = 1, 2, 3, 6,$$

where $\phi_{ir,1}$, $\phi_{ir,2}$ and $\phi_{kr,1}$, $\phi_{kr,2}$ are the mass-normalized mode shapes of mode r in the i and k directions at the first and second contact points.

For the rail, as discussed in section 6.4.2, an analytical model is adopted. The procedure to determine the final state-space model of the rail changes when compared with the state-space model obtained considering one contact point. The mobility matrix that relates the velocities and the friction forces at the two contact points of the rail is available and described in Eq.(7.9) where the directions taken into account for each contact point are always longitudinal, lateral, vertical and spin. For each mobility curve, it is possible to find an equivalent system with a transfer function expressed in the form of a ratio of two polynomials:

$$H(s) \equiv \frac{B(s)}{A(s)} = \frac{b_1 s^{m-1} + b_2 s^{m-2} + \dots + b_m}{s^m + a_1 s^{m-1} + a_2 s^{m-2} + \dots + a_m}, \quad (7.52)$$

where the order of the denominator is one order higher than that of the numerator. Normally, the higher the order of the equivalent system assumed, the less is the error of the system identification results. However, if the order of the system is very high, the performance of the equivalent system is sensitive to the coefficients and may be unstable. To seek appropriate coefficients, the ‘*invfreqs*’ function provided by the Signal Processing Toolbox of MATLAB [47] can be adopted. Then, by means of another MATLAB routine ‘*tf*’, the transfer function in Eq.(7.52) can be determined to represent the equivalent system of each mobility where the coefficients a_1, a_2, \dots, a_m and b_1, b_2, \dots, b_m are the parameters obtained by means the ‘*invfreqs*’ function. The transfer functions obtained can be collected and represented in matrix form:

$$[G(s)] = \begin{bmatrix} H_{11,11} & H_{12,11} & H_{13,11} & H_{16,11} & H_{11,12} & H_{12,12} & H_{13,12} & H_{16,12} \\ H_{21,11} & H_{22,11} & H_{23,11} & H_{26,11} & H_{21,12} & H_{22,12} & H_{23,12} & H_{26,12} \\ H_{31,11} & H_{32,11} & H_{33,11} & H_{36,11} & H_{31,12} & H_{32,12} & H_{33,12} & H_{36,12} \\ H_{61,11} & H_{62,11} & H_{63,11} & H_{66,11} & H_{61,12} & H_{62,12} & H_{63,12} & H_{66,12} \\ \hline H_{11,21} & H_{12,21} & H_{13,21} & H_{16,21} & H_{11,22} & H_{12,22} & H_{13,22} & H_{16,22} \\ H_{21,21} & H_{22,21} & H_{23,21} & H_{26,21} & H_{21,22} & H_{22,22} & H_{23,22} & H_{26,22} \\ H_{31,21} & H_{32,21} & H_{33,21} & H_{36,21} & H_{31,22} & H_{32,22} & H_{33,22} & H_{36,22} \\ H_{61,21} & H_{62,21} & H_{63,21} & H_{66,21} & H_{61,22} & H_{62,22} & H_{63,22} & H_{66,22} \end{bmatrix}. \quad (7.53)$$

Finally, by means of the ‘*ss*’ function of MATLAB, it is possible, from the transfer function matrix $[G(s)]$, to calculate the system matrix $[A^r]$ and the input and output matrices $[B^r]$, $[C^r]$ to represent the complete state-space model of the rail:

$$\dot{\bar{r}} = [A^r]\bar{r} + [B^r]\bar{f}^r, \quad (7.54)$$

$$\bar{v}^r = [C^r]\bar{r}, \quad (7.55)$$

where the vector of the state variables is:

$$\bar{r} = \{r_1 \quad r_2 \quad \dots \quad r_l\}^T, \quad (7.56)$$

with l the total system order, while the input dynamic forces \bar{f}^r and the output dynamic velocities \bar{v}^r are defined as:

$$\bar{f}^r = \{f_{1,1}^r \quad f_{2,1}^r \quad f_{3,1}^r \quad f_{6,1}^r \quad f_{1,2}^r \quad f_{2,2}^r \quad f_{3,2}^r \quad f_{6,2}^r\}^T, \quad (7.57)$$

$$\bar{v}^r = \left\{ v_{1,1}^r \quad v_{2,1}^r \quad v_{3,1}^r \quad v_{6,1}^r \quad v_{1,2}^r \quad v_{2,2}^r \quad v_{3,2}^r \quad v_{6,2}^r \right\}^T. \quad (7.58)$$

Now, in accordance with section 6.5, a general self-excited vibration model can be developed by combining the wheel/rail structural models and the wheel/rail rolling contact model in a loop as shown in Figure 6.4. For the consideration regarding the self-excited vibration loop see section 6.5 keeping in mind that all the system extended with the second contact point has to be considered.

To conclude the explanation of the attempt made to have two contact points in the time domain model it is important to point out that the reason for the solution not being convergent is believed to be in the usage of ratios of polynomials to describe the rail frequency responses. In fact, the analytical models of the rail are quite complicated and can not always easily be represented in terms of poles and zeros in the frequency range considered. MATLAB routine '*invfreqs*' estimates polynomial coefficients according to a specific order given by the user; although a stability check can be performed on each estimated transfer function there is no a-priori guarantee that the solution of the self-excited loop that adopts these transfer functions will converge. Further research is recommended in this direction by either following through the identification problem to get stable solution of the time domain loop or exploring the usage of different rail models like 2.5 D [49] and/or finite element models with opportune tapered and damped elements at the ends [50].

7.3 Results

In order to verify the model in the frequency domain a comparison between numerical results and experimental ones is necessary. From a numerical point of view, the same analysis performed for the model with one contact point has been performed for the model with two contact point as well.

As discussed in Chapter 6, to understand better and represent the dependence of the results on input parameters, some variables are defined as uncertain. In practice it is found that small changes in humidity, in the contact positions, in the velocity or in the normal forces at the contact can cause the squeal noise to change. Since the reality is affected by such uncertainty and variability, a deterministic model may be too simple to describe this complex phenomenon. The most important input parameters of the model have been defined in a range using a uniform distribution and for each case a random combination of these

parameters is extracted and the eigenvalues of the open loop are calculated for all frequencies.

Both the examples described in Chapter 2 are addressed below. First that of the Sprinter trains in North Wales have been taken into account and reproduced with this model. Then, the case analyzed with the Sirio tram in Milan has been modelled as well.

Considering its structural dynamics, the monobloc wheel mounted on the Sprinter shows clearly separated and lightly damped natural modes. This fact may be helpful in interpreting curve squeal model results and this is the reason why the Sprinter case is presented first.

The resilient wheel of the Sirio tram represents an example of greater complexity and is addressed later in section 7.3.2

7.3.1 Case of British Rail Class 150 Sprinter

The problem with this train, as discussed in section 2.2, was the severe squeal noise occurred on some curving routes, with high amplitude sustained tones in the region 2 to 5 kHz. For safety reasons the track on these curves was fitted with check rails and the vertical stick/slip forces acting between the check rail and the wheel flange back was believed to be the cause of this particular squeal problem. The radial modes with 2, 3, 4, 5 and 8 nodal diameters were found to occur, with the mode with 4 nodal diameters at 3.6 kHz being the most commonly found.

The aim of this investigation is to reproduce with this model the contact condition believed to occur in reality and to compare unstable frequencies of the model with the tones recorded during tests.

Considering a right curve run in steady-state, a contact point between flange back and check rail occurs on the inner front wheel. In Figure 7.3 the contact condition between wheel and rail/check rail is shown. Since only analytical models of rails are available, the UIC 60 one has been used to reproduce the effect of the check rail in contact with the wheel flange back and the effect of the bullhead rail in contact with the wheel tread (see Figure 7.3). In this case the rail mobilities at the two contact points can be considered decoupled and the cross rail mobilities can be considered equal to zero (see Eq.(7.9)).

In this case, from a dynamic point of view, a numerical model to simulate this kind of train in a curve was not available, therefore the input parameters for the model have been estimated and are summarized in Table 7.1.

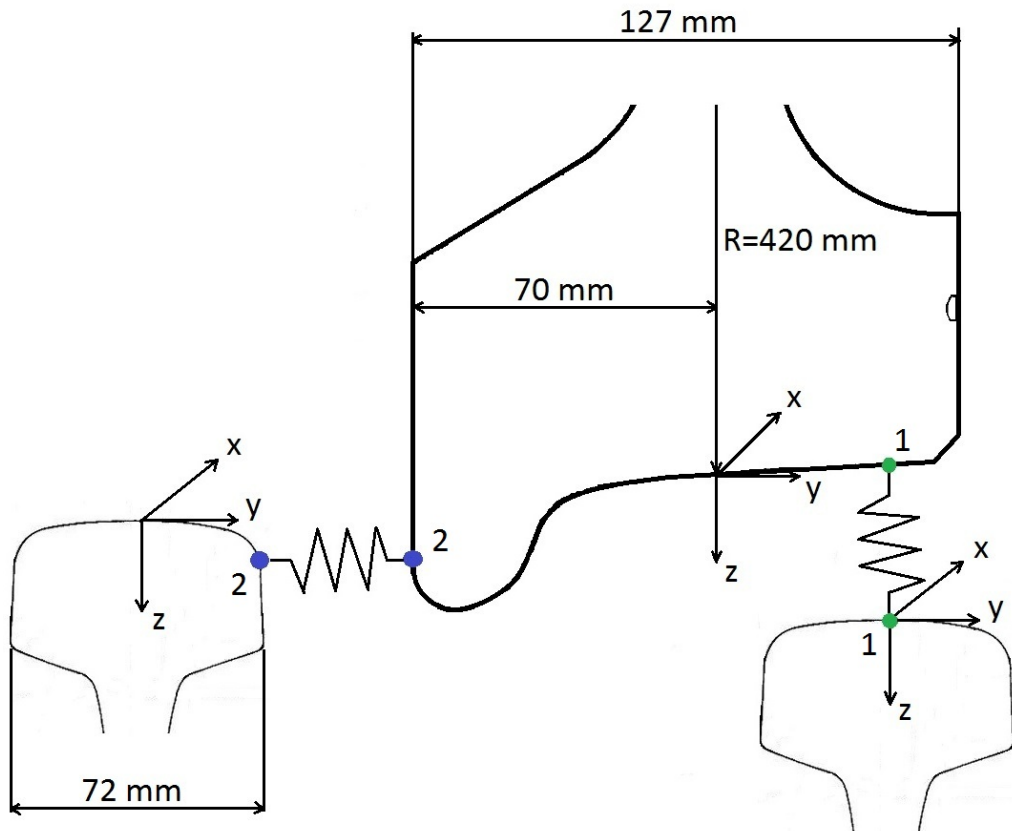


Figure 7.3: Contact condition between wheel and rail/check rail.

Description	Name	Unit	Values
Normal contact force	$N_{0,1}$	[kN]	$U(40, 60)$
	$N_{0,2}$	[kN]	$U(24, 36)$
Curving velocity	V	[m/s]	$U(8.4, 15.6)$
Nominal radius of the wheel	Rw	[m]	0.42
Transverse curve radius of the wheel	Rwt_1	[m]	0
	Rwt_2	[m]	0.01
Transverse curve radius of the rail	Rrt_1	[m]	0.3
	Rrt_2	[m]	0.013
Contact position on the wheel	$[x\ y\ z]_1$	[mm]	$[0\ U(32, 52)\ 0]$
	$[x\ y\ z]_2$	[mm]	$[0\ -70\ U(12, 18)]$
Contact position on the rail	$[x\ y\ z]_1$	[mm]	$[0\ 0\ 0]$
	$[x\ y\ z]_2$	[mm]	$[0\ 36\ 14]$
Contact angle between wheel/rail	θ_1	[°]	0
	θ_2	[°]	$U(74, 88)$
Longitudinal creepage	$\gamma_{10,1}$	-	$U(0, 0.005)$
	$\gamma_{10,2}$	-	$U(-1.5, -0.5)$
Lateral creepage	$\gamma_{20,1}$	-	$U(0.0075, 0.0125)$
	$\gamma_{20,2}$	-	Eq.(7.60)
Spin creepage	$\gamma_{60,1}$	[1/m]	0
	$\gamma_{60,2}$	[1/m]	Eq.(7.61)
Coloumb coefficient	μ	-	0.4
Falling ratio	λ_1	-	0
	λ_2	-	0.65
Saturation coefficient	κ_1	-	0
	κ_2	-	$U(0.03, 0.3)$

Table 7.1: Input parameters at contact points for outer front wheel.

For the lateral creepage on the tread the approximation:

$$\gamma_{20,1} = \frac{b}{R} \cong 0.01, \quad (7.59)$$

can be used, where b , equal to 2.5 m is the distance between the two wheelset while R is the curve radius (200 m). Variability is added to this parameter in a uniform range distribution as shown in Table 7.1.

For the lateral and spin creepage on the flange back, the following approximation equation can be used:

$$\gamma_{20,2} = \frac{\gamma_{20,1}}{\cos(\theta_2)}, \quad (7.60)$$

$$\gamma_{60,2} = \frac{\sin(\theta_2)}{R_w}, \quad (7.61)$$

where θ_2 is the contact angle between wheel flange back and check rail, while R_w is the nominal radius of the wheel. Since $\gamma_{20,1}$ and θ_2 are defined in a uniform range distribution, $\gamma_{20,2}$ and $\gamma_{60,2}$, that are dependent on $\gamma_{20,1}$ and θ_2 , will consequently be variable.

In order to focus on the excitation in the radial direction, the values of κ_1 and λ_1 regarding the friction characteristics at the tread contact point, have been, in a first attempt, chosen equal to zero in such a way as to obtain a slope of friction curve in the falling region equal to zero and avoid, therefore, that axial modes are excited. Introducing a negative slope at the tread contact point would simply result in an increased number of possible unstable frequencies.

In Figures 7.4, 7.5, 7.6 and 7.7 four examples are reported of noise measurements recorded at the inner and outer front wheels. In each case the leading inner wheel showed the highest levels. The noise measured at the outer wheel may be due to sound radiated by the inner wheel. The model predicts unstable frequencies (see Figure 7.8) that are very close to measured ones. In particular the most important frequency involved in squeal noise 3.6 kHz is the most likely to be unstable in the model as well. Also other frequencies that, although present in the measurements, have less importance in terms of levels and persistence are found in the predictions, like 2.2, 2.8 and 4.4 kHz. Moreover, from Table 7.2 it can be noticed that all the predicted frequencies are very close to the natural mode, apart from the frequencies in range 4465 - 4478 Hz that are slightly lower than the corresponding natural mode at 4517 Hz.

By modifying damping ratios in the wheel modal model the effect of damping

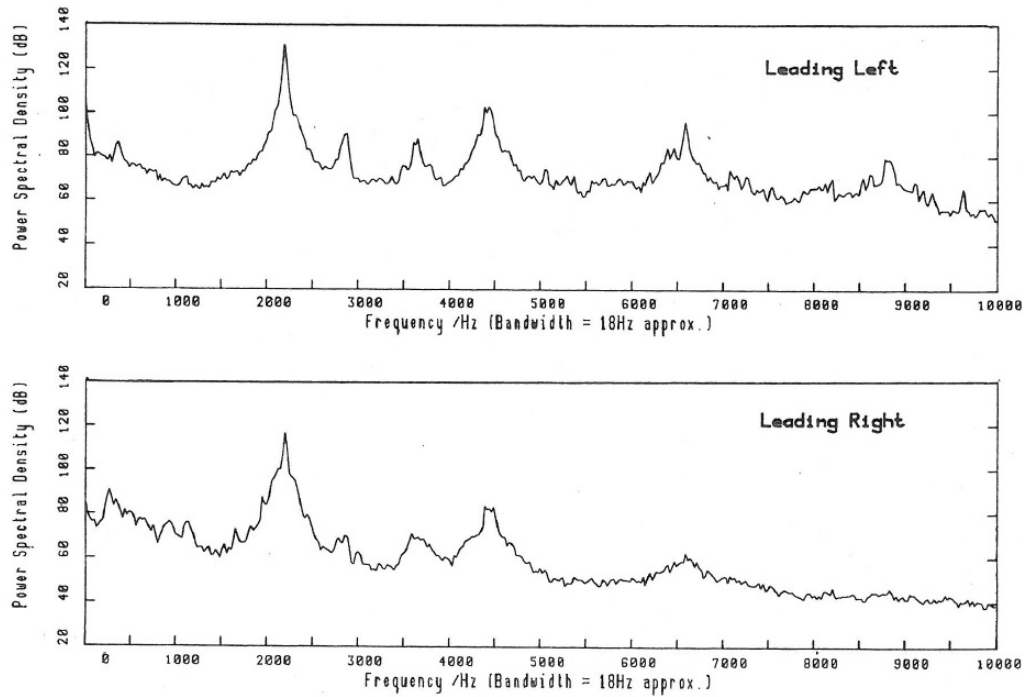


Figure 7.4: Example of squeal at 2.2 kHz measured on leading left and right wheel. Left hand curve [7].

Numerical modes involved in squeal	Frequency range predicted by model	Experimental frequencies involved in squeal
2220 Hz (2 ND)	2222 - 2229 Hz	around 2200 Hz
2880 Hz (3 ND)	2882 - 2891 Hz	around 2800 Hz
3645 Hz (4 ND)	3637 - 3646 Hz	around 3600 Hz
4517 Hz (5 ND)	4465 - 4478 Hz	around 4400 Hz
4948 Hz (Circum)	4947 - 4948 Hz	

Table 7.2: Numerical modes involved in squeal compared with the experimental frequencies involved in squeal and frequency range predicted by the model.

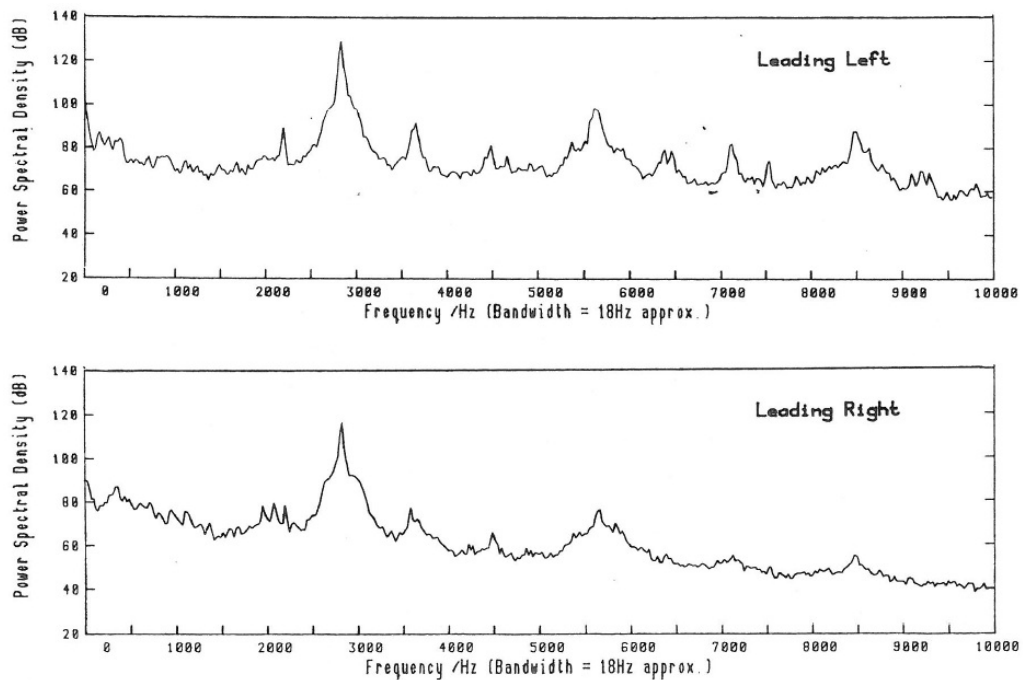


Figure 7.5: Example of squeal at 2.8 kHz measured on leading left and right wheel. Left hand curve [7].

can be readily analyzed. Figure 7.9 shows the curve squeal occurrences diagram in the case of a damped wheel. The measured damping ratios used in the model are those measured on the damped wheel described in Chapter 2 and listed in Table 2.4. It can be seen that the highest damping value corresponds to the prevalent radial mode found in experimental data at 3.6 kHz. The predicted frequencies reported in Figure 7.9 confirm that the frequency at 3645 Hz occurs much less often than in the undamped wheel case. Interestingly can also be observed that the occurrences at this frequency are now lower than at 2220 Hz and 2880 Hz; the damping ratio is 3-4 times larger.

Commenting on Figure 7.9 it can be argued that, with the increased damping, curve squeal is expected to disappear completely, as it was measured with the damped wheel. However the variability of the input parameters chosen is likely to produce combinations of inputs that are too severe to represent the reality.

The model in the frequency domain with variable inputs is not expected to give deterministic results but can be useful to understand the likelihood of curve squeal. In this sense it is possible to say that, according to the model and within the input parameter range, a wheel with increased damping would squeal in much less cases

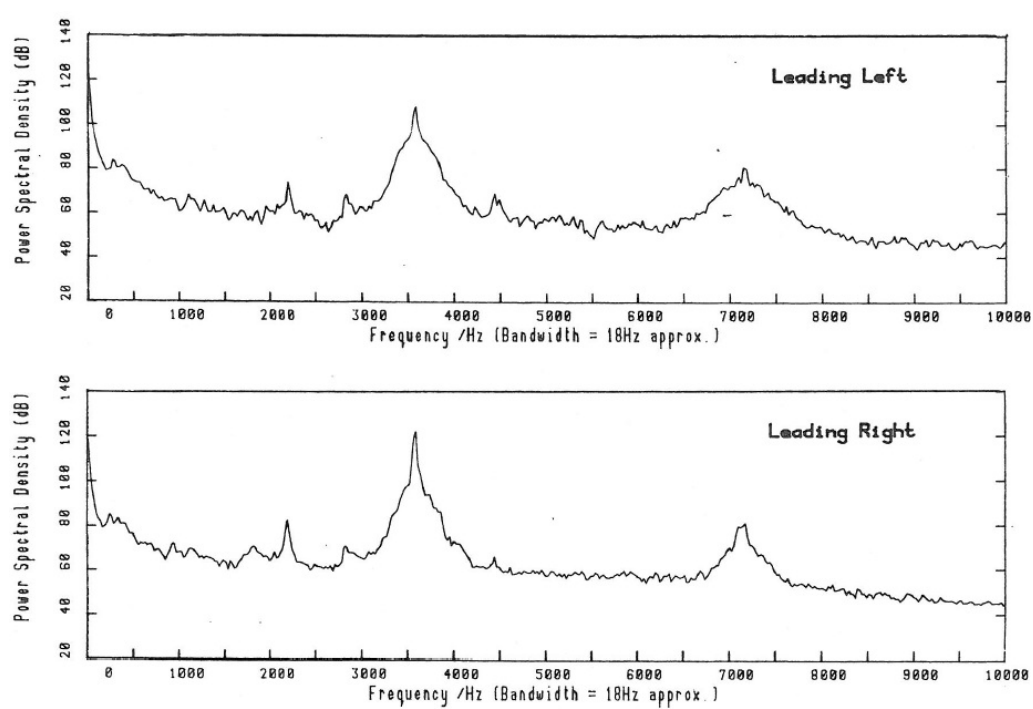


Figure 7.6: Example of squeal at 3.6 kHz measured on leading left and right wheel. Right hand curve [7].

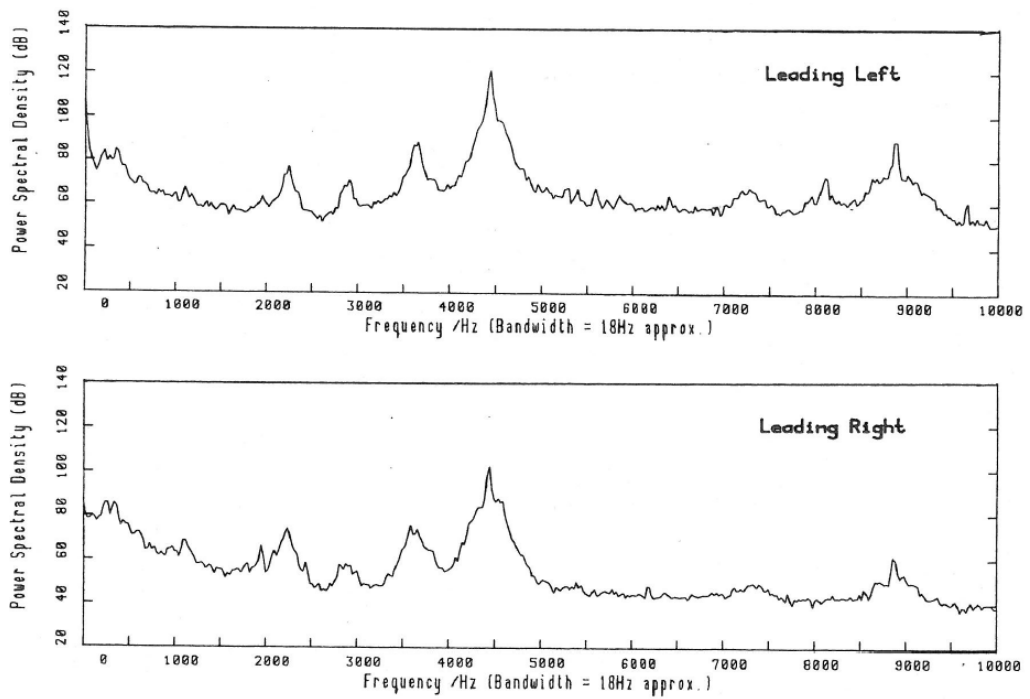


Figure 7.7: Example of squeal at 4.4 kHz measured on leading left and right wheel. Left hand curve [7].

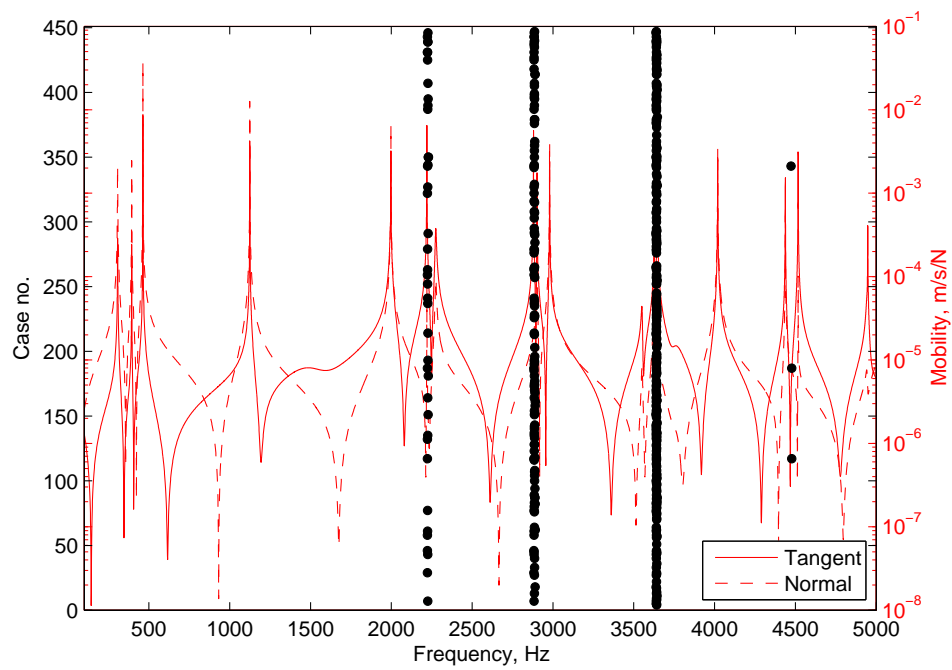


Figure 7.8: Curve squeal occurrences diagram for the undamped outer front wheel. Occurrences of the most predicted frequency: more than 60 % of the 450 cases considered.

(for each predicted frequency less than 8 % of the 450 cases considered) than the undamped one but this may not be enough to stop the phenomenon. However some parameters defining the friction curve (the biggest unknown of the problem) can be modified to allow the model simulate a series of cases closer to reality (i.e. with no curve squeal on the damped wheel).

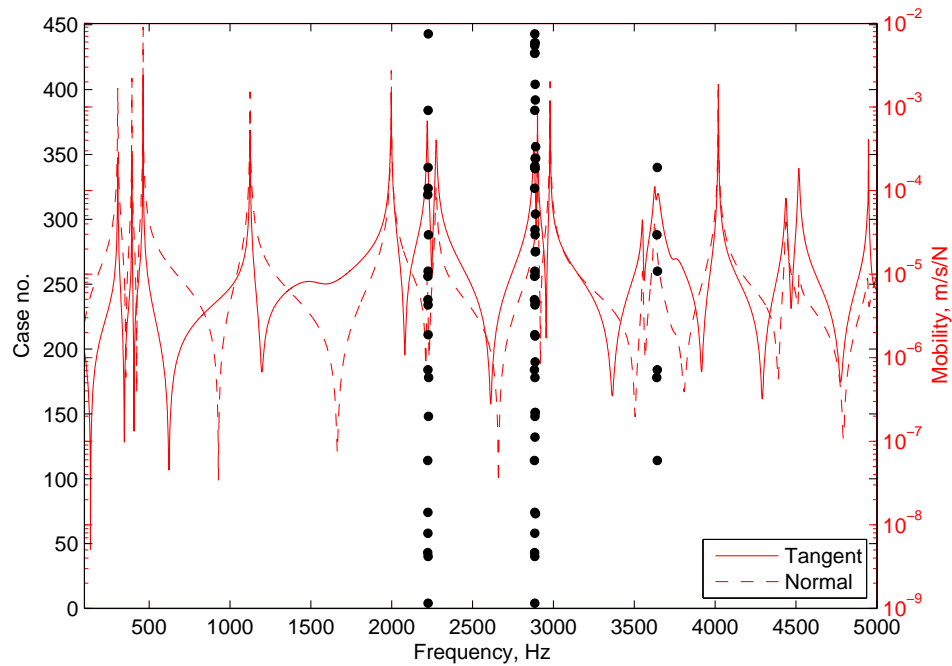


Figure 7.9: Curve squeal occurrences diagram for the damped outer front wheel. Occurrences of the most predicted frequency: less than 8 % of the 450 cases considered

Therefore, 450 cases have been simulated with the same input parameters listed in Table 7.1 but with λ equal to 0.6. Figures 7.10 and 7.11 report the curve squeal occurrences diagram for undamped and damped wheel. It is interesting to observe that when the λ value decreases the slope of the friction characteristic in the falling region decreases as well; therefore, the occurrences of the predicted unstable frequencies decrease. In particular the case with the undamped wheel predicts that the occurrences of the most common frequencies are less than 60 % of the 450 cases considered while for the case with the damped wheel are less than 6 %.

Finally, in Figure 7.12 the same case reported in Figure 7.10 is shown and

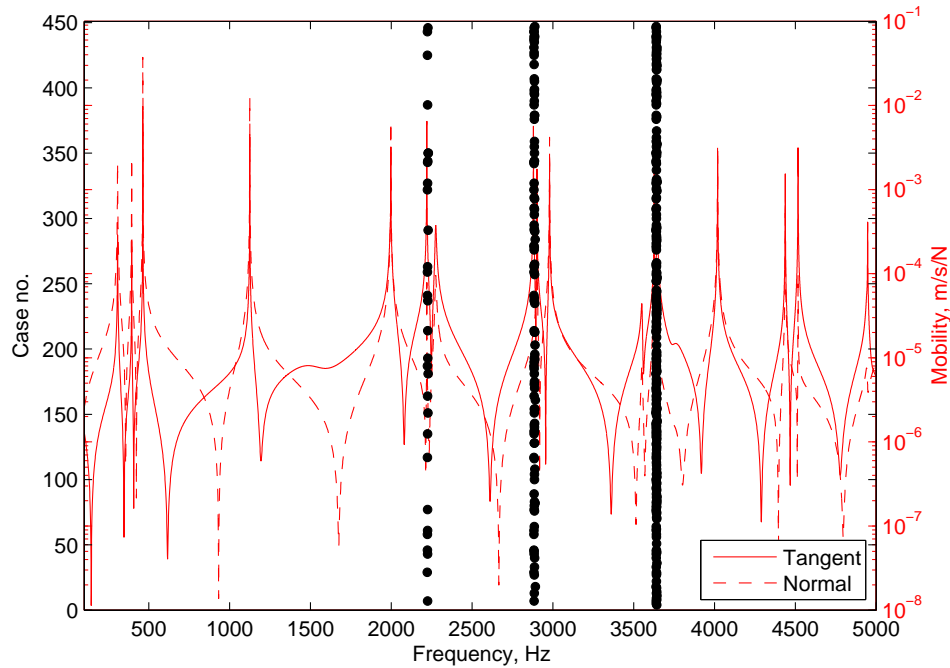


Figure 7.10: Curve squeal occurrences diagram for the undamped outer front wheel with λ equal to 0.6. Occurrences of the most predicted frequency: less than 60 % of the 450 cases considered

the frequency range is extended up to 10 kHz. In fact during the measurement campaign the presence of a tone between 7 and 7.5 kHz was recorded and the radial mode with 8 nodal diameters was believed to be responsible. The model can be pushed to higher frequency range in order to assess the presence of higher frequency modes. Focusing on the frequencies above 5 kHz it can be observed that the first clear instability is at around 6.5 kHz. By varying damping ratios it has been found that there are two modes that are squealing here. One is the 7 nodal diameters radial mode at 6500 Hz and the other is the 4 nodal diameters and 2 nodal circles (predominately) axial mode at 6495 Hz. It is important to point out that considering the value of the contact angle and the mode shape also axial mode (though not as easily as radial ones) can be excited with a contact point on the flange. In some cases measurements have shown squeal at this frequency.

At around 7.3 kHz instabilities are due to the axial mode with 2 nodal circles and 5 nodal diameters. This is in contrast to what was deduced when the measurement campaign was performed but is consistent with the results of the model

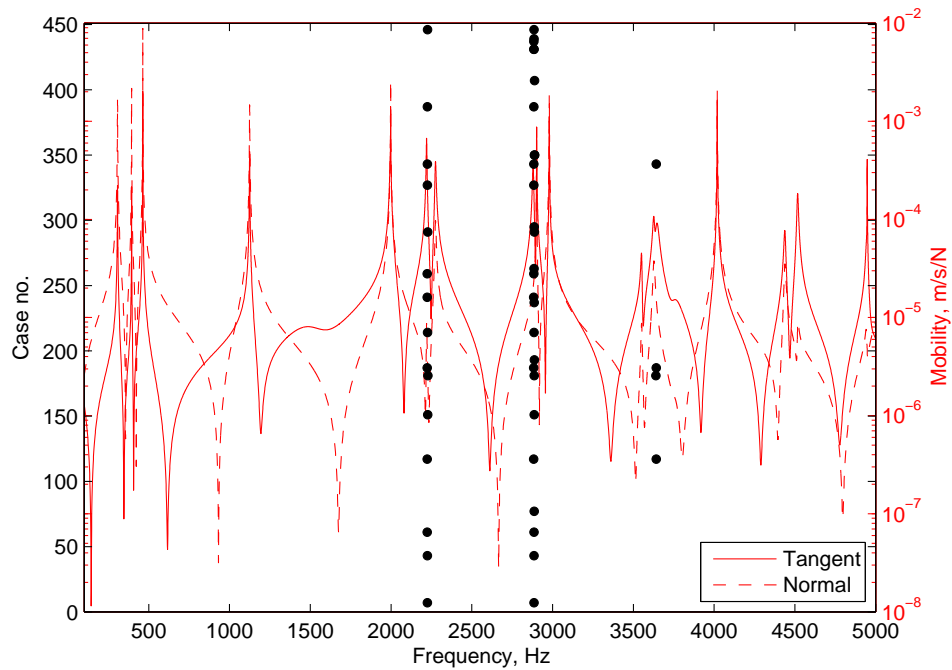


Figure 7.11: Curve squeal occurrences diagram for the damped outer front wheel with λ equal to 0.6. Occurrences of the most predicted frequency: less than 6 % of the 450 cases considered.

and now believed to be correct.

There are other possible contributions for squeal at 8.3 kHz and 9.4 kHz. Although these appear to be components present in the microphone measurements of Figures 7.7 they are harmonics of lower frequency modes.

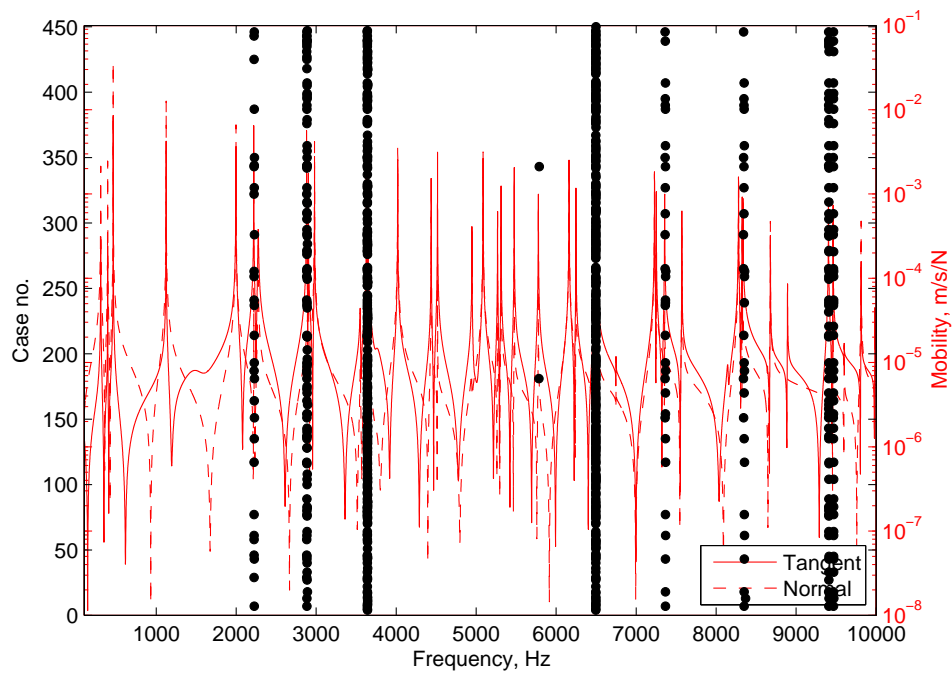


Figure 7.12: Curve squeal occurrences diagram for the undamped outer front wheel with λ equal to 0.6.

7.3.2 Case of Sirio tram in Milan

The Sirio tram case has been reproduced with this model and the predicted frequencies have been compared with the experimental ones. What was clear from the beginning, by looking at the measurements, was the simultaneous presence of more than one contact point. For the front inner wheel of a bogie, the flange back was often in contact with the rail grooved head while the flange of the outer wheel was in contact with the rail running head. From a steady-state vehicle dynamic numerical simulation for a left curve with gauge of 1447 mm, the results showed contact conditions similar to those observed in reality (see Figure 7.13). In Table 7.3 the uncertain and deterministic input parameters for the squeal model are summarized considering the system of reference in the wheel and rail nominal contact point shown in Figure 7.13.

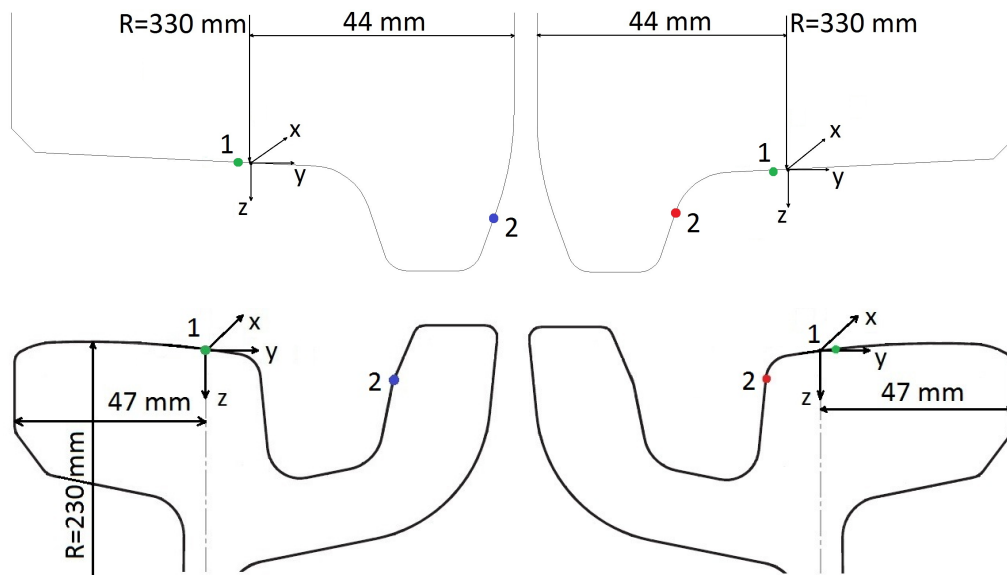


Figure 7.13: Contact points position on the inner and outer front wheel and inner and outer rail.

Figures 7.14 and 7.16 show the curve squeal occurrences diagrams for the inner and outer front wheel, while Figures 7.15 and 7.17 show the spectrograms of inner and outer front wheel vibration acceleration measured during the tram pass-by. By looking at these Figures, it can be seen that the predicted frequencies are very close to the measured ones. In particular, as found from the predicted frequencies of the model with one contact point (see Chapter 6), the important frequency at 2550 Hz is unstable in the model as well. Moreover, since the contact point occurs

Description	Name	Unit	Values	
			Inner	Outer
Normal contact force	$N_{0,1}$	[kN]	$U(17, 25)$	$U(14.5, 21.7)$
	$N_{0,2}$	[kN]	$U(0, 6.5)$	$U(0, 12)$
Curving velocity	V	[m/s]	$U(1.9, 3.6)$	$U(1.9, 3.6)$
Nominal radius of the wheel	Rw	[m]	0.33	0.33
Transverse curve radius of the wheel	Rwt_1	[m]	0	0
	Rwt_2	[m]	0	0
Transverse curve radius of the rail	Rrt_1	[m]	0.230	0.230
	Rrt_2	[m]	0.006	0.006
Contact position on the wheel	$[x\ y\ z]_1$	[mm]	$[0\ U(-9.5, 0.5)\ -0.22]$	$[0\ U(-9.1, 1)\ 0.2]$
	$[x\ y\ z]_2$	[mm]	$[50.1\ 40.2\ 10.4]$	$[50.6\ -20\ 8]$
Contact position on the rail	$[x\ y\ z]_1$	[mm]	$[0\ 0\ 0]$	$[0\ 3.5\ -0.5]$
	$[x\ y\ z]_2$	[mm]	$[50.1\ 48\ 10]$	$[50.6\ -13\ 7]$
Contact angle between wheel/rail	θ_1	[°]	$U(2.4, 3.4)$	$U(-3.4, -2.4)$
	θ_2	[°]	$U(-73, -63)$	$U(-76, -66)$
Longitudinal creepage	$\gamma_{10,1}$	-	$U(0.0038, 0.0057)$	$U(0.0067, 0.0101)$
	$\gamma_{10,2}$	-	$U(-0.0310, -0.0207)$	$U(-0.0193, -0.0128)$
Lateral creepage	$\gamma_{20,1}$	-	$U(-0.0651, -0.0434)$	$U(-0.0651, -0.0434)$
	$\gamma_{20,2}$	-	$U(-0.1587, -0.1058)$	$U(-0.2000, -0.1334)$
Spin creepage	$\gamma_{60,1}$	[1/m]	Eq(6.74).	Eq(6.74).
	$\gamma_{60,2}$	[1/m]	Eq(6.74).	Eq(6.74).
Coloumb coefficient	μ	-	0.4	0.4
Falling ratio	λ_1	-	0.8	0.8
	λ_2	-	0.8	0.8
Saturation coefficient	κ_1	-	$U(0.04, 0.06)$	$U(0.04, 0.06)$
	κ_2	-	$U(0.12, 0.17)$	$U(0.12, 0.17)$

Table 7.3: Input parameters at contact points 1 and 2 for the inner and outer front wheel.

on the flange and flange back, it is expected that the radial modes are involved in squeal. In fact, the radial mode at 1417 Hz is excited and found to be unstable in the model and the predicted frequency at 1550 Hz is very close to measured one. Also other frequencies that, although present in the measurement, have less importance in terms of levels and persistency are found in the predictions, like 2100 Hz, 2300 Hz, 3600 Hz and 3700 Hz.

As shown in the results for the model with one contact point (see Chapter 6), also in this case the model finds that, often, unstable eigenvalues have higher frequencies than the corresponding natural mode. In order to understand which predicted frequency corresponds to which excited mode, fictitious damping has been added to each mode in turn; as a consequence the analyzed unstable frequency disappears. In order to understand better the shift in frequency, as seen with the model with one contact point, the contact angles between wheel and rail can be changed in an unrealistic way in order to excite the direction of the mode of interest. The presence of two contact points will make the reasoning proposed for one contact point more complicated but it is still useful for explaining the reason for the shift in the model.

Finally, it is interesting also to observe that the predicted range for unstable frequency is wide (see Tables 7.4 and 7.5), as can also be observed in the wheel vibration spectrogram. This may indicate that in reality where contact conditions are variable along the curve, unstable frequency will not always appear at the same value.

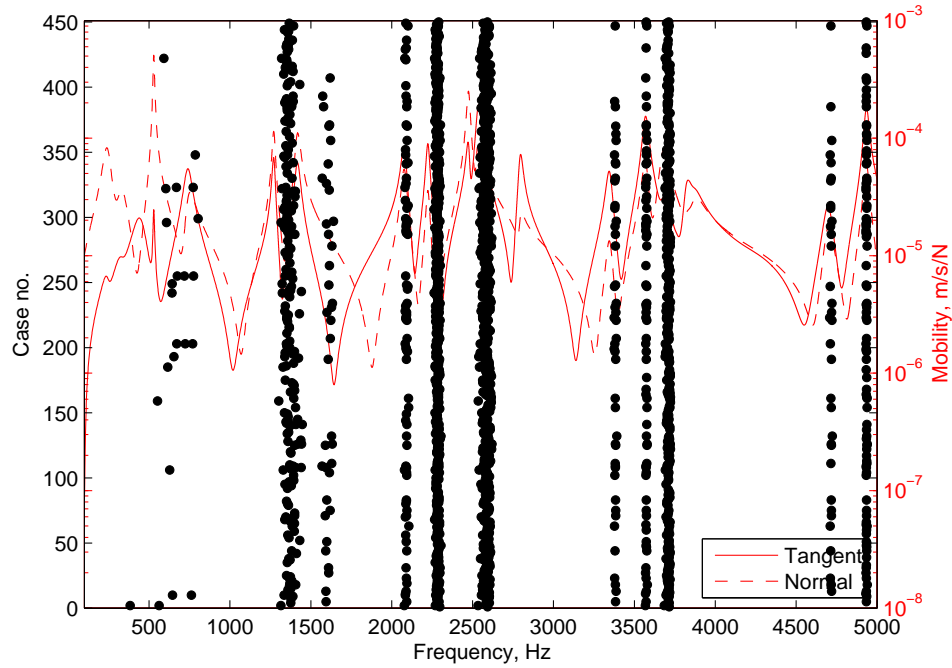


Figure 7.14: Curve squeal occurrences diagram for the inner front wheel.

Numerical modes involved in squeal	Frequency range predicted by model	Experimental frequencies involved in squeal
529 Hz	552 - 674 Hz	around 530 Hz
740 Hz	718 - 803 Hz	
1271 Hz	1302 - 1447 Hz	around 1330 Hz
1417 Hz	1569 - 1640 Hz	around 1550 Hz
2078 Hz	2079 - 2106 Hz	around 2100 Hz
2224 Hz	2261 - 2304 Hz	around 2300 Hz
2475 Hz, 2536 Hz	2534 - 2620 Hz	around 2550 Hz
3346 Hz	3374 - 3391 Hz	
3569 Hz	3568 - 3580 Hz	around 3600 Hz
3680 Hz	3685 - 3723 Hz	around 3700 Hz
4697 Hz	4707 - 4723 Hz	
4934 Hz	4931 - 4939 Hz	

Table 7.4: Numerical modes involved in squeal compared with the experimental frequencies involved in squeal and frequency range predicted by the model (inner front wheel).

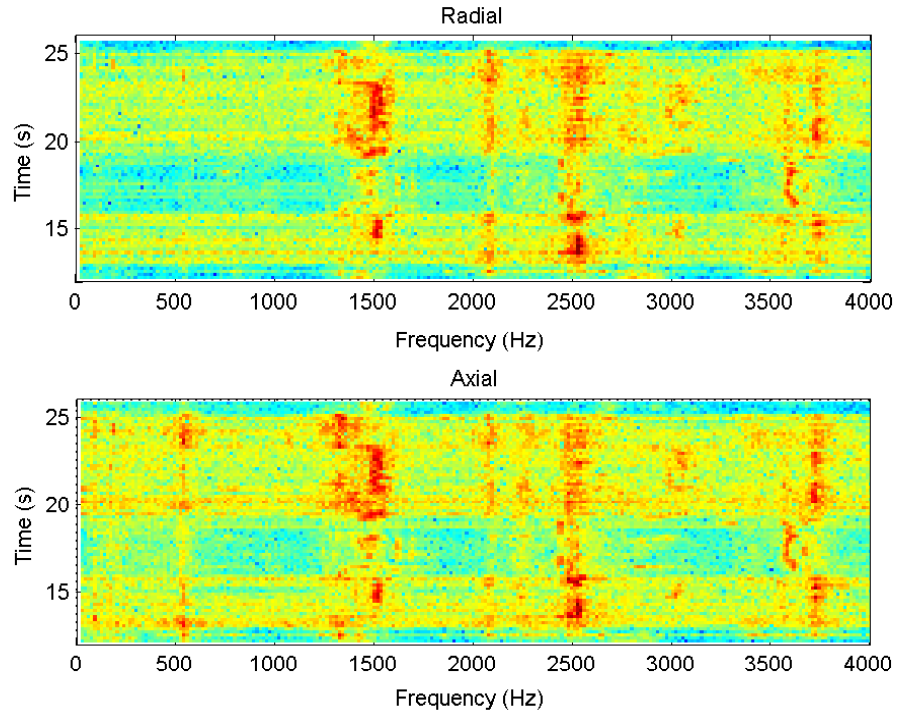


Figure 7.15: Spectrogram of inner front wheel vibration acceleration during tram pass-by.

Numerical modes involved in squeal	Frequency range predicted by model	Experimental frequencies involved in squeal
1417 Hz	1355 - 1575 Hz	around 1550 Hz
2475 Hz	2488 - 2521 Hz	around 2550 Hz
2536 Hz	2528 - 2675 Hz	around 2550 Hz
3680 Hz	3671 - 3745 Hz	around 3700 Hz
4934 Hz	4935 - 4975 Hz	

Table 7.5: Numerical modes involved in squeal compared with the experimental frequencies involved in squeal and frequency range predicted by the model (outer front wheel).

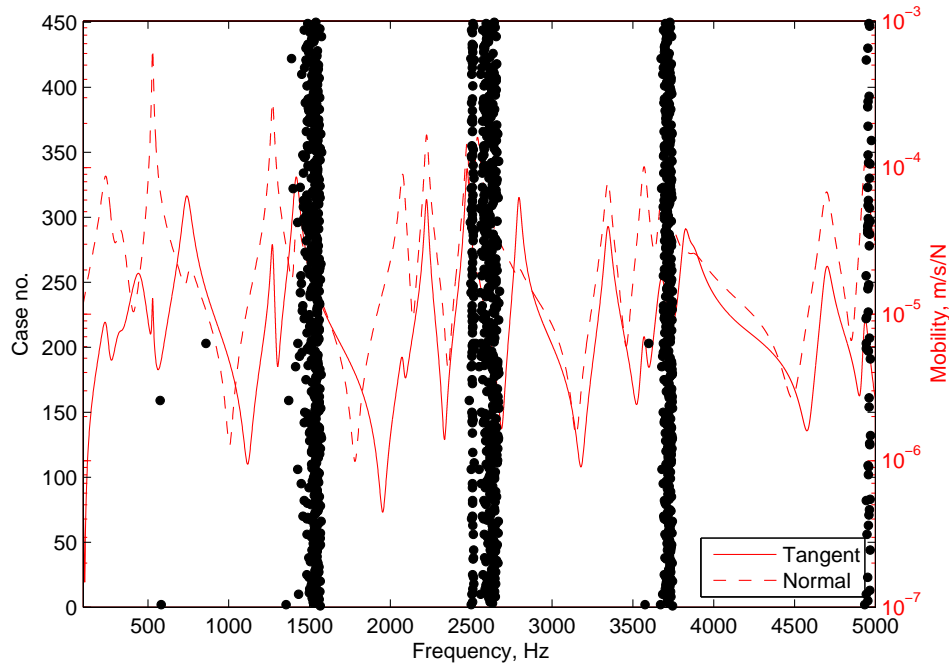


Figure 7.16: Curve squeal occurrences diagram for the outer front wheel

Finally, by modifying the damping ratios in the wheel modal model, those values capable of decreasing the chances of instabilities can be sought. In this case, multiplying the damping ratios of the modes by factors reported in Table 7.6, respectively, would largely decrease the occurrence of squeal. By repeating the same analysis that generated Figures 7.14 and 7.16 it has been found that, with this amount of added damping, these modes are likely to be involved in squeal in less than 6 % of the 450 cases considered (see Figures 7.18 and 7.19). It is interesting to observe that the damping ratio of the mode at 2475 Hz has been increased by a factor larger than the mode at 1417 Hz. This is due to the fact that the mode at 1417 Hz was already more highly damped so needed a smaller factor.

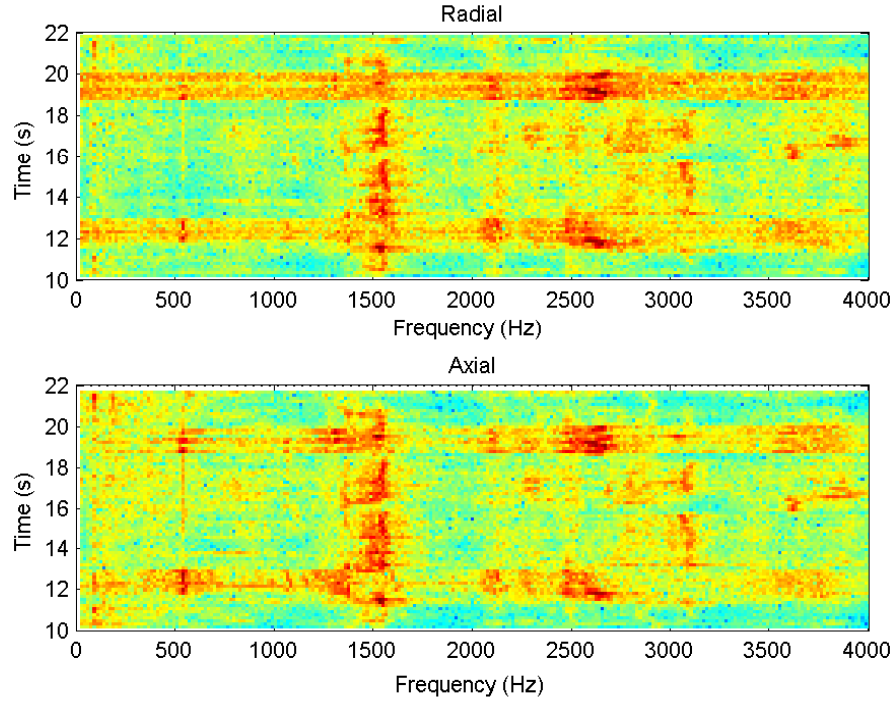


Figure 7.17: Spectrogram of outer front wheel vibration acceleration during tram pass-by.

Numerical modes	Damping ratio of undamped wheel	Multiplicative factor	Damping ratio of damped wheel
529 Hz	0.8 %	4	3.2 %
1271 Hz	0.72 %	8	5.76 %
1417 Hz	1.19 %	6	7.14 %
2224 Hz	0.5 %	6	3 %
2475 Hz	0.42 %	15	6.3 %
2536 Hz	0.59 %	6	3.54 %
3680 Hz	0.78 %	4	3.12 %
Other modes		3	

Table 7.6: Damping ratio of the damped wheel.

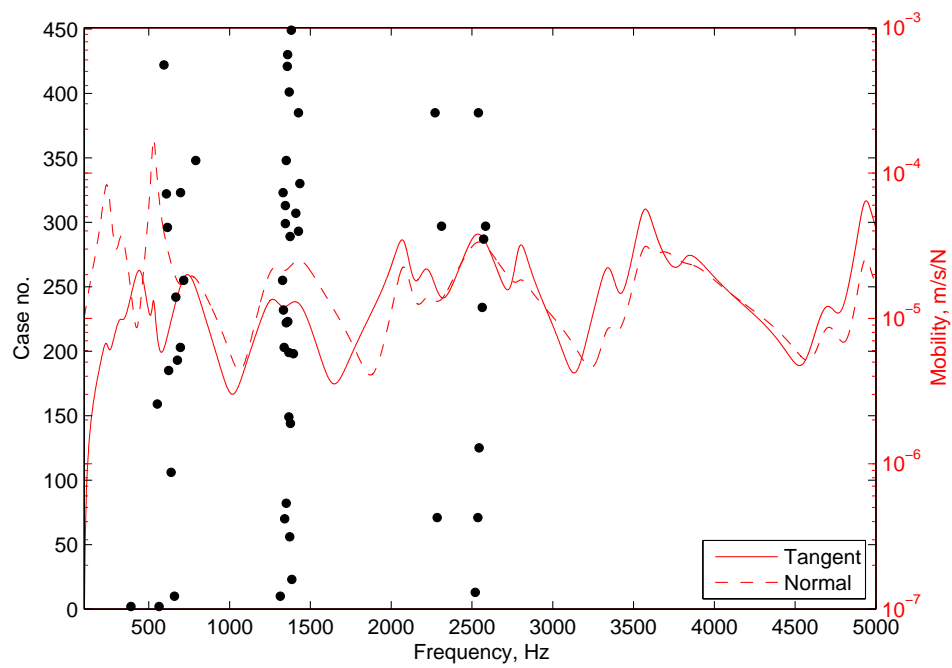


Figure 7.18: Curve squeal occurrences diagram for the damped inner front wheel. Occurrences of the most predicted frequency: less than 6 % of the 450 cases considered

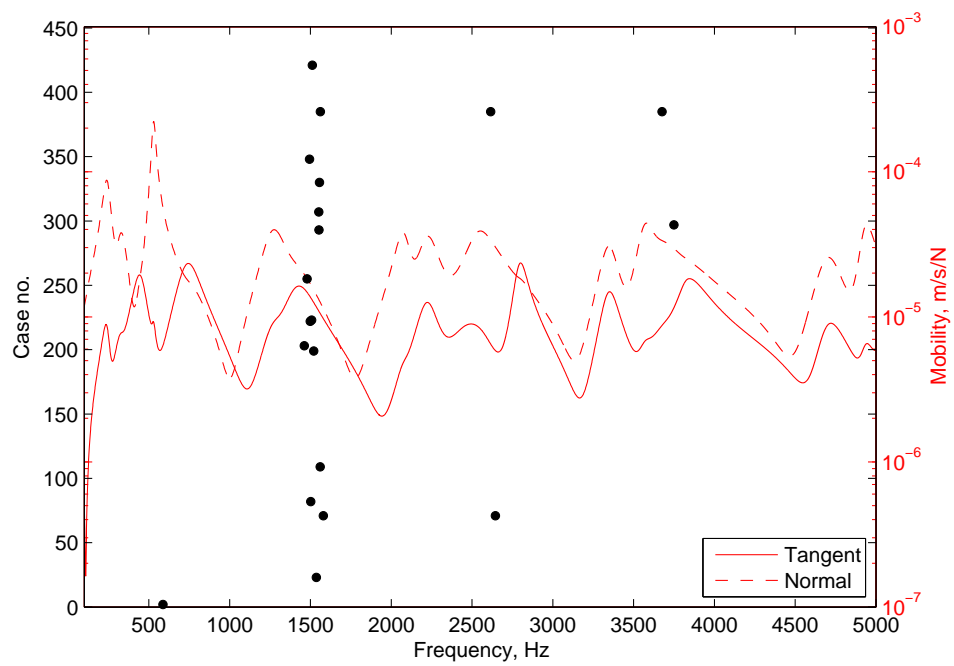


Figure 7.19: Curve squeal occurrences diagram for the damped outer front wheel. Occurrences of the most predicted frequency: less than 3 % of the 450 cases considered

Conclusions

The motivation of this research has its origin in an experimental campaign that happened in Milan in 2010-2011 involving Politecnico di Milano and the local transport service ATM. It was aimed at investigating the high level of curve squeal noise present in several tight curves around the city during the passages of the newest rolling stock tram named Sirio. What was clear from the beginning was the simultaneous presence of more than one contact point. For the front inner wheel of a bogie, the flange back was often in contact with the rail grooved head while the flange of the outer wheel was in contact with the rail running head. Then, the Class 150 Sprinter units has been investigated. When this train was introduced in North Wales, a number of complaints arose from the intense squealing noise generated during curving. In this case it was clear that the frequencies involved in squeal were correlated with radial modes of the wheel. The cause of this particular squeal problem was believed to be due to vertical stick/slip forces acting between the check rail and the wheel flange.

Despite the relatively low interest in the railway noise literature in squeal due to flange contact, these two cases have demonstrated that curve squeal can also occur due to flange contact; moreover, when a grooved rail or a check rail is fitted to the track, the flange back contact can also have a significant role.

From a modelling point of view, contact between wheel and rail was initially only allowed at a single position but part of the research work described in this thesis has been devoted to improving the original model of Huang [3] to allow two contact positions at the same time. Moreover, since it is known that the curve squeal phenomenon is far from being deterministic and parameters like temperature, humidity and even dirt and particles on the rail can have a strong effect on its occurrence, in the frequency-domain model with one and two contact points, some input parameters have been defined as uncertain variables in the updated version of the software. As a result, the model has been used to give the

frequency values of possible unstable eigenvalues of the system while the range of uncertain parameters has been randomly spanned.

Qualitative comparison with measurements showed that the most important tones recorded during the tram pass-by can be found in the predictions.

Regarding the Sprinter case, it is interesting to observe that no shift in frequency occurs at the radial modes predicted by the model. This is probably due to the fact that the contact points between wheel and rail are in a good conditions to excite predominantly the radial mode. This is reinforced by the fact that the radial modes, in this case, present a predominantly vertical displacement without particular coupling with lateral displacement.

Regarding the Sirio case, since the tram dynamic behaviour changes during the curve, it is expected that the tram passes between conditions with one and two contact points continuously, therefore, both results, obtained from the model with one and two contact points, are useful to be compare with experimental ones. Noticeably, the same frequency shift between wheel natural frequency and unstable frequency value as measured is found in the predictions. In order to understand this visible shift in frequency, it has been verified that neither the high damping values related to the resilient wheel nor the presence of the rail in the model can be considered responsible. Moreover it has also been measured that the position of the peaks in the wheel FRF is hardly influenced by the vehicle load (see Figure 2.23); therefore this also cannot explain the shift in frequency. From a model point of view, as discussed in section 6.6.3, the reason for this shift has been shown to be due to the fact that the direction of the contact angle between wheel and rail is not the same as the displacement direction of the excited mode shape. Moreover, it is reinforced by the fact that the axial and radial modes are more coupled than in the Sprinter case and the peaks are close together.

In order to verify which of the predicted unstable frequencies would actually appear as squeal and what the noise levels would be, a time domain solution of the same loop is being developed and will be presented in the near future.

Appendix A

Rigid transformation of dynamic properties

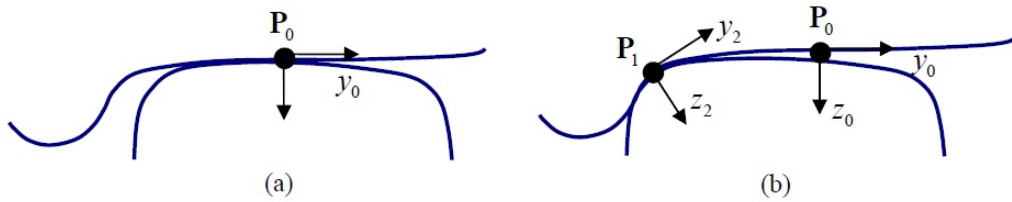


Figure A.1: Typical wheel/rail contact position: (a) nominal contact position P_0 , (b) flange contact position P_1 and the relative relation between two frames. Huang [3]

When the bogie is under curving conditions, the contact position between wheel and rail shifts from the nominal position to the flange position. Consequently, the contact plane rotates by a large contact angle, as shown in Figure A.1. The dynamic properties of a structure may be different from one position to another. Therefore, the wheel and rail mobilities obtained at the nominal contact point cannot be applied for the analysis of other positions. Hence, a method is required to make the transformation of the dynamic properties possible for both wheel and rail models.

For vibration in steel with a frequency up to 5000 Hz, the minimum wavelength of shear waves is about 640 mm. Since the distance between the nominal contact point and the flange contact point is about 50 mm (about 1/12 of the wavelength at the highest frequency vibration), the structural motion between them can be considered as rigid. Thus, the assumption of a rigid transformation is valid for

the wheel and railhead below at least 5000 Hz, which is the upper limit of the current curve squeal analysis. The application of this method is as follows.

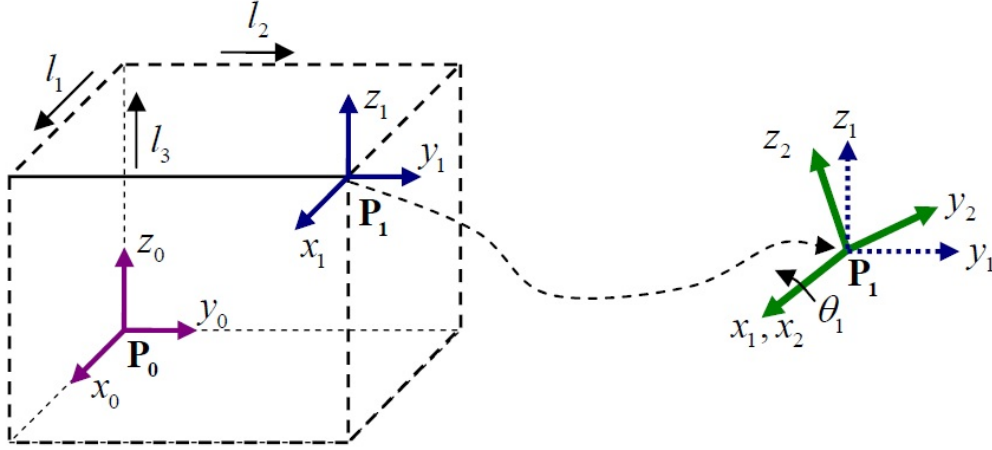


Figure A.2: Rigid transform: translating from P_0 to P_1 and then rotating about the x -axis. Huang [3]

The mode shapes of the wheel system, modelled by FE analysis, are available. So, the modal matrix can be created with the mode shapes of all modes:

$$[\Phi] = \begin{bmatrix} \phi_{1,1} & \phi_{1,2} & \dots & \phi_{1,n} \\ \phi_{2,1} & \phi_{2,2} & \dots & \phi_{2,n} \\ \vdots & \vdots & & \vdots \\ \phi_{6,1} & \phi_{6,2} & \dots & \phi_{6,n} \end{bmatrix}, \quad (\text{A.1})$$

where n is the total modes number.

The modal matrix $[\Phi]_0$ at point P_0 in the frame x_0, y_0, z_0 can be translated to the new position P_1 in the frame x_1, y_1, z_1 by distances (l_1, l_2, l_3) . Then, it is rotated by an angle θ_1 around the x_1 -axis to give the new modal matrix $[\Phi]_2$ in the frame x_2, y_2, z_2 , as shown in Figure A.2. The total transform is expressed as:

$$[\Phi]_2 = [T_{rot}][T_{off}][\Phi]_0 \equiv [T_{tot}][\Phi]_0, \quad (\text{A.2})$$

where the translation matrix $[T_{off}]$ is:

$$[T_{off}] = \left[\begin{array}{ccc|ccc} 1 & & & 0 & l_3 & -l_2 \\ & 1 & & -l_3 & 0 & l_1 \\ & & 1 & l_2 & -l_1 & 0 \\ \hline & & & 1 & & \\ [0] & & & & 1 & \\ & & & & & 1 \end{array} \right], \quad (\text{A.3})$$

the rotation matrix $[R_{rot}]$ is

$$[T_{rot}] = \left[\begin{array}{ccc|ccc} 1 & 0 & 0 & & & \\ 0 & \cos \theta_1 & \sin \theta_1 & & [0] & \\ 0 & -\sin \theta_1 & \cos \theta_1 & & & \\ \hline & & & 1 & 0 & 0 \\ [0] & & & 0 & \cos \theta_1 & \sin \theta_1 \\ & & & 0 & -\sin \theta_1 & \cos \theta_1 \end{array} \right], \quad (\text{A.4})$$

and the total transformation matrix $[T_{tot}]$ is:

$$[T_{tot}] = \left[\begin{array}{ccc|ccc} 1 & 0 & 0 & 0 & l_3 & -l_2 \\ 0 & \cos \theta_1 & \sin \theta_1 & -l_3 \cos \theta_1 + l_2 \sin \theta_1 & -l_1 \sin \theta_1 & l_1 \cos \theta_1 \\ 0 & -\sin \theta_1 & \cos \theta_1 & l_3 \sin \theta_1 + l_2 \cos \theta_1 & -l_1 \cos \theta_1 & -l_1 \sin \theta_1 \\ \hline & & & 1 & 0 & 0 \\ [0] & & & 0 & \cos \theta_1 & \sin \theta_1 \\ & & & 0 & -\sin \theta_1 & \cos \theta_1 \end{array} \right]. \quad (\text{A.5})$$

Now, the modal matrix defined in the Eq.(A.2) can be used to calculate the wheel mobilities in the new contact point using the Eq.(6.20).

For the rail system, since only the mobilities but not the mode shapes are available, the transformation must be performed in terms of mobilities.

Considering the case shown in Figure A.2, the relation between the dynamic velocities and the dynamic forces at point P_0 in the frame x_0, y_0, z_0 can be written as:

$$\begin{Bmatrix} V_1^r \\ V_2^r \\ \vdots \\ V_6^r \end{Bmatrix}_0 = \begin{bmatrix} Y_{11}^r & Y_{12}^r & \dots & Y_{16}^r \\ Y_{21}^r & Y_{22}^r & \dots & Y_{26}^r \\ \vdots & \vdots & \ddots & \vdots \\ Y_{61}^r & Y_{62}^r & \dots & Y_{66}^r \end{bmatrix}_0 \begin{Bmatrix} F_1 \\ F_2 \\ \vdots \\ F_6 \end{Bmatrix}_0, \quad (\text{A.6})$$

$$\bar{V}_0^r = [Y_{ik}^r]_0 \bar{F}_0. \quad (\text{A.7})$$

where the matrix $[Y_{ik}^r]_0$ indicate the rail mobilities at point P_0 in the frame x_0, y_0, z_0 . The dynamic velocities and the dynamic forces used in Eq.(A.6) can be transformed and redefined at point P_1 in the frame x_2, y_2, z_2 using the total transformation matrix $[T_{tot}]$:

$$\bar{V}_2^r = [T_{tot}] \bar{V}_0^r, \Rightarrow \bar{V}_0^r = [T_{tot}]^{-1} \bar{V}_2^r, \quad (\text{A.8})$$

$$\bar{F}_2 = [T_{tot}]^{-T} \bar{F}_0 \Rightarrow \bar{F}_0 = [T_{tot}]^T \bar{F}_2. \quad (\text{A.9})$$

Substituting the Eqs.(A.9) and (A.8) in Eq.(A.7), it is possible to obtain the relation between the dynamic velocities and the dynamic forces at point P_1 in the frame x_2, y_2, z_2 :

$$\bar{V}_2^r = [T_{tot}][Y_{ik}^r]_0[T_{tot}]^T \bar{F}_2 = [Y_{ik}^r]_2 \bar{F}_2, \quad (\text{A.10})$$

where the matrix $[Y_{ik}^r]_2$:

$$[Y_{ik}^r]_2 = \begin{bmatrix} Y_{11}^r & Y_{12}^r & \dots & Y_{16}^r \\ Y_{21}^r & Y_{22}^r & \dots & Y_{26}^r \\ \vdots & \vdots & \ddots & \vdots \\ Y_{61}^r & Y_{62}^r & \dots & Y_{66}^r \end{bmatrix}_2 = [T_{tot}] \begin{bmatrix} Y_{11}^r & Y_{12}^r & \dots & Y_{16}^r \\ Y_{21}^r & Y_{22}^r & \dots & Y_{26}^r \\ \vdots & \vdots & \ddots & \vdots \\ Y_{61}^r & Y_{62}^r & \dots & Y_{66}^r \end{bmatrix}_0 [T_{tot}]^T, \quad (\text{A.11})$$

indicates the rail mobilities at point P_1 in the frame x_2, y_2, z_2 .

The transformation performed in terms of mobilities can also be adopted to transform the mobilities of the wheel from the nominal contact point to the new contact point.

In order to verify the rotation and translation, the mobility calculated in a particular contact point with a FE model is compared with that calculated by means of the rotation/translation procedure from the nominal contact point. The results in Figures A.3 and A.4 show that the agreement between the two curves is good in the frequency range considered.

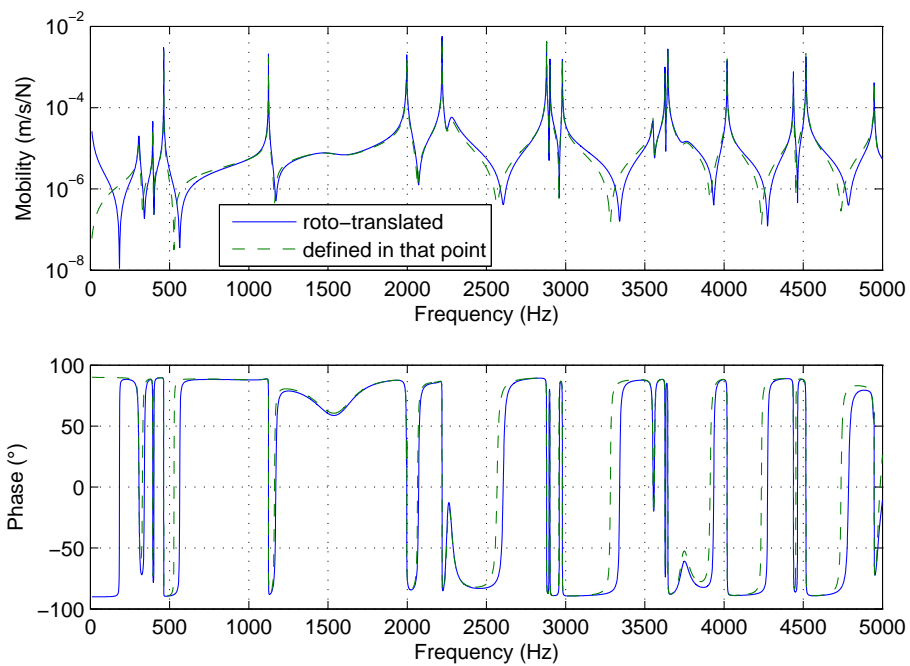


Figure A.3: Comparison between the mobility and phase defined in a contact point with that ones obtained by means of rotation/translation from the nominal contact point (vertical direction).

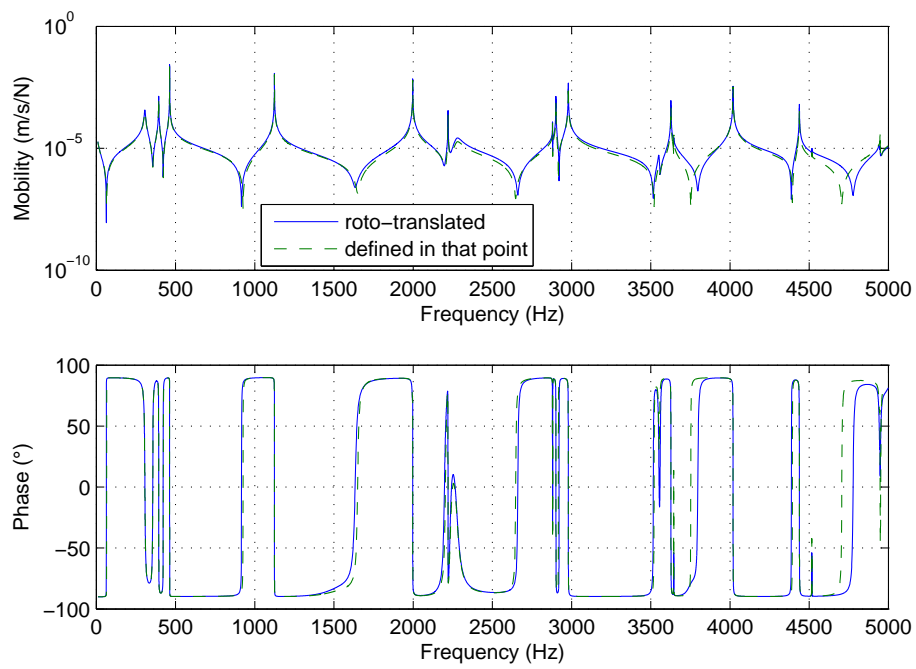


Figure A.4: Comparison between the mobility and phase defined in a contact point with that ones obtained by means of rotation/translation from the nominal contact point (lateral direction).

Bibliography

- [1] Clifford F. Bonnett. *Practical railway engineering*. World Scientific Publishing Company, 2005.
- [2] Thompson and Jones. A review of the modelling of wheel/rail noise generation. *Journal of Sound and Vibration*, 231(3):519–536, March 2000.
- [3] Z. Huang. *Theoretical modelling of railway curve squeal*. PhD thesis, ISVR, University of Southampton, 2007.
- [4] R. Corradi, P. Crosio, S. Manzoni, and G. Squicciarini. Experimental investigation on squeal noise in tramway sharp curves. In *Proceedings of the 8th International Conference on Structural Dynamics, EURO DYN 2011*, Leuven, Belgium, July 2011.
- [5] P. Belforte, F. Cheli, R. Corradi, and A. Facchinetti. Software for the numerical simulation of tramcar vehicle dynamics. *International Journal of Heavy Vehicle Systems*, 10(1):48–69, January 2003.
- [6] F. Cheli, G. Diana, R. Corradi, and A. Facchinetti. Validation of a numerical model for the simulation of tramcar vehicle dynamics by means of comparison with experimental data. *Journal of Computational and Nonlinear Dynamics*, 2(4):299–309, 2007.
- [7] D. J. Thompson, C. J. C. Jones, and G. R. Moutl. Analysis of curve squeal noise from a class 150 Sprinter unit on the Llandudno to Blaenau Ffestiniog line. Technical report, British Rail Research Technical Memorandum TM SAV 22, 1988.
- [8] H. Von Stappenbeck. Streetcar curve noise. *Zeitschrift Vereinschaft Deutscher Ingenieuren*, pages 171–175, 1954.

-
- [9] M. J. Rudd. Wheel/rail noise - Part II: Wheel squeal. *Journal of Sound and Vibration*, 46(3):381–394, June 1976.
- [10] K. Kraft. Der Einfluß der Fahrgeschwindigkeit auf den Haftwert zwischen Rad und Schiene. *AET 22 addendum to ETR*, pages 58–78, 1967.
- [11] C. J. M. van Ruiten. Mechanism of squeal noise generated by trams. *Journal of Sound and Vibration*, 120(2):245–253, January 1988.
- [12] P. J. Remington. Wheel/rail squeal and impact noise: What do we know? What don't we know? Where do we go from here? *Journal of Sound and Vibration*, 116(2):339–353, July 1987.
- [13] U. Fingberg. A model of wheel-rail squealing noise. *Journal of Sound and Vibration*, 143(3):365–377, December 1990.
- [14] J. J. Kalker. Survey of Wheel - Rail Rolling Contact Theory. *Vehicle System Dynamics*, 8(4):317–358, September 1979.
- [15] D. I. Fletcher and S. Lewis. Creep curve measurement to support wear and adhesion modelling, using a continuously variable creep twin disc machine. *Wear*, 298-299:57–65, February 2013.
- [16] F. Périard. *Wheel-rail noise generation: curve squealing by trams*. PhD thesis, Technische Universiteit Delft, 1998.
- [17] Maria A. Heckl and I. D. Abrahams. Curve squeal of train wheels, part 1: Mathematical model for its generation. *Journal of Sound and Vibration*, 229(3):669–693, January 2000.
- [18] Maria A. Heckl. Curve squeal of train wheels, part 2: Which wheel modes are prone to squeal? *Journal of Sound and Vibration*, 229(3):695–707, January 2000.
- [19] Maria A. Heckl and X. Y. Huang. Curve squeal of train wheels, part 3: Active control. *Journal of Sound and Vibration*, 229(3):709–735, January 2000.
- [20] F. G. de Beer, M. H. A. Janssens, and P. P. Kooijman. Squeal noise of rail-bound vehicles influenced by lateral contact position. *Journal of Sound and Vibration*, 267(3):497–507, October 2003.

- [21] D. J. Thompson and M. H. A. Janssens. Theoretical manual, version 2.4. TNO report TPD-HAG-RPT-930214. *TWINS - Track-wheel interaction noise software*, 1997.
- [22] A. Monk-Steel and D. J. Thompson. Models for railway curve squeal noise. In *8th Conf. on Recent Advances in Structural Dynamics*, Southampton, UK, July 2003.
- [23] O. Chiello, J. B. Ayasse, N. Vincent, and J. R. Koch. Curve squeal of urban rolling stock - Part 3: Theoretical model. *Journal of Sound and Vibration*, 293(3-5):710–727, June 2006.
- [24] J. R. Koch, N. Vincent, H. Chollet, and O. Chiello. Curve squeal of urban rolling stock - Part 2: Parametric study on a 1/4 scale test rig. *Journal of Sound and Vibration*, 293(3-5):701–709, June 2006.
- [25] N. Vincent, J. R. Koch, H. Chollet, and J. Y. Guerder. Curve squeal of urban rolling stock-Part 1: State of the art and field measurements. *Journal of Sound and Vibration*, 293(3-5):691–700, June 2006.
- [26] T. G. Bleedorn and B. Johnstone. Steerable steel wheel systems and wheel noise suppression. *IEEE Industry Application Society Annual Meeting Paper*, 37-E:957–963, 1977.
- [27] STARDAMP. *Help file and documentation for mp-editor*, 2012.
- [28] C.J.C. Jones and D. J. Thompson. Rolling noise generated by railway wheels with visco-elastic layers. *Journal of Sound and Vibration*, 231(3):779–790, March 2000.
- [29] A.A. Shabana. *Dynamics of Multibody Systems*. Cambridge university press, 1998.
- [30] J. P. Pascal and G. Sauvage. The Available Methods to Calculate the Wheel/Rail Forces in Non Hertzian Contact Patches and Rail Damaging. *Vehicle System Dynamics*, 22(3-4):263–275, January 1993.
- [31] ZY Shen, JK Hedrick, and JA Elkins. A comparison of alternative creep force models for rail vehicle dynamic analysis. *Vehicle System Dynamics*, 12(1-3):79–83, 1983.

-
- [32] R. Corradi, G. Diana, and A. Facchinetti. Sharp Curve Negotiation Analysis of Tramcar Vehicles with Different Bogie Architectures. In *Proceedings of the First International Conference on Railway Technology: Research, Development and Maintenance*, Civil-Comp Press, Stirlingshire, Scotland, 2012.
- [33] Uni 3142. *Rotaie a gola di acciaio per linee tramviarie. Profili, dimensioni, qualità, prescrizioni e prove*. June 1996.
- [34] A. J. McMillan. A non-linear friction model for self-excited vibrations. *Journal of Sound and Vibration*, 205(3):323–335, August 1997.
- [35] J.J. Kalker. A fast algorithm for the simplified theory of rolling contact. *Vehicle System Dynamics*, 11(1):1–13, 1982.
- [36] H. Hertz. On the contact of elastic solids. *Journal für die Reine und Angewandte Mathematik*, 92:156–171, 1881.
- [37] S. S. Rao. *Mechanical Vibrations*. Upper Saddle River, NJ, 4th edition, 2003.
- [38] D. J. Thompson. *Railway noise and vibration: mechanisms, modelling and means of control*. Elsevier Science, 2009.
- [39] T. X. Wu and D. J. Thompson. Analysis of lateral vibration behavior of railway track at high frequencies using a continuously supported multiple beam model. 106(3):1369–1376, September 1999.
- [40] T. Wu and D. Thompson. Application of a multiple-beam model for lateral vibration analysis of a discretely supported rail at high frequencies. 108(3):1341–1344, September 2000.
- [41] T. Wu. *Development and application of theoretical models for high frequency vibrations of railway track*. PhD thesis, ISVR, University of Southampton, 2000.
- [42] D. E. J. Lurcock. *An investigation into the longitudinal vibration properties of railway track*. BEng dissertation, ISVR, University of Southampton, 2004.
- [43] A. G. J. MacFarlane and I. Postlethwaite. The generalized Nyquist stability criterion and multivariable root loci. *International Journal of Control*, 25(1):81–127, January 1977.

- [44] R. Brockett and C. Byrnes. Multivariable Nyquist criteria, root loci, and pole placement: A geometric viewpoint. *Automatic Control, IEEE Transactions on*, 26(1):271–284, February 1981.
- [45] John F. Barmanj and Jacob Katzenelson. A generalized Nyquist-type stability criterion for multivariable feedback systems. *International Journal of Control*, 20(4):593–622, October 1974.
- [46] C. Desoer and Yung-Terng Wang. On the generalized nyquist stability criterion. *Automatic Control, IEEE Transactions on*, 25(2):187–196, April 1980.
- [47] The MathWorks. *Signal processing toolbox for use with MATLAB: user’s guide*. 2012.
- [48] D. J. Thompson and C. J. C. Jones. Sound radiation from a vibrating railway wheel. *Journal of Sound and Vibration*, 253(2):401–419, May 2002.
- [49] C. M. Nilsson, C. J. C. Jones, D. J. Thompson, and J. Ryue. A waveguide finite element and boundary element approach to calculating the sound radiated by railway and tram rails. *Journal of Sound and Vibration*, 321(3-5):813–836, April 2009.
- [50] Jiannan Yang. *Time domain models of wheel/rail interaction taking account of surface defects*. PhD thesis, ISVR, University of Southampton, 2012.

List of Figures

1.1	Sub-models in the general curve squeal model. Huang [3]	18
2.1	Photo of a Sirio tram. Reproduced from http://www.milanotrasporti.org/	22
2.2	(a) Experimental modal analysis set-up, (b) The 48 measuring points on the wheel, [4].	23
2.3	Axial receptance measured at the tyre point 2 for an axial input at the same point on the suspended wheel.	24
2.4	Axial receptance measured at the web point 1 for an axial input at the same point on the suspended wheel.	25
2.5	Radial receptance measured at a point on the tyre tread for a radial input at the same point on the suspended wheel.	26
2.6	1st peak 535 Hz, out-of-plane mode with 2 nodal diameters	27
2.7	2nd peak 1273 Hz, out-of-plane mode with 3 nodal diameters	27
2.8	3rd peak 1423 Hz, in-plane mode with 3 nodal diameters	27
2.9	4th peak 2230 Hz, in-plane mode with 4 nodal diameters	28
2.10	5th peak 2479 Hz, out-of-plane mode with 4 nodal diameters	28
2.11	6th peak 3367 Hz, in-plane mode with 5 nodal diameters	28
2.12	7th peak 3736 Hz, out-of-plane mode with 5 nodal diameters	29
2.13	8th peak 4662 Hz, in-plane mode with 6 nodal diameters	29
2.14	9th peak 5112 Hz, out-of-plane mode with 6 nodal diameters	29
2.15	10th peak 6040 Hz, in-plane mode with 7 nodal diameters	30
2.16	11th peak 1353 Hz, web flexural mode with 2 nodal diameters	30
2.17	12th(a) peak 1560 Hz, web flexural mode with 0 nodal diameters	30
2.18	12th(b) peak 1604 Hz, web flexural mode with 0 nodal diameters	31
2.19	13th 1951 Hz, web flexural mode with 3 nodal diameters	31
2.20	14th peak 2765 Hz, web flexural mode with 4 nodal diameters	31
2.21	15th peak 3678 Hz, web flexural mode with 5 nodal diameters	32

2.22	16th peak 4585 Hz, web flexural mode with 6 nodal diameters . . .	32
2.23	Blue curve: axial receptance measured at the tyre point 2 for an axial input at the same point considering only the suspended wheel. Red line: axial receptance measured at the tyre point 4 for an axial input at the tyre point 22 considering the whole tram with the wheel resting on the rail.	33
2.24	Curve used to perform the line test, [4].	34
2.25	The tramcar during line test, [4].	34
2.26	(a) Position and sensing direction of the wheel accelerometers, (b) Position and sensing direction of the rail accelerometers, (c) Location and height of the microphones, instrumented wheel on the left side. Dimensions in metres, [4].	35
2.27	Time history and harmonic analysis of the acceleration signals obtained from the inner and outer WA2 sensor (axial direction). . . .	37
2.28	Time-frequency analysis of the acceleration signals obtained from the inner (left Figure) and outer (right Figure) WA2 sensor (axial direction).	37
2.29	Vibration levels of the acceleration signals obtained from the inner (left Figure) and outer (right Figure) WA2 sensor (axial direction). . . .	38
2.30	Time history and harmonic analysis of the acceleration signals obtained from the inner and outer WA3 sensor (radial direction). . . .	38
2.31	Time-frequency analysis of the acceleration signals obtained from the inner (left Figure) and outer (right Figure) WA3 sensor (radial direction).	39
2.32	Vibration levels of the acceleration signals obtained from the inner (left Figure) and outer (right Figure) WA3 sensor (radial direction). . . .	39
2.33	Time history and harmonic analysis of the acceleration signals obtained from the inner and outer R1 sensor.	40
2.34	Time-frequency analysis of the acceleration signals obtained from the inner (left Figure) and outer (right Figure) R1 sensor.	40
2.35	Vibration levels of the acceleration signals obtained from the inner (left Figure) and outer (right Figure) R1 sensor.	41
2.36	Time history and harmonic analysis of the microphone signals obtained from the inner and outer M1 sensor.	41
2.37	Time-frequency analysis of the microphone signals obtained from the inner (left Figure) and outer (right Figure) M1 sensor.	42

2.38	Sound pressure levels obtained from the inner (left Figure) and outer (right Figure) M1 sensor.	42
2.39	Time history and harmonic analysis of the acceleration signals obtained from the WA3, WA2 and R1 sensors. Left Figure: inner side. Right Figure: outer side.	43
2.40	Time history and harmonic analysis of the acceleration signals in the range 13.74 - 13.86 s. The last Figure represent the comparison between them.	44
2.41	Time history and harmonic analysis of the acceleration signals in the range 14.68 - 14.8 s. The last Figure represent the comparison between them.	45
2.42	Time history and harmonic analysis of the acceleration signals in the range 20.12 - 20.18 s. The last Figure represent the comparison between them.	46
2.43	Time history and harmonic analysis of the acceleration signals in the range 23.4 - 23.6 s. The last Figure represent the comparison between them.	47
2.44	Time history and harmonic analysis of the acceleration signals in the range 24.5 - 24.54 s. The last Figure represent the comparison between them.	48
2.45	Photo of the Class 150 Sprinter diesel multiple unit train. Reproduced from http://en.wikipedia.org/	50
2.46	Example of noise spectra measured at each wheel right hand curve of 240 m [7].	51
2.47	Photograph of the test set-up at Pullmans, Cardiff.	52
2.48	Diagram of measurement positions.	53
2.49	Modal identification for undamped Class 15x wheel (0-5 kHz).	54
2.50	Modal identification for undamped Class 15x wheel (5-10 kHz).	54
3.1	Wheel geometry of the model considered to study this example.	59
3.2	Example of screenshot of the software [27].	61
3.3	CAD model of the Sirio wheel	62
3.4	FE model of the Sirio wheel: axi-symmetric model. The coloured vectors indicate the positions where the FRFs are calculated.	63
3.5	Radial receptance at a point on the tyre tread for a radial input at the same point.	64

3.6	Axial receptance at a tyre point for an axial input at the same point.	64
3.7	Axial receptance at a web point for an axial input at the same point.	65
3.8	FE model of the complete Sirio wheel: axi-symmetric model.	66
3.9	CAD model of the complete Sirio wheel	66
3.10	Axial receptance at a web point for an axial input at the same point.	67
3.11	Bond between the hollow axle and the axle.	68
3.12	Axial receptance at a web point for an axial input at the same point.	68
3.13	FE model of the wheel with hollow axle.	69
3.14	Radial receptance at a point on tyre tread for a radial input at the same point.	70
3.15	Axial receptance in a tyre point for an axial input in the same point.	71
3.16	Axial receptance at a web point for an axial input at the same point.	71
3.17	FE model of cross-section of the Class 15x wheel.	77
3.18	Example of mode shapes of Class 15x wheel with n=2.	78
3.19	Diagram of calculation model showing radial excitation at flange- back and running rail connected through contact spring at wheel tread.	80
3.20	Calculated radial receptance of undamped Class 15x wheel at flange- back. (red line) free wheel, (black line) wheel coupled to rail, (blue dotted lines) natural frequencies of radial modes.	80
4.1	Low-floor articulated tramcar (four type A modules and three type B modules). [6]	82
4.2	(a) Frames of reference adopted for each type B module. (b) Frames of reference adopted for each type A module. [6]	83
4.3	Yaw angles of the two axles of a tramway bogie with respect to the track: (a) 'geometric contribution' associated with the ratio be- tween wheelbase and curve radius; (b) 'clearance' contribution cor- responding to the lateral clearance ($\pm c$) between the wheelset and the track [32].	86
4.4	(a) Typical distribution of the lateral contact forces on the four wheels of a tramway bogie. (b) Longitudinal contact forces on a bogie with solid axles: the forces indicated in black and in grey respectively correspond to the effect of the inner rail radius being smaller than that of the outer one and to the effect of a wheelset lateral displacement (with respect to the centred position) [32]. . .	87

4.5	Relative wheel-rail lateral displacement of the second module A.	88
4.6	Relative wheel-rail lateral displacement of the first module A.	89
4.7	Vertical forces on each wheel of the second module A.	90
4.8	Lateral forces on each wheel of the second module A.	91
4.9	Longitudinal forces on each wheel of the second module A.	92
4.10	System of reference adopted in the nominal contact.	93
4.11	Tangents at the contact points of the second module A.	94
4.12	Normal contact forces on the wheels of the second module A.	95
4.13	Transverse contact forces on the wheels of the second module A.	96
4.14	Distribution of the normal and transverse contact forces on the front wheelset of the second module A at 15 seconds into the sim- ulation.	96
4.15	Longitudinal contact forces on the wheels of the second module A.	97
4.16	Longitudinal creepages on the wheels of the second module A.	98
4.17	Transverse creepages on the wheels of the second module A.	99
4.18	Difference in radius of the wheel contact points.	100
4.19	Contact point positions on the front wheelset of the second module A at 15 seconds into the simulation.	100
4.20	Geometry of the rail (grooved rail Ic UNI 3142) adopted for the experimental campaign [33].	101
4.21	Contact point positions on the rails at 15 seconds into the simulation.	102
4.22	Tangents and normal, transverse and longitudinal forces at the contact points of the inner front wheel.	103
4.23	Tangents and normal, transverse and longitudinal forces at the contact points of the outer front wheel.	104
4.24	Longitudinal and transverse creepages at the contact points of the inner and outer front wheels.	105
4.25	Contact point positions on the inner and outer front wheels and inner and outer rails.	106
4.26	Tangents and normal, transverse and longitudinal forces at the contact points of the inner front wheel.	107
4.27	Tangents and normal, transverse and longitudinal forces at the contact points of the outer front wheel.	108
4.28	Longitudinal and transverse creepages at the contact points of the inner and outer front wheel.	109

4.29	Contact point positions on the inner and outer front wheel and inner and outer rail.	110
5.1	Schematic diagram of friction curve, (a) friction force with respect to the sliding velocity, (b) non-dimensional friction force with respect to the creepage. Huang [3]	114
5.2	Mass-on-moving-belt system, (a) friction driven mass-spring-damper system, (b) schematic diagram of the forces acting on the mass. Huang [3]	116
5.3	Feedback loop of the mass-on-moving-belt system. Huang [3]	119
5.4	Equivalent damping effects of the friction force. Huang [3]	120
6.1	Forces and velocities of the wheel/rail contact system: (a) schematic diagram of the wheel/rail contact system, (b) forces acting on the wheel and rail in the contact area, (c) velocities of the wheel and rail. Huang [3]	124
6.2	Multiple beam model for lateral and torsional vibration of rail [39].	130
6.3	Frequency-domain self-excited vibration loop of the wheel/rail contact system. Huang [3]	135
6.4	General self-excited vibration loop of the wheel/rail contact system. Huang [3]	143
6.5	State-space self-excited vibration loop of the wheel/rail contact system. Huang [3]	143
6.6	Lateral friction coefficient versus lateral creepage for different value of λ and κ . In the first graph, the κ value is fixed at 0.05. In the second graph the λ value is fixed at 0.5.	145
6.7	Contact point position on the inner front wheel and inner rail.	146
6.8	Lateral friction versus lateral creepage for λ equal to 0.8 and κ values of 0.04, 0.05 and 0.06.	147
6.9	Curve squeal occurrences diagram for the inner front wheel.	149
6.10	Spectrogram of inner front wheel vibration acceleration during tram pass-by.	150
6.11	Curve squeal occurrences diagram for the inner front wheel with the mode at 2536 Hz suppressed.	151
6.12	Curve squeal occurrences diagram for the inner front wheel with the mode at 2475 Hz suppressed.	152
6.13	Contact point position on the outer front wheel and inner rail.	153

6.14	Curve squeal occurrences diagram for the outer front wheel.	155
6.15	Spectrogram of outer front wheel vibration acceleration during tram pass-by.	156
6.16	Curve squeal occurrences diagram for the outer front wheel in case with increased damping ratio at 1271 Hz.	157
6.17	Curve squeal occurrences diagram for the outer front wheel in case with increased damping ratio at 1417 Hz.	158
6.18	Curve squeal occurrences diagram for the outer front wheel in case with the mode at 1271 Hz suppressed.	159
6.19	Curve squeal occurrences diagram for the outer front wheel in case with the mode at 1417 Hz suppressed.	160
6.20	Curve squeal occurrences diagram for the outer front wheel in case with increased damping ratio at 2224 Hz.	161
6.21	Curve squeal occurrences diagram for the outer front wheel in case with increased damping ratio at 2475 Hz.	162
6.22	Nyquist plots of the eigenvalues.	163
6.23	First one: numerical mode at 529 Hz. Second one: numerical mode at 1271 Hz. Third one: numerical mode at 1417 Hz.	165
6.24	Curve squeal occurrences diagram for the outer front wheel with contact angle between wheel and rail of 30°.	165
6.25	Curve squeal occurrences diagram for the outer front wheel with contact angle between wheel and rail of -45°.	166
6.26	Nyquist plots of the eigenvalues in the case with the real contact angle between wheel and rail.	168
6.27	Nyquist plots of the eigenvalues in the case with contact angle of 30°	169
6.28	Nyquist plots of the eigenvalues in the case with contact angle of -45°	170
6.29	Nyquist plots of the eigenvalues in the case with the real contact angle between wheel and rail and the mode at 1417 Hz suppressed.	171
6.30	Lateral responses of the wheel and rail at the contact position, First Figure: lateral dynamic velocities of the wheel, rail and sliding velocity between wheel and rail, normalized by the vehicle speed V_0 , Second Figure: spectra of the lateral responses of the wheel and rail.	173

6.31	Vertical responses of the wheel and rail at the contact position, First Figure: vertical deflection between wheel and rail; Second Figure: spectra of vertical responses of the wheel and rail.	174
6.32	Noise radiation from the wheel: A-weighted SPL.	175
6.33	Nyquist stability analysis. First figure: Nyquist plots of the eigen- values. Second figure: modulus of the Bode diagram of eigenvalues. Red points: unstable frequencies.	176
7.1	Typical wheel/rail contact position: (a) nominal contact position P_0 , (b) flange (P_2) and tread (P_1) contact positions during left curve negotiation	178
7.2	Frequency domain self-excited vibration loop of the wheel/rail con- tact system with two contact points.	189
7.3	Contact condition between wheel and rail/check rail.	195
7.4	Example of squeal at 2.2 kHz measured on leading left and right wheel. Left hand curve [7].	198
7.5	Example of squeal at 2.8 kHz measured on leading left and right wheel. Left hand curve [7].	199
7.6	Example of squeal at 3.6 kHz measured on leading left and right wheel. Right hand curve [7].	200
7.7	Example of squeal at 4.4 kHz measured on leading left and right wheel. Left hand curve [7].	201
7.8	Curve squeal occurrences diagram for the undamped outer front wheel. Occurrences of the most predicted frequency: more than 60 % of the 450 cases considered.	202
7.9	Curve squeal occurrences diagram for the damped outer front wheel. Occurrences of the most predicted frequency: less than 8 % of the 450 cases considered	203
7.10	Curve squeal occurrences diagram for the undamped outer front wheel with λ equal to 0.6. Occurrences of the most predicted fre- quency: less than 60 % of the 450 cases considered	204
7.11	Curve squeal occurrences diagram for the damped outer front wheel with λ equal to 0.6. Occurrences of the most predicted frequency: less than 6 % of the 450 cases considered.	205
7.12	Curve squeal occurrences diagram for the undamped outer front wheel with λ equal to 0.6.	206

7.13 Contact points position on the inner and outer front wheel and inner and outer rail.	207
7.14 Curve squeal occurrences diagram for the inner front wheel.	210
7.15 Spectrogram of inner front wheel vibration acceleration during tram pass-by.	211
7.16 Curve squeal occurrences diagram for the outer front wheel	212
7.17 Spectrogram of outer front wheel vibration acceleration during tram pass-by.	213
7.18 Curve squeal occurrences diagram for the damped inner front wheel. Occurrences of the most predicted frequency: less than 6 % of the 450 cases considered	214
7.19 Curve squeal occurrences diagram for the damped outer front wheel. Occurrences of the most predicted frequency: less than 3 % of the 450 cases considered	215
A.1 Typical wheel/rail contact position: (a) nominal contact position P_0 , (b) flange contact position P_1 and the relative relation between two frames. Huang [3]	219
A.2 Rigid transform: translating from P_0 to P_1 and then rotating about the x-axis. Huang [3]	220
A.3 Comparison between the mobility and phase defined in a contact point with that ones obtained by means of rotation/translation from the nominal contact point (vertical direction).	223
A.4 Comparison between the mobility and phase defined in a contact point with that ones obtained by means of rotation/translation from the nominal contact point (lateral direction).	224

List of Tables

2.1	Experimental frequencies involved in squeal phenomenon observed from the WA2, WA3 and WA6 sensors of the inner front wheel for different time ranges. Values in Hz.	49
2.2	Experimental frequencies involved in squeal phenomenon observed from the WA2, WA3 and WA6 sensors of the outer front wheel for different time ranges. Values in Hz.	49
2.3	Measured natural frequencies and damping ratios of undamped Class 15x wheel.	55
2.4	Measured natural frequencies and damping ratios of damped Class 15x wheel.	55
3.1	Experimental natural frequencies, damping ratio and mode shapes of the wheel in comparison with the numerical ones.	76
3.2	Calculated natural frequencies of Class 15x wheel.	78
3.3	Differences between measured and predicted natural frequencies of Class 15x wheel.	79
4.1	Spin creepages at the contact points of the inner and outer front wheel at 15 seconds into the simulation.	99
4.2	Contact point positions of the inner and outer front wheel at 15 seconds into the simulation	101
4.3	Contact point positions of the inner and outer rail at 15 seconds into the simulation	102
4.4	Spin creepage at the contact points of the inner and outer front wheel at 15 seconds into the simulation.	104
4.5	Contact point positions of the inner and outer front wheels and inner and outer rails at 15 seconds into the simulation.	107

4.6	Spin creepage at the contact points of the inner and outer front wheel at 15 seconds into the simulation.	108
4.7	Contact point positions of the inner front wheel and inner rail at 15 seconds into the simulation.	110
6.1	Input parameters at contact point on the tread of the inner front wheel.	146
6.2	Numerical modes involved in squeal compared with the experimental frequencies involved in squeal and frequency range predicted by the model.	150
6.3	Input parameters at contact point on the tread of the outer front wheel.	153
6.4	Numerical modes involved in squeal compared with the experimental frequencies involved in squeal and frequency range predicted by the model.	156
7.1	Input parameters at contact points for outer front wheel.	196
7.2	Numerical modes involved in squeal compared with the experimental frequencies involved in squeal and frequency range predicted by the model.	198
7.3	Input parameters at contact points 1 and 2 for the inner and outer front wheel.	208
7.4	Numerical modes involved in squeal compared with the experimental frequencies involved in squeal and frequency range predicted by the model (inner front wheel).	210
7.5	Numerical modes involved in squeal compared with the experimental frequencies involved in squeal and frequency range predicted by the model (outer front wheel).	211
7.6	Damping ratio of the damped wheel.	213

